2017

A Comparative Study of Sensory Neuron Synaptic Activity and the Role of Presynaptic Diversity, Specificity, and Regulation in Caenorhabitis Elegans

Donovan Ventimiglia

A COMPARATIVE STUDY OF SENSORY NEURON SYNAPTIC ACTIVITY AND THE ROLE OF PRESYNAPTIC DIVERSITY, SPECIFICITY, AND REGULATION IN *CAENORHABITIS ELEGANS*

A Thesis Presented to the Faculty of

The Rockefeller University

in Partial Fulfillment of the Requirements for

the degree of Doctor of Philosophy

by

Donovan Ventimiglia

June 2017

A COMPARATIVE STUDY OF SENSORY NEURON SYNAPTIC ACTIVITY AND THE ROLE OF PRESYNAPTIC DIVERSITY, SPECIFICITY, AND REGULATION IN *CAENORHABITIS ELEGANS*

Donovan Ventimiglia, Ph.D.

The Rockefeller University 2017

Chemical synapses are complex structures that have a diversity of specific activities that shape nervous system computation. To understand how this diversity contributes to specific circuit functions, we sought to characterize synaptic release in the stereotyped and defined neural circuitry of *C. elegans*. Here we use pHluorin imaging (Vglut-pH) to monitor presynaptic glutamate release from single chemosensory neurons in intact animals and characterize the dynamics of endo- and exocytosis from two types of glutamatergic neurons, AWC^{ON} and ASH.

In Chapter 1, we describe the optimization of Vglut-pH, we introduce a reagent for measuring synaptic calcium influx by tethering GCaMP to synaptic vesicles, and we provide our initial characterization of glutamate release in AWC^{ON} and ASH. Our results indicate that AWC^{ON} and ASH have distinct exocytosis dynamics and that AWC^{ON} exhibits synaptic release properties similar to vertebrate photoreceptors and retinal bipolar neurons, aligning with previous results from functional calcium imaging, gene expression, and circuitry.

In Chapter 2, we characterize the dynamics of endocytosis in AWC^{ON} and ASH. We find that synaptic vesicle endocytosis in these neurons have kinetic features and timescales similar to that of mammalian neurons. We show that endocytosis appears to be homeostatically regulated by previous neuronal activity and is composed of at least two kinetically distinct modes, fast and slow. We show that fast retrieval is dependent on the clathrin adaptor protein AP180/CALM, suggesting that clathrin-mediated endocytosis is important for synaptic vesicle retrieval in these sensory neurons.

In Chapter 3, we compare and contrast the dependences of AWC^{ON} and ASH Vglut-pH responses on the core synaptic vesicle release machinery and its regulators: syntaxin, synaptobrevin, SNAP-25, *unc-13, unc-18,* RIM, complexin, and tomosyn. We find that Vglut-pH responses are highly dependent on the core components of the SNARE complex and its regulators, but we detected significant differences in the residual responses in these mutants that suggest AWC^{ON} and ASH synapses are distinct from each other and from those of the neuromuscular junction. We find that complexin appears to act as an inhibitor of SV release in AWC^{ON} and ASH, and we find an unexpected role for tomosyn in regulating calcium influx.

In Chapter 4, we describe activity-dependent cytoplasmic pH changes in AWC^{ON} and ASH, and we conduct a series of experiments to show that these pH changes do not interfere with the measurement or interpretation Vglut-pH signals. Our results indicate that these activity-dependent pH changes are consistent with a depolarization-generated acidosis and are correlated with calcium influx. We

show that these pH changes in response to stimulation are not dependent on *unc-13* or *unc-18* and are thus are largely independent of synaptic release. Finally, we show that in contrast to intracellular pH, extracellular pH changes are not detected in response to sensory stimulation.

In Chapter 5, we investigate the role of synaptotagmins in AWC^{ON} and ASH glutamate release using Vglut-pH imaging. We find that AWC^{ON} basal release is highly dependent on *snt-1*, whereas ASH exocytosis is intact in *snt-1* null mutants and slightly diminished in *snt-6* mutants. Our results indicate that AWC and ASH synapses have distinct requirements for *snt-1* and may use a combination of calcium sensors to mediate glutamate release.

In Chapter 6, we use a combination of genetics, behavior, calcium imaging, and Vglut-pH imaging to investigate how loss-of-function mutations in *pkc-1* (protein kinase C epsilon) modulate AWC^{ON} butanone olfactory preference. We find that *pkc-1* functions in AWC^{ON} downstream of presynaptic calcium influx to modulate *eat-4* dependent glutamate release and a second form of AWC^{ON} output that is important for specifying butanone olfactory preference. We identify the receptor-type guanylate cyclase *gcy-28* and Gqα as additional important regulators of AWC^{ON} synaptic release, and identify *unc-31* (CAPS) as an additional genetic determinant of butanone olfactory preference. Finally, we suggest a model for a dual function Gqα/DAG/*pkc-1* signaling pathway that regulates synaptic vesicle release and butanone preference in AWC^{ON}.

Our work in this thesis extends the characterization of *C. elegans* synapses from the neuromuscular junction to the presynaptic terminals of central synapses and supports a role for presynaptic diversity among distinct neuronal cell types in *C. elegans.* Our work emphasizes that presynaptic diversity and regulation of neurotransmitter release are important components to specifying circuit function and suggest that *C. elegans* will provide a deeper understanding of how presynaptic diversity, both in terms of molecular components and activity dynamics, contribute to nervous system function.

For my family

ACKNOWLEDGEMENTS

I would like to truly thank my advisor, Cori Bargmann, for her mentorship, guidance, inspiration, and friendship over the past 7 years. In addition to giving me extraordinary scientific freedom to explore my interests, Cori has bestowed on me her passion for the study of animal behavior, something that will continue to shape my interests for years to come.

I would like to thank my thesis committee, Tim Ryan and Gaby Maimon. I have greatly appreciated your support, expertise, and insight throughout my PhD. I would also like to thank Jeremy Ditttman for graciously agreeing to serve as my external committee member and for reviewing this thesis.

The best way to do science is alongside a good friend. Johannes Larsch has been my partner in science and is a very dear friend. Johannes' passion for science and rigorous critique is a treasured part of my time as a PhD student.

I would like to thank the many members of the Bargmann Lab. You have all made the laboratory a fun, vibrant place, and have made the lab feel like a second home. It was great learning from all of you. I would like to especially thank my bay-mates, Andrew Gordus and May Dobosiewicz, you have added so much life and happiness to my time in the lab. Andres Bendesky taught me how to do molecular biology 'the fast way' – and it does work. Steve Flavell was always there to provide encouragement and experimental expertise, I learned many things from your guidance. Sagi Levi is an extremely thorough experimentalist and rigorous thinker; I have very much enjoyed our time working together.

I am lucky enough to have a brother-in-law who is a professor of mathematics at NYU. I want to thank Adi Rangan for his help in analyzing the kinetics of endocytosis and building kinetic models. The many afternoons we spent together were some of the most fun occasions I have had analyzing data.

I would like to thank my parents, especially my mother, for always supporting my many different directions in life. Without her encouragement to pursue whatever passion I had, I would had never found science.

When I arrived at Rockefeller I met a group of fellow students who have become like family to me: Roman Corfas, Kate Leitch, Tom McDonagh, Monica Mugnier, and Ben Sabari. We have lived together, studied together, traveled together, and done pretty much everything else in-between together for the past 7 years. I want to thank each of you for your friendship and support over the years, and for being the most rad group of weirdos ever.

The greatest thing I have gained from my time at Rockefeller is my wife Kavita Rangan and my daughter Fable Ventimiglia. Kavi is brilliant, an extraordinary scientist and experimentalist, and is truly talented in most everything that she does. She is my source for inspiration, imagination, and passion in life, and she is my best friend. Thank you for all your support during the process of completing this thesis. I am so lucky to have created a wolf pack with you.

TABLE OF CONTENTS

LIST OF FIGURES

Thesis Introduction

Chapter 1

Chapter 2

Chapter 3

Chapter 5

Chapter 6

Supplemental Methods

Thesis Introduction

Information processing and communication in the nervous system occurs through synapses, specialized structures between neurons where the release of chemical neurotransmitters propagates information from one neuron to the next. The structure of these connections and their specific attributes are the basis for the action of the neural circuits that give rise to all functions of the nervous system. A central question in neuroscience is understanding how synaptic organization and the regulation of neurotransmitter release contribute to circuit design and function. Neurotransmitter release is a highly regulated and complex process that produces a diversity of properties at different synapses (Atwood and Karunanithi, 2002). Synapses using the same type of neurotransmitter can have a wide range of dynamics, timescales, and requirements for neurotransmitter release, all of which can be modified over time by intrinsic and extrinsic factors. How these cellular properties contribute to information processing, circuit function, and ultimately behavior, are important areas of research.

Different forms of synaptic vesicle (SV) release have been evident from some of the earliest characterizations of neuronal signaling. For example, the subthreshold spontaneous release of neurotransmitter that gave rise to the quantal vesicle hypothesis (Fatt and Katz, 1952; Katz, 1969), is a salient form of neurotransmitter release in all synapses that is molecularly and functionally partially distinct from the release generated by an action potential (Kavalali, 2015). Early recordings from crustaceans found ‘phasic’ and ‘tonic’ glutamatergic motor neurons that had specialized forms of release (Kennedy and Takda, 1965;

Millar and Atwood, 2004). Phasic neurons fire in brief bursts and release large amounts of glutamate, whereas tonic neurons fire with a higher frequency but release much less glutamate. The difference in the amount of neurotransmitter released from a synapse is called synaptic strength, and this feature has been found to vary widely among synapses (Atwood and Karunanithi, 2002). The variation in synaptic strength is particularly apparent at the small synapses of the central nervous system, reflecting their probabilistic release of neurotransmitter in response to a single action potential (Korber and Kuner, 2016). The probability of SV release ranges from less than 10% in neurons like Rat L5/6 pyramidal neurons to greater than 90% in the climbing fibers of the cerebellum (Branco and Staras, 2009). Differences in release probabilities can also be heterogeneous among the synapses of a single neuron, with activities that are specific to their post-synaptic partners (Branco and Staras, 2009). Furthermore, some synapses are present in a dormant or ‘silent’ state and can be activated by intracellular signaling, potentially allowing communication with distinct postsynaptic partners in a conditional manner (Kim and Ryan, 2010; Kim and Ryan, 2013).

The dynamics of the release process also varies among synapses. Two major forms of calcium-triggered release in spiking neurons are fast and asynchronous release (Kaeser and Regehr, 2014). Fast release represents the synchronous fusion of synaptic vesicles with the arrival of an action potential. It occurs within a millisecond after the action potential enters the presynaptic terminal and ends within a millisecond or two after the action potential. This type of release is most common among vertebrate CNS neurons and has been

extensively characterized. Asynchronous release refers to synaptic release that continues after the arrival of an action potential and can last for tens of seconds (Kaeser and Regehr, 2014). Sustained high-frequency activation at some synapses can trigger asynchronous release following fast synchronous release. In other neurons, a single stimulation can result in asynchronous release. Although less common than fast release, asynchronous release is a prominent feature at certain specialized synapses of the hypothalamus, dorsal horn, and the deep cerebellar nuclei (Kaeser and Regehr, 2014). Another prominent form of synaptic release is tonic or graded synaptic release. The most well-characterized graded synapses are those of the vertebrate retina, photoreceptor, and bipolar neurons (Heidelberger, 2007). Here, synaptic release that occurs continuously and scales directly with membrane potential is thought to provide an increased potential for information encoding (de Steveninck and Laughlin, 1996; Heidelberger, 2007).

Synapses can also have unique responses to the pattern of neural activity, termed short-term plasticity (Regehr, 2012). In response to repeated neural activity, specific synapses facilitate or depress release over time. For example, under the same stimulation pattern, the synapses from climbing fibers to Purkinje cells become depressed with repeated stimulation, whereas the connections from parallel fibers become facilitated (Dittman et al., 2000). Such activity-dependent diversity in synaptic release is thought to add nuance to information processing (Abbott and Regehr, 2004).

Diversity in presynaptic activity may stem from a variety of sources, including active zone morphology, presynaptic calcium, diversity in vesicle pools, second messengers (such as protein kinases or lipid signaling pathways), and the molecular machinery associated with SV release (Atwood and Karunanithi, 2002; Crawford and Kavalali, 2015; Kasai et al., 2012) (Figure 1). Variation in the expression of presynaptic proteins among different synapses is another striking indication of presynaptic diversification (O'Rourke et al., 2012). For example, even the basic components of the synaptic vesicle fusion machinery, such as the SNARE proteins syntaxin, synaptobrevin, and SNAP-25, encode multiple isoforms that are differentially expressed throughout the nervous system (Boschert et al., 1996; Ruiz-Montasell et al., 1996; Trimble et al., 1990). Another prominent example is the distribution of the synaptic vesicle calcium sensors, the synaptotagmins (Sudhof, 2002; Ullrich et al., 1994). Synaptotagmins are responsible for triggering the release of SVs in response to calcium influx, and there are three major synaptotagmins expressed throughout the rat brain that mediate fast synaptic transmission. Each of these synaptotagmins has distinct calcium binding properties and effects on the kinetics of SV release (Xu et al., 2007).

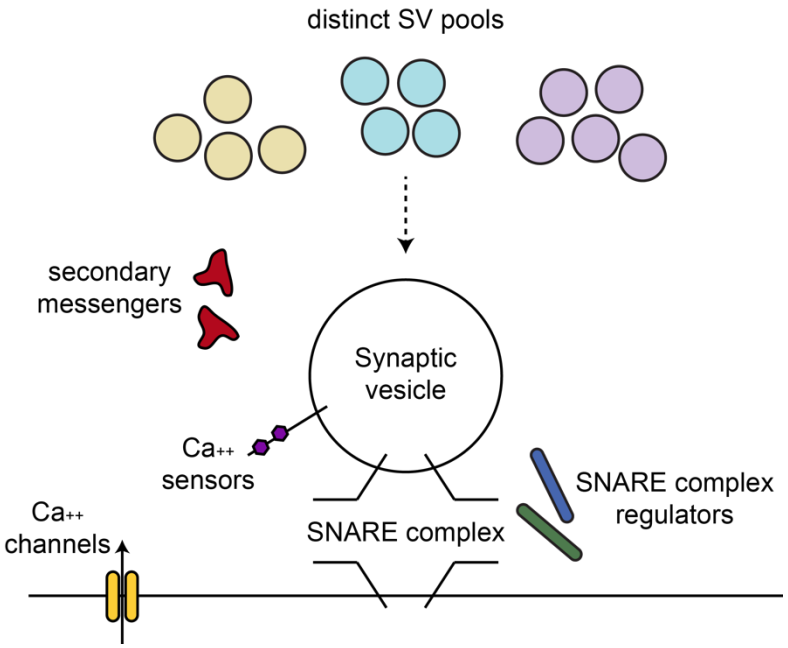

Figure 1. Classes of presynaptic diversity.

Simplified diagram of the presynaptic terminal highlighting some of the important contributors to synaptic diversity. In this thesis, we will focus on the exploring the roles of the SNARE complex and its regulators, the calcium sensors mediating synaptic release (synaptotagmins). We will also address roles of second messengers implicated in modulating synaptic release, such protein kinase C and DAG (lipid) signaling downstream of presynaptic G protein-coupled receptors (not shown in this diagram).

Although presynaptic diversity is widely documented, its functional roles in the nervous system have been difficult to elucidate. Genetically disrupting synaptic components often leads to non-viable progeny and techniques used to measure presynaptic strength are not easily applicable to *in vivo* systems (Atwood and Karunanithi, 2002; Borst, 2010). In addition, given the prevalence of activity-dependent changes in synaptic activity, physiological patterns of activity may be important to understand a given synaptic state (Regehr, 2012). Moreover, the complexity of most circuits and the difficulty of obtaining a measurable output of circuit function makes it difficult to assess how one particular presynaptic property contributes to circuit function.

The well-studied neural circuitry of *C. elegans* eliminates some of these key issues and provides an opportunity to study presynaptic diversity. *C. elegans* has 302 neurons with approximately 9000 reproducible synaptic connections; it represents the only metazoan whose nervous system has a complete wiring diagram (Varshney et al., 2011; White et al., 1986). This synaptic map, combined with the genetic tractability and fast life cycle of *C. elegans*, provides an exceptional tool to study neural circuitry. Extensive prior work has mapped specific *C. elegans* behaviors to genes and neural circuits (de Bono and Maricq, 2005; Dittman, 2009). In addition, most synaptic proteins are conserved, with readily available mutants that are viable (Richmond, 2005). This background provides a framework to examine the roles of presynaptic properties in discrete circuit functions.

C. elegans lack voltage-gated sodium channels, and most of its neurons are thought to exhibit graded release (Bargmann, 2006; Goodman et al., 1998; Liu et al., 2009). Although graded release is phenomenologically distinct from synaptic release driven by action potentials, the underlying mechanisms controlling graded release are thought to be similar (Liu et al., 2009). Blocking action potentials in spiking neurons allows synaptic release to vary linearly with membrane potential similar to graded release, indicating that the action potential mainly fixes the duration of depolarization at the synaptic terminal (Katz and Miledi, 1967b; Llinas et al., 1981). Accordingly, the examination of synaptic properties of *C. elegans* has provided insights that are broadly applicable to the understanding of synaptic function.

Behavioral genetics in *C. elegans* led to the first identification of many components essential to the process to synaptic vesicle fusion, such as the SNARE assembly proteins *unc-13* and *unc-18* (Brenner, 1974; Richmond, 2005; Sieburth et al., 2005). However, the study of synaptic transmission in *C. elegans* has been almost exclusively limited to the neuromuscular junction (NMJ) due the organism's relative inaccessibility to electrophysiological analysis (Schafer, 2006). Thus, the potential synaptic diversity among CNS connections important for mediating behavior have remained largely unexplored. Recently, the advent of genetically-encoded fluorescent activity reporters (Akerboom et al., 2012; Tian et al., 2009) has provided new inroads to analyze the dynamic activity of intact neural circuits. In particular, the development of pHluorin (Miesenböck et al.,

1998), a genetically encoded reporter of presynaptic activity, offers the possibility of exploring presynaptic release in intact circuitry in *C. elegans*.

C. elegans interacts with its environment in large part through 12 pairs of bilaterally symmetric chemosensory neurons located in the head of the animal (Bargmann, 2006). Many distinct behaviors, such as chemotaxis to specific odorants or escape from harsh chemicals, are localized to specific sensory neurons (Bargmann, 2006; de Bono and Maricq, 2005). This feature allows different circuits to be probed starting with well-defined sensory inputs and presents an ideal case for examining how presynaptic diversity contributes to specific neural functions in response to natural stimuli.

In this thesis, we use pHluorin imaging in *C. elegans* to explore the roles of synaptic diversity, specificity, and regulation on neural circuit function by examining the synapses of two glutamatergic chemosensory neurons, AWC and ASH. AWC regulates chemotaxis to attractive odors whereas ASH mediates escape behavior to aversive stimuli. AWC and ASH are well-characterized neurons that provide an opportunity to examine how the dynamics of glutamate release mediates two very different behaviors. In Part 1, we compare and contrast features of AWC and ASH synaptic release. We optimize pHluorin imaging as a reporter of synaptic activity in *C. elegans,* and characterize the dynamics of exocytosis and endocytosis in AWC and ASH. We also explore the dependency of AWC and ASH synaptic activity on the core synaptic vesicle machinery and its regulators as well as the synaptotagmins. In Part 2, we explore how regulators of neurotransmitter release contribute to specific behavioral

outputs, by investigating synaptic signaling pathways known to modulate AWC's butanone olfactory preference.

Chapter 1: Development of Vglut-pH Imaging and characterization of AWC and ASH synaptic release

AWC neurons are a bilateral pair of glutamatergic sensory neurons that mediate chemotaxis to attractive volatile odors (Bargmann, 2006). Each ciliated AWC neuron is located in the head of the animal, where it sends a dendritic sensory process through the anterior amphid to the nose, and sends an axonal process into the nerve ring, a bundle of neuronal processes where the majority of neuronal connections are made (White et al., 1986). AWC detects odor cues through G-protein-coupled receptors (GPCRs) located in the cilia, initiating a signal transduction cascade that regulates cGMP levels through receptor guanylate cyclases, resulting in the modulation of cGMP-gated ion-channels (Bargmann, 2006). The two AWC cells are functionally distinct; they detect both unique and overlapping odors and have distinct gene expression profiles, and are termed AWC^{ON} and AWC^{OFF} based on the expression of the GPCR gene *str-2* (Troemel et al., 1999; Wes and Bargmann, 2001). This functional distinction between neurons is determined stochastically in development, such that AWC^{ON} may be either the left or right cell (Troemel et al., 1999). The identity of each AWC cell can be determined by cell-specific expression markers, and their promoters also permit each AWC to be manipulated independently. Functional calcium imaging indicates that AWC hyperpolarizes upon odor stimulation, and depolarizes on stimulus removal (Chalasani et al., 2007; Zaslaver et al., 2015) (Fig 1.1A).

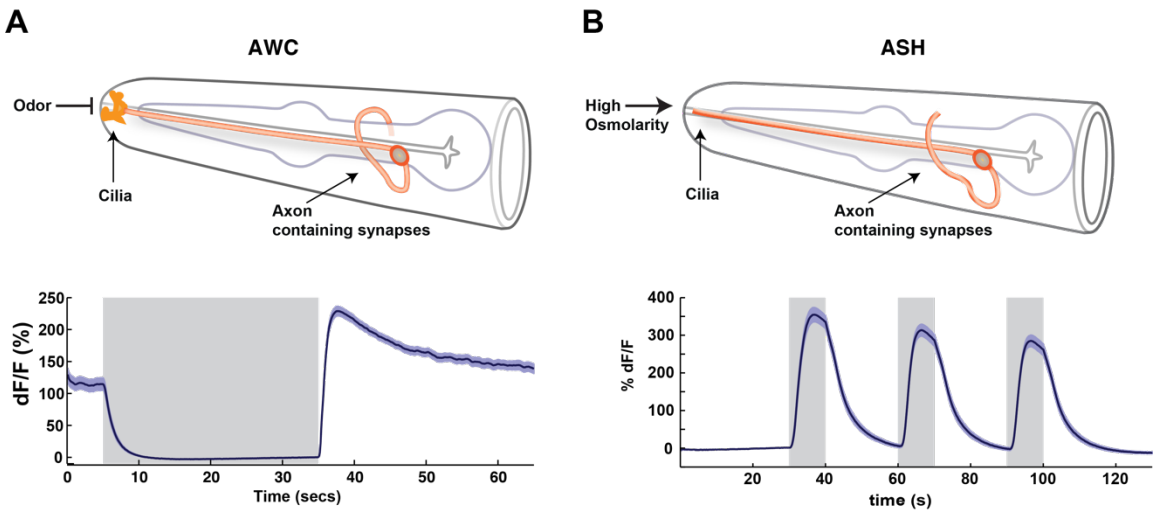

Figure 1.1 AWC and ASH calcium signals in response to sensory stimulation.

(A) Top: Diagram of AWC^{ON} anatomy. Bottom: AWC GCaMP5 responses measured at the cell body in response to butanone stimulation. n = 47 trials, from 16 animals, 2-3 trials each. Gray bar = stimulus, 11.2 uM butanone. **(B**) Top: Diagram of ASH anatomy. Bottom: ASH GCaMP3 responses measured at the cell body in response to high osmolarity NaCl stimulation. n = 39 trials from 13 animals, 3 trials each. Gray bar = stimulus, 500 mM NaCl. Anatomy diagrams redrawn and adapted from WormAtlas.com by Gautam Rangan.

AWC has also been suggested to exhibit tonic neurotransmitter release, with a similar signaling pattern to vertebrate photoreceptors; at rest, neurotransmitter is tonically released; during hyperpolarization, release decreases; and upon depolarization, release increases (Chalasani et al., 2007; Zhang and Cote, 2005). As the two AWC neurons are functionally distinct and have overlapping axonal processes, we focused solely on AWC^{ON} and its specific odorant butanone. As well as being the best characterized neuron of the AWC pair, AWC^{ON} also has a unique form of olfactory plasticity (Colbert and Bargmann, 1995; Torayama et al., 2007), in which a pathway regulating neurotransmission can switch the innate butanone preference from attraction to repulsion and is examined in Chapter 6 (Tsunozaki et al., 2008).

A second bilateral pair of glutamatergic chemosensory neurons are the ASH neurons. Instead of mediating chemotaxis, they function as polymodal nociception receptors for chemical and mechanical repellents; unlike AWC, the left and right ASH neurons have similar functions (Bargmann, 2006). Detection of nociceptive stimuli causes the animal to immediately reverse and change direction (Goodman, 2006; Kaplan and Horvitz, 1993). ASH, like AWC, is located in the head of the animal where it sends a ciliated dendrite to the nose and a single axonal process into the nerve ring (White et al., 1986). Noxious chemicals, high osmolarity, or nose touch trigger a strong increase in calcium levels (Hilliard et al., 2005; Kato et al., 2014). ASH detects noxious chemicals through G-protein-coupled receptors (GPCRs) located in the cilia, initiating a signal

transduction cascade that regulates TRPV and voltage-gated calcium channels (Kato et al., 2014). In this thesis, we use a high osmolartiy NaCl stimulus, which triggers a robust and rapid increase in calcium in ASH that immediately decreases upon stimulus removal (Chatzigeorgiou et al., 2013; Kato et al., 2014) (Fig 1.1B). Such temporal properties are ideal for correlating calcium responses with exocytosis and endocytosis.

To measure synaptic release from AWC^{ON} and ASH, we used a pHluorin-based imaging technique widely used to monitor synaptic exo- and endocytosis. Developed by Miesenbock and coworkers, this method, diagrammed in Figure 1.2, exploits the acidic pH of synaptic vesicles (SVs) to monitor vesicle fusion by measuring changes in pH (Miesenböck et al., 1998). In this method, a highly pH-sensitive variant of green fluorescent protein (termed pHluorin) is targeted to the lumen of synaptic vesicles, which are normally acidified by a vacuolar H^+ ATPase that generates the electrochemical gradient necessary to load vesicles with neurotransmitter. During synaptic vesicle fusion, the luminal contents are released and the acidic pH instantly equilibrates with extracellular medium, driving an increase in pHluorin fluorescence. Upon vesicle retrieval and re-acidification, pHluorin fluorescence is again quenched, providing a readout of endocytosis (Dittman and Ryan, 2009).

At the core of this method is an enhanced form of pHluorin, termed super-ecliptic, that undergoes large fluorescence changes in response to changes in pH (Sankaranarayanan et al., 2000). This variant is nearly quenched at the pH of

mammalian SVs (pH ~5.6) and exhibits an ~20-fold fluorescence increase upon shifting to the neutral pH of the extracellular medium (pH ~7.4).

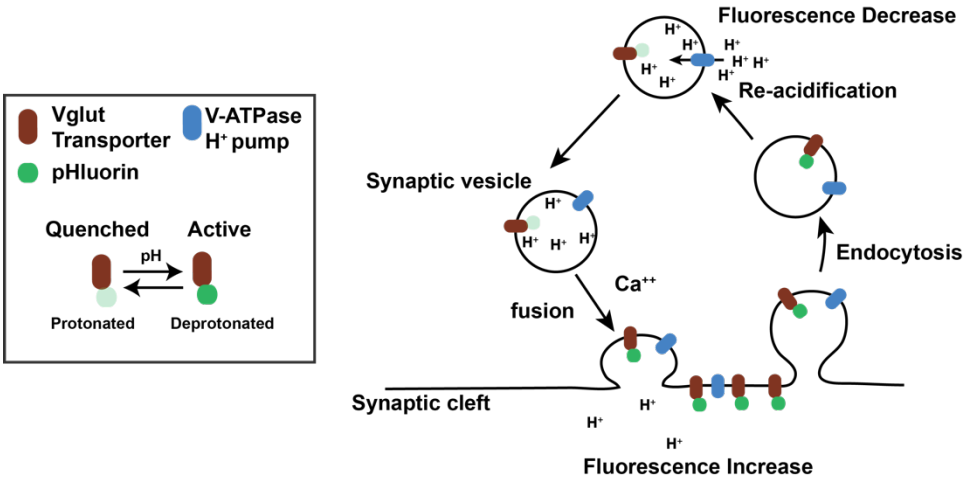

Figure 1.2. Monitoring synaptic release and recycling with Vglut-pH

Super-ecliptic pHluorin is fused within the first luminal domain of the *C. elegans* Vglut-1 transporter *eat-4*, targeting pHluorin within glutamatergic synaptic vesicles (SVs). The lumen of SVs before fusion are acidified by the V-ATPase proton pump that produces the electrochemical gradient needed for neurotransmitter loading. The fluorescence of pHluorin, with a pKa of ~7.1, is nearly quenched within the acidified SV. Upon SV fusion, the lumen of the vesicle is exposed to the extracellular environment causing an instantaneous increase in pH, generating an increase in fluorescence signal as pHluorin molecules become deprotonated. Endocytosis coupled with re-acidification generates a decrease in fluorescence signal as pHluorin again becomes protonated and quenched. Redrawn from (Dittman and Ryan, 2009).

The first pHluorin-based measurements of synaptic activity targeted pHluorin to the luminal domain of synaptic vesicles by fusing the reporter to the SNARE vesicle fusion protein synaptobrevin (Miesenböck et al., 1998). pHluorin has since been appended to numerous synaptic vesicle proteins to study the recycling dynamics of specific SV proteins as well as specific classes of synaptic vesicles (Dean et al., 2012; Dittman and Kaplan, 2006; Fernández-Alfonso et al., 2006; Mani and Ryan, 2009; Pan and Ryan, 2012; Voglmaier et al., 2006). pHluorin imaging has been extensively used to study cells *in vitro*, and under the proper optical arrangement, pHluorin-based measurements can be highly sensitive and report the exo- and endocytosis of single SVs (Balaji and Ryan, 2007). In addition, pHluorin imaging has been applied to measure population level synaptic activity within intact circuitry, such as in the olfactory bulb of mice, the antennal lobe of flies, and the retina of zebrafish. (Bozza et al., 2004; Odermatt et al., 2012; Shang et al., 2007). However, pHluorin has not been previously used to monitor vesicle fusion with single neuron resolution *in vivo*.

To monitor synaptic activity in the glutamatergic AWC and ASH sensory neurons of *C. elegans*, we used the method designed by Susan M. Voglmaier and Robert Edwards in which super-ecliptic pHluorin is fused within the first luminal loop of the vesicular glutamate transporter Vglut-1 (here termed Vglut-pH) (Voglmaier et al., 2006). The vesicular glutamate transporter has a very brief plasma membrane residence time after vesicle exocytosis, providing a key advantage compared to other pHluorin targeting methods. Its rapid endocytosis greatly increases the signal-to-background ratio of Vglut-pH compared to other

pHluorin reporter constructs, such as synaptobrevin-pHluorin, making Vglut-pH better suited to study synaptic release within intact circuitry (Balaji and Ryan, 2007; Dreosti and Lagnado, 2011).

In this chapter, we present our initial optimization and characterization of Vglut-pH in AWC^{ON} and ASH sensory neurons. We report that Vglut-pH is a robust and sensitive reporter of synaptic vesicle release and recycling from single neurons within intact animals. Vglut-pH imaging of stimulus-triggered activity was consistent with the general effects on synaptic transmission predicted from AWC^{ON} and ASH functional calcium imaging, and provided additional insights suggesting that glutamate release from these two sensory neurons have distinct dynamics.

Results

To generate Vglut-pH, we used homology alignment to the mammalian Vglut-1 to insert super-ecliptic pHluorin within the first luminal domain of the *C. elegans* Vglut-1 homolog *eat-4*. We expressed this construct in AWC^{ON} using the cell-specific promoter *str-2p* and found that Vglut-pH was exclusively localized to the axon, with a semi-discontinuous distribution consistent with synaptic vesicles (Fig 1.3A). We imaged stimulus-evoked Vglut-pH responses in microfluidic chips that immobilize the animal and allow for precise delivery and removal of chemical stimuli (Fig 1.3B) (Chalasani et al., 2007; Chronis et al., 2007).

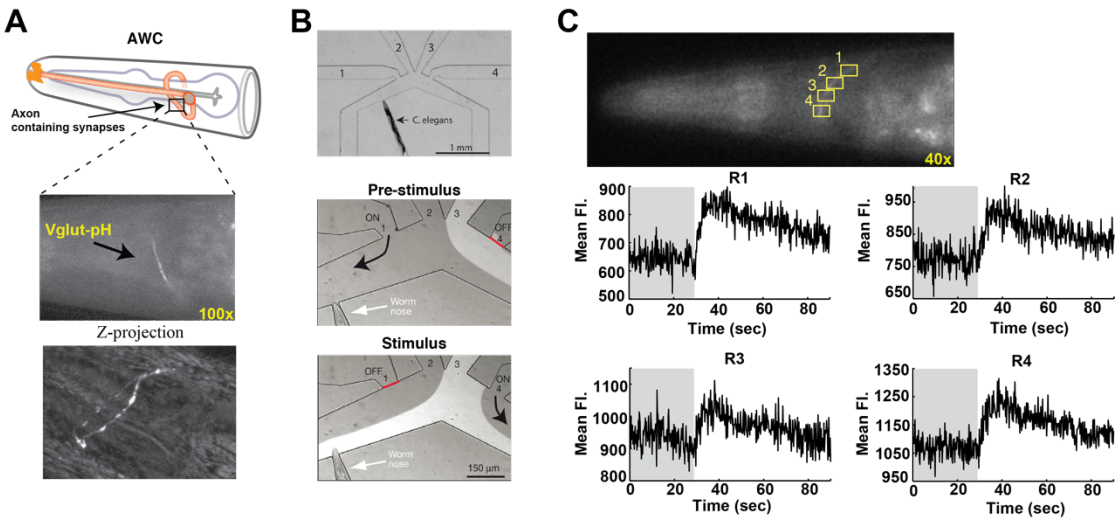

Figure 1.3. Vglut-pH fluorescence signals can be detected in AWC^{ON}

(A) Top: Diagram of AWC^{ON} indicating the location of axon containing presynaptic sites. Middle: Vglut-pH localization within AWC^{ON} axon in wide-field microscope used for imaging experiments. Bottom: Maximum intensity projection of a confocal stack showing that Vglut-pH is localized exclusively to the axon. **(B)** Microfluidic device used for Vglut-pH and calcium imaging. Top: overview of device with an animal trapped in the loading chamber. Middle: Pre-stimulus flow conditions. Buffer is driven to the nose from channel 2. Odor stimulus in channel 3 is directed away from animal's nose. Bottom: Turning off channel 1 and switching on channel 4 directs the stimulus to the nose of the animal. Switch time ~50-200 msec. Adapted from (Chalasani et al., 2007) **(C)** Initial measurements of Vglut-pH in AWC^{ON}. Top: single plane of raw image. Bottom: Raw fluorescence traces from four locations along the axon, indicated in the image above. Fluorescence increases can be detected after a strong 5-minute stimulus of 11.2 uM butanone is removed. Gray bar = odor.

Although baseline Vglut-pH fluorescence was only slightly above background auto-fluorescence, our initial measurements nevertheless detected stimulus-evoked fluorescence increases in AWC^{ON} in response to butanone removal (Fig 1.3C).

We optimized our imaging system for low-signal detection by changing our illumination to a more stable LED-based light source, using narrow bandwidth excitation and high transmission efficiency filter sets, replacing the 40x 1.3NA objective with an 100x 1.4NA objective, and acquiring images with an EMCCD camera designed for low-light detection (see also supplemental methods). These modifications significantly improved the signal-to-noise ratio, allowing for more sensitive and reliable measurements and providing single trial resolution under a variety of stimulus conditions. In addition, these modifications allowed us to obtain recordings in which fluorescence changes along the axon could be quantified. With the optimized pHluorin detection system, addition and removal of the odorant butanone resulted in small, but detectable, Vglut-pH fluorescence changes throughout the axon of AWC^{ON} (Fig 1.4A). Maximal signal changes occurred in punctal regions, consistent with the punctate localization of synaptic vesicles at active zones (Saheki and Bargmann, 2009; White et al., 1986). Although there were some minor variations in response magnitude along the axon, the signals along all segments of the axon were correlated (see supplemental methods). Therefore, we quantified fluorescence across the entire in-focus segment of the axon as an integrated single measurement, which increased the signal-to-noise ratio of our measurements (Fig 1.4B).

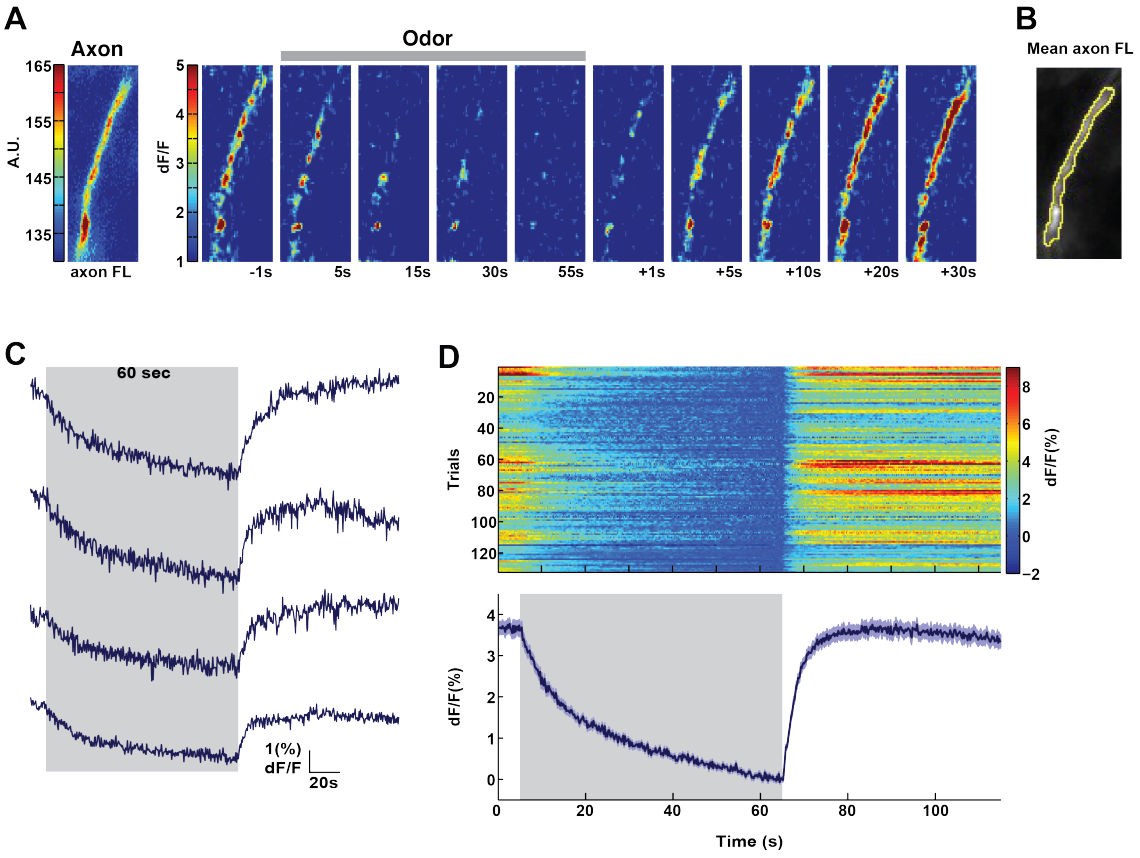

Figure 1.4. Characterization of Vglut-pH signals in AWC^{ON}

(A) Kineograph of an individual AWC^{ON} Vglut-pH response. Left: Fluorescence intensity of Vglut-pH along the axon prior to stimulation. Right: Images of Vglut-pH fluorescence change over time during stimulation. Fluorescence change is measured as the change in signal compared to the point immediately prior to odor removal. Numbers below each image panel indicate the time relative to odor addition (minus = before stimulus, plus = after stimulus). Recording was smoothed using a running average in both time and space (3 frames, 3 pixels in x and y). **(B)** Image showing how the axon in (A) is outlined and the mean intensity quantified as a single integrated measurement. **(C)** Single trials of AWC^{ON} Vglut-pH responses from four individuals. Top trace is from the axon in (A). **(D)** Population of AWC^{ON} Vglut-pH responses from 132 trials from 44 animals, 3 trials each. Top: Heat map of individual trials, 3 per animal, presented in sequential order. Bottom: Mean response from all trials. Gray Bar = 11.2 uM butanone. Shading = S.E.M.

Vglut-pH fluorescence in the AWC^{ON} axon decreased immediately upon odor onset and continued to decrease while the stimulus was present with approximately exponential kinetics. Odor removal resulted in an increase in the Vglut-pH signal, which rapidly returned the Vglut-pH signal to pre-stimulus levels (Fig 1.4C-D). AWC^{ON} Vglut-pH responses were largely dependent on the conserved SV fusion machinery, indicating that Vglut-pH signals indeed report SV release and recycling (Chapter 3 and 4). The dynamics of the AWC^{ON} Vglut-pH response are consistent overall with the suggestion that AWC signals in a manner similar to photoreceptors in the vertebrate retina (Chalasani et al., 2007), but extend this model to the associated vesicle release. The Vglut-pH signal suggests that at rest, neurotransmitter is tonically released, and endo- and exocytosis are balanced at steady state to generate a stable Vglut-pH surface population and signal. Addition of the odor, which decreases neuronal calcium and likely hyperpolarizes AWC^{ON}, results in decreased exocytosis and continued endocytosis-reacidification of Vglut-pH from the surface pool, generating a decrease in the Vglut-pH signal. Removal of the odor triggers rapid calcium influx and increased exocytosis that returns AWC^{ON} to the pre-stimulus fluorescence balance in ~20s.

The response to odor removal had at least three kinetically distinct phases that we termed the fast phase, the transitional phase, and the basal release phase (Fig 1.5A). These three phases can be identified by transitions in the time derivative of the Vglut-pH odor-removal signal and are detectable in individual responses (Fig 1.5B-C).

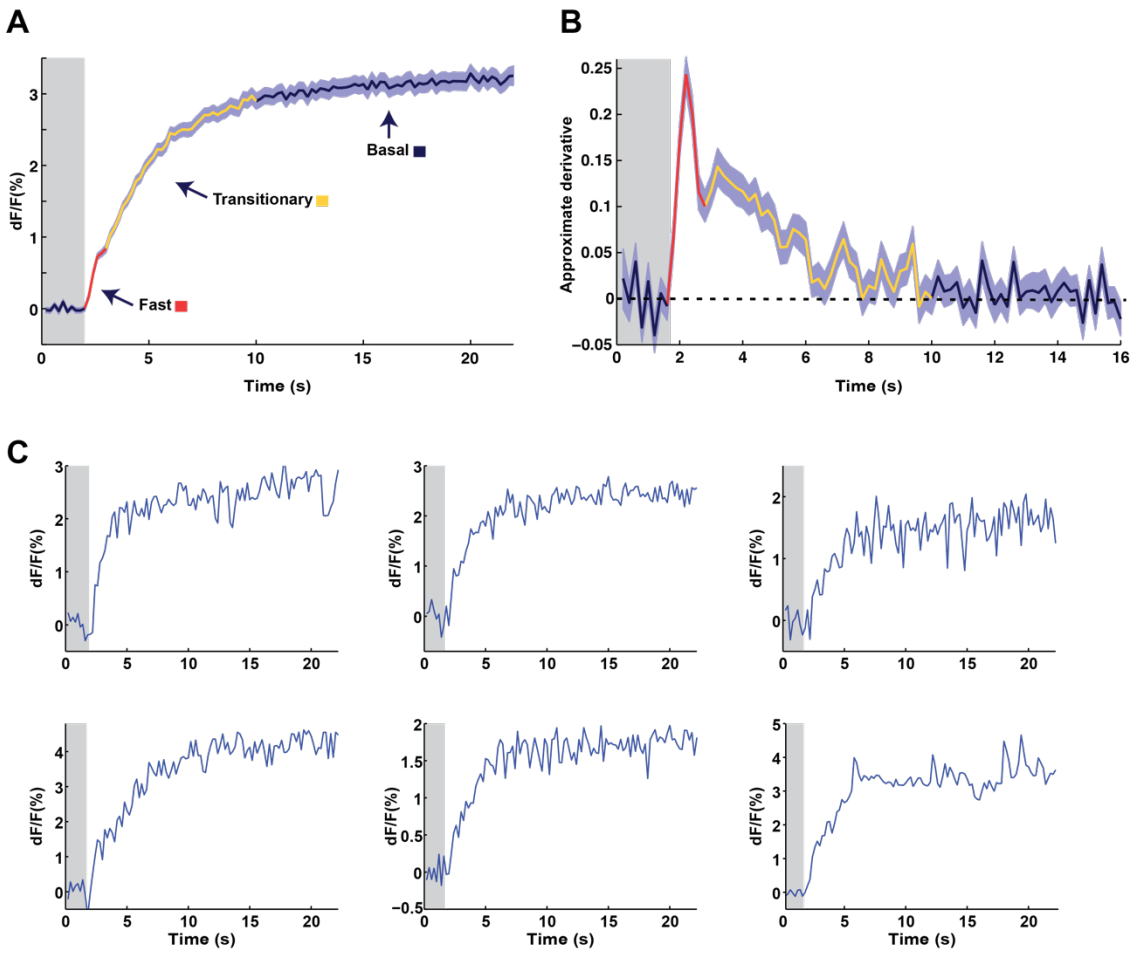

Figure 1.5. The exocytic response of Vglut-pH in AWC^{ON} has three kinetically distinct components.

(A) Mean AWC^{ON} Vglut-pH signal in response to odor removal (60 second stimulus). Trace is colored according to transitions in the slope of the time derivative in (B). 219 trials, 1-3 trials per animal. **(B)** Mean time derivative of AWC^{ON} Vglut-pH signals as in (A). Each individual trial was smoothed with a running average (3 frames) before taking the derivative. Trace is colored based on distinct transitions and magnitudes. Units are change in dF/F (%) per 200 msec. **(C)** Individual traces from data in (A). Gray bar = stimulus, 11.2 uM butanone. Shading = S.E.M.

The fast phase occurs immediately following odor removal and is an acute and rapid increase in signal that likely represents the synchronized fusion of many SVs. This phase is followed by the transitional phase, which is characterized by a slower rise in fluorescence representing a lower, but still elevated, rate of SV release. This phase slowly transforms into a stable signal representing basal release that is balanced by endocytosis to create a steady-state equilibrium.

AWC's response to odor removal is modulated by the duration of the stimulus (Chalasani et al., 2007). Increasing the stimulus duration increases the magnitude of AWC's calcium response in the cell body as well as the probability of initiating behavioral responses after odor removal (reorientations) (Albrecht and Bargmann, 2011; Chalasani et al., 2007). To extend this understanding to presynaptic calcium levels at release sites, we localized GCaMP3 to synaptic vesicles by fusion to synaptogyrin (*sng-1)*, the predominate tetraspan synaptic vesicle protein expressed in *C. elegans* synapses (Abraham et al., 2011; Zhao and Nonet, 2001). A similar approach was developed by Lagnado *et al* in vertebrates in which GCaMP2 was localized to synaptophysin, another tetraspan synaptic vesicle protein (Dreosti et al., 2009). *C. elegans sng-1(lf)* mutants do not have major defects in synaptic transmission (Abraham et al., 2011), suggesting that *sng-1* would be a useful carrier protein to localize GCaMP to SVs without impacting synaptic function.

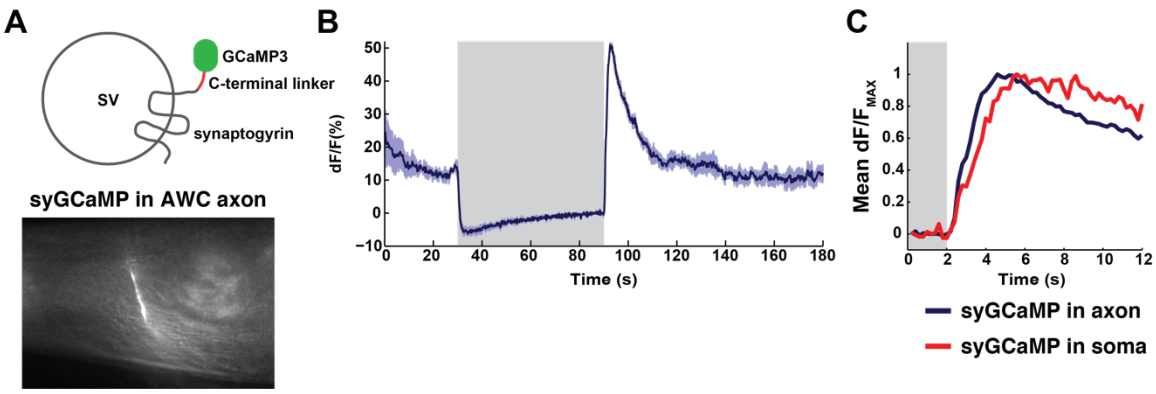

Figure 1.6. AWC^{ON} SyGCaMP calcium responses in a representable animal.

(A) Diagram outlining reagent construction and localization to the AWC^{ON} axon (bottom image). **(B)** Mean response of AWC^{ON} syGCaMP from a single individual animal (3 trials). **(C)** SyGCaMP responses are faster than cell body based measurements. Blue trace is the average response in (B) to odor-removal. Red trace is average response in (B) measured from syGCaMP that was localized in the cell body. Gray bar = stimulus, 11.2 uM butanone. Shading = S.E.M.

GCaMP3 fused to the C-terminus of *sng-1* (termed here as syGCaMP) was highly enriched in the AWC^{ON} axon, consistent with synaptic localization (Fig 1.6A), with lower fluorescence in the soma and occasionally in the dendrite and sensory cilia (data not shown). Chemotaxis to the AWC^{ON} detected odorant butanone was intact in animals expressing syGCaMP in AWC^{ON}.

Axonal syGCaMP responded to butanone stimuli with similar calcium decreases and increases as the cell body, but with faster kinetics (Fig 1.6B-C). This faster response likely reflects the opening of voltage-gated calcium channels at the synapse. Removal of odor after 10 second, 60 second, and 3 minute pulses of butanone (11.2μM) resulted in AWC^{ON} syGCaMP responses whose magnitude increased with pulse duration between 10- and 60-seconds (Fig 1.7A), and whose kinetics became faster at each successive duration (Fig 1.7B-D).

Increasing pulse duration also generated stronger AWC^{ON} Vglut-pH responses to odor removal, detectable both in an increased response magnitude and in faster kinetics (Fig 1.8A-C). The increase in magnitude after longer pulses may be a passive response to the greater reduction in fluorescence signal produced by odor addition. The dynamics changes are likely to be active, however, and included a greater contribution of the fast release phase and a faster full recovery to prestimulus levels. Normalizing the response magnitudes for each pulse duration indicated that each response transitioned through fast and intermediate release phases in a similar manner reflecting shared underlying mechanisms with a shift in dynamics (Fig 1.8D).

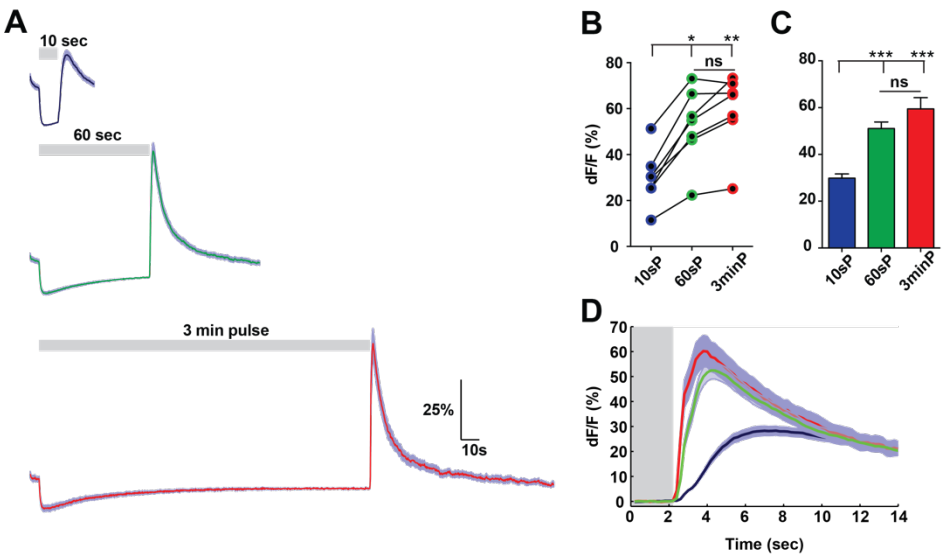

Figure 1.7. AWC^{ON} axonal calcium responses are modulated by stimulus duration.

(A) AWC^{ON} syGCaMP responses to 10-second, 60-second, and 3-minute pulses of butanone from a set of 7 animals. Inset: zoomed comparison of odor-removal response. Scale bar = dF/F (%) and time in seconds. 10-sec pulses: n = 42 trials, from 7 animals, 6 trials each. 60-sec pulses: n = 21 trials, from 7 animals, 3 trials each. 3-min pulses: n = 7 trials, from 7 animals, 1 trial each. Stimuli were delivered in this order. **(B)** Average peak odor-removal response in individual animals. Each point represents the average of multiple trials in (A). Line connecting points represents the same animal. Repeated measures one-way ANOVA. Tukey multiple comparison correction. * p = 0.0011, ** p = 0.0005. Error = S.E.M. **(C)** Odor-removal responses across a population of animals. 10 sec pulses: n = 42 trials, from 7 animals, 6 trials each. 60-sec pulses: n = 36 trials, from 12 animals, 3 trials each. 3-min pulses: n = 12 trials, from 12 animals, 1 trial each. One-way ANOVA, Tukey correction. *** p <0.0001, Error = S.E.M. **(D)** Comparison of odor-removal responses in (A). Colors consistent with labeling through figure. 10sP = 10-second stimulus, 60sP = 60-second stimulus, 3minP = 3-minute stimulus. Gray bar = 11.2 uM butanone. Shading = S.E.M.

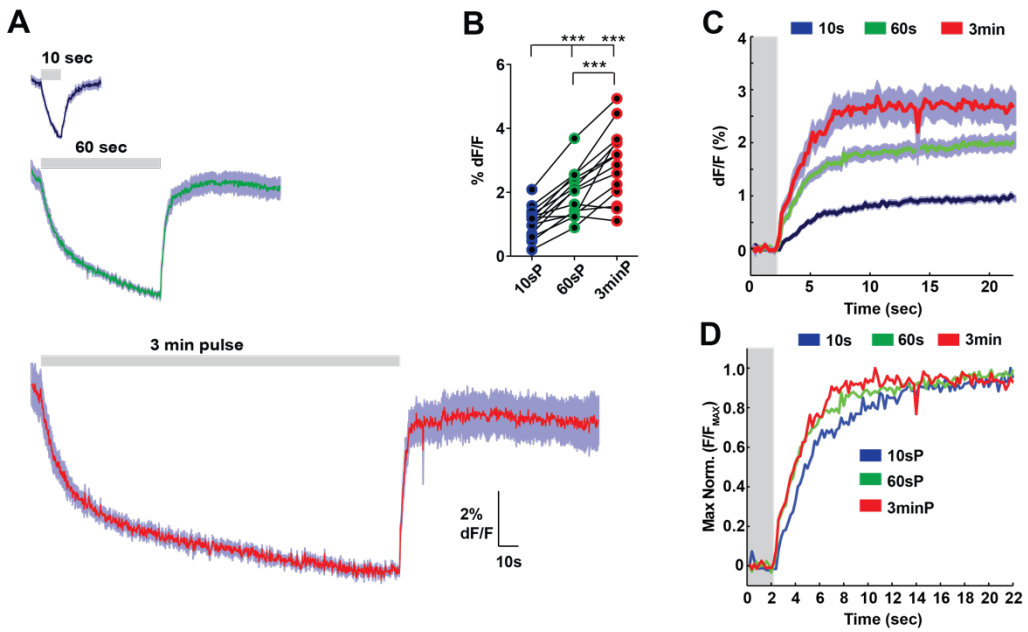

Figure 1.8. AWC^{ON} Vglut-pH responses are modulated by stimulus duration.

(A) AWC^{ON} Vglut-pH responses to 10-second, 60-second, and 3-minute pulses of butanone from a set of 14 animals. 10-sec pulses: n = 120 trials, from 20 animals, 6 trials each. 60-sec pulses: n = 59 trials, from 21 animals, 2-3 trials each. 3-min pulses: n = 14 trials, from 14 animals, 1 trials each. Stimuli were delivered in this order. **(B)** Average peak odor-removal response within individual animals. Each point represents the average of trials in (A). Line connecting points represents the same animal. Repeated measures one-way ANOVA. Tukey multiple comparison correction. *** = p <0.0001. Error= S.E.M. **(C)** Comparison of odor-removal responses in (A). **(D)** Comparison of the average odor-removal responses in (C) after normalizing the response magnitude. Gray bar = stimulus, 11.2 uM butanone. Shading = S.E.M.

As a comparative approach, we then examined Vglut-pH responses in the ASH sensory neurons, which are acutely depolarized upon the presentation of noxious stimuli. Expression of Vglut-pH in ASH under the *sra-6* promoter was also exclusively localized to the ASH axons (Fig 1.9A). Stimulation of ASH with a noxious osmotic stimulus of 500 mM NaCl generated fluorescence changes throughout the axon (Fig 1.9B). We quantified ASH Vglut-pH responses in a similar fashion to AWC^{ON}, using the entire in-focus segment of the axon as a single integrated measurement. NaCl addition generated a strong increase in the ASH Vglut-pH signal that plateaued during the stimulus and began to decrease immediately after the removal of the stimulus (Fig 1.9C-D). The dynamics of Vglut-pH were similar to those of ASH calcium in the cell body (Fig 1.9E). The exocytic component of ASH Vglut-pH responses upon stimulation appeared to be dominated by a single component (Fig 1.9F), unlike the biphasic exocytic responses in AWC^{ON} after odor removal. The comparison suggests that SV release in these two sensory neurons may have distinct kinetics. The decrease in ASH Vglut-pH signal after stimulus removal had exponential dynamics similar to the decrease in AWC^{ON} Vglut-pH signal upon odor addition, suggesting similar endocytic mechanisms.

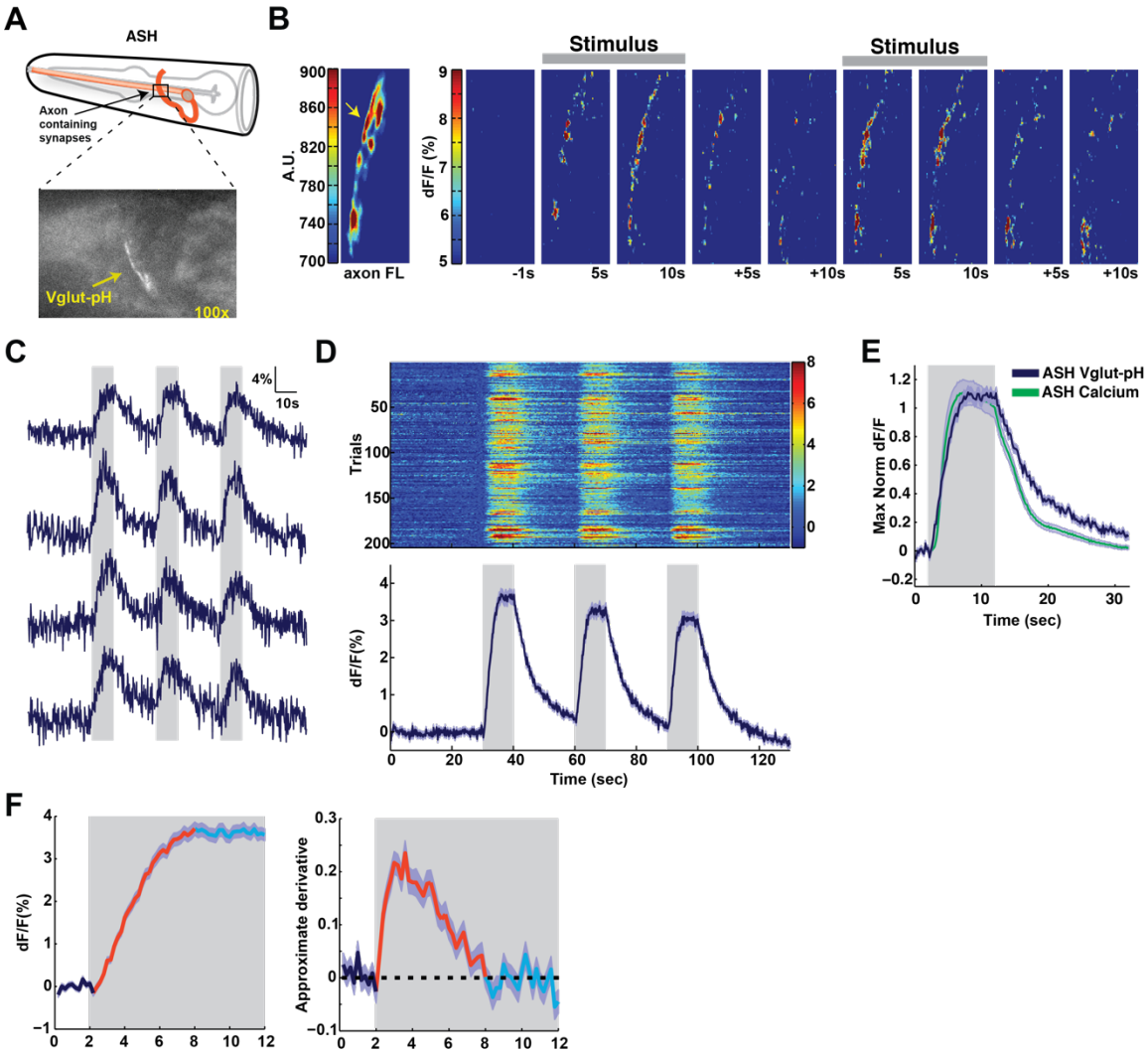

Figure 1.9. Vglut-pH signals in ASH sensory neurons

(A) Top: Diagram of ASH indicating the location of axon containing presynaptic sites. bottom: Vglut-pH localization within ASH axon. **(B)** Kineograph of an ASH Vglut-pH stimulation. Analyzed as described in Fig 3, but with reference value at t =1 seconds before stimulation. Yellow arrow indicates ASH axon. **(C)** Single ASH Vglut-pH responses from four individuals. Top trace is from the axon in (A). **(D)** Population of ASH Vglut-pH responses. 204 trials from 68 animals, 3 trials each. Top: Heat map of individual trials, 3 per animal, presented in sequential order. Bottom: Mean response from all trials. **(E)** Comparison of ASH GCaMP3 and Vglut-pH responses after normalization of response magnitude (signal over time divided by peak response). Vglut-pH data from (D), first pulse. GCaMP3 signals were measured in the cell body. n = 39 trials from 13 animals, 3 trials each. **(F)** Left: Mean ASH Vglut-pH response to stimulus onset, colored corresponding to transitions in the slope of the time-derivative (right). Right: Units are change in dF/F (%) per 200 msec. Data from (D), first pulse. Gray bar = 500 mM NaCl. Shading = S.E.M.

Discussion

Our results indicate that Vglut-pH imaging is a robust and sensitive method to measure SV release and recycling at single neuron resolution from central synapses in *C. elegans*. *C. elegans* neurons are typically non-spiking cells that lack sodium-based action potentials and have graded synaptic release (Goodman et al., 1998; Liu et al., 2009). Vglut-pH signals in both AWC^{ON} and ASH were consistent with the properties of graded synaptic release, and were consistent with the effects on synaptic transmission predicted from calcium imaging: increases and decreases in calcium correlated with increases and decreases in SV release (Liu et al., 2009). The dynamics of Vglut-pH fluorescence decreases were consistent with the exponential kinetics expected of endocytosis, which are analyzed in detail in Chapter 2 (Smith et al., 2008).

Our results indicate that both AWC^{ON} and ASH synapses can be highly reliable, as virtually every stimulus triggered a detectable Vglut-pH response. Sensory-evoked calcium responses in these neurons are also reliable across trials (Kato et al., 2014). Together, these results indicate that sensory information is represented in efficient sensory transduction and synaptic regulation in AWC^{ON} and ASH.

AWC^{ON} Vglut-pH imaging supports the hypothesis that AWC^{ON} tonically releases neurotransmitter at rest and that this is effectively suppressed by the addition of odor (Chalasani et al., 2007; Chalasani et al., 2010; Gordus et al., 2015). Odor removal leads to a recovery, but not overshoot, of the signal, a result that appears different from the AWC^{ON} calcium response after long odor pulses.

The dynamics of the Vglut-pH response suggest that stimulus-induced glutamate release is dominated by the decrease in, and return to, basal release levels. Exactly this pattern is described in vertebrate photoreceptors, where suppression and recovery yield linear changes in glutamate release (Rieke and Schwartz, 1996; Thoreson et al., 2004). At the same time, the AWC^{ON} calcium response to odor removal that overshoots pre-stimulus levels closely matches the behavioral response of increased reversals, suggesting that a longer odor pulse does lead to a behaviorally relevant signal in neurotransmission (Albrecht and Bargmann, 2011; Chalasani et al., 2007). These results can be harmonized by proposing that the increased rate of glutamate release following the removal of a long odor pulse may be the relevant signaling mechanism for mediating odor-evoked behavioral responses.

The AWC^{ON} Vglut-pH response to odor removal has two distinct phases of release before the return to basal release, the balanced steady-state of exo- and endocytosis. Increasing the odor pulse duration increased both the magnitude of the fast phase of the response and the rate of the following transitional phase, suggesting that these phases may represent distinct modes of release or endocytosis. Goldfish retinal OFF bipolar neurons also exhibit multiple modes of release, the dynamics of which are essentially identical to those we observe in AWC^{ON} (Neves and Lagnado, 1999) (Fig 1.10A). Furthermore, in zebrafish retinal OFF bipolar neurons, both measurements of presynaptic calcium influx, using synaptophysin tagged with GCaMP2, and SV release, using synaptophysin-

pHluorin, display strikingly similar dynamics to AWC^{ON} (Fig 1.10B-C) (Odermatt et al., 2012).

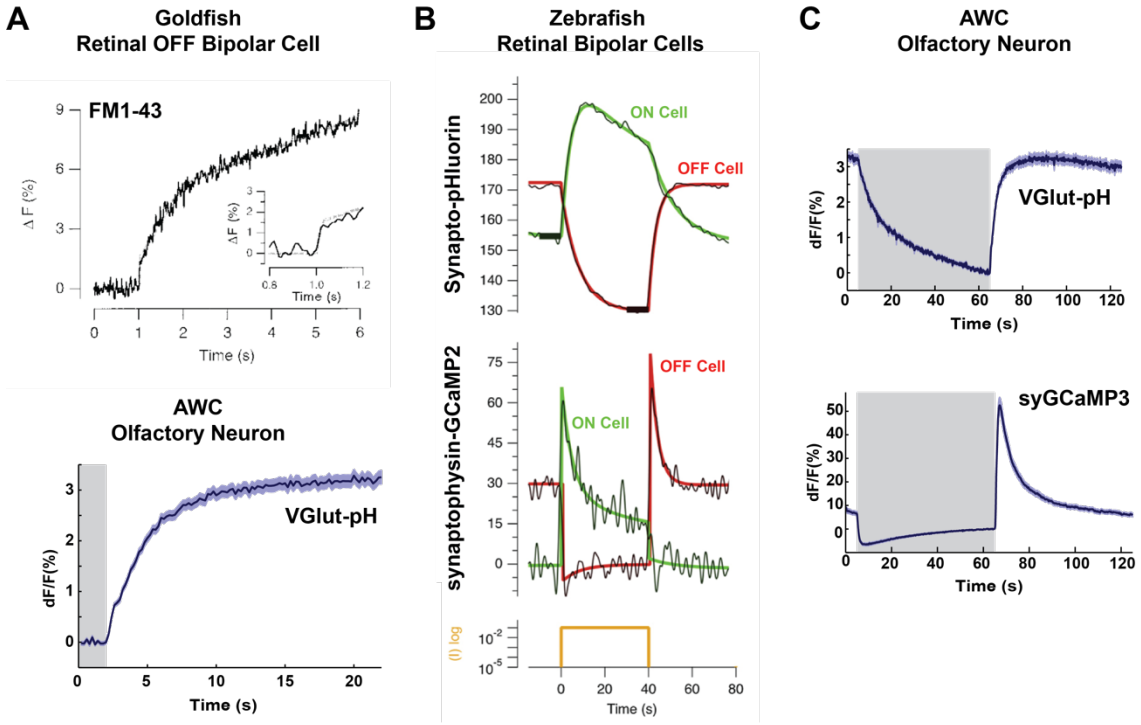

Figure 1.10. Comparison of AWC^{ON} synaptic activity to vertebrate retinal OFF bipolar neurons.

(A) Exocytosis in goldfish retinal OFF-bipolar neurons and AWC olfactory neurons has multiple components. Top: adapted from (Neves and Lagnado, 1999). Stimulation of OFF bipolar cells via direct depolarization, synaptic release measured using FM1-43 dye. Bottom: AWC^{ON} Vglut-pH, from Fig 4. **(B)** Synaptic activity of zebrafish retinal bipolar neurons in response to changes in light intensity. Top: Synaptic vesicle release measured with synaptophysin-pHluorin. Bottom: presynaptic calcium influx measured with synaptophysin tagged with GCaMP2. Adapted from (Odermatt et al., 2012) **(C)** AWC synaptic activity measured with Vglut-pH and syGCaMP has similar dynamics to zebrafish OFF bipolar neurons. Top: data from Fig 3D. Bottom: Data from Fig 6A.

These similarities highlight and extend the conclusion that retinal processing in vertebrates and AWC^{ON} olfactory processing in *C. elegans* have either conserved or convergent signaling strategies for sensory information processing (Chalasani et al., 2007).

The transformation from calcium to SV release appears to be more straightforward in ASH. ASH Vglut-pH responses closely matched the shape of calcium responses, and in contrast to AWC^{ON}, the exocytic component of ASH Vglut-pH responses appeared to occur at a single rate. Given that we can only measure relative changes in calcium and release levels, it is difficult to directly compare the relationship between calcium and Vglut-pH between neurons. However, the relative differences we observe suggest that the underlying synaptic machinery may be distinct between these two sensory neurons, and is explored further in Chapters 3 and 5.

In this chapter we outlined the development and initial characterization of Vglut-pH imaging from central synapses in *C. elegans,* and present the first presynaptic measurements of the dynamics of synaptic vesicle release and recycling from any synapse in this organism. Our results indicate that AWC^{ON} exhibits similar synaptic release properties to vertebrate photoreceptors and retinal bipolar neurons, aligning with previous results from functional calcium imaging, gene expression, and circuitry (Chalasani et al., 2007). Furthermore, the dynamics of Vglut-pH responses in AWC^{ON} and ASH suggest that these neurons have distinct synaptic release properties. Our results suggest that pHluorin-

based imaging of neurotransmitter release will be a widely applicable and useful reagent for the *in vivo* interrogation of synaptic function and signaling in *C. elegans*.

Chapter 2: Characterization of endocytosis dynamics

The modern study of synaptic vesicle endocytosis began after the formulation of the quantal hypothesis of neurotransmission, electron micrographs of synapses that displayed invaginated curvatures in the presynaptic membrane that appeared to be pinched off to regenerate synaptic vesicles (SVs) (Del Castillo and Katz, 1954; Heuser and Reese, 1973; Heuser et al., 1979; Katz and Miledi, 1967a). Endocytosis lives at the heart of several questions: How is the supply of synaptic vesicles maintained? What are the mechanisms that regulate SV retrieval? And how are these pathways regulated to meet the demands of ever-changing rates of SV release? The study of these questions has been an intense area of research for over four decades, and much progress been made in understanding the mechanisms, molecules, and pathways mediating SV endocytosis. However, the dynamics of SV retrieval has only explored in a few neural cell types. In this chapter, we report our observations and characterization of SV retrieval in *C. elegans* using Vglut-pH in the two sensory neurons AWC^{ON} and ASH.

The dominate form of SV endocytosis is clathrin-mediated endocytosis (Dittman and Ryan, 2009). Clathrin forms a honeycomb-like lattice on the target membrane and acts as a scaffold to provide the driving force for membrane invagination that shapes the resulting SV (Robinson, 2015). Clathrin adaptor proteins help assemble the clathrin lattice, link it to the membrane, and coordinate clathrin assembly with specific cargo for endocytosis (Slepnev and

Camilli, 2000). Clathrin adaptor proteins also appear to mark endocytosed SVs for specific pathways (Kononenko and Haucke, 2015). Together, clathrin and its adaptors form the core module for clathrin-mediated endocytosis. The major clathrin adaptors for synaptic vesicle endocytosis are AP-2 and AP180. After the endocytic bud forms, it is separated from the membrane by the GTPase dynamin. After separation from the membrane, the clathrin coat is then rapidly shed and a new SV is produced (Dittman and Ryan, 2009; Kononenko and Haucke, 2015).

SV endocytosis can occur through several distinct pathways (Kononenko and Haucke, 2015; Sudhof, 2004) (Fig 2.1). The classical model of endocytosis depicts mature SVs being produced by endocytosis directly from the plasma membrane with a subset being trafficked to the early endosome for additional processing. A form of vesicle fusion and recapture termed kiss-and-run has also been proposed, although it has been a topic of significant debate. In this model, SVs do not fully collapse into the plasma membrane, but instead release neurotransmitter through a transient fusion pore (Alabi and Tsien, 2013). Here, endocytosis would represent the closure of the fusion pore and would be exceptionally fast. Current evidence appears to argue against kiss-and-run as a major mechanism of SV retrieval (Dittman and Ryan, 2009). Endocytosis can also proceed from the plasma membrane by formation of endosomal intermediates that are then subject to clathrin-mediated endocytosis to produce SVs. Recent work has described an ‘ultrafast’ endocytic pathway that works in this fashion (Watanabe et al., 2013b; Watanabe et al., 2014).

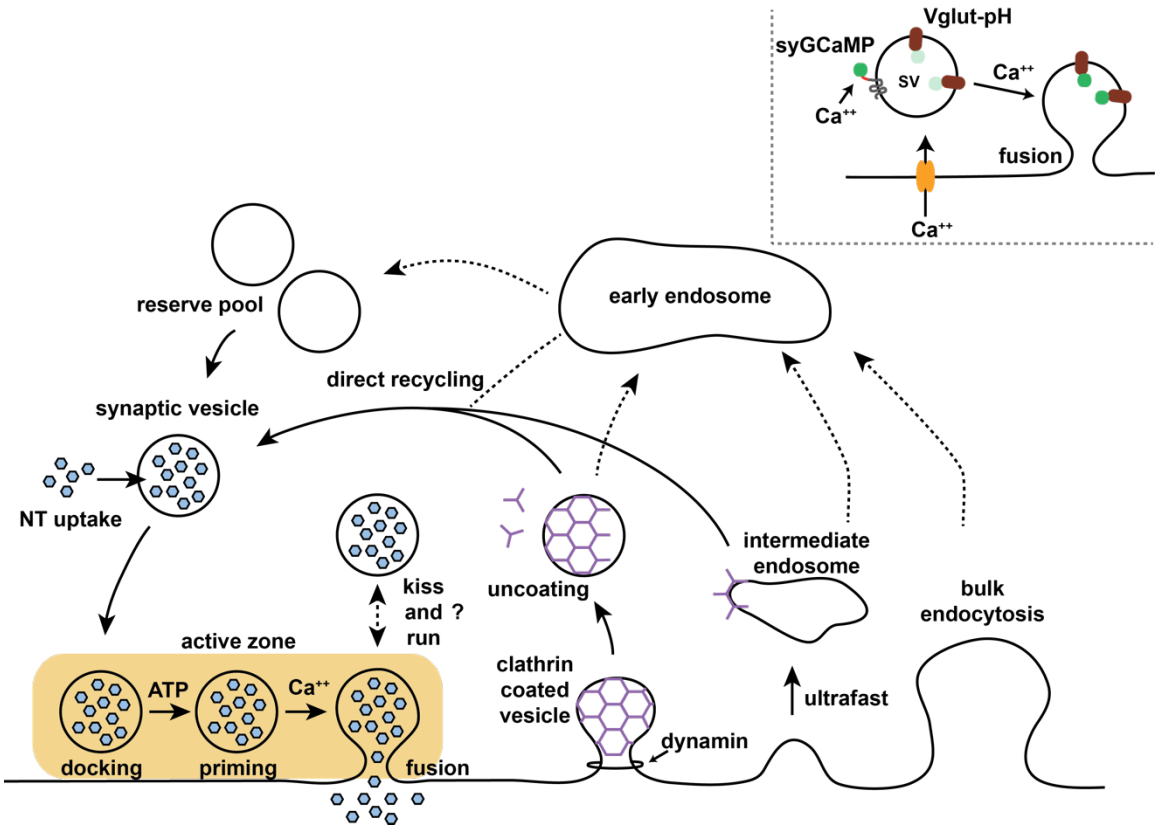

Figure 2.1. Synaptic endocytosis pathways.

Outline of the major pathways of synaptic vesicle endocytosis. After synaptic vesicle fusion endocytosis may take place directly from the plasma membrane or through an intermediate endosome pathway (direct recycling). Either of these process may generate mature SVs or may require further processing at the early endosome. Clathrin is not required for ultrafast retrieval and formation of the intermediate endosome, but is required for SV production from this structure. Strong and prolonged SV release may trigger bulk endocytosis of the presynaptic membrane. SVs produced from the early endosome may go directly into the release pool or the reserve pool. Top Inset: Diagram of the reagents used to measure synaptic activity in this chapter. Both are present on SVs and may be present throughout these recycling pathways. See main text for more details and references. Based on Reinhard & Fasshauer, Nature 2012.

Here, non-clathrin-mediated endocytosis from the plasma membrane occurs very rapidly (50 ms-100 ms) to generate an intermediate endosome that then undergoes clathrin-mediated endocytosis. This mechanism is proposed to regenerate SVs on a timescale of ~5-6 seconds. Lastly, large and deep invaginations of the plasma membrane can be observed after strong stimulation and are termed bulk endocytosis (Clayton and Cousin, 2009).

The study of the kinetics of endocytosis has shown that each of these pathways contributes distinctly to the dynamics of the endocytic process. Several approaches have been used to study the kinetics of SV retrieval. Electrical capacitance recordings provide a direct readout of membrane surface area but are limited to select preparations that have giant synapses such as retinal bipolar cells and auditory hair cells (Parsons et al., 1994; von Gersdorff and Matthews, 1994). Capacitance recordings have revealed that both fast and slow modes of endocytosis can be detected with time constants of ~1 second and ~10 seconds respectively (Neves and Lagnado, 1999). Instances of bulk endocytosis have also been detected after strong stimulation (Holt et al., 2003). Fluorescence dyes have also been used as optical tracers, such as the amphipathic dye FM 1-43. This approach can be used to label vesicle pools and measure overall vesicle turnover, but this method does not directly monitor SV endocytosis in real-time. The use of pHluorins has provided high-fidelity readouts of endocytosis and accompanying vesicle re-acidification. Using this approach, the time constant for endocytosis of hippocampal neurons has been estimated from ~15 seconds at room temperature, to as fast as ~6 seconds at 37 °C (Balaji and Ryan, 2007).

Disruption of various components of clathrin-mediated endocytosis has demonstrated that most individual components are not essential (Dittman and Ryan, 2009). In fact, SV retrieval can occur without clathrin itself, indicating that a non-clathrin mediated pathway exists (Kim and Ryan, 2009; Kononenko et al., 2014). This is particularly apparent in *C. elegans* where disruption of either AP-2 or clathrin appears to have only subtle effects on endocytosis at the neuromuscular junction (Gu et al., 2008; Sato et al., 2009). The large number of components, their synergistic effects on endocytosis, and the existence of distinct but overlapping endocytic pathways, may allow for significant functional overlap (Dittman and Ryan, 2009). This system with its multiple components and pathways likely allows endocytosis to be fine-tuned to balance the exocytic demands of a given synapse.

We show here using Vglut-pH imaging that SV endocytosis in the *C. elegans* sensory neurons AWC^{ON} and ASH has kinetic features and timescales similar to mammalian synapses. SV endocytosis appears to be homeostatically regulated based on previous neuronal activity levels, and is composed of at least two kinetically distinct modes of endocytosis, fast and slow. The fast mode of retrieval is dependent on the clathrin adaptor protein UNC-11, the homolog of AP180/CALM, suggesting that clathrin-mediated endocytosis is important for SV retrieval in these neurons.

Results

Comparison of AWC^{ON} and ASH Endocytosis Rates

To characterize Vglut-pH endocytosis rates in AWC^{ON} and ASH we recorded Vglut-pH fluorescence changes in response to sensory stimulation and analyzed stimulus-triggered fluorescence decreases in Vglut-pH signals. Stimulation of AWC^{ON} with butanone suppresses the neuron allowing us to monitor the Vglut-pH response in association with the decrease in basal release levels (Chalasani 2007, and this work Chapter 1). Stimulation of ASH with 500 mM NaCl acutely depolarizes the neuron and upon stimulus removal, allows us to monitor the Vglut-pH signal response associated with the decrease in activity as ASH returns to pre-stimulus activity levels (Chapter 1). VGlut-pH measures endocytosis indirectly by the coupled process of vesicle re-acidification (Sankaranarayanan et al., 2000), which has not been measured in *C. elegans*. For this reason, the rates we report represent only a proxy for the rate of endocytosis and not the rate directly (see discussion).

Vglut-pH fluorescence decreases in both AWC^{ON} and ASH displayed exponential kinetics (Smith et al., 2008). To estimate the rate of VGlut-pH endocytosis in these neurons, we fit fluorescence decreases from individual trials to a single exponential decay function and compared the decay constants from these fits (Fig 2.2A-B). ASH fluorescence decreases were significantly faster than those in AWC^{ON}, with the entire distribution of ASH decay constants shifted to faster time scales (Fig 2.2C-D).

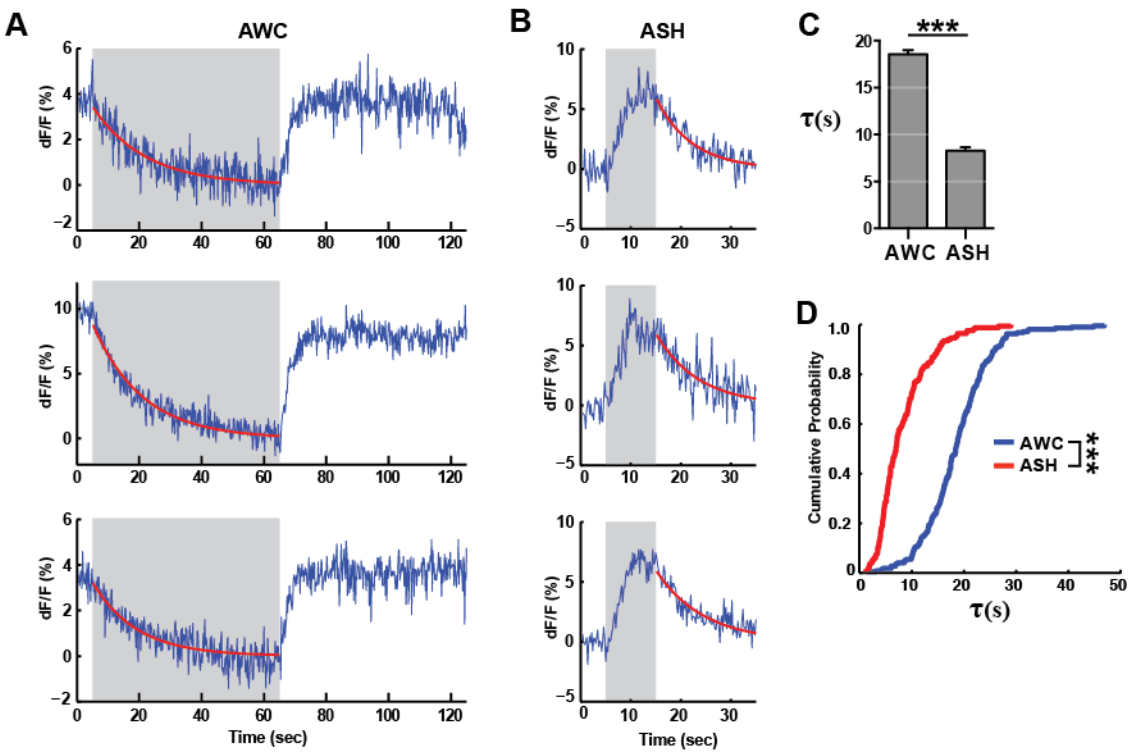

Figure 2.2. AWC^{ON} and ASH Vglut-pH signals decay at distinct rates.

(A) Three examples of exponential fits to single trials of AWC^{ON} Vglut-pH decays induced by odor stimuli. Each trace is from a different animal. Red line is a single-term exponential fit. Gray bar = stimulus period. Stimulus = 11.2 uM butanone. **(B)** Three examples of exponential fits to single trials of ASH Vglut-pH decays after the removal of a high osmolarity NaCl stimulus. Each trace is from a different animal. Red line is a single-term exponential fit. Gray bar = stimulus period. Stimulus = 500 mM NaCl. **(C)** Average time constant of AWC^{ON} and ASH decay from single-term exponential fits (A) & (B). AWC^{ON} n=219 trials, from 76 animals, 2-3 trials each. ASH n=168 trials, from 56 animals, 2-3 trials each. *** $p < 0.0001$, unpaired t-test. **(D)** Empirical cumulative distribution plot of data in (C). Distributions differ by Kolmogorov-Smirnov test, *** $p<0.0001$.

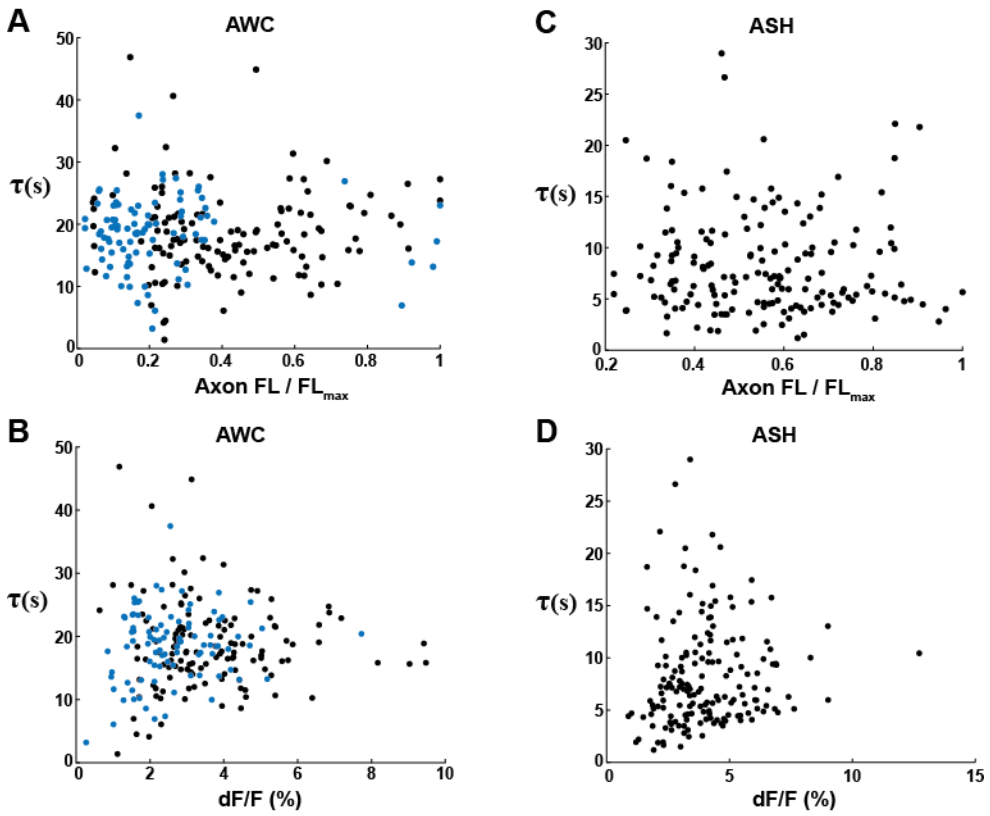

Figure 2.3. Vglut-pH decay time constants are not correlated with expression level or response magnitude.

(A) Scatter plot of AWC^{ON} VGlut-pH decay time constants and axon fluorescence intensity before decay onset. Two different lines of wild-type AWC Vglut-pH transgenic lines were used in this study, represented by the black and blue points. Axon intensities were normalized to the brightest axon detected (FL_{MAX}). Time constants are from single exponential fits, as in Figure 2. Correlation coefficient =0.01, p=0.89, not significant. **(B)** AWC^{ON} decay time constants plotted against the magnitude of basal release (dF/F (%) prior to stimulus onset). Correlation coefficient =0.024, p=0.73, not significant. **(C-D)** Scatter plots using a single transgenic line showing decay time constants vs axon fluorescence (C) and response magnitude induced by stimulation (D). Correlation coefficient = -0.029, p =0.72 (C) & 0.058, p =0.46 (D). Not significant. AWC^{ON} n=219 trials, from 76 animals, 2-3 trials each. ASH n=168 trials, from 56 animals, 2-3 trials each.

Measured decay constants did not correlate with axon fluorescence or response magnitudes before endocytosis (Fig 2.3), suggesting that the difference rates within and between each neuron were independent of variations in VGlut-pH surface or expression levels which might lead to saturation of the endocytic machinery (Sankaranarayanan and Ryan, 2000).

The distinct endocytosis rates in AWC^{ON} and ASH could reflect either cell-intrinsic or stimulus-dependent processes, because the neurons respond oppositely to sensory stimuli. With AWC^{ON}, endocytosis is measured by the reduction in basal exocytosis, whereas with ASH endocytosis is measured after a large peak of stimulus-evoked exocytosis. Axonal calcium levels associated with the measurement of endocytosis in each neuron is similarly different (Fig 2.4A-B, arrows).

To distinguish between these possibilities, we used odor protocols to generate different activity states in AWC^{ON}. Odor removal after a 60 second stimulus results in a calcium peak in AWC^{ON} that rebounds to baseline levels in ~ 30 seconds, producing a signal magnitude at ~ 15 seconds that is comparable to the magnitude of ASH's calcium response at stimulus removal (Fig 2.4A-B). This observation allowed a two-step odor protocol in which odor was added twice to stimulate endocytosis from both a basal level and a higher level of activity, producing two phases in which Vglut-pH fluorescence decreases could be monitored (Fig 2.4C). The endocytosis rates during the first and the second odor pulses were compared across the two pulses in each individual trace.

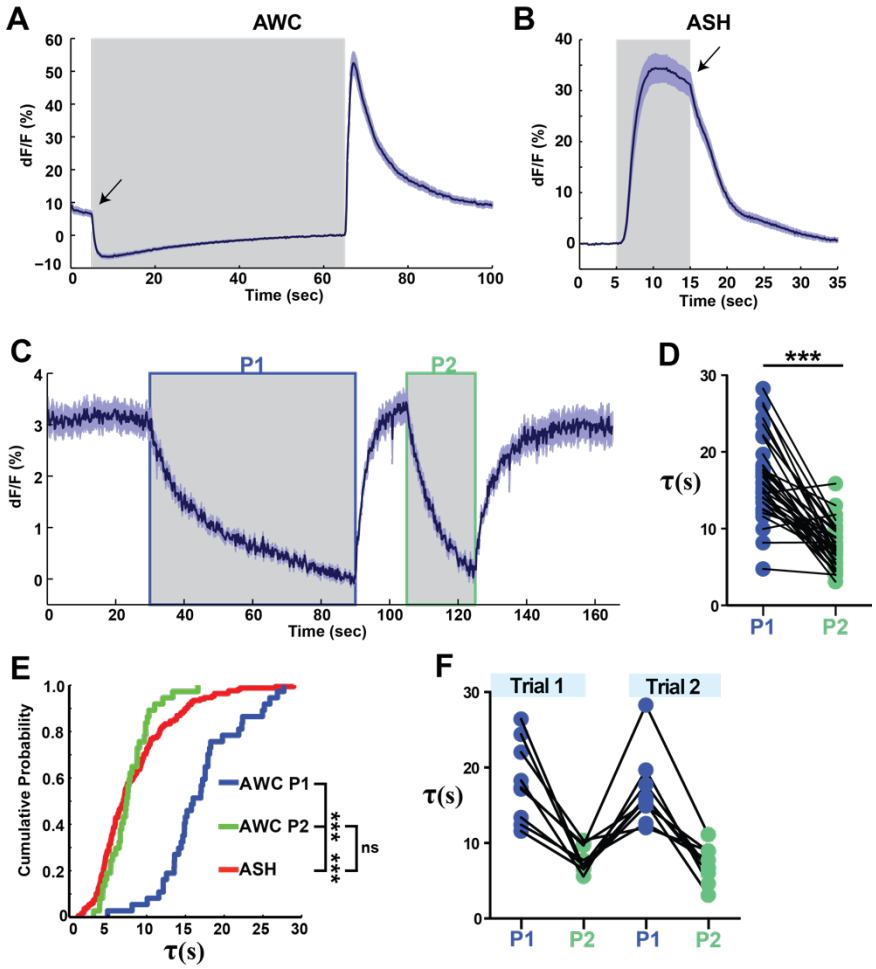

Figure 2.4. Recent Neural activity modulates endocytosis rates.

(A) AWC^{ON} Axonal calcium flux induced by odor addition and removal. Measured with syGCaMP. n = 21 trials, from 7 animals, 3 trials each. **(B)** ASH axonal calcium flux in response to addition and removal of 500 mM NaCl measured with soluble GCaMP3 at the axon. n = 21 trials, from 7 animals, 3 trials each. In (A-B) arrows marks point of Vglut-pH decay that was used to characterize endocytosis rates. **(C)** Average AWC^{ON} Vglut-pH response to two successive odor stimuli, applied for 60s (P1) and 20s (P2). n = 39 trials (13 animals, 3 trials each). **(D)** Time constants from single-term exponential fits to P1 and P2 from (C) performed on the initial 20s of the decay for each pulse. Paired t-test, *** p<0.0001. **E)** Cumulative distribution plot of time constants for AWC P1, AWC P2, and ASH Vglut-pH decays. Time constants are from single-term exponential fits as in (D). Kruskal-Wallis test for multiple comparisons, *** p< 0.0001, ns = p > 0.999. **(F)** Time constants of P1 and P2 in two repeated trials of the stimulation protocol in (C) per animal (8 animals, 70s between trials). (A-C) Gray bar = stimulus. AWC^{ON} stimulus = 11.2 uM butanone. ASH stimulus = 500 mM NaCl. Shading = S.E.M.

Strikingly, the time constant for the second pulse decreased by about half, resulting in a mean and overall distribution indistinguishable from those in ASH upon stimulus removal (Fig 2.4D-E). This enhancement in endocytic capability was temporary (lasting < 70 seconds) but could be induced after another 60 second odor pulse (Fig 2.4F). These results indicate that endocytosis in AWC^{ON} is subject to modification after changes in neural activity.

Endocytosis in AWC^{ON} and ASH occurs on multiple timescales

As endocytosis in many systems is composed of multiple kinetically distinct modes (Smith et al., 2008a), we suspected that the VGlut-pH endocytosis signal might also be composed of multiple processes. Endocytosis data were analyzed by comparing single, double, and triple exponential fits for each trace using Akaike's information criterion (AIC) (Motulsky and Christopoulos, 2004) (see methods for details). A significant fraction of AWC^{ON} and ASH traces had a high probability of containing two exponential time scales (AWC^{ON} 48%, ASH 23%), while the triple exponential model was supported by less than 6% of our data (Fig 2.5 and 2.6). Restricting analysis to the initial 12 seconds of endocytosis significantly reduced the fraction of double exponential fits supported by AICp (Fig 2.5D and Fig 2.6D). This analysis suggests that the two time scales we detect are separable processes.

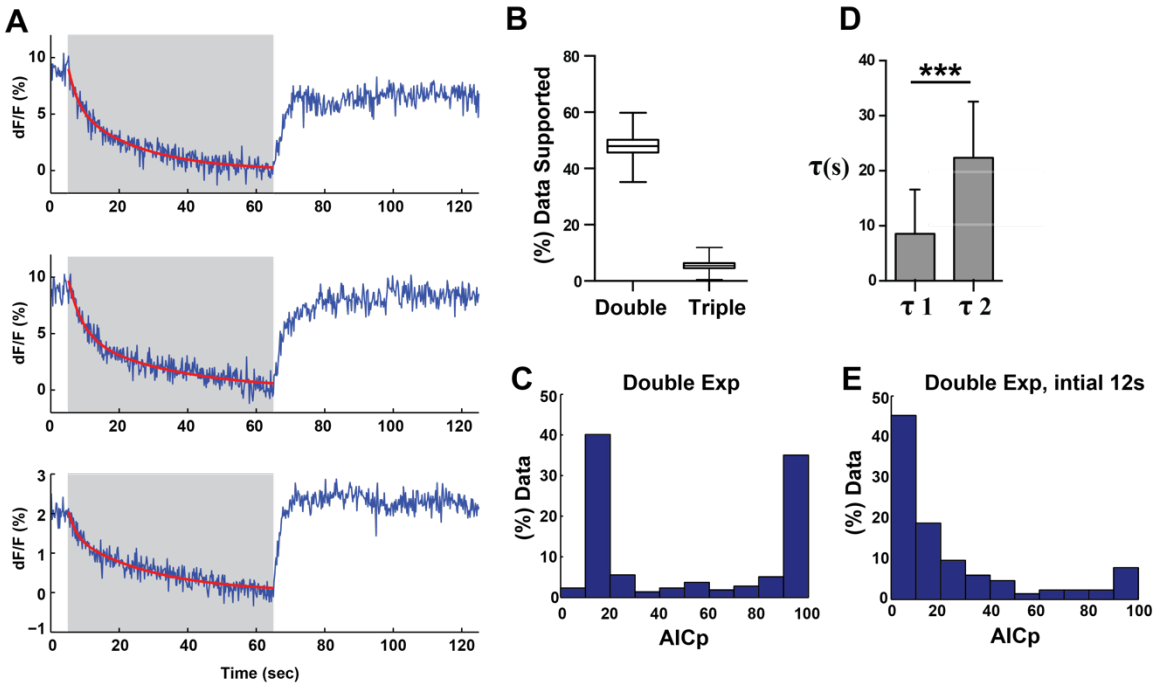

Figure 2.5. AWC^{ON} Vglut-pH decays contains multiple time constants.

(A) Three individual examples of AWC^{ON} Vglut-pH decays that fit a double exponential decay model with greater than 95% likelihood based on AICp (see Methods). **(B)** Percent of AWC^{ON} Vglut-pH data that fits a single versus double, or a double versus triple exponential model with a greater than a 50% likelihood (AICp > 50%). Box and whisker plot created by 10,000 sampled bootstrap sampling. **(C)** Frequency histogram of AICp-based likelihood values for double exponential fits to AWC Vglut-pH data. An AICp value of >50 supports a double exponential fit with increasing likelihood; an AICp of less than 50 supports a single exponential with increasing likelihood. **(D)** Average decay constants from double exponential fits. Error bars = S.T.D. t-test p <0.0001. **(E)** Frequency histogram of AICp-based likelihood values for double exponential fits to AWC^{ON} Vglut-pH data using only the initial 12s of the decay. For panels (B-E), n=219 trials, from 76 animals, 2-3 trials each. Gray bar = stimulus 11.2 uM butanone.

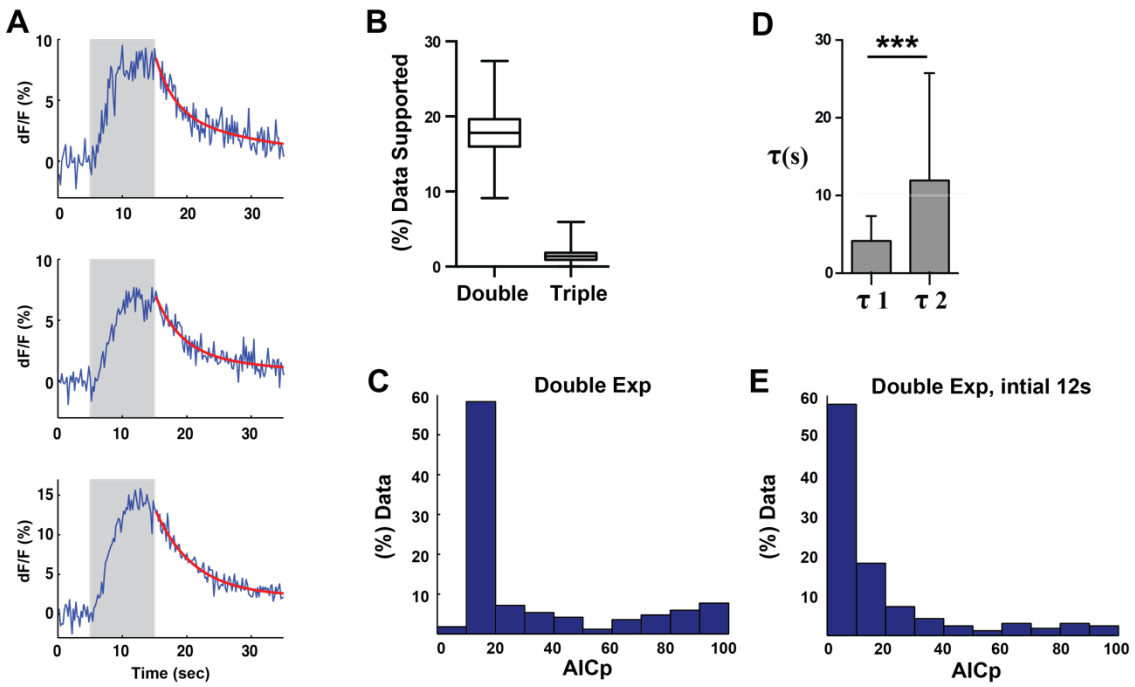

Figure 2.6. ASH Vglut-pH decays contain multiple time constants

(A) Three individual examples of ASH Vglut-pH decays that fit a double exponential decay model with greater than 95% likelihood base on AICp. **(B)** Percent of ASH Vglut-pH data that fits a double or triple exponential model with greater than a 50% likelihood (AICp > 50%). Box and whisker plot created by 10,000 sampled bootstrap sampling. **(C)** Frequency histogram of AICp-based likelihood values for double exponential fits to ASH Vglut-pH data (an AICp value of >50 supports a double exponential fit with increasing likelihood; an AICp of less than 50 supports a single exponential with increasing likelihood). **(D)** Average decay constants from double exponential fits. Error bars = S.T.D. t-test p <0.0001. **(E)** Frequency histogram of AICp-based likelihood values for double exponential fits to ASH Vglut-pH data using only the initial 12s of the decay. For panels (B)- (E), n=168 trials, from 56 animals, 2-3 trials each. Gray bar = stimulus 500 mM NaCl.

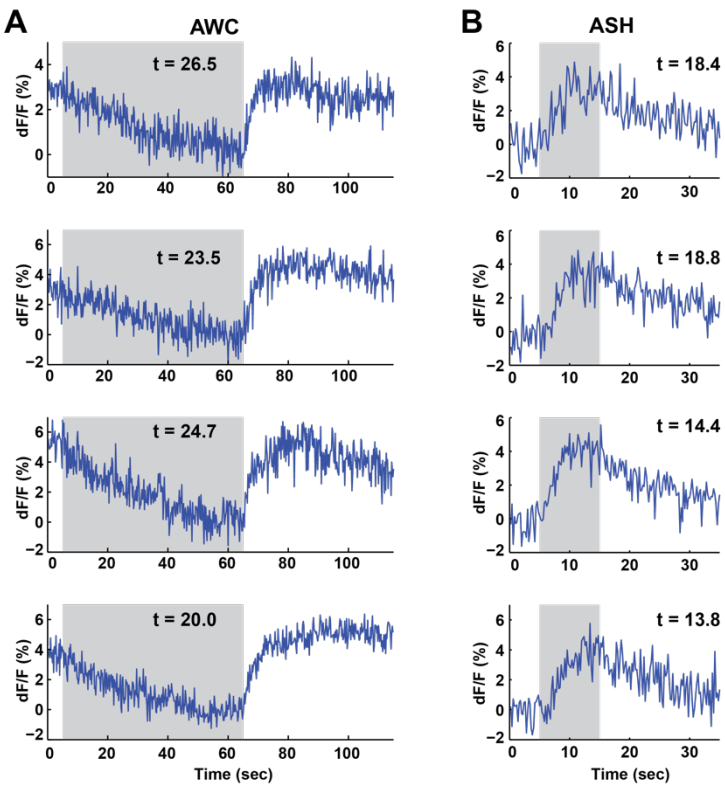

Figure 2.7. A subset of AWC and ASH Vglut-pH traces exhibit a single slow mode of endocytosis.

(A-B) Four individual examples of AWC and ASH Vglut-pH decays that appear to indicate a single slow mode endocytosis. Reported decay constants (t) for single exponential fits. Gray bar = stimulus period. AWC stimulus = 11.2 uM butanone. ASH stimulus = 500mM NaCl.

This was further supported by a small subset of Vglut-pH traces which exhibited a single slow endocytic mode which resembled the slower endocytic process from the double exponential traces (Fig 2.7). These results suggest that endocytosis of Vglut-pH in AWC^{ON} and ASH consists of a mixture of fast and slow modes.

AP180 is required for the fast VGlut-pH endocytic pathway

The mammalian VGlut-1 transporter corresponding to *C. elegans* VGlut is endocytosed by competing fast and slow pathways that depend on AP-2 and AP-3, respectively (Voglmaier et al., 2006). The clathrin adaptor protein AP180 that is important for cargo selection interacts directly with AP-2 (Koo et al., 2015) to promote clathrin assembly (Hao et al., 1999). Furthermore, the *Drosophila* vesicular glutamate transporter (DVGLUT) co-immunoprecipitates with AP180 from *Drosophila* brain lysates (Vanlandingham et al., 2014). To ask if AP180 might also contribute to AWC^{ON} and ASH Vglut-pH endocytic kinetics, we tested a null mutant in the *C. elegans* AP180/CALM homolog *unc-11(e47)* (Nonet et al., 1999).

VGlut-pH endocytosis was dramatically slowed in both AWC^{ON} and ASH in *unc-11(e47)* mutants (Fig 2.8A-D). A fraction of traces failed to respond to stimulation and this was more prominent in ASH (10% for AWC^{ON}, 58% for ASH) (Fig 2.8E, and see supplemental methods). Baseline Vglut-pH fluorescence was higher in *unc-11(e47)* mutants than in wild type, consistent with increased Vglut-pH on the surface due to compromised endocytosis (Fig 2.8F-G).

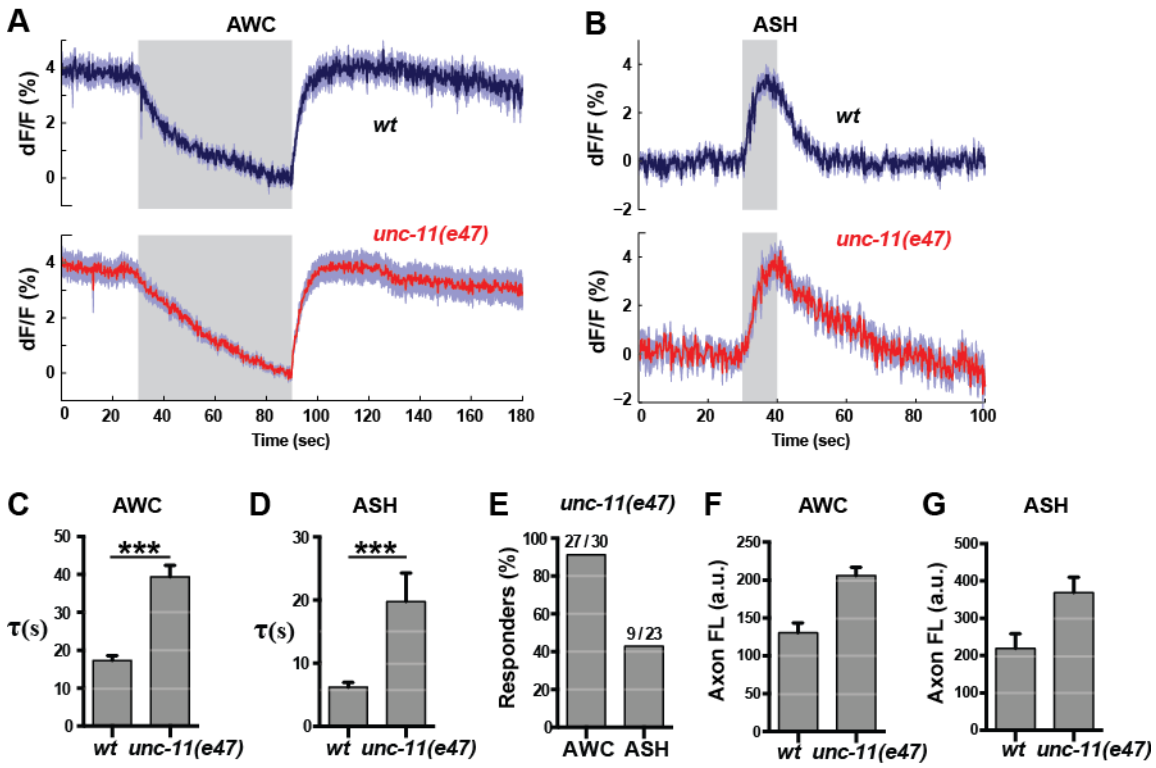

Figure 2.8. AP180 is required for the fast Vglut-pH endocytic pathway.

(A-B) Average Vglut-pH responses in AWC^{ON} and ASH in *unc-11(e47)* mutants. *unc-11(e47)* non-responders removed (see supplemental methods). AWC^{ON} *wt* n=15 trials (5 animals, 3 trials each). AWC^{ON} *unc-11(e47)* n=30 trials (12 animals, 2-3 trials each). ASH *wt* n= 21 trials (7 animals, 3 trials each). ASH *unc-11(e47)* n= 9 trials (6 animals 1-3 trials per animal). Gray bar = stimulus period. AWC^{ON} stimulus = 11.2 uM butanone. ASH stimulus = 500 mM NaCl. Shading= S.E.M. **(C-D)** Average time constants from single exponential fits (initial 20s of decay) of data in (A,B). Un-paired t-test, $p < 0.0001$. **(E)** Percent of non-responders in *unc-11(e47)* mutants. **(F-G)** Average axon fluorescence (first 5 frames of the recording). AWC^{ON} *wt* n=12 animals, *unc-11(e47)* n=19 animals. ASH *wt* n= 7 animals, *unc-11(e47)* n=8 animals. Un-paired t-test, $p < 0.0001$.

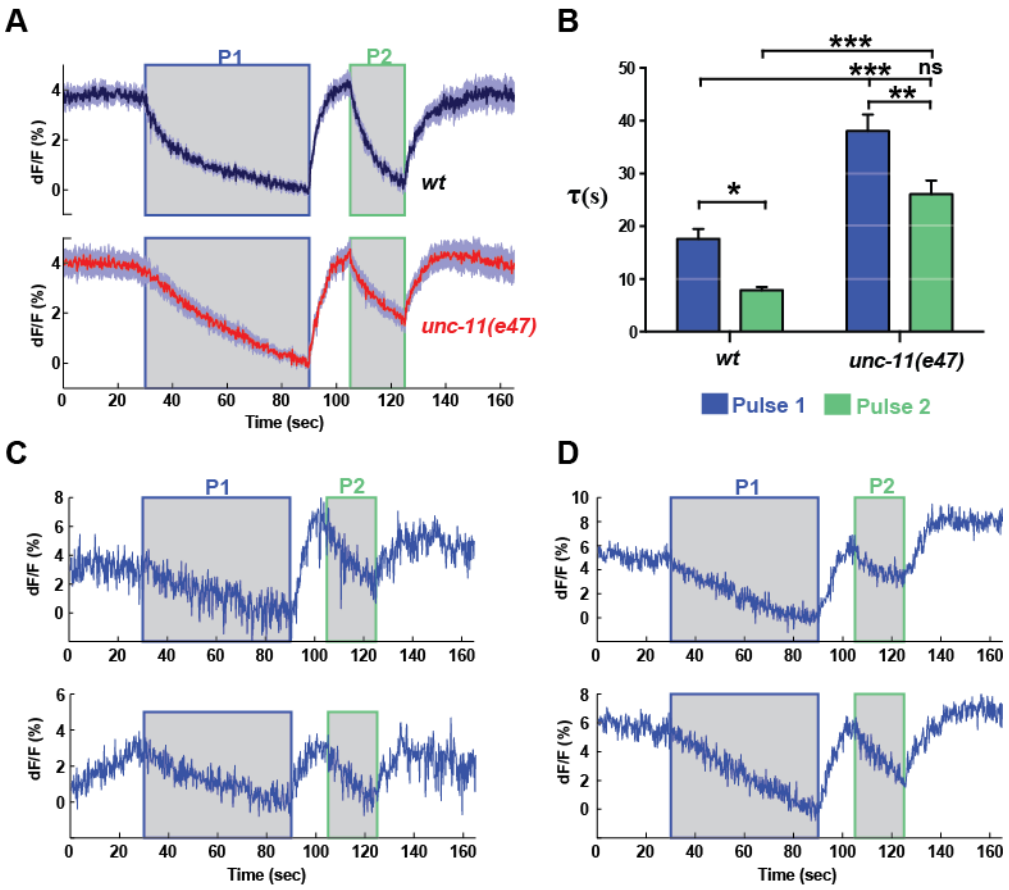

Figure 2.9. Enhancement of AWC^{ON} endocytosis by neural activity does not require AP180.

(A) Average AWC Vglut-pH signals in *wt* and *unc-11(e47)* mutants. *wt* n=21 trials, from 7 animals, 3 trials each. *unc-11(e47)* n=26 trials (9 animals, 3 trials each) (two non-responding trials removed). **(B)** Average time constants from single exponential fits (initial 20s of decay) of data in (A). Two-way ANOVA, *** p<0.0001, ** p<0.001, * p<0.01 **(C)** Two individual examples of Vglut-pH signals in *unc-11(e47)* mutants in which P2 induced rapid endocytosis. **(D)** Two individual examples of Vglut-pH signals in *unc-11(e47)* mutants in which P2 did not induce rapid endocytosis. Gray bar = stimulus, 11.2 uM butanone. Shading = S.E.M.

The double-stimulus protocol that accelerated AWC^{ON} endocytosis in wild-type animals could also accelerate endocytosis in *unc-11* mutants (although this was not the case for all trials) (Fig 2.9). The changes in AWC^{ON} and ASH VGlut-pH dynamics in *unc-11(e47)* mutants indicate that AP180 increases the speed and efficiency of endocytosis in *C. elegans* sensory neurons.

Quantitative analysis of Vglut-pH endocytosis

The Vglut-pH reporter measures endocytosis indirectly by measuring the coupled process of vesicle re-acidification. A simplified model of Vglut-pH endocytosis can be written as a two-step consecutive first-order rate equation (Balaji and Ryan, 2007) where k_1 and k_2 are the rate constants of endocytosis and vesicle re-acidification, respectively.

$$Eq.1\ (A)\ Surface\ pHluorin \overset{k_1}{\rightarrow} (B)\ Endocytosed\ vesicle \overset{k_2}{\rightarrow} (C)\ Acidified\ Vesicle$$

The rate equation for each component is:

$$Eq.2 \quad \begin{bmatrix} \frac{d[A]}{dt} = -k_1[A] \\ \frac{d[B]}{dt} = k_1[A] - k_2[B] \\ \frac{d[C]}{dt} = k_2[B] \end{bmatrix}$$

We explored the dynamics of this simple kinetic model to ask to what extent these two coupled processes could produce exponential decays with two distinct

timescales. In our data, the onset of endocytosis in AWC^{ON} proceeds from a steady-state equilibrium between exo- and endocytosis, and the stable Vglut-pH signal before odor application represents tonic release. This condition allowed us to analytically solve this system of differential equations, giving the integrated rate equations for the fluorescence species of the Vglut-pH reporter as:

$$Eq.3 \qquad \begin{bmatrix} [A] = A_o e^{-k_1 t} \\ [B] = \left(\frac{k_1}{k_2 - k_1}\right) A_o e^{-k_1 t} - \left(\frac{k_1}{k_2 - k_1} - \frac{k_1}{k_2}\right) A_o e^{-k_2 t} \end{bmatrix}$$

where A_o is amount of Vglut-pH on the surface at t=0 and k_1 and k_2 are the rate constants of endocytosis and vesicle re-acidification, respectively. Here we assume that during odor addition there is not significant additional exocytosis.

Here $[A]$ represents the amount of Vglut-pH on the cell surface and $[B]$ represents the endocytosed Vglut-pH that has yet to be acidified. The sum of $[A]$ and $[B]$ represents the total fluorescence at any given time. This model is also likely applicable to ASH Vglut-pH endocytosis at the end of the osmotic stimulus, since on average, the Vglut-pH signals in ASH reach a plateau before the stimulus is removed and endocytosis begins. We substituted various values for the rate constant of endocytosis (τ = 4.1-24 sec) and fixed the rate of vesicle re-acidification to 4 seconds based on measurements from hippocampal synapses (Atluri and Ryan, 2006). With these constraints, the decay response of the model closely approximated a single exponential decay for all values (Fig 2.10A) generating a linear profile on a semi-log plot (Fig 2.10B). By contrast, taking the AWC^{ON} data that was predicted to fit a double exponential by AICp (Fig 2.5), our data showed a strong deviation from linearity (Fig 2.10, red traces).

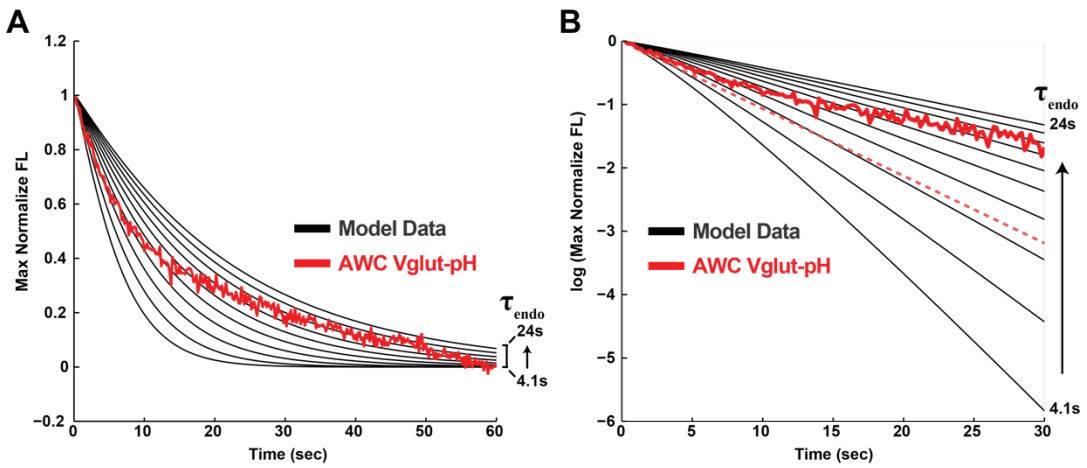

Figure 2.10. The coupled process of endocytosis and re-acidification are not sufficient to generate exponential decays with two time scales.

(A) Predicted decay of Vglut-pH fluorescence with varying endocytosis time constants (4.1s – 24s, 2 second intervals) produced by the model in Eq. 3. The time constant of re-acidification was fixed at 4s. Red trace is the average AWC Vglut-pH trace during odor addition (added at t=0) from the traces that fit a double exponential model with high likelihood (AICp > 90%, 76 traces. See also Figure 5). **(B)** Semi-log plot for the first 30s of the traces in (A). A straight line would indicate a single exponential process. AWC Vglut-pH data strongly deviates from a linear trajectory (dashed red line).

A similar analysis that fixed the rate of endocytosis and varied the rate of vesicle re-acidification generated similar results (data not shown). Therefore, the two coupled processes of endocytosis and re-acidification are unlikely to produce the multiple timescales of endocytosis observed in AWC^{ON} and ASH.

Discussion

The characterization of endocytosis in AWC^{ON} and ASH chemosensory neurons indicates that many mechanisms described in other systems are shared by the central synapses of *C. elegans*. AWC^{ON} and ASH differ in their apparent rate of endocytosis, with ASH having a faster rate. However, the distribution of AWC^{ON} decay rates was shifted to faster timescales after a previous stimulation with odor (the acceleration effect), producing a distribution similar to that of ASH. Several potential mechanisms could accelerate endocytosis rates. Increased calcium levels have been demonstrated to increase endocytic rates in several systems (Leitz and Kavalali, 2015; Neves et al., 2001; Sankaranarayanan and Ryan, 2001); the acceleration effect in AWC^{ON} endocytosis is preceded by a large calcium influx generated by the removal of the first 60 second odor pulse. ASH endocytosis is normally preceded by a large calcium influx, a necessary result of its stimulation. Thus calcium-sensitive endocytosis rates could explain the difference between ASH and AWC^{ON} decay rates in the first stimulation, as well as explaining acceleration in AWC^{ON} on the second stimulation. Calcium-mediated facilitation might occur via enhancement of dynamin function through

calcineurin-mediated dephosphorylation (Armbruster et al., 2013; Kononenko and Haucke, 2015), a process that could reasonably account for the ~20 second timescale of accelerated AWC^{ON} endocytosis.

Second messengers represent another potential mechanism by which endocytosis could be regulated. AWC^{ON} odor stimulation modulates levels of cGMP, which is known to accelerate SV endocytosis (Bargmann, 2006; Petrov et al., 2008). Endocytosis can also be modulated by pH and accelerated by alkalinization (Zhang et al., 2010), and the AWC^{ON} axon becomes significantly alkalinized during odor stimulation (see Chapter 4). In each case, acceleration could either increase the rate of a particular endocytic process/pathway, or bias the neuron toward the faster of two endocytic pathways (Neves et al., 2001).

The ability of AWC^{ON} to accelerate endocytosis after previous stimulation, and more generally, the distribution of endocytic rates in both ASH and AWC^{ON}, suggests that endocytosis rates are modulated by neural activity. This ability has been observed in many *in vitro* systems; and our results indicate that these processes take place within intact neural circuitry and function under natural states of neural activity.

Endocytic rates and multiple modes of endocytosis

Vglut-pH endocytosis in AWC^{ON} and ASH includes multiple time constants. This conclusion is supported by the analysis of exponential fit likelihood, the activity-dependent plasticity in AWC^{ON}, and the wide distribution of decay times in each neuron. Kinetic models suggest that it is unlikely that these changes stem

from the two timescales inherent to the endocytosis and acidification of the Vglut-pH reporter. Multiple modes of endocytosis with a broad range of rates have been extensively reported in other systems. The rate constants of these modes range from 50 milliseconds to 50 seconds (Smith et al., 2008b). Notably, photoreceptors and OFF bipolar neurons, which have highly similar signaling properties to AWC^{ON} (Chapter 1), also have multiple modes of endocytosis (Wu et al., 2007). Moreover, in OFF bipolar neurons in the goldfish retina, calcium promotes the fast mode of endocytosis (Neves et al., 2001).

Since we do not know the rate of synaptic vesicle re-acidification in AWC^{ON} and ASH, we cannot extract the precise decay constants for endocytosis. From our double exponential fits, the average fast and slow time constants in AWC^{ON} are approximately ~8 seconds and ~22 seconds respectively. Correcting for re-acidification will shift these values by a few seconds. These values are within the range reported for endocytosis in other systems. The time constant of endocytosis in hippocampal neurons at physiological temperatures is ~6 seconds (Balaji and Ryan, 2007). In the case of retinal OFF bipolar cells, the time constants for fast and slow endocytosis, measured using a capacitance clamp, were 1 second and >10 seconds, respectively (Neves and Lagnado, 1999). Ultrafast endocytosis takes place in *C. elegans* motor neurons (Watanabe et al., 2013a). If this takes place in *C. elegans* sensory neurons, the ‘fast’ time constant we measure is likely to resemble the rate of re-acidification, and our ‘fast’ time constant may represent the rate of vesicle re-acidification.

The existence of multiple endocytic modes has been proposed to compensate for the large changes in exocytosis rate that a neuron exhibits (Smith et al., 2008). Our results from AWC^{ON} and ASH, as discussed above, suggests a similar role. The mechanisms underlying the fast and slow endocytic components in AWC^{ON} and ASH remain to be elucidated. Given the multiple types of endocytic pathways and intermediates described (Royle and Lagnado, 2003), there are a number of possibilities (see Fig 2.1). One study found that SV retrieval outside of the active zone comprised the slow component and that restricting analysis to the focal point of SV release resulted in a single endocytic mode (Granseth et al., 2006). The fast and slow pathways could be competing for synaptic vesicles from the plasma membrane or be independent pathways that contain different intermediate steps. These distinct pathways are likely specified by specific sorting adaptors proteins (Traub, 2009). In hippocampal neurons, the Vglut-1 transporter is specifically recruited, through its interaction with endophilin, to be recycled through an AP-2 dependent pathway (Voglmaier et al., 2006). Disruption of Vglut-1's interaction with endophilin results in Vglut1 endocytosis through a slower AP-3 dependent pathway. Furthermore, inhibition of this AP-3 pathway restores Vglut1 endocytosis through the AP-2 pathway, indicating that AP-2 and AP-3 pathways compete for Vglut-1. This work suggests a plausible model for Vglut-pH endocytosis that encompasses many of our results. The mixture of fast and slow endocytic pathways we observe could be a parallel to the competing AP-2 and AP-3 pathways. In *C. elegans*, endocytosis can still occur in mutants that disrupt AP-2 function (Gu et al., 2008), indicating

an additional endocytic pathway is present. Increases in neuronal activity might bias Vglut-pH toward the AP-2 pathway, accounting for the enhancement effect in AWC^{ON}. The effect of disrupting VGlut-1 interactions with endophilin and the ability to restore Vglut-1 endocytosis by shutting down the AP-3 pathway, are also somewhat reminiscent of the effects in *C. elegans* AP180/CALM mutants: the fast component of Vglut-pH endocytosis was disrupted, but was partially restored by the enhancement effect. AP180 binds directly to AP-2, and they function together in clathrin assembly (Hao et al., 1999), suggesting a link between our fast endocytic pathway, AP180, and AP-2. Given these similarities, we suggest that the fast and slow endocytic components we see may be mediated by the AP-2 and AP-3 pathways, respectively.

The role of AP180 in AWC^{ON} and ASH endocytosis

Our results indicate that the AP180/CALM homolog UNC-11 is required for fast retrieval in AWC^{ON} and ASH. However, the mechanism that can enhance AWC^{ON} endocytic rates and distinguish AWC^{ON} and ASH endocytosis rates is retained in *unc-11* mutants.

The most prominent role of AP180 is its interaction with clathrin. AP180 strongly promotes the formation of clathrin cages and stabilizes their size *in vitro* (Lindner and Ungewickell, 1992). This function reflects its function *in vivo,* as AP180 mutants in both *C. elegans* and *Drosophila* have fewer, and more heterogeneously-sized, SVs (Nonet et al., 1999; Zhang et al., 1998). In *C.*

elegans, AP180 mutants have uncoordinated movement, indicating that motor neuron function is compromised.

AP180 is also required for the proper localization of synaptobrevin (Nonet et al., 1999). Knockout of AP180 in hippocampal neurons decreased the apparent rate of endocytosis of SVs marked with pHluorin-tagged synaptobrevin-2, but not pHluorin-tagged synaptotagmin-1 (Koo et al., 2015). This suggests that AP180 may regulate the sorting of cargo and/or the endocytosis of specific cargo containing vesicles, and furthermore demonstrates that AP180 is not essential for endocytosis itself. This would be consistent with the model proposed above, that in *unc-11(e47)* mutants, Vglut-pH is inappropriately sorted into a slower endocytic pathway. This could be a direct effect, as the *Drosophila* Vglut transporter has been shown to directly interact with AP180 (Vanlandingham et al., 2014), or an indirect effect due to mis-sorting of other factors, such as synaptobrevin or other VAMPs.

The dependency of endocytosis on clathrin is heterogeneous (Dittman and Ryan, 2009). In addition to clathrin-independent pathways, it is likely that the extent to which clathrin-dependent endocytosis mediates ‘fast’ or ‘slow’ retrieval depends on the synapse and on the conditions of the assay. In *C. elegans*, mechanisms for clathrin-independent endocytosis exist, but the strong effect we observe in *unc-11(e47)* mutants supports a role for clathrin in AWC^{ON} and ASH endocytosis.

In this chapter, we used Vglut-pH to characterize the dynamics of endocytosis in AWC^{ON} and ASH. We found that the rates of endocytosis in these

two neurons can be regulated in response to neural activity. We also described two modes of endocytosis, fast and slow, and identified the clathrin adaptor protein UNC-11, a homolog of AP180/CALM, as required for the fast mode of endocytosis. Our study represents the first direct measurements of endocytosis dynamics in *C. elegans*, and will provide a basis for future work on the regulatory mechanisms of synaptic vesicle endocytosis.

Chapter 3: The synaptic release machinery and its regulators

The release of neurotransmitter through the fusion of synaptic vesicles is a complex and highly organized process. The molecular machinery dedicated to this process is conserved from *C. elegans* to humans and is essential for the basic processes of cellular exocytosis and membrane fusion (Bargmann, 1998; Malsam et al., 2008). The composition and regulation of this machinery gives rise to the elementary properties of chemical synapses and is responsible for some of the most astonishing capabilities of the nervous system, such as learning and memory (Bailey et al., 2015). Although the individual components of the fusion machinery are highly conserved, diversity in the assembly of these components can produce modes of release that are functionally distinct (Atwood and Karunanithi, 2002). In this chapter, we characterize the synapses of AWC^{ON} and ASH, and evaluate the dependency of Vglut-pH responses on key members of the canonical synaptic vesicle fusion machinery.

Synaptic vesicle (SV) fusion is defined by three morphologically or molecularly defined stages: docking, priming, and fusion (Sudhof, 2004). Docking involves the localization of neurotransmitter loaded SVs from a reserve pool to the active zone. The active zone is an area of dense protein localization within synapses that contains components of the fusion machinery, scaffolding proteins, and presynaptic calcium channels necessary for efficient release (Ackermann et al., 2015). Priming occurs during or after docking, and is associated with an ATP-dependent process that makes SVs competent for fusion (Banerjee et al., 1996). Fusion is triggered by calcium influx and results in the formation of a fusion pore

between the SV and the plasma membrane that allows release of neurotransmitter (Sudhof, 2004). Modulation of the molecular machinery that regulates these stages gives rise to the basic functional properties of neurotransmitter release.

At the core of the synaptic vesicle fusion machinery is the SNARE complex. SNAREs (Soluble N-ethylmaleimide-sensitive factor attachment receptors) catalyze the fusion of vesicles with the plasma membrane and are universally involved in all types of membrane fusion (Malsam et al., 2008). They contain a ~60-residue conserved sequence motif (the SNARE domain) and come in two types: v-SNAREs and t-SNAREs. v-SNAREs reside on vesicles and interact directly with t-SNAREs, which are localized on the target fusion membrane. Synaptic vesicles use the v-SNARE synaptobrevin, which interacts with two different t-SNAREs, syntaxin and SNAP-25, on the presynaptic active zone to form the SNARE complex. Synaptobrevin, syntaxin, and SNAP-25 form a tight bundle of alpha helices that brings the two membranes together (Poirier et al., 1998; Sollner et al., 1993). Fusion is generated by energy released through the SNARE complex assembly and is thought to compress the two opposing membranes together, forcing the two negatively charged membranes into a pre-fusion state that rapidly transitions to a fusion pore, allowing the release of neurotransmitter (Rizo and Xu, 2015). The SNARE complex is then disassembled and regenerated by the cytoplasmic ATPase NSF and its adaptor protein SNAP.

Synaptobrevin, syntaxin, and SNAP-25 are together sufficient to catalyze the fusion of synaptic vesicles *in vitro*, but they do not fully account for the speed, efficiency, and calcium dependency observed at synapses (Weber et al., 1998). These abilities are generated and orchestrated by other members of the synaptic release machinery (Rizo and Sudhof, 2012; Rizo and Xu, 2015). These components are highly interconnected and form a large macromolecular protein complex. Although the detailed mechanisms and order of events are not completely understood, many of the molecular players crucial to SV release have been identified.

Of critical importance are the proteins UNC-13/*Munc13* and UNC-18/*Munc18*, which act as assembly chaperones of the SNARE complex, and have functions in priming, docking, and fusion (Rizo and Sudhof, 2012). The protein RIM, along with *Munc*13, forms a critical part of the active zone scaffolding cytomatrix, which is important for docking SVs and clustering presynaptic calcium channels in the active zone (Betz et al., 2001; Sudhof, 2004). The calcium dependency of SV release is mediated by a family of synaptic vesicle proteins known as synaptotagmins, which couple calcium influx to conformational changes in the SNARE complex, triggering fusion (Südhof, 2013b). Complexin and tomosyn are both SNARE interacting proteins important for tuning the activity of the SNARE complex (Malsam et al., 2008; McMahon et al., 1995; Rizo and Xu, 2015). Together, these components constitute key members of the macromolecular complex that regulate SV release (Figure 3.1).

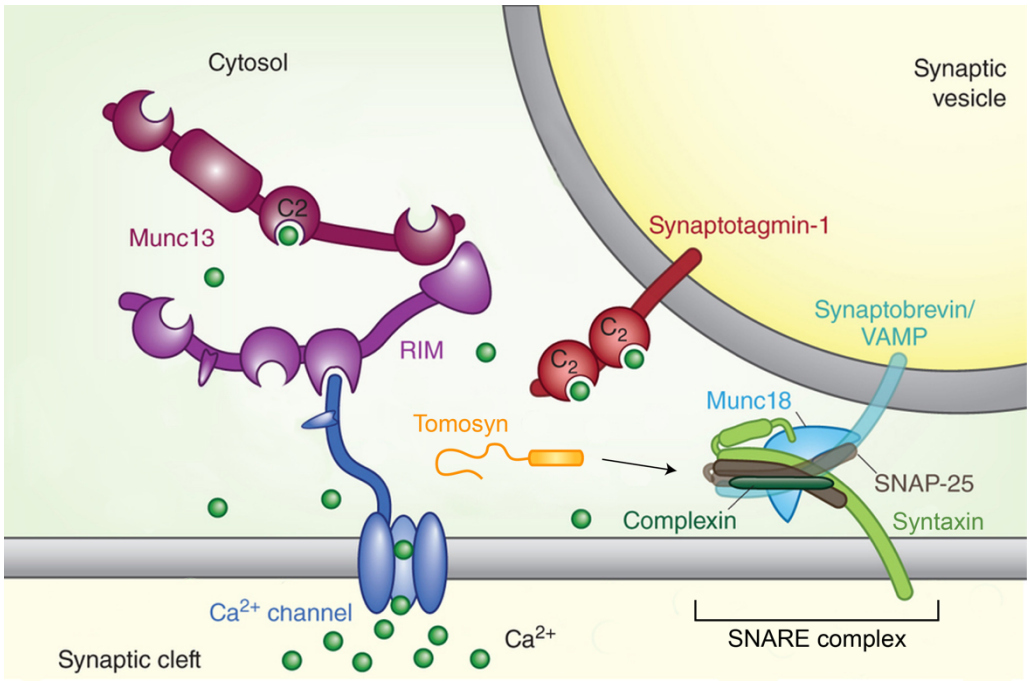

Figure 3.1 The synaptic vesicle release machinery and its regulators

Diagram of the presynaptic terminal showing the components that will be examined in this Chapter (synaptotagmins are examined separately in Chapter 5): the SNARE complex (syntaxin, synaptobrevin, and SNAP) and its regulators *unc-13, unc-18,* tomosyn, and complexin regulate the highly coordinated process of SV fusion. *unc-13* and RIM also function together to tightly couple presynaptic calcium influx to SV release. Adapted and modified from (Südhof, 2013a).

In *C. elegans*, the role of these components in SV release has been investigated at the neuromuscular junction (NMJ) (Richmond, 2005), but the function of these proteins in other synapses has not been well characterized.

The diversity in presynaptic release activity driven by distinct synaptic vesicle pools (Alabi and Tsien, 2012; Hua et al., 2011) and the use of 'non-canonical' release machinery indicates that the presynapse is an important level of diversification of the functional characteristics of synapses (Ramirez and Kavalali, 2012). Here we use Vglut-pH imaging to characterize the dependency

of AWC^{ON} and ASH synapses on the canonical members of the release machinery, namely: synaptobrevin, syntaxin, SNAP25, *Munc-13*, *Munc-18*, RIM, complexin, and tomosyn. The dependency on synaptotagmins is discussed separately in Chapter 5. In the section below, we introduce each of these proteins separately along with our results. We find that both AWC^{ON} and ASH are highly dependent on the SNARE complex. AWC^{ON} and ASH are also highly dependent on *unc-13*, *unc-18*, and RIM, but we detected significant differences in the residual responses in these mutants. Complexin appears to act as an inhibitor of SV release in AWC^{ON} and ASH, and we find an unexpected role for tomosyn in regulating calcium influx. Our results indicate that AWC^{ON} and ASH synapses are distinct from those of the NMJ and provide a framework for future work on the regulation of neurotransmitter release in these sensory neurons.

Results

The SNARE complex is required for glutamate release.

To characterize the core SV release machinery of AWC^{ON} and ASH, we first focused on the SNARE complex. To evaluate the role of the v-SNARE synaptobrevin in SV release, we cell-specifically expressed tetanus toxin (TeTx) in either AWC or ASH and monitored Vglut-pHlorin responses. TeTx specifically cleaves synaptobrevin and is commonly used to block synaptic release (Schiavo et al., 1992). Vglut-pHluorin responses were completely absent in TeTx-expressing animals for both AWC^{ON} and ASH (Fig 3.2A-B). We calculated the

frequency of responders by counting the number of trials that showed any stimulus-correlated Vglut-pH changes (see supplemental methods) and found none in TeTx-expressing animals (Fig 3.2A-B, right). At the *C. elegans* neuromuscular junction (NMJ), partial loss of function in the t-SNAREs syntaxin (*unc*-64) and SNAP-25 (*ric-4)* produced strong defects in SV release (Liu et al., 2005; Martin et al., 2011). In AWC^{ON} and ASH *unc-64(e246)* produced a similar result to TeTx, with most animals not responding (Fig 3.2C-D). Vglut-pHluorin responses in the SNAP-25 mutant *ric-4(md1088)* were present but strongly diminished (Fig 3.2E-F). The difference between *unc-64* and *ric-4* mutants is likely the result of differences in the strength of these partial loss-of-function alleles. Indeed, the *unc-64(e246)* mutants have highly uncoordinated movements and are most often paralyzed, whereas the *ric-4(md1088)* mutants can move. Overall, these results are consistent with glutamate release in AWC^{ON} and ASH being highly dependent on the canonical SNARE complex, and are consistent with results from the NMJ.

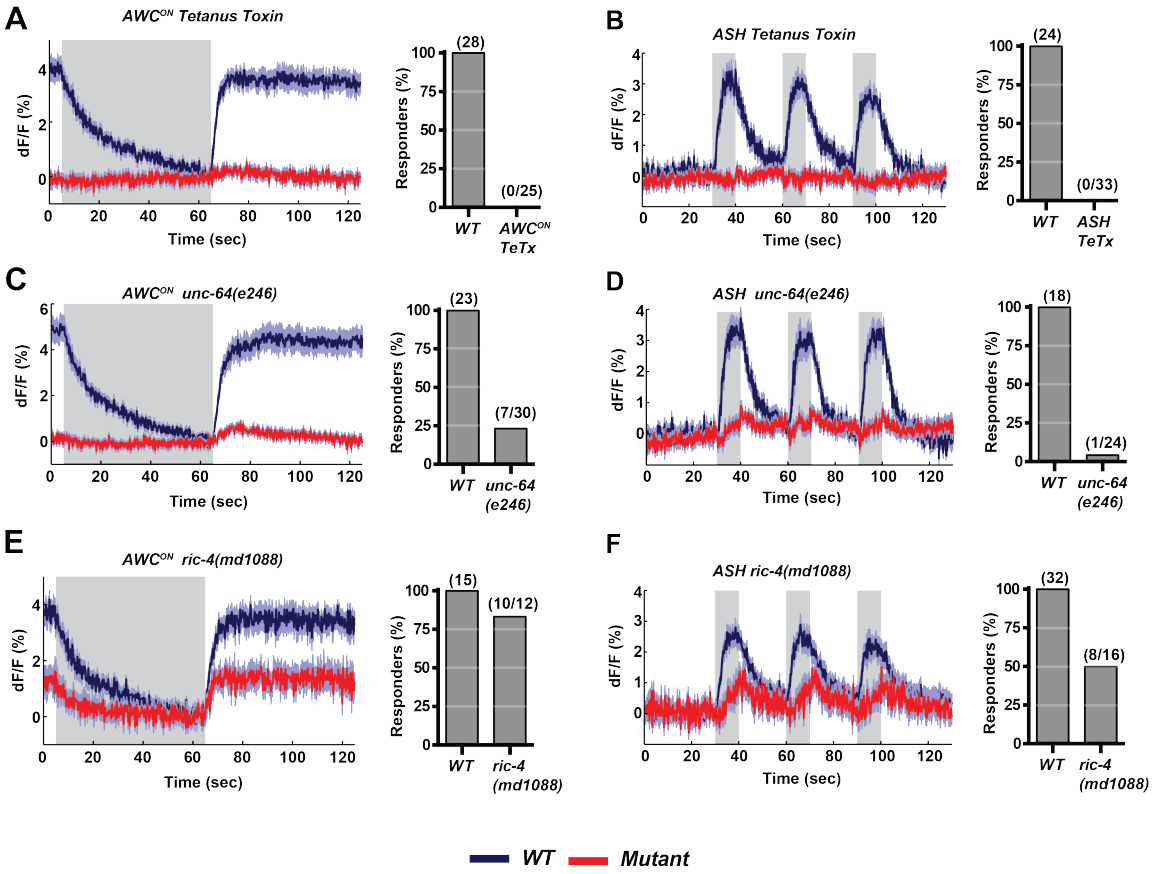

Figure 3.2 Vglut-pH responses are dependent on SNARE complex.

(A-B) AWC^{ON} and ASH Vglut-pH responses are eliminated in by cell-specific expression of TeTx. AWC^{ON} *wt* n= 28 trials, from 10 animals, 2-3 trials each (*wt* = Tetx array negative animals). AWC^{ON} *str-2* promoter driving Tetx n = 25 trials, from 9 animals, 2-3 trials each. ASH *wt* n= 24 trials, from 8 animals, 3 trials each (*wt* = Tetx array negative animals). ASH *Sra-6* promote driving Tetx n = 33 trials, from 11 animals, 3 trials each. **(C-D)** Average AWC^{ON} and ASH Vglut-pH responses in *unc-64(e246)* mutants. AWC^{ON} *wt* n= 23 trials, from 9 animals, 2-3 trials each. AWC^{ON} *unc-64(e246)* n= 30 trials, from 10 animals, 3 trials each. ASH *wt* n= 18 trials, from 6 animals, 3 trials each. ASH *unc-64(e246)* n= 24 trials, from 8 animals, 3 trials each. **(E-F)** Average AWC^{ON} and ASH Vglut-pH responses in *ric-4(md1088)* mutants. AWC^{ON} *wt* n= 15 trials, from 5 animals, 3 trials each. AWC^{ON} *ric-4(md1088)* n= 12 trials, from 4 animals, 3 trials each. ASH *wt* n= 32 trials, from 11 animals, 2-3 trials each. ASH *ric-4(md1088)* n= 16 trials, from 6 animals, 2-3 trials each. Bar graph right to each all traces indicates number of detected responses. Gray bar = stimulus period. AWC^{ON} Stimulus = 11.2 uM butanone. ASH Stimulus = 500 mM NaCl. Shading = S.E.M.

Vglut-pH responses are largely dependent on *unc-13* and *unc-18*

unc-13 and *unc-18* are essential for efficient SV release. *unc-13* and *unc-18* regulate the assembly of the SNARE complex that prepare SVs for fusion, and current models based on the *C. elegans* NMJ have functionally implicated these proteins in the priming and docking stages of the SV fusion cycle, respectively (Richmond, 2005). Electrophysiological recordings from the NMJ have demonstrated that loss of *unc-13* function severely impairs synaptic transmission (Richmond et al., 1999). SV release defects at the NMJ in *unc-18(lf)* animals are severe, but not as severe as those of *unc-13(lf)* animals (Gracheva et al., 2010; Weimer et al., 2003). In mammalian hippocampal neurons, deletion of either *Munc-18* or all *Munc-13* isoforms completely eliminates SV release (Augustin et al., 1999; Varoqueaux et al., 2002; Verhage et al., 2000).

To evaluate the role of these proteins in synaptic transmission in AWC^{ON} and ASH, we measured Vglut-pH responses in *unc-13(lf)* and *unc-18(lf)* mutants. We found that Vglut-pH responses in both AWC^{ON} sand ASH were strongly dependent on *unc-13*, but small Vglut-pH responses in response to odor removal could be still be detected in AWC^{ON} (Fig 3.3A-B).

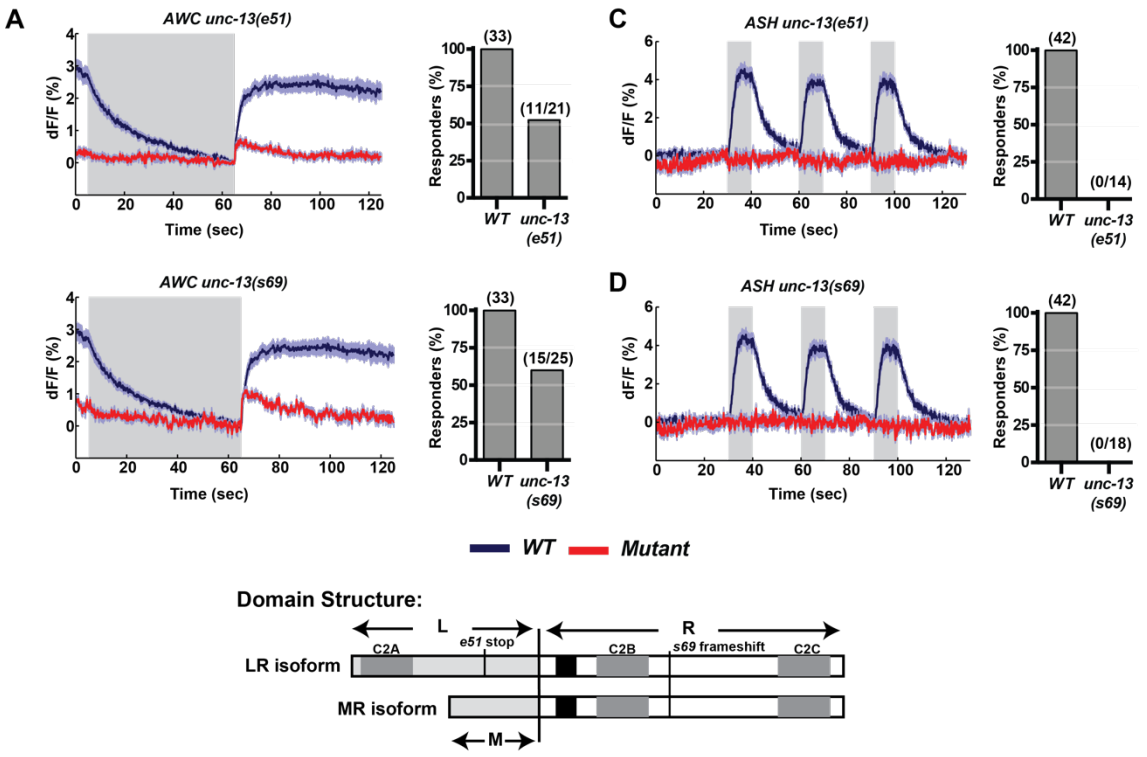

Figure 3.3 AWC^{ON} and ASH Vglut-pH responses are compromised in *unc-13(lf)* mutants.

(A-B) Average AWC^{ON} Vglut-pH responses in *unc-13(e51) and unc-13(s69)* mutants. Non-responders were not included in the average traces. Both alleles tested in parallel with the same *wt* control. *wt* n= 33 trials, from 11 animals, 3 trials each. *unc-13(e51)* n= 11 trials, from 7 animals, 1-3 trials each. *unc-13(s69)* n= 15 trials, from 9 animals, 1-3 trials each. **(D-E)** Average ASH Vglut-pH responses in *unc-13(e51) and unc-13(s69)* mutants. Both alleles were tested together in parallel with the same *wt* control. *wt* n= 42 trials, from 14 animals, 3 trials each. *unc-13(e51)* n= 14 trials, from 5 animals, 1-3 trials each. *unc-13(s69)* n= 18 trials, from 7 animals, 1-3 trials each. In all panels, bar graph indicates the number of detected responses (see supplemental methods). Gray bar = stimulus period. AWC^{ON} Stimulus = 11.2 uM butanone. ASH Stimulus = 500 mM NaCl. Shading = S.E.M. Bottom of figure: The domain structure of *unc*-13. Redrawn from *Richmond et al., 1999*. The *unc-13(e51)* allele is a missense mutation that generates an early translational stop. The *unc-13(e51)* allele is a null allele for the LR isoform. The *unc-13(s69)* allele is a small deletion resulting in a frameshift and effects both LR and MR forms. Complete *unc-13* nulls are lethal (Kohn et al., 2000; Richmond et al., 1999).

These small responses were present in the majority of both *unc-13(e51)* and *unc-13(s69)* mutant animals tested. AWC^{ON} responses in *unc-13* mutants had significantly altered dynamics, showing very weak or no response to odor addition and a blunted but sharp response to odor removal that slowly returned to baseline. These dynamics suggest that AWC^{ON} tonic release cannot be maintained in *unc-13(lf)* mutants, and only after a large calcium influx (resulting from odor removal) can some SVs be released. By contrast, no Vglut-pH responses were detected in ASH (Fig 3.3C-D).

Similar to our results with *unc-13*, Vglut-pH responses from both AWC^{ON} and ASH were largely defective in *unc-18* animals (Fig 3.4). In AWC^{ON}, the frequency of *unc-18* mutant Vglut-pH responses was lower than the *unc-13(lf)* mutants, with most animals/trials showing no response to stimulation. In animals that did respond, the dynamics of the AWC^{ON} response were similar to those observed in *unc-13* mutants (Fig 3.4A). In ASH, the frequency of detected responses was higher than in AWC^{ON}. In trials that showed responses in ASH, responses were weak with slow dynamics (Fig 3.4B).

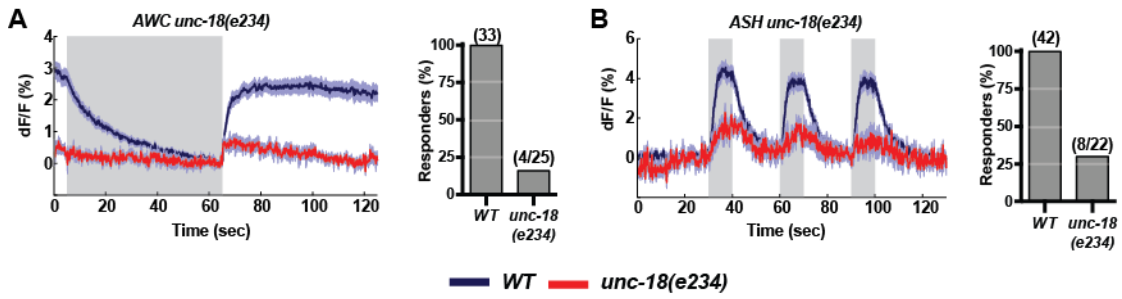

Figure 3.4 AWC^{ON} and ASH Vglut-pH are responses are compromised in *unc-18* null mutants.

(A-B) Average AWC^{ON} and ASH Vglut-pH responses in *unc-18(e234)* mutants. Non-responders were not included in the average traces. AWC^{ON} *wt* n= 33 trials, from 11 animals, 3 trials each. AWC^{ON} *unc-18(e234)* n= 4 trials, from 4 animals, 1 trial each. ASH *wt* n= 42 trials, from 14 animals, 3 trials each. ASH *unc-18(e234)* n= 8 trials, from 7 animals, 1-2 trial each. Bar graph right to each all traces indicates number of detected responses. Gray bar = stimulus period. AWC^{ON} Stimulus = 11.2 uM butanone. ASH Stimulus = 500 mM NaCl. Shaded-cloud around traces = S.E.M. The *unc-18(e234)* allele is a missense mutation that results in an early translational stop.

Loss of RIM decreases Vglut-pH responses

RIM is a multi-domain protein that interacts directly with both the release machinery and presynaptic calcium channels and is an important regulator of calcium influx and SV release (Sudhof, 2004). Separate from its function in regulating calcium influx, RIM also functions in presynaptic homeostatic modulation (Muller et al., 2015; Muller et al., 2012). Some of the roles of RIM appear to be conserved in *C. elegans,* as RIM is localization to presynaptic calcium channels (Gracheva et al., 2008a; Koushika et al., 2001) and null mutants exhibit reduced SV release. RIM has also been described to play roles in SV docking, and EM sections from the *C. elegans* NMJ of RIM null mutants were shown to have less SVs present at active zones (Gracheva et al., 2008b; Weimer et al., 2006).

To evaluate the role of RIM in SV release of AWC^{ON} and ASH, we analyzed Vglut-pH responses in the RIM null mutant *unc-10(md1117)*. We found that Vglut-pH responses were compromised in both AWC^{ON} and ASH in *unc-10(md1117)* mutants (Fig 3.5). The overall dynamics of AWC^{ON} responses appeared similar to *unc-13* and *unc-18*, with the apparent loss of tonic release. However, *unc-10(lf)* animals lacked the sharp rise associated with odor removal that we observed in *unc-13* and *unc-18* mutants (Fig 3.5A). In addition, a significant fraction of trials were entirely unresponsive to odor stimulation (Fig 3.5B). In ASH, the response magnitude in *unc-10(md117)* mutants was decreased and the VGlut-pH signal began to decay before the stimulus was removed (Fig 3.5C).

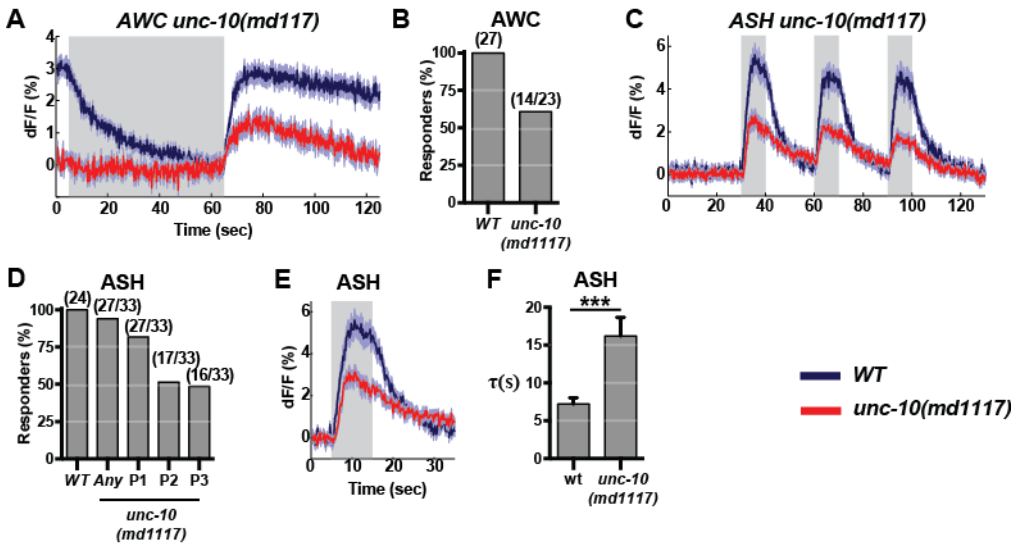

Figure 3.5 AWC^{ON} and ASH Vglut-pH responses in *unc-10* null mutants.

(A-B) Average AWC^{ON} Vglut-pH response in *unc-10(md117)* mutants. Non-responders were not included in the average traces. AWC^{ON} *wt* n= 27 trials, from 9 animals, 3 trials each. *unc-10(md117)* n= 23 trials, from 8 animals, 1-3 trials each. **(B)** Number of detected responses in AWC^{ON}. **(C)** Average ASH Vglut-pH responses in *unc-10(md117)* mutants. Non-responders (for all pulses only) removed. ASH *wt* n= 24 trials, from 8 animals, 3 trials each. *unc-10(md117)* n= 27 trials, from 11 animals, 1-3 trials each. **(D)** Percent of ASH Vglut-pH responses detected in each pulse. **(E)** Average ASH Vglut-pH responses to the first stimulus pulse with non-responders removed. **(F)** Mean ASH Vglut-pH endocytosis time constant, first stimulus pulses only. Single exponential fit. Unpaired t-test, *** $p < 0.0001$. From data in (E). Gray bar = stimulus period. AWC^{ON} Stimulus = 11.2 uM butanone. ASH Stimulus = 500 mM NaCl. Shading = S.E.M.

Interestingly, we found significant variability in the responsiveness between pulses in ASH (Fig 3.5D). The first pulse most consistently produced a response, whereas pulses two and three produced a response only about half the time. When responses did occur, the sharp rise trigger by stimulus addition was intact, indicating that the rate of exocytosis in not altered in *unc-10(md1117)* mutants (Fig 3.5E). Active zone scaffold proteins, such as RIM, have been suggested to important for coupling the process of exo- and endocytosis (Haucke et al., 2011). Consistent with this notion, the VGlut-pH decay was slower than wild-type, indicative of an endocytic defect (Fig 3.5F). These results indicate that SV release in AWC^{ON} and ASH are partially dependent on RIM function, and suggest an additional role for *unc-10* in endocytosis. These defects are generally consistent with those reported at of the *C. elegans* NMJ, as well as from synapses lacking RIM in *Drosophila* and mammalian neurons.

Loss of complexin increases Vglut-pH responses.

Complexin is a cytoplasmic protein that interacts with synaptobrevin and syntaxin and binds to the assembled SNARE complex (Malsam et al., 2008; McMahon et al., 1995; Rizo and Xu, 2015). Complexin has dual functions in both promoting and inhibiting SV release, and these functions are localized to particular domains of the protein (Martin et al., 2011; Wragg et al., 2013; Xue et al., 2009). In particular, complexin differentially regulates spontaneous/tonic release and evoked release, either suppressing one or enhancing the other. Variation in the relative strength of these facilitatory and inhibitory domains

between ortho- and paralogs has been suggested to be important for tuning the release dynamics of a given synapse and contributing to synaptic diversity and specificity (Xue et al., 2009a).

In *C. elegans*, loss of complexin-1 (*cpx-1*) greatly enhances tonic release at NMJs, while simultaneously abolishing stimulus-evoked release (Martin et al., 2011). A similar effect is observed at the *Drosophila* NMJ (Xue et al., 2009a). In contrast, AWC^{ON} VGlut-pH responses to odor removal were slightly in increased in *cpx-1(ok1552)* mutants, whereas ASH Vglut-pH responses were increased more than 2-fold (Fig 3.6A-B). These increases were not associated with any significant changes in the rate of the exocytic responses or with changes in endocytosis rates (Fig 3.6C-F).

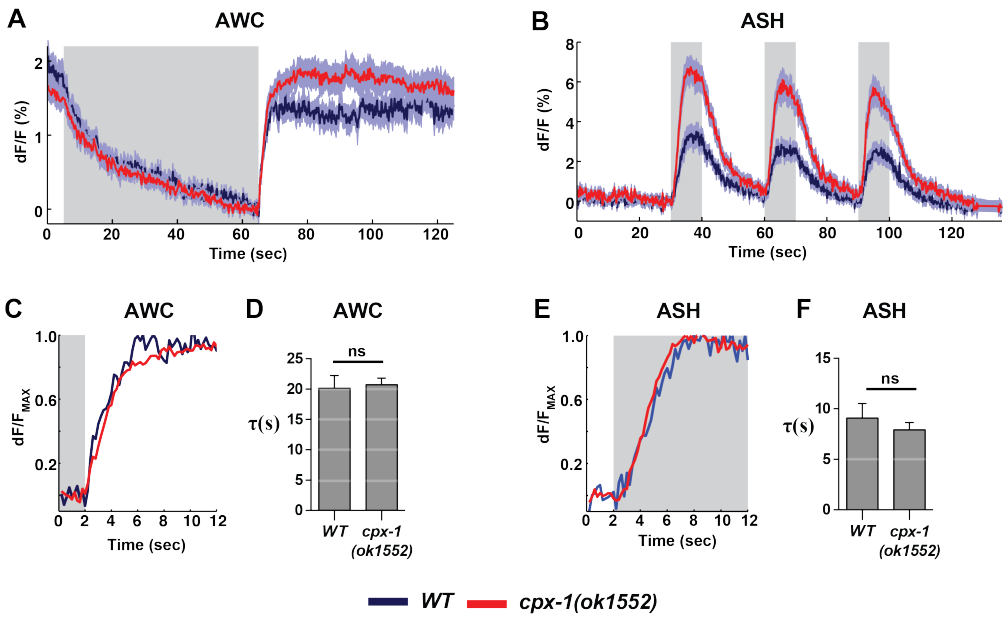

Figure 3.6 AWC^{ON} and ASH Vglut-pH responses in *cpx-1 null* mutants.

(A) Average AWC^{ON} Vglut-pH response in *cpx-1(ok1552)* mutants. AWC^{ON} *wt* n= 17 trials, from 6 animals, 2-3 trials each. *cpx-1(ok1552)* n= 36 trials, from 12 animals, 3 trials each. **(B)** Average ASH Vglut-pH response in *cpx-1(ok1552)* mutants. ASH *wt* n= 33 trials, from 11 animals, 3 trials each. *cpx-1(ok1552)* n= 38 trials, from 13 animals, 2-3 trials each. **(C)** Average AWC^{ON} Vglut-pH odor removal responses from (A) magnitude normalized. **(D)** Mean AWC^{ON} Vglut-pH endocytosis time constants, single exponential fit. Unpaired t-test, ns = p >0.05. From data in (A). **(E)** Average ASH Vglut-pH responses (pulse 1) from (B) magnitude normalized by peak signal (F/F_{MAX}). **(F)** Mean ASH Vglut-pH endocytosis time constants, single exponential fit. Unpaired t-test, ns = p >0.05. From data in (B). Gray bar = stimulus period. AWC^{ON} Stimulus = 11.2 uM butanone. ASH Stimulus = 500 mM NaCl. Shading = S.E.M.

Tomosyn modulates both Vglut-pH responses and calcium influx

Tomosyn is a soluble protein that was first isolated as a syntaxin binding protein from rat brain lysates (Fujita et al., 1998). Similar to synaptobrevin, tomosyn forms a SNARE complex-like structure with syntaxin and SNAP25 (Hatsuzawa et al., 2003). *In vitro* binding assays have found that synaptobrevin and tomosyn competitively bind the SNARE complex, and displacement of one with the other requires prior disassembly of the SNARE complex by NSF. Furthermore, over-expression of tomosyn inhibits depolarization-induced exocytosis in several cell types (Ashery et al., 2009). Together, these results suggest that tomosyn functions as a negative regulator of exocytosis and SV release through regulation of the SNARE complex.

C. elegans encodes a single tomosyn gene (*tom-1*) that produces three alternatively spliced variants. Electrophysiological recordings at the *C. elegans* NMJ have shown that *tom-1(lf)* mutants display increased, and greatly prolonged, evoked post-synaptic currents (Gracheva et al., 2006b). Furthermore, *tom-1(lf)* mutants have an increased response to hyperosmotic stimulation and an increased number of SVs at active zones, consistent with a negative role in SV priming.

In *tom-1(ok285)* mutants, the exocytic phases of the AWC^{ON} and ASH responses were greatly increased in both magnitude and in speed (Fig 3.7A-D). The rate of endocytosis did not appear to be affected in either AWC^{ON} or ASH (Fig 3.7E-F). The increase in AWC^{ON} Vglut-pH magnitude was not significant for 60 second pulses, but the time to peak was faster (Fig 3.7C). For shorter 10

second pulses, the response magnitude was significantly larger, overshooting baseline activity levels (Fig 3.7G). In ASH, stimulation of *tom-1(lf)* mutants resulted in a ~3-fold increase in the VGlut-pH magnitude, that was not sustained during the stimulus period (Fig 3.7B). Similar to AWC^{ON}, ASH responses also peaked more quickly (Fig 3.7D). These observations contrast with the effect of *cpx-1(lf)* on ASH responses, where the magnitude was increased but the rate of exocytic response was not (see Fig 3.6E).

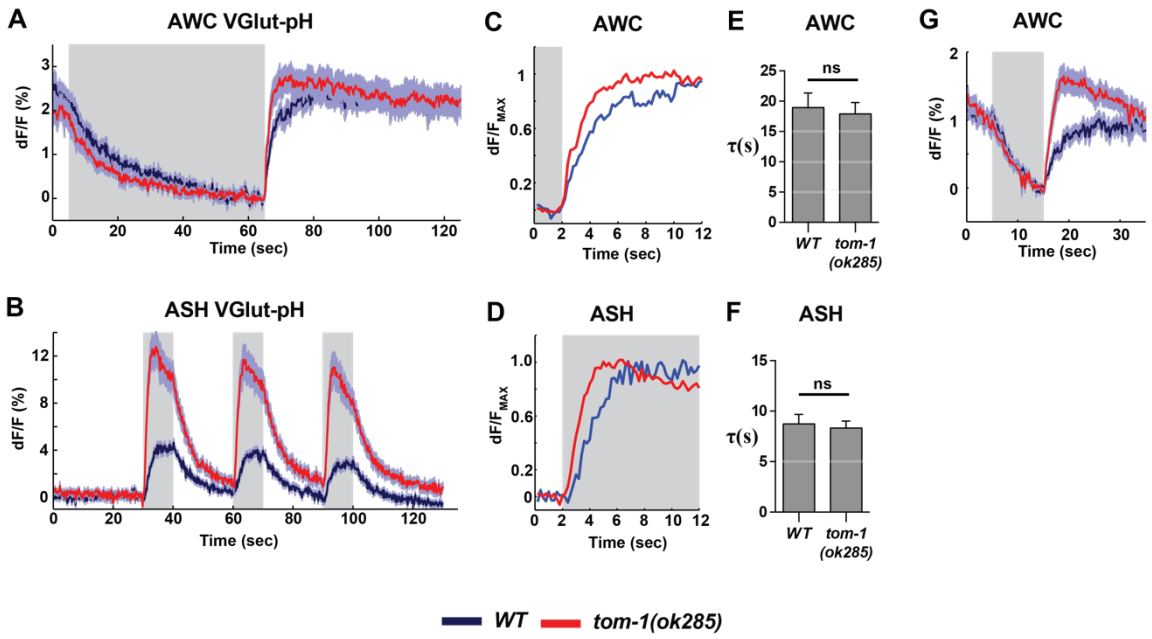

Figure 3.7 Tomosyn negatively regulates exocytosis in AWC^{ON} and ASH.

(A) Average AWC^{ON} Vglut-pH response to 60 second odor pulses. *wt* n= 18 trials, from 6 animals, 2-3 trials each. *tom-1(ok285)* n= 23 trials, from 8 animals, 2-3 trials each. **(B)** Average ASH Vglut-pH responses. *wt* n= 24 trials, from 6 animals, 3 trials each. *tom-1(ok285)* n= 29 trials, from 10 animals, 2-3 trials each. **(C)** Average AWC^{ON} Vglut-pH odor removal response from (A) magnitude normalized. **(D)** Average ASH Vglut-pH responses (pulse 1) from (E) magnitude normalized. **(E)** Mean AWC^{ON} Vglut-pH endocytosis time constants, single exponential fit. Unpaired t-test, ns = p >0.05. From data in (A). **(F)** Mean ASH Vglut-pH endocytosis time constants, single exponential fit. Unpaired t-test, ns = p >0.05. From data in (B). **(G)** Average AWC^{ON} Vglut-pH responses to 10 second odor pulses. *wt* n= 42 trials, from 7 animals, 6 trials each. *tom-1(ok285)* n= 42 trials, from 7 animals, 6 trials each. AWC^{ON} Stimulus = 11.2 uM butanone. ASH Stimulus = 500 mM NaCl. Shading = S.E.M.

To gain further insight into the effect of *tom-1(lf)* at synapses, we conducted calcium imaging of *tom*-1 mutants in AWC^{ON} using syGCaMP. To our surprise, the magnitude of AWC^{ON} axonal calcium responses was substantially increased for both 60 second and 10 second stimuli in *tom-1(ok285)* mutants (Fig 3.8A-B). The initial rate of signal change also appeared more rapid (Fig 3.8A inset). To determine whether this effect was unique to AWC^{ON}, we tested ASH GCaMP responses in *tom-1(lf)* mutants. In ASH, we found that the magnitude of soluble GCaMP3 responses was not significantly different from wild-type, but peaked more quickly in both the axon and in the cell body (Fig 3.8C-E). These results indicate that tomosyn modulates both calcium and Vglut-pH signals in AWC^{ON} and ASH.

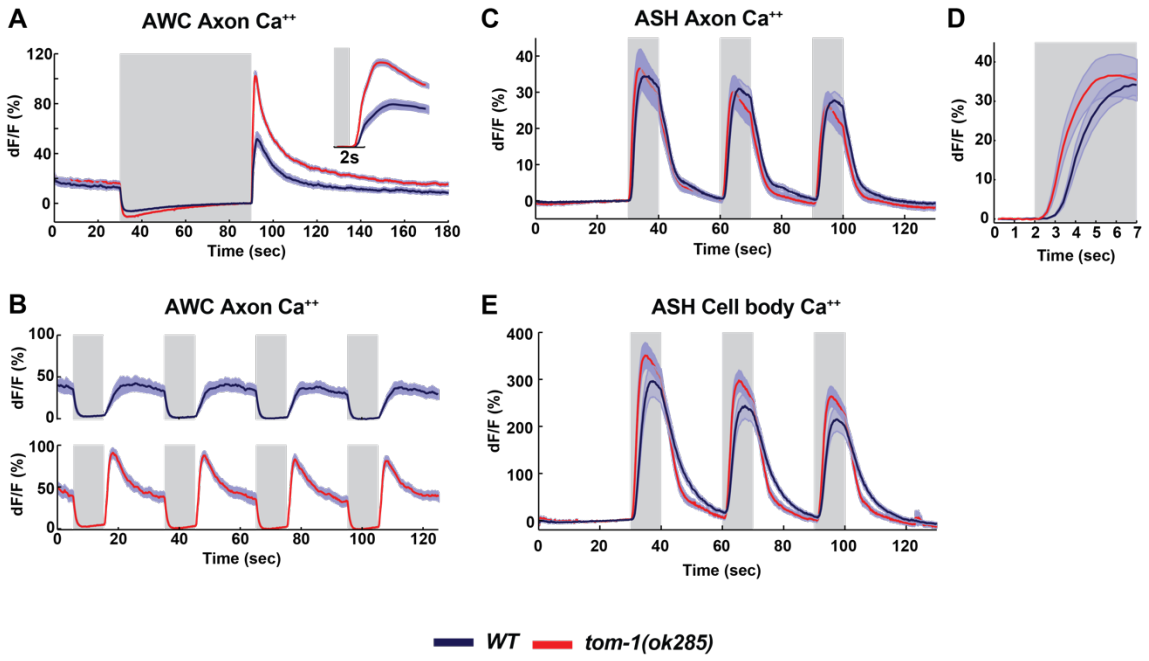

Figure 3.8. Tomosyn negatively Ca^{++} influx in AWC^{ON} and ASH.

(A) Average response of the AWC^{ON} axon measured with syGCaMP to 60 second odor pulses. *wt* n= 18 trials, from 6 animals, 2-3 trials each. *tom-1(ok285)* n= 23 trials, from 8 animals, 2-3 trials each. Inset zoomed view of odor removal response. **(B)** Average response of the AWC^{ON} axon measured with syGCaMP to 10 second odor pulses. *wt* n= 8 animals. *tom-1(ok285)* n= 8 animals. **(C)** Average response of the ASH axon (soluble GCaMP3). *wt* n= 21 trials, from 7 animals, 3 trials each. *tom-1(ok285)* n= 21 trials, from 7 animals, 3 trials each. **(D)** Close-up of first stimulus pulse in (C). **(E)** ASH cell body responses from data in (C).

Discussion

Together our results from this chapter indicate that Vglut-pH signals are highly dependent on many of the molecular components of the synaptic vesicle release machinery. Disruption of the SNARE complex or components critical to its regulation either eliminated or strongly reduced Vglut-pH responses, validating that Vglut-pH reports signals reflecting synaptic vesicle release and recycling. In addition to validating Vglut-pH as a reagent, our comparative study of AWC^{ON} and ASH synapses revealed that each neuron had different levels of dependency for the components of the fusion machinery: Vglut-pH response dynamics, as well as the components required for SV release, varied between these two neurons and were distinct from results predicted from electrophysiological recordings at the NMJ.

In *unc-13(lf)* mutants, AWC^{ON} had significant residual responses distinguishing it from ASH and the NMJ. *unc-13* independent priming/release has been suggested to occur in mouse photoreceptor ribbon synapses (Cooper et al., 2012). As highlighted in Chapter 1, AWC^{ON} and vertebrate photoreceptor/OFF bipolar neurons have several similarities in terms of sensory transduction machinery, SV release dynamics, and transcription factors that control neuronal differentiation, so it might be another similarity that they also have the ability to prime some SVs in an *unc-13* independent manner. In *unc-18(lf)* mutants, we observed differences in the response frequency between AWC^{ON} and ASH, with many detectable responses in ASH and only a few in AWC^{ON}. At the NMJ, *unc-18(lf)* strongly diminishes responses but is not essential for SV release (Weimer

et al., 2003). The synaptic requirement for *unc-13* and *unc-18* may differ across different synapses or conditions, or may be affected by the cell type-specific presence of other proteins with overlapping functions. In wild-type animals, there are various mechanisms that could affect the requirement for *unc-13* and *unc-18* at the synapse. Both *unc-13* and *unc-18* are multi-domain proteins and are the direct targets of cellular regulation through mechanisms including phosphorylation or interaction with effector lipids like DAG (Edwards et al., 2012; Kohn et al., 2000). Different isoforms of *unc-13* can differentially affect SV release (Hu et al., 2015), and in mammals, specific isoforms appear to preferentially regulate specific types of synapses (*e.g.* glutamatergic vs GABGergic) (Augustin et al., 1999; Varoqueaux et al., 2002). In addition, SV release defects in *unc-13(lf)* mutants can be bypassed by 'open syntaxin,' a mutation in the t-SNARE syntaxin which locks it into a permissive priming state (Richmond et al., 2001). Within this perspective, these results suggest that AWC^{ON} may have distinct requirements for vesicle priming, while those of ASH may be more similar to the NMJ.

Complexin was another component that appeared to distinguish these synapses. At the NMJ, *cpx-1(lf)* increases tonic release and eliminates evoked responses (Martin et al., 2011). In contrast, SV release in AWC^{ON} and ASH appeared enhanced in *cpx-1(lf)* mutants. These results suggest that AWC^{ON} and ASH synapses are either distinctly regulated by *cpx-1* or that they lack the equivalent of the NMJ evoked response. Based on calcium imaging of sensory-evoked responses in AWC^{ON} and ASH, we initially drew a comparison between

the periods of high calcium influx (observed after odor removal in AWC^{ON} and upon stimulus addition in ASH) to the stimulus-evoked SV release observed at NMJs. Similarly, we compared the tonic component of the NMJ response to be a component of AWC^{ON}'s baseline activity and mostly absent in ASH. Therefore, in *cpx-1(lf)* mutants, we expected the AWC^{ON} Vglut-pH response to odor addition to be increased and the response to odor removal to be diminished in *cpx-1* mutants. Similarly, we expected ASH Vglut-pH responses to be weak or absent in *cpx-1* mutants. Within the context of the existing model for *cpx-1* function, our results indicate that both AWC^{ON} and ASH Vglut-pH responses are entirely composed of the 'tonic release' component.

At the NMJ, the physiological relevance of the evoked response is questionable. In mutants that disrupt both tonic and evoked release at the NMJ, such as *unc-13* or *unc-64* mutants, animal locomotion, speed, and movement patterns are significantly decreased, and in most cases they are paralyzed. In complexin mutants, where tonic release at the NMJ is still intact and only the evoked response is diminished (to similar levels as *unc-64* mutants), animal locomotion is largely intact (Martin et al., 2011). In fact, *cpx-1(lf)* has been shown to restore tonic (but not evoked) release to *unc-64* mutants at the NMJ, and this is sufficient to restore locomotion speed to wild-type like levels. These findings suggest that the tonic release component measured at the NMJ is likely the physiologically relevant aspect of SV release in *C. elegans*. The fact that *cpx-1* mutants increase Vglut-pH responses in AWC^{ON} and ASH is consistent with this idea, especially given that the Vglut-pH responses we measure are truly

physiological. It is possible, however, that AWC^{ON} and ASH synapses either lack an evoked component or our stimulation conditions were not sufficient to elicit it. Alternatively, as mentioned above, it is also possible that complexin has neuron/synapse specific effects and that the *cpx-1* mutant responses in AWC^{ON} and ASH represent a distinct phenotype from the NMJ. The existence of *cpx-2,* which does not function redundantly with *cpx-1* at the NMJ and has a more restricted expression pattern (Martin et al., 2011), suggests another possibility for distinguishing these synapses. Future studies will have to be done to distinguish amongst these possibilities.

In contrast to the other components discussed, tomosyn appeared to have the same effect on AWC^{ON}, ASH and NMJ synaptic release, increasing VGlut-pH responses. However, we revealed an additional role for tomosyn in the regulation of AWC^{ON} and ASH calcium influx. This is contrary to the standard view of tomosyn function (Ashery et al., 2009). In a study that looked at the effects of tomosyn overexpression on secretion, changes to calcium influx were not observed (Yizhar et al., 2004). But outside of this study, the presynaptic calcium responses in *tom-1(lf)* have not been measured. In AWC^{ON}, the effects of *tom-1(lf)* on presynaptic calcium could easily account for the effects we observe on Vglut-pH responses. In ASH, the magnitude of calcium signals in *tom-1* mutants trended larger than wild-type, but was not significantly different (although the time to peak was shifted). It is possible that our ASH stimulation conditions are saturating either our GCaMP3 sensor or ASH calcium levels, preventing us from observing large increases in magnitude in *tom-1* mutants. Additional experiments

using a range of stimulus concentrations should help answer this question. Until this is resolved, it is unclear whether the effects of *tom-1(lf)* on ASH Vglut-pH signals could be caused by the changes in ASH calcium responses. Given the network-like structure of protein interactions at the synapse, which includes interactions between the SNARE complex components and presynaptic calcium channels, it is possible that tomosyn could affect calcium currents either directly or indirectly.

Although the phenotypes described in this chapter are intriguing, factors such as cell-autonomy, differences in stimulation strength, or unexpected changes in calcium dynamics (as was the case for tomosyn) need to be addressed in future work. The sources of calcium that drive exocytosis in each condition should also be defined, in particular the relative contributions of the *egl-19* (CaV1) and *unc-2* (CaV2) voltage-gated calcium channels. Nevertheless, our results highlight the potential for synaptic diversity. The advent of new genome editing tools, such as CRISPR/cas9, as well as more fine scale manipulations such as cell-specific knockouts or targeting of specific core machinery isoforms will permit a more thorough examination of synapse function within defined neural circuitry.

Chapter 4: Neuronal activity results in changes in cytoplasmic pH.

In our earlier studies we found that Vglut-pH responses were dependent on the vesicle fusion machinery (Chapter 3). However, we have not directly shown that pHluorin is localized within synaptic vesicles, as pHluorin localization to the luminal domain of the VGlut transporter is only predicted based on its homology to the mammalian vesicular glutamate transporter. Furthermore, during the process of transport or vesicle recycling, Vglut-pH could potentially localize to vesicular compartments other than synaptic vesicles. To confirm that Vglut-pH signals are associated with the synaptic vesicle cycle, we asked if stimulus-induced cytoplasmic pH changes occur in AWC^{ON} and ASH, and if so, whether they could interfere with the measurement or interpretations of Vglut-pH signals.

Activity-dependent changes in neuronal pH have been extensively documented in both vertebrate and invertebrate systems (Chesler, 1990). pH changes in response to activity are likely present to some extent in all neurons. Within vertebrates, pH changes in response to neural activity have been observed in neurons from the cerebral cortex (Ou-yang et al., 1993; Yao et al., 1999), hippocampus (Raley-Susman et al., 1991; Raley-Susman et al., 1993; Rangaraju et al., 2014; Trapp et al., 1996), cerebellum (Gaillard and Dupont, 1990; Rangaraju et al., 2014), spinal cord (Brechenmacher and Rodeau, 2000), retina (Krizaj et al., 2011), medullary neurons (Ritucci et al., 1998), and the sympathetic nervous system (Tolkovsky and Richards, 1987). In most cases, these pH changes were measured using either pH microelectrodes or chemical

probes, and were acute with rapid kinetics that spanned several seconds and covered several tenths of a pH unit (Chesler and Kaila, 1992). In addition, two recent studies using cytoplasmically-expressed pHluorin demonstrated activity-dependent pH changes in the synaptic terminals of *Drosophila* (Rossano et al., 2013) and mouse motor neurons (Zhang et al., 2010).

Several mechanisms can generate activity-dependent pH changes (Chesler, 1990). Depolarization can generate a calcium-dependent decrease in pH (acidosis) that is linked with calcium extrusion through the plasma membrane calcium ATPase (PMCA) (Schwiening and Willoughby, 2002; Trapp et al., 1996), metabolic acid production (Wang et al., 1994), or mitochondrial Ca^{++}/H^{+} exchange (Werth and Thayer, 1994). Alkaline responses to depolarization have also been noted (Brechenmacher and Rodeau, 2000; Gaillard and Dupont, 1990; Zhan et al., 1997). Two large families of acid transporters function to regulate cytoplasmic pH changes and include Na^{+}/H^{+} and HCO_3^{-} exchangers (Chesler, 1990; Ruffin et al., 2014).

Here, we show that AWC and ASH have robust stimulus-induced changes in cytoplasmic pH. These changes are consistent with a depolarization-generated acidosis and correlate with calcium influx. The dynamics of these signals are significantly different than Vglut-pH, and unlike Vglut-pH, they are not dependent on the vesicle fusion machinery. We conclude that Vglut-pH signals represent a distinct signal from cellular pH changes and are most consistent with the dynamics of synaptic vesicle release and recycling, whereas cytoplasmic pH may be more closely related to ongoing calcium dynamics.

Results

To test for stimulus-induced cytoplasmic pH changes, we expressed super-ecliptic pHluorin in AWC^{ON} and imaged the fluorescent changes associated with odor stimulation under the same conditions used in Vglut-pH and calcium imaging experiments (here termed cytoplasmic-pH, cyto-pH). Expression of cyto-pH resulted in uniform fluorescence throughout the cell, resembling GFP. Stimulation triggered fluorescence changes in AWC^{ON} that were strongest in the axon, detectable in the cell body, and weak in the dendrite (Fig 4.1). The dynamics of these signals were similar to Vglut-pH, but were opposite in sign: stimulus addition resulted in fluorescence increases and stimulus removal resulted in fluorescence decreases. Stimulus-induced cyto-pH fluorescence changes were also present in ASH. Similar to AWC^{ON}, these fluorescence signals were strongest in the axon and sign inverted in comparison to ASH Vglut-pH responses (Fig 4.2).

Unlike Vglut-pH responses, AWC^{ON} cyto-pH signals were not dependent on the synaptic vesicle release components *unc-13* or *unc-18* (Fig 4.3, also see Chapter 3). These results indicate that intracellular pH flux and Vglut-pH signals do not represent the same signal. They also indicate that the Vglut-pH reporter is isolated from intracellular pH changes, consistent with localization within synaptic vesicles.

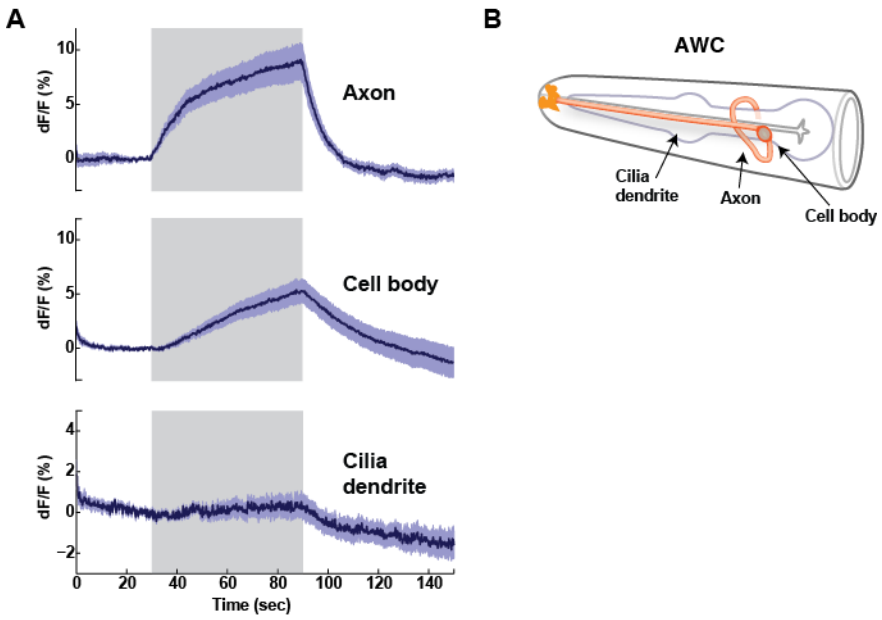

Figure 4.1. Cytoplasmic pH changes in AWC^{ON}.

(A) Average cyto-pH signals at different subcellular sites of AWC^{ON}. Shading = S.E.M. Gray bar = stimulus period. Stimulus = butanone 10^{-6} dilution. Axon and cell body, n = 9 trials, from 3 animals, with three trials per animal. Cilia = 6 trials, 3 trials from 2 animals. (**B)** Diagram of AWC location within the head of the animal, labeled with locations of measurements in (A).

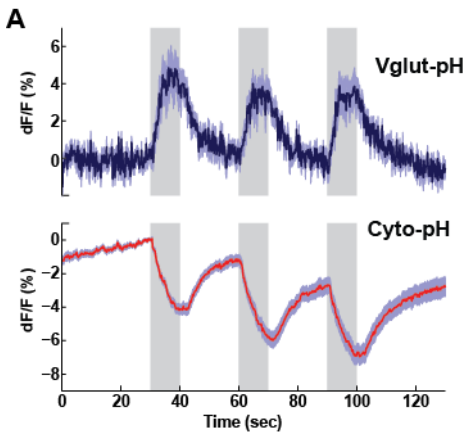

Figure 4.2. Comparison of Vglut-pH and cytoplasmic pH changes in ASH.

A) Top: Average of ASH Vglut-pH response. Bottom red trace: average ASH cyto-pH response. Vglut-pH and cyto-pH were tested together under the same stimulus conditions. Vglut-pH n=9 trials, from 3 animals, 3 trials each. cyto-pH n=27 trials, from 9 animals, 3 trials each. Shading = S.E.M. Gray bar = stimulus period. Stimulus = 500 mM NaCl.

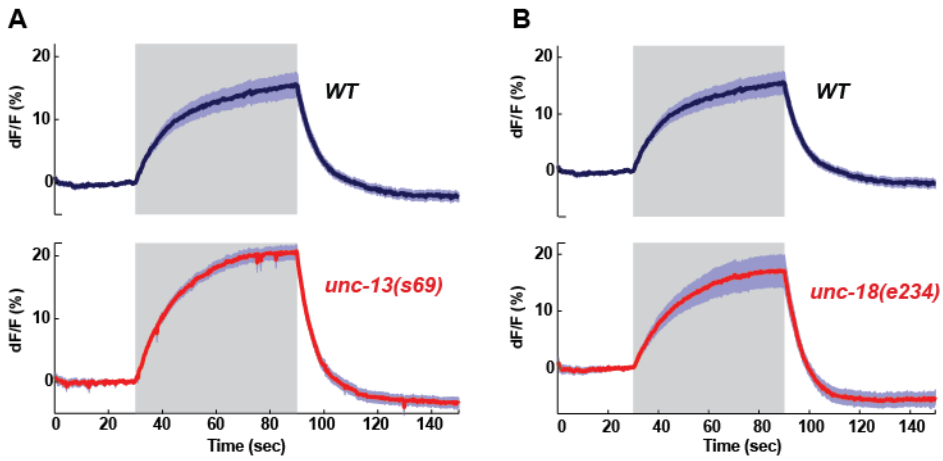

Figure 4.3. Stimulus-evoked cytoplasmic pH changes are independent of synaptic transmission.

(A-B) Average AWC^{ON} cyto-pH responses in *unc-13(s69)* and *unc-18(e234)* mutants. *unc-13(s69)* and *unc-18(e234)* were tested in parallel with same wild-type control. *wt* n=18 trials, from 6 animals, 3 trials each. *unc-13(s69)* n=15 trials, from 5 animals, 3 trials each. *unc-18(e234)* n=11 trials, from 4 animals, 2-3 trials each. Shading = S.E.M. Gray bar = stimulus period. Stimulus = 11.2 uM butanone.

During Vglut-pH endocytosis, cyto-pH kinetics mirrored those of Vglut-pH (Fig 4.4). The average time constant of inverted cyto-pH signals closely matched that of Vglut-pH endocytosis in both AWC^{ON} and ASH (Fig 4.4A-C). In ASH, the cyto-pH response was delayed with respect to the Vglut-pH signal (Fig 4.4B), but the average time constant of the response was still similar to the Vglut-pH signal.

We previously showed that the rate of AWC^{ON} endocytosis is compromised in *unc-11(e47)* mutants (AP180), but is briefly enhanced immediately after a strong stimulus (Fig 4.5A-B and see Chapter 2). By contrast, cyto-pH signals were indistinguishable from wild-type in *unc-11(e47)* (Fig 4.5C) and did not exhibit enhancement during the second odor stimulus (Fig 4.5C-D). Therefore, the rate of Vglut-pH endocytosis can be uncoupled from cytoplasmic pH changes.

To ask if extracellular pH also changes in response to stimulation, we localized pHluorin to the extracellular surface of the cell by tethering super-ecliptic pHluorin to the extracellular domain of mammalian CD4, labeling the extracellular surface including synaptic regions. When this fusion protein was expressed in ASH we did not detect any fluorescence changes upon stimulation (Fig 4.6), suggesting that unlike the intracellular pH, extracellular pH does not change appreciably in response to stimulation.

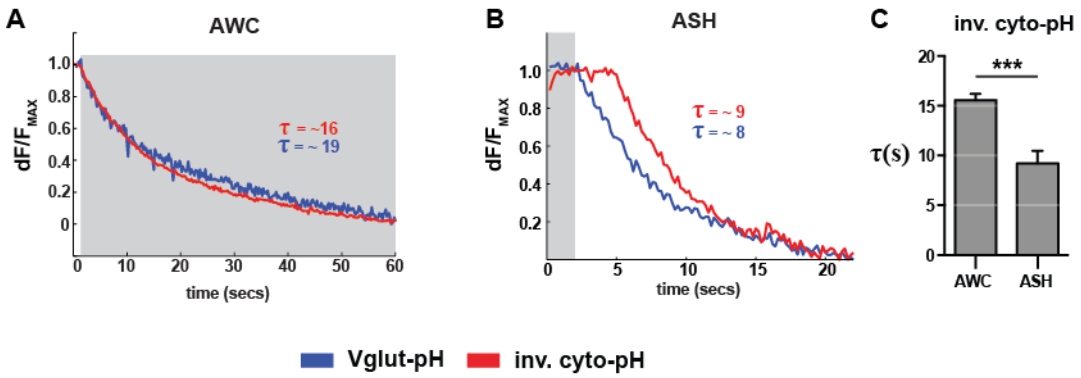

Figure 4.4. Cyto-pH responses are correlated with Vglut-pH endocytosis rates.

(A) Average response of AWC^{ON} Vglut-pH and sign-inverted cyto-pH during endocytosis. Magnitude normalized. (**B)** Average response of ASH Vglut-pH and sign inverted cyto-pH during endocytosis. Note that the cyto-pH decay starts several seconds after the Vglut-pH response. In (A-B) the magnitudes of each trace were normalized by the initial value of the trace. Gray bar = stimulus period. AWC^{ON} Stimulus = 11.2 uM butanone. ASH Stimulus = 500 mM NaCl. **(C)** Mean sign-inverted cyto-pH time constants for single exponential fits. Unpaired t-test, *** p <0.0001. AWC Stimulus = 11.2 uM butanone. ASH Stimulus = 500 mM NaCl.

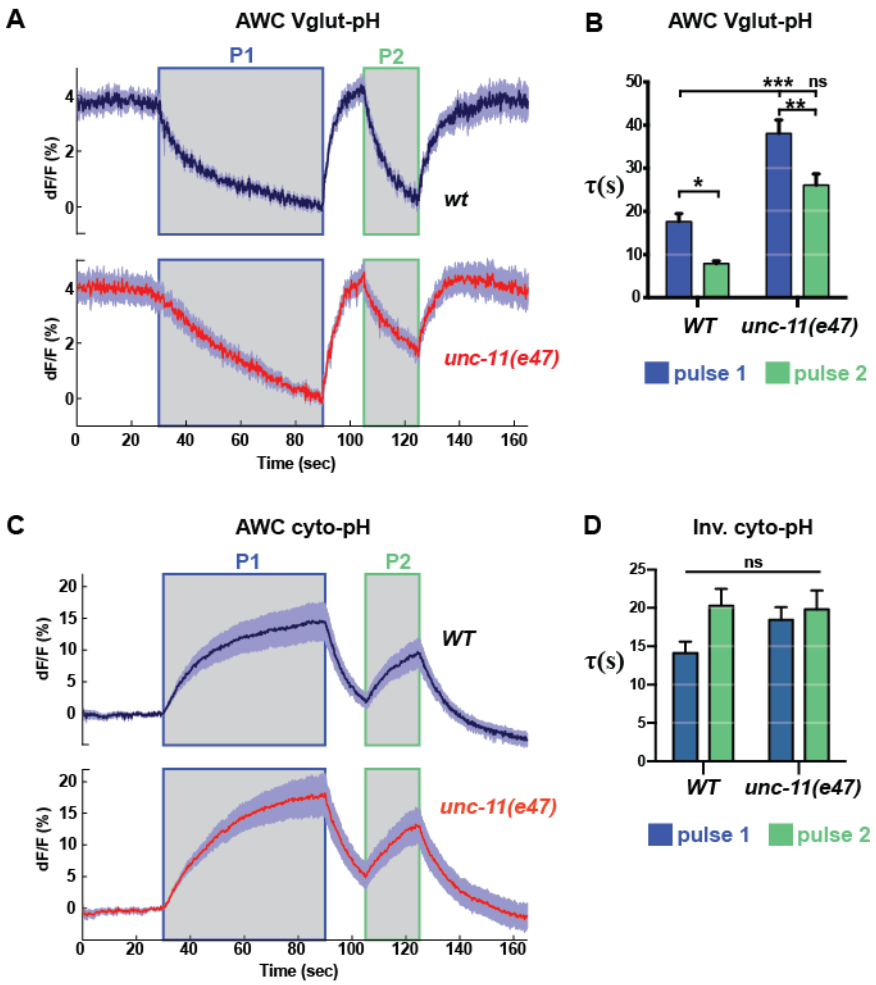

Figure 4.5. Unlike endocytosis, cyto-pH responses are not enhanced by neural activity and are not dependent on AP180.

(A-B) Reproduced from Chapter 2, Figure 10. **(A)** Average AWC^{ON} Vglut-pH signals in *wt* and *unc-11(e47)* mutants. *wt* n=21 trials, from 7 animals, 3 trials each. *unc-11(e47)* n=26 trials, from 9 animals, 3 trials each (two non-responding trials removed). **(B)** Average time constants from single exponential fits (initial 20s of decay) of data in (A). Two-way ANOVA, *** p<0.0001, ** p<0.001, * p<0.01. **(C)** Average AWC^{ON} cyto-pH responses. *wt* n=10 trials, from 5 animals, 2 trials each. *unc-11(e47)* n=10 trials, from 5 animals, 2 trials each. **(D)** Average time constants from single exponential fits (initial 20s of decay) to sign-inverted data in (C). Shading = S.E.M. Gray bar = stimulus period. Stimulus = 11.2 uM butanone.

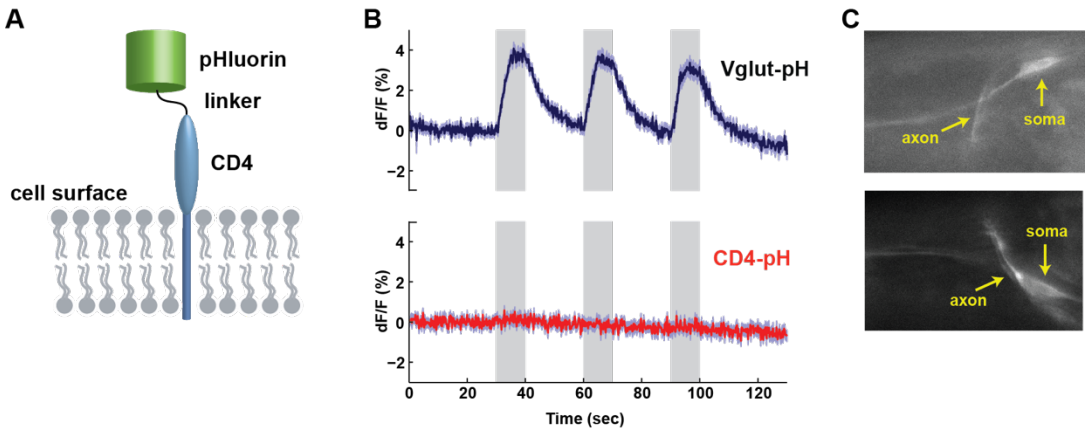

Figure 4.6. Stimulus-evoked extracellular pH changes are not detected with extracellularly localized pHluorin.

(A) Diagram of CD4-pH construct used to target pHluorin to the extracellular surface of ASH. **(B)** Top trace: Average response of ASH Vglut-pH control. n=39 trials, from 13 animals, 3 trials each. Bottom trace: Average response of ASH CD4-pH. n=33 trials, from 11 animals, 3 trials each. No response was detected. **(C)** Two animals expressing CD4-pH with the ASH promoter *sra-6*. ASH axon and cell body indicated by yellow arrows. Images taking from recordings in (B) and are averages of the first 5 frames. Gray bar = stimulus period. Stimulus = 500 mM NaCl. Shading = S.E.M.

Discussion

The robust stimulus-induced cytoplasmic pH changes we observed in AWC and ASH and may affect a diverse set of cellular properties (Ruffin et al., 2014) and their presence should be a consideration in the future study of neuron function. They have the potential to interfere with measurements of neural activity with any fluorescence probe that is sensitive to pH changes. For example, GCaMP fluorescence can increase by as much as 10% for a 0.1 pH unit increase (Kneen et al., 1998; Nakai et al., 2001). This effect might explain the slow increase in AWC^{ON}'s syGCaMP3 signal during odor suppression (Fig 4.7).

Taking these effects into account, four lines of evidence support the interpretation of Vglut-pH as monitoring the process of synaptic vesicle release: (1) Stimulus-induced cytoplasmic pH changes are sign-inverted with respect to Vglut-pH signals, and therefore cannot be the source of Vglut-pH signals. (2) In mutants that disrupt synaptic transmission, cytoplasmic pH changes are intact, whereas VGlut-pH signals are compromised. Vglut-pH signals in these mutants do not resemble cyto-pH signals, indicating that Vglut-pH is completely isolated from intracellular pH changes. (3) Extracellularly targeted pHluorin did not detect any extracellular pH changes induced by stimulation. (4) Cyto-pH dynamics are not altered under conditions in which Vglut-pH dynamics are significantly altered (see also Chapter 6, Fig 6.5).

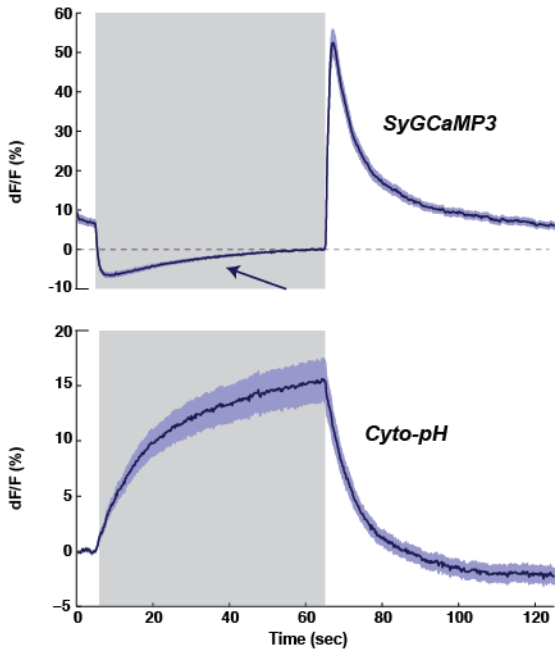

Figure 4.7. Potential effects of intracellular pH changes on GCaMP signals.

A) Comparison of AWC^{ON} axonal GCaMP responses and cytoplasmic pH changes. GCaMP fluorescence is sensitive to pH levels and increases by as much as 10% for a 0.1 pH unit increase. This may explain the increase in axon GCaMP fluorescence as the axon becomes alkalinized during odor stimulation (indicated by arrow in the top trace). SyGCaMP3 = synaptogyrin tagged GCaMP3. SyGCaMP3 n = 21 trials, from 7 animals, 3 trials each. Cyto-pH n=18 trials, from 6 animals, 3 trials each (*wt* data from Figure 3). Shading = S.E.M. Gray bar = stimulus period. Stimulus = 11.2 uM butanone.

Thus, Vglut-pH signals are distinct from cytoplasmic changes, and are not measuring extracellular pH changes. These lines of evidence support the use of Vglut-pH as a tool for monitoring synaptic vesicle release and recycling.

The direction of the cyto-pH signals in AWC^{ON} and ASH is consistent with acidosis evoked by increases in calcium levels. These changes might be caused by proton mobilization during calcium extrusion by pumps such as the plasma membrane calcium ATPase (PMCA) (Schwiening and Willoughby, 2002; Trapp et al., 1996). Similar phenomena have been reported in the synaptic terminals of mouse (Zhang et al., 2010) and *Drosophila* motor neurons (Rossano et al., 2013). During periods of elevated calcium levels, pumps are active and acidify the neuron by exchanging protons for calcium ions; when the activity of the neuron decreases and calcium is extruded, activity of the pumps decreases, and the neuron returns to baseline pH levels (Trapp et al., 1996).

The kinetics of cyto-pH, although sign-inverted and somewhat slower, were similar to Vglut-pH signals. This can be seen more clearly by sign changing the cyto-pH signals and comparing the magnitude-normalized mean traces (Fig 4.8A-B). If plasma membrane pumps drive these pH changes, then an intracellular pH change might be accompanied by a reciprocal extracellular pH change. Stimulus-induced extracellular pH changes have been reported (Chesler, 1990; Chesler and Kaila, 1992), but these were elicited by synchronous stimulation of hundreds to thousands of neurons, raising question as to whether these changes could be elicited locally by stimulating a single neuron.

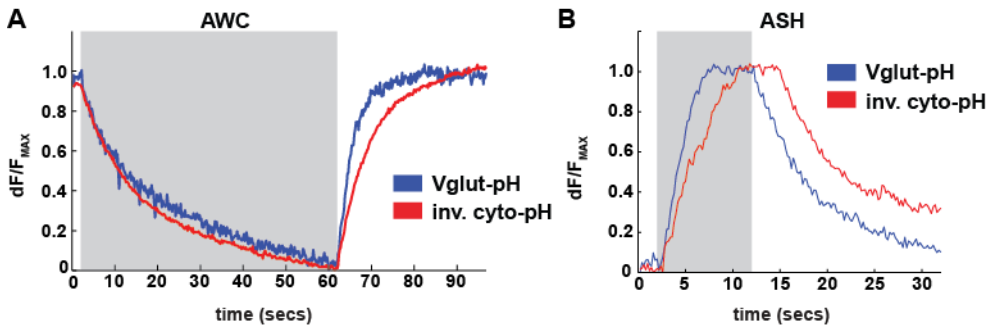

Figure 4.8. Comparison of Vglut-pH and cyto-pH average dynamics

(A) Average AWC^{ON} Vglut-pH and sign-inverted cyto-pH response. Magnitude normalized by maximum. **(B)** Average ASH Vglut-pH and sign inverted cyto-pH response. In (A-B) traces are normalized to their peak value (F/F_{MAX}). Gray bar = stimulus period. AWC Stimulus = 11.2 uM butanone. ASH Stimulus = 500 mM NaCl.

In *C. elegans*, extracellular pH changes generated by intestinal cells have been shown to be important for triggering muscle contraction during the defecation cycle (Beg et al., 2008), which suggests that such pH changes can occur. Our results using extracellularly targeted pHluorin suggest that such extracellular changes in pH are not detectable in the nerve ring.

The kinetics of Vglut-pH endocytosis resembled the alkalinization component of cyto-pH responses. In ASH, this cyto-pH component was delayed in comparison to Vglut-pH, possibly indicating that calcium extrusion continues briefly after stimulus removal, as calcium levels are still high. Cytosolic pH can modulate endocytosis rates, so these signals may be functionally coupled in some conditions (Lindgren et al., 1997). It is interesting to consider that the enhancement of AWC^{ON} endocytosis during the second odor pulse could be due to the preceding alkalinization of AWC^{ON} terminals. Such an effect has been demonstrated at mouse motor neuron terminals, where it was reported that alkalinization after exocytosis facilitates endocytosis (Zhang et al., 2010). With respect to the correlation between rates of endocytosis and cyto-pH alkalinization, it is notable that enhancement of AWC^{ON} endocytosis rates shifts AWC^{ON} endocytosis to ASH-like rates (Chapter 2), but does not shift the corresponding cyto-pH responses. Thus, the rate of endocytosis and cytoplasmic alkalinization are unlikely to be directly coupled in this setting. Further work may better define the relationships between these cellular signals and compartments.

Chapter 5: Cell-specific roles of synaptotagmins

Neurotransmitter release is exquisitely sensitive to changes in presynaptic calcium levels (Korber and Kuner, 2016; Schneggenburger and Neher, 2005). Synaptotagmins, the molecular sensors that mediate calcium-dependent synaptic vesicle release, are critical components of synaptic diversity and neural circuit function (Sudhof, 2002; Sugita et al., 2002; Xu et al., 2007). In this chapter, we characterize the dependency of AWC^{ON} and ASH synapses on the *C. elegans* synaptotagmins by monitoring glutamate release using Vglut-pH imaging.

Synaptotagmins are an evolutionarily conserved family of integral membrane proteins or membrane-associated proteins that contain at least two cytoplasmic tandem C_2 domains. Several are known to act in calcium-triggered vesicle exocytosis in both neuronal and endocrine cells (Moghadam and Jackson, 2013). Many synaptotagmins sense calcium directly with their C2 domains, which can interact with calcium, PIP_2 and PIP_3 membrane lipids, or both calcium and lipids (Bai et al., 2004; Moghadam and Jackson, 2013b; Schiavo et al., 1996). Different synaptotagmins sense distinct ranges of calcium concentrations, suggesting that synaptotagmins are specialized to mediate distinct forms of release in response to specific levels of calcium (Bhalla et al., 2005; Crawford and Kavalali, 2015; Sugita et al., 2002).

The canonical and the most thoroughly characterized synaptotagmin is Synaptotagmin 1, which mediates fast synaptic vesicle (SV) release.

Synaptotagmin 1 resides on synaptic vesicles and interacts with the SNARE complex to trigger vesicle fusion upon calcium binding (Sudhof, 2012) (See Chapter 3, Fig 3.1). Inactivation of synaptotagmin 1 strongly impairs fast and synchronous SV release in hippocampal neurons and both the excitatory and inhibitory synapses of cortical neurons (Geppert et al., 1994; Maximov and Sudhof, 2005). In each case, another form of SV release called asynchronous release is still intact, and this is likely mediated by synaptotagmin 7 (Bacaj et al., 2013). Although synaptotagmin 1 is broadly implicated as the primary calcium sensor in many types of neurons and different nervous systems (Littleton et al., 1993; Nonet et al., 1993), synaptotagmin 1 is not the main calcium sensor for SV release in all neurons. For example, in rodent, three major synaptotagmins isoforms have been proposed to regulate fast synaptic release at different locations: synaptotagmin 1 in the forebrain, synaptotagmin 2 in the brainstem and spinal cord, and synaptotagmin 9 in the striatum and limbic system (Xu et al., 2007). These three synaptotagmins each have different calcium sensitivities and confer distinct release speeds, properties that are thought to provide neurons of each brain region with distinct release properties (Xu et al., 2007).

In mammals, there are 16 different synaptotagmin isoforms (Craxton, 2010), and at least thirteen are expressed exclusively in neurons and neuroendocrine cells (Sudhof, 2002). Many neurons express multiple synaptotagmins, which might either act together to produce a distinct SV response, or act separately to regulate distinct populations of vesicles (Cao et al., 2011; Littleton et al., 1999; Osborne et al., 1999; Sugita et al., 2002). Some

synaptotagmins are required for peptide and hormone release or other recycling processes (Dean et al., 2012; Moghadam and Jackson, 2013a)

Given the potential for synaptotagmins to confer specific release properties within and among neurons, we asked which synaptotagmins were required for glutamate release in AWC^{ON} and ASH. The *C. elegans* genome encodes seven synaptotagmins (*snt*). Synaptic transmission at the NMJ is impaired, but not eliminated, in *C. elegans* synaptotamin-1 (*snt-1)* null mutants (Liewald et al., 2008; Nonet et al., 1993), suggesting that additional calcium sensors likely mediate SV release. The role of other synaptotagmins in *C. elegans* SV release has not been reported. We find that AWC^{ON} basal release is highly dependent on *snt-1*, whereas ASH exocytosis is intact in *snt-1* null mutants and slightly diminished in *snt-6* mutants. *snt-2, snt-3, snt-4, snt-5* appeared not to affect ASH Vglut-pH responses. We also find that *snt-1* is required for fast endocytosis in AWC^{ON} and ASH, in agreement with its role in vesicle recycling at the NMJ (Jorgensen et al., 1995). Our results indicate that AWC and ASH synapses have distinct requirements for *snt-1* and may use a combination of calcium sensors to mediate glutamate release.

Results

To characterize the role of synaptotagmins in AWC^{ON} and ASH glutamate release, we imaged Vglut-pH fluorescence responses to sensory stimuli in synaptotagmin null mutants. AWC^{ON} Vglut-pH responses to butanone were strongly affected by *snt-1(md290)* and *snt-1(md172)* null mutations (Fig 5.1A-B). The endocytosis response to odor addition was largely absent in these mutants. The exocytosis response to odor removal was nearly normal in magnitude, but decayed after reaching peak and slowly returned to pre-stimulus baseline levels. However, in some trials of *snt-1(lf)* mutants, odor addition triggered a small decrease in Vglut-pH signal consistent with endocytosis of the surface localized reporter, but for the most part these responses were absent (Fig 5.1C-D).

Regulatory proteins associated with SV release often act at multiple steps to exert their effects. As calcium increases are upstream of SV release, we therefore examined calcium responses in *snt-1(lf)* mutants. Preliminary results from AWC^{ON} axonal calcium imaging experiments using syGCaMP suggest that AWC^{ON} calcium responses are strongly enhanced in *snt-1(md290)* mutants (Fig 5.2). These results indicate that the AWC^{ON} Vglut-pH defects observed in *snt-1(lf)* mutants are downstream of calcium influx. Interestingly, the enhanced calcium influx in *snt-1(lf)* mutants after odor removal suggests that the nearly wild-type Vglut-pH response may actually represent a compensated response to the higher calcium levels (see Discussion).

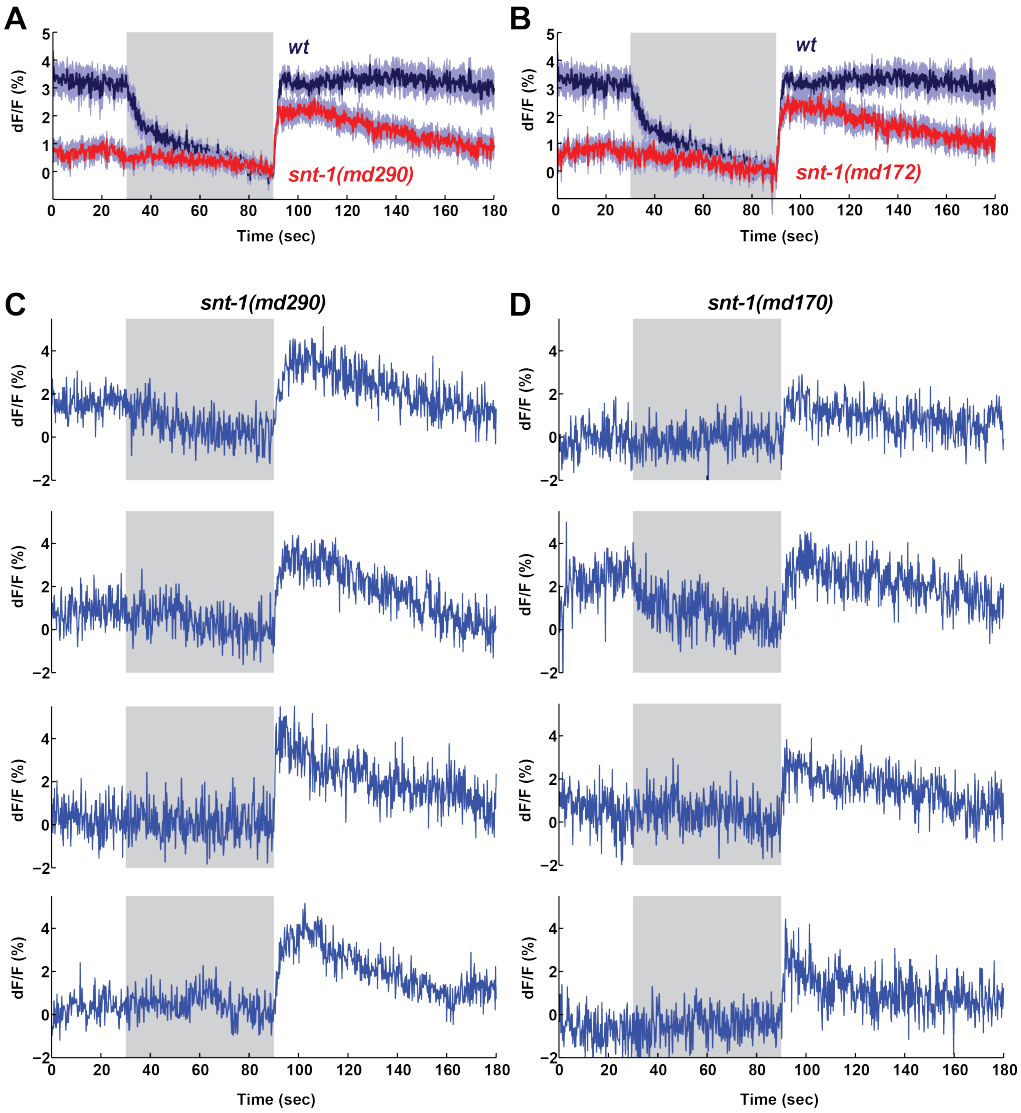

Figure 5.1. AWC^{ON} Vglut-pH responses are dependent on *snt-1*.

(A)-(B) AWC Vglut-pH responses in *snt-1(lf)* mutants (red traces). wt n = 18 trials, from 6 animals, 3 trials each. *snt-1(md290)* n = 22 trials, from 8 animals, 2-3 trials each. *snt-1(md172)* n = 15 trials, from 5 animals, 3 trials each. *snt-1(md290)* and *snt-1(md172)* were tested together with same *wt* controls. **(C)** Individual trials of *snt-1(md290)* mutants from (A). **(D)** Individual trials of *snt-1(md172)* mutants from (B). Gray Bar = stimulus, 11.2 uM butanone. Shading = S.E.M.

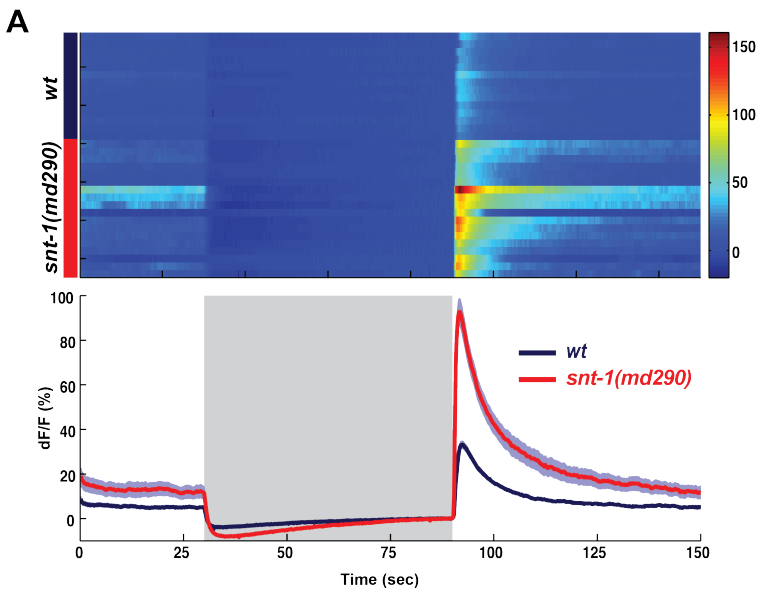

Figure 5.2. Axonal calcium responses are increased in *snt-1(md290)* mutants.

(**A**) AWC^{ON} syGCaMP responses in *snt-1(md290)* mutants. Top: Heat map showing individual trials for both genotypes. Bottom: Average response from data in heat map. *wt* n = 14 trials, from 5 animals, 2-3 trials each. *snt-1(md290)* n = 18 trials, from 6 animals, 3 trials each. Gray Bar = 11.2 uM butanone. Shading = S.E.M. Further experiments should be done to confirm this result. Experiment performed by rotation student Bennett Ferris.

A potential role for *snt-1* in endocytosis was also observed in ASH. Stimulation of ASH with 500 mM NaCl yielded normal exocytic Vglut-pH responses in both *snt-1(md290)* and *snt-1(md172)* mutants (Fig 5.3A-D). A slow recovery after the end of each stimulus indicated that *snt-1* is required for endocytosis (Fig 5.3A-D). In wild-type animals, Vglut-pH fluorescence recovered fully in the 20 seconds between stimuli, but in *snt-1(lf)* mutants, only partial recovery was observed. Perhaps as a result, the exocytic responses in the second and third stimuli were reduced compared to the first in *snt-1(lf)* mutants (Fig 5.3E-F). These results suggest that ASH glutamate release is not highly dependent on *snt-1* and that an additional synaptotagmin or another protein might be the primary calcium sensor for NaCl-evoked SV release in ASH.

To search for a possible synaptotagmin mediating Vglut-pH exocytic responses in ASH, we tested loss-of-funtion (*lof)* mutations in synaptotagmins 2, 3, 4, 5 and 6. ASH Vglut-pH responses showed a trend toward a larger response in *snt-2(tm1711)* mutants, but this was not statistically significantly (Fig 5.4A). A similar trend was observed in AWC^{ON} (Fig 5.4B).

As a *snt-3(lf)* allele was not readily available, we used CRISPR/cas9 mutagenesis to generate a frameshift and early translational stop in the first exon of *snt-3,* designated *snt-3(ky1034)* (Fig 5.5). ASH Vglut-pH responses in *snt-3(ky1034), snt-4(ok503),* and *snt-5(tm3786)* mutants all appeared similar to wild-type controls (Fig 5.6).

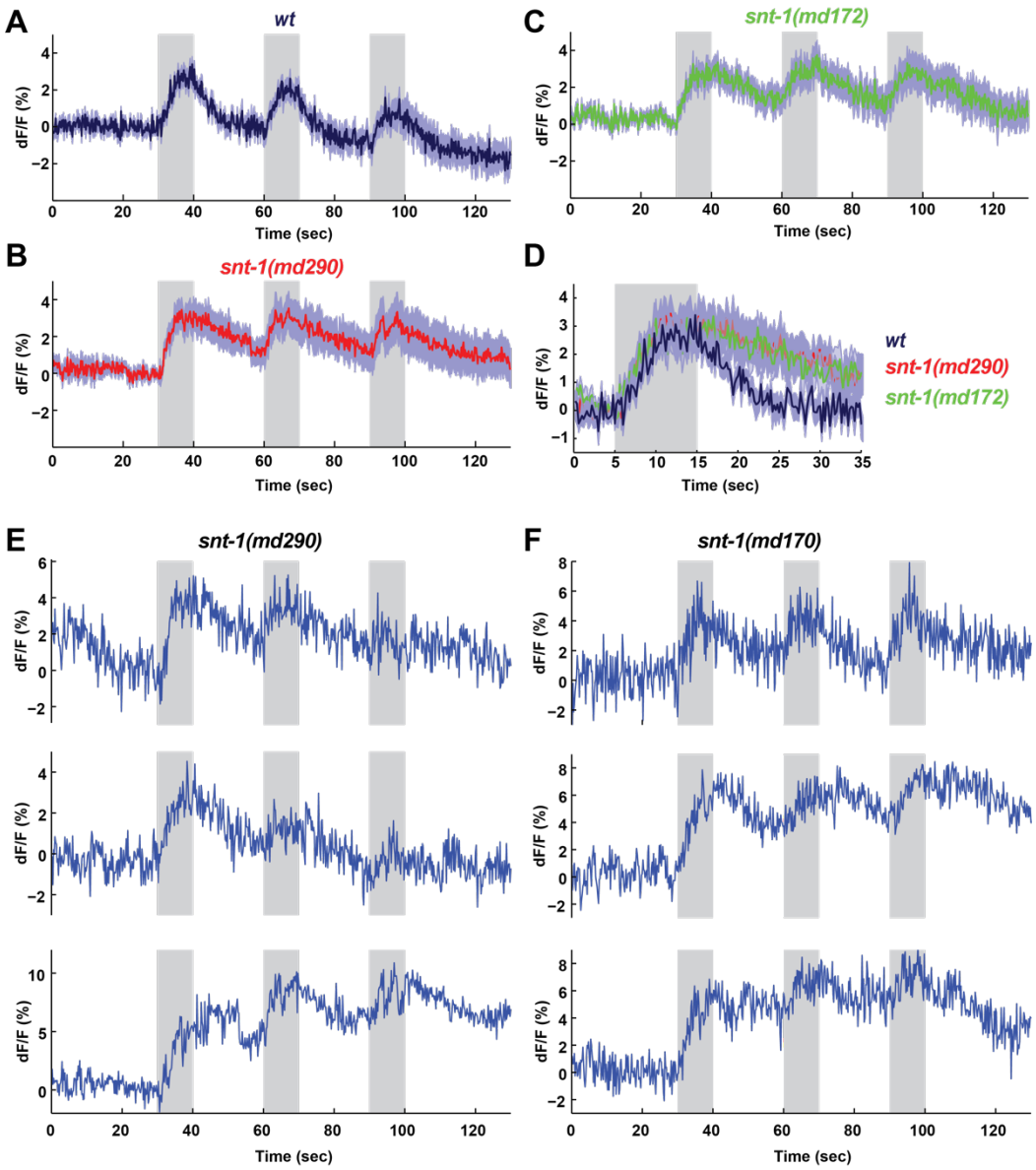

Figure 5.3. ASH Vglut-pH responses in *snt-1(lf)* mutants.

(A)-(C) ASH Vglut-pH responses in *snt-1(lf)* mutants. *wt* n = 12 trials from 4 animals, 3 trials each. *snt-1(md290)* n = 12 trials, from 4 animals, 3 trials each. *snt-1(md172)* n = 12 trials from 4 animals, 3 trials each. All experiments were conducted in parallel. **(D)** ASH Vglut-pH responses to the first stimulus. Data from (A)- (C). **(E)** Individual trials of *snt-1(md290)* mutants from (B). **(F)** Individual trials of *snt-1(md172)* mutants from (C). Gray bar = 500 mM NaCl. Shading = S.E.M.

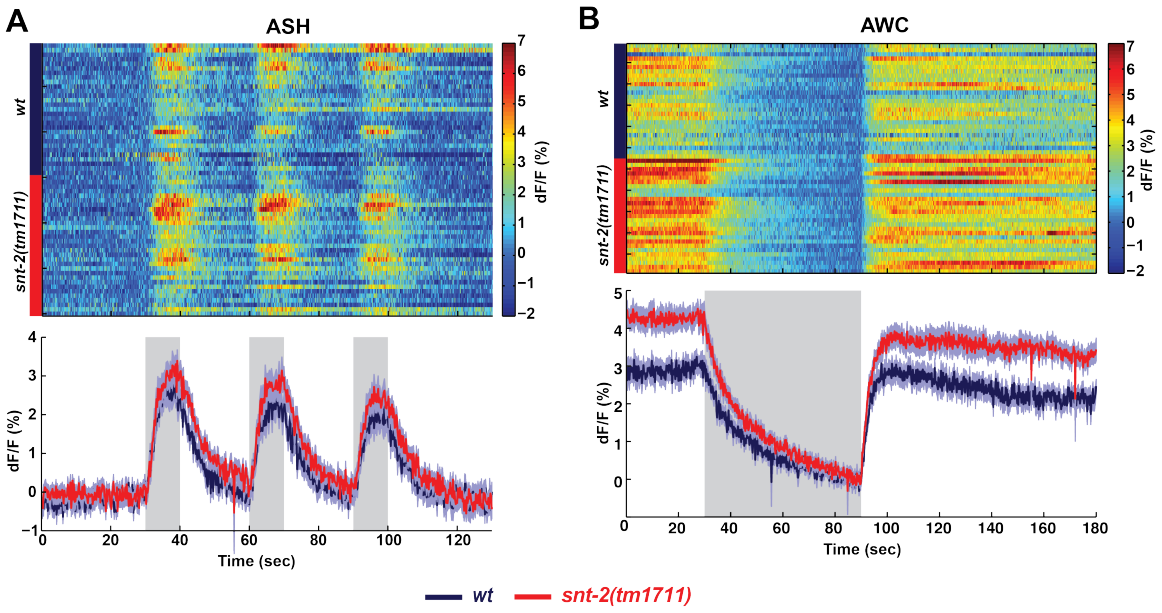

Figure 5.4. AWC^{ON} and ASH Vglut-pH responses in *snt-2(lf) mutants.*

(A) ASH Vglut-pH responses in *snt-2(tm1711)* mutants (red trace). *wt* n = 30 trials from 10 animals, 3 trials each. *snt-2(tm1711)* n = 30 trials from 10 animals, 3 trials each. Gray bar = 500 mM NaCl. Shading = S.E.M. **(B)** AWC Vglut-pH responses in *snt-2(tm1711)* mutants (red trace). *wt* n = 27 trials from 9 animals, 3 trials each. *snt-2(tm1711)* n = 27 trials from 9 animals, 3 trials each. Butanone 10-6 dilution. Gray bar = 11.2 uM butanone. Shading = S.E.M.

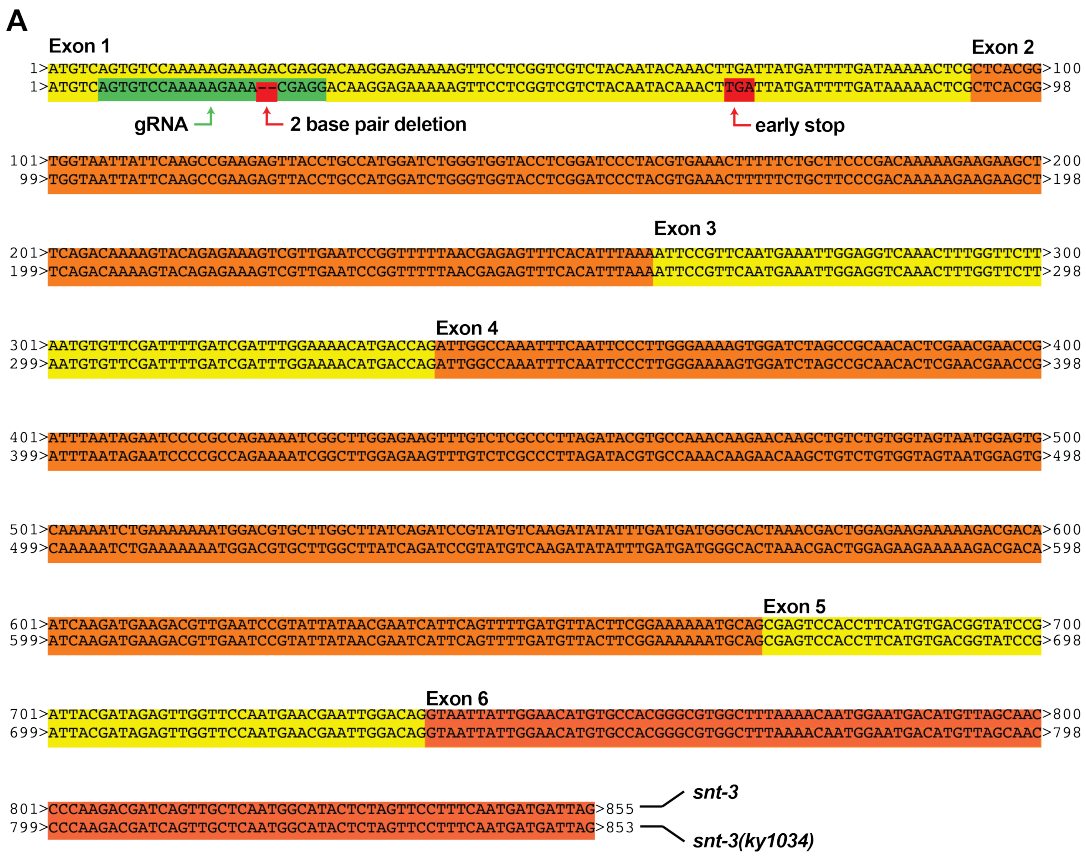

Figure 5.5. *snt-3(ky1034)* mutant generated with CRISPR/Cas-9 mutagenesis.

(A) Spliced coding sequence of *snt-3* aligned with *snt-3(ky1034)* mutant generated with CRISPR/Cas-9. Exons highlighted with alternating yellow/orange coloring. Green box highlights guide-RNA targeting sequence (gRNA), which overlaps with the induced 2-bp deletion that results in a frameshift and early stop in *snt-3*.

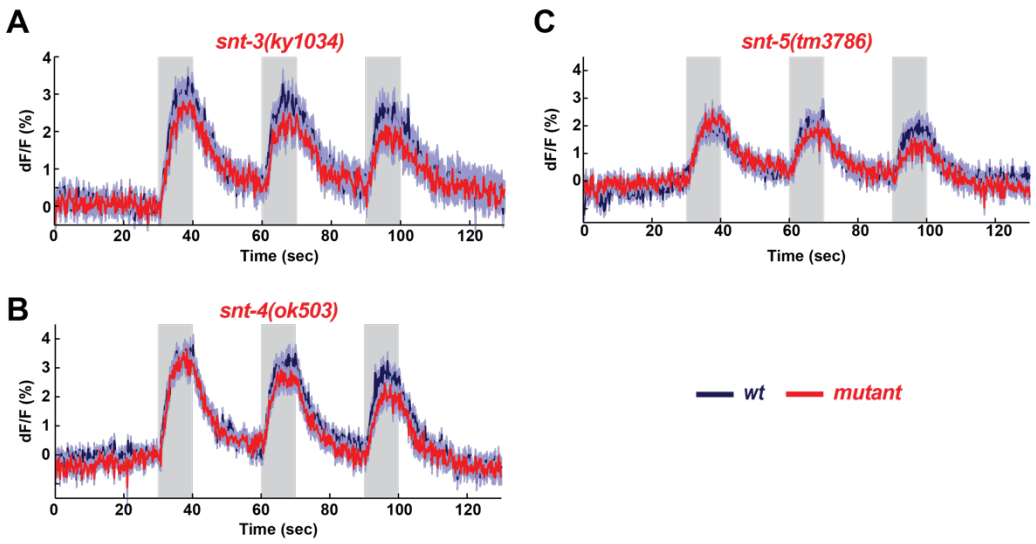

Figure 5.6. ASH Vglut-pH responses are not dependent on *snt-3, snt-4,* or *snt-5.* **(A)-(C)** ASH Vglut-pH repsonses in mutants of indicated genotypes. (A) *snt-3(ky1034)* n = 20 trials from 7 animals, 2-3 trials each. *wt* n = 20 trials from 7 animals, 2-3 trials each. (B) *snt-4(ok503)* n = 30 trials from 10 animals, 3 trials each. *wt* n = 29 trials from 10 animals, 2-3 trials each. (C) *snt-5(tm3786)* n = 24 trials from 8 animals, 3 trials each. *wt* n = 24 trials from 8 animals, 3 trials each. Gray bar = 500 mM NaCl. Shading = S.E.M.

snt-6(tm3686) mutants had a small reduction in their ASH Vglut-pH response (Fig 5.7A). Endocytosis in *snt-6(tm3686)* mutants was not strongly affected. We suspected that *snt-6* might serve a redundant role with another synaptotagmin, and examined *snt-1(lf)* because its effect on endocytosis (Fig 5.3) suggested that *snt-1* is present in ASH. If these proteins are redundant for exocytosis, the predicted Vglut-pH response is a stronger defect than either single mutant. Instead, ASH Vglut-pH responses in *snt-6(tm3686);snt-1(md290)* double mutants resembled those of *snt-1(md290)* and were stronger than that of *snt-6(tm3686)* mutants (Fig 5.7B). These results indicate that the ASH Vglut-pH response is likely mediated by some other combination of calcium sensors other than *snt-1* and *snt-6*.

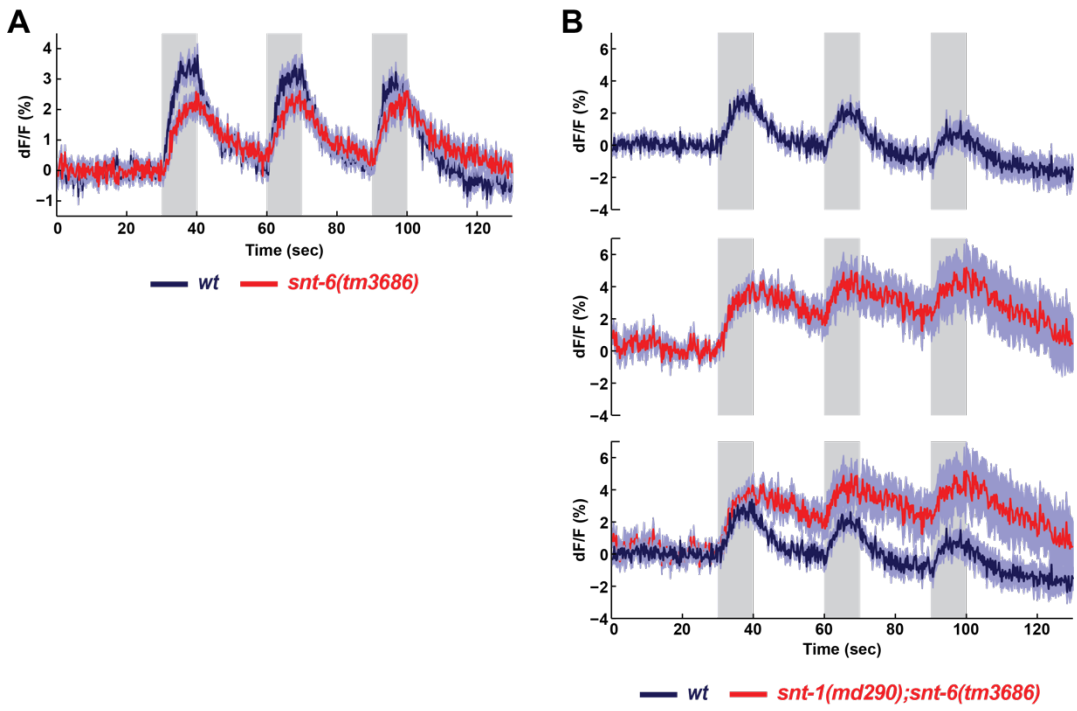

Figure 5.7. ASH Vglut-pH responses are weakly dependent on *snt-6*.

(A) ASH Vglut-pH responses in *snt-6(tm3686)* mutants. *snt-6(tm3686)* n = 30 trials from 10 animals, 3 trials each. *wt* n = 29 trials from 10 animals, 2-3 trials each. **(B)** ASH Vglut-pH responses in *snt-1(md290);snt-6(tm3686)* double mutants. *snt-1(md290);snt-6(tm3686)* n = 7 trials from 5 animals, 1-3 trials each. *wt* n = 12 trials from 4 animals, 3 trials each. Last panel in (B) plots *wt* and *snt-1(md290);snt-6(tm3686)* traces on the same axis. Note resemblance to *snt-1(lf)* mutants (Fig 3B,C).Gray bar = 500 mM NaCl. Shading = S.E.M.

Discussion

Our results indicate that AWC^{ON} and ASH synapses have different dependencies on *snt-1* and likely use a combination of calcium sensors to mediate calcium-triggered SV release. In both AWC^{ON} and ASH, *snt-1(lf)* decreased the rate of endocytosis, but did not eliminate endocytosis altogether. These defects are consistent with the SV recycling defects reported at the *C. elegans* NMJ and at synapses of synaptotagmin 1 *lof* mutants in other animals (Jorgensen et al., 1995; Nicholson-Tomishima and Ryan, 2004; Poskanzer et al., 2003). In AWC^{ON}, Vglut-pH responses in *snt-1(lf)* mutants selectively lost the response to odor addition, which represents endocytosis of surface reporter produced by basal SV release. Given that endocytosis can still be detected in *snt-1(lf)* mutants, our data suggests that the missing odor addition response represents the absent of AWC^{ON} basal release in *snt-1(lf)* mutants and not a pure defect in endocytosis. However, further study is needed to support this hypothesis.

Our preliminary results indicate that AWC^{ON} synaptic calcium responses are strongly enhanced in *snt-1(md290)* mutants. This is an intriguing finding as synaptotagmin 1 can interact directly with presynaptic calcium channels (Charvin et al., 1997). In addition, synaptotagmin 1 has been shown to slow the inactivation of the voltage-gated potassium channel Kv1.4, increasing the duration of depolarization after an action potential (Xie et al., 2014). Such an action could contribute to the effect we observe. Our results hint at additional roles for *snt-1* in the regulation of neuronal excitability of AWC^{ON}.

The AWC^{ON} Vglut-pH response to odor-removal was normal in *snt-1(lf)* function mutants. Since *snt-1(md290)* has greatly increased AWC^{ON} synaptic calcium at this point, the magnitude of the Vglut-pH odor-removal response is difficult to compare directly to wild-type controls. Synaptic calcium can be increased when odor removal follows a longer duration of stimulation in wild-type animals, and is also increased in *tom-1(lf)* mutants at similar magnitudes to *snt-1(lf)*. These conditions correspondingly generate larger Vglut-pH responses than the standard wild-type response (see Chapter 1 and 3). This comparison suggests that the AWC^{ON} odor-removal response in *snt-1(lf)* mutants might be actually blunted relative to the calcium signal that induced it. This suggests that very high levels of calcium are needed to generate significant SV release in *snt-1(lf)* mutants. The 500 mM NaCl stimulus used to measure Vglut-pH responses in ASH generate a saturating calcium response in ASH. Following the logic of AWC^{ON} given above, saturating calcium in ASH could potentially mask a *snt-1(lf)* defect. Conducting a dose-response analysis of AWC^{ON} and ASH Vglut-pH responses in *snt-1(lf)* mutants should help clarify this issue. Furthermore, examination of ASH calcium flux in *snt-1(lf)* mutants is also desirable.

We observe that Vglut-pH responses appeared to be absent at relatively low calcium (AWC^{ON} basal levels) but intact at relatively high calcium (after odor removal in AWC^{ON}, and upon stimulation with 500 mM NaCl in ASH). We suggest that *snt-1* may function as a high-affinity calcium sensor, mediating the release of SVs at lower levels of calcium.

Our screen of synaptotagmins mutants revealed that no single synaptotagmin was required for ASH Vglut-pH responses to 500 mM NaCl. We suspect that some of these synaptotagmins may regulate the release of neurotransmitters other than glutamate, such as peptides. *snt-7* was not tested in our study, but could be examined in future work. *snt-2(tm1711)* mutants slightly increased Vglut-pH responses in both AWC^{ON} and ASH. *snt-2* is expressed in the gut, where it mediates release of the neuropeptide *nlp-40* (Wang et al., 2013). It is possible that the effects of *snt-2* are indirect and not cell-autonomous. Alternatively, *snt-2* co-expression with other synaptotagmins in AWC^{ON} and ASH could play an inhibitory role in SV release.

ASH Vglut-pH responses were slightly decreased in *snt-6(tm3686)* mutants, hinting that *snt-6* may have a role in mediating SV release in ASH. Calcium imaging and cell-specific rescue need to be conducted to confirm this result. *snt-1(md290);snt-6(tm3686)* double mutants resembled *snt-1(md290)* single mutants, masking the decreased response found in *snt-6(tm3686)* mutants. Again, dose-response curves at weaker stimulus levels as well as ASH calcium imaging will be crucial for guiding our interpretation of this result.

Together, our results indicate that both AWC^{ON} and ASH synapses use multiple calcium sensors to mediate glutamate release. The diversity of synaptotagmins, their divergent expression patterns, and their potential combinatorial effects have been hypothesized to fine-tune and diversify synapse function (Sudhof, 2002; Sugita et al., 2002). *C. elegans* provides an opportunity to study how synaptotagmin diversity contributes to circuit function and behavior

and perhaps even to discover new calcium sensors. Future work would benefit from examining the requirements for synaptotagmins in glutamate release in other neurons, and the release of different classes of neurotransmitters.

Part II

Chapter 6: The role of *pkc-1* in specifying AWC^{ON} olfactory preference

In the first part of this thesis, we characterized the activity of AWC^{ON} and ASH synapses in response to sensory stimuli and asked how conserved synaptic vesicle and SNARE proteins contributed to the dynamics of neurotransmitter release. In this chapter, we ask how changes in neurotransmitter release contribute to neural circuit function. Modulation of neurotransmitter release is a basic mechanism of synapse regulation (Abbott and Regehr, 2004), but how changes in the amount of neurotransmitter contribute to neural communication and specific circuit computations is incompletely understood. AWC^{ON} initiates chemotaxis behavior to a variety of attractive odors. Mutant studies have shown that AWC^{ON} has the potential to encode both attraction and repulsion to the same odor, but the mechanism of this plasticity is not clear. Here we use Vglut-pH imaging to monitor neurotransmitter release from AWC^{ON} and use the chemotaxis circuit to ask how regulated neurotransmitter release contributes to specific behavioral outputs.

AWC mediates chemotaxis by signaling to downstream interneurons that regulate probabilistic turning and reversal events (Chalasani et al., 2007; Gordus et al., 2015; Gray et al., 2005). Navigation in response to chemical stimuli has features resembling the biased random walk described for bacterial chemotaxis (Berg and Brown, 1972; Pierce-Shimomura et al., 1999).

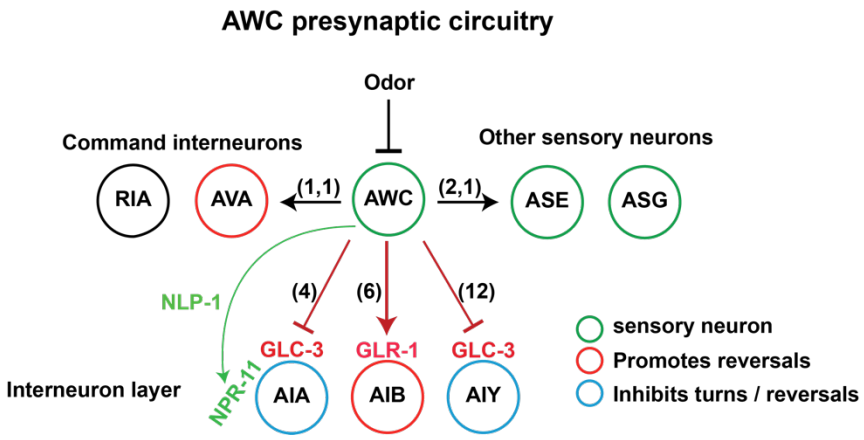

Figure 6.1. Simplified wiring diagram of AWC presynaptic connections.

AWC uses both glutamate and neuropeptides as neurotransmitters. Red connections represent glutamate signaling and the green line neuropeptide signaling. GLC-3: inhibitory glutamate-gated chloride channel. GLR-1: excitatory AMPA-type glutamate receptor. NPR-11: Neuropeptide Receptor. NLP-1: Neuropeptide- like protein. Numbers on connections indicate ~ number of synapse from AWC. AWC is thought to mediate chemotaxis by differentially regulating the activity of interneurons that impose biases on turning and reversal frequencies. Inhibition of AWC by odor decreases the excitatory connection to AIB, decreasing reversal frequency. Simultaneously, decreased inhibition on AIA and AIY increases their ability to inhibit turns and reversals. Together these actions bias the locomotion into straighter trajectories in the direction of the odor source. Refs: (Chalasani et al., 2007; Chalasani et al., 2010; Gray et al., 2005; Tsalik and Hobert, 2003; Wakabayashi et al., 2004; White et al., 1986).

In this strategy, straight trajectories are interrupted by reorienting turns and reversals, the rates of which are modulated and biased by sensory information. Over time, this produces prolonged runs in the preferred direction of movement. From the *C. elegans* wiring diagram, AWC's main synaptic output is to the interneurons AIA, AIB, and AIY (White et al., 1986). A combination of genetics and calcium imaging has revealed how these interneurons respond to AWC signals, and has identified some of the underlying neurotransmitters and receptors (Chalasani et al., 2007; Chalasani et al., 2010). AWC^{ON} signals to downstream interneurons using both glutamate and neuropeptides as neurotransmitters (Figure 6.1). AWC inhibits AIA and AIY and activates AIB. Through ablation experiments and acute manipulations, AIA and AIY have been found to inhibit reversals, whereas AIB increases reversals (Gordus et al., 2015; Gray et al., 2005; Piggott et al., 2011; Pokala et al., 2014). The coordinated regulation of these interneurons links a decrease in odor concentration to an increase in reversal frequency.

C. elegans is innately attracted to the AWC^{ON}-sensed odor butanone, but pairing butanone with food deprivation for several hours can generate butanone avoidance that requires AWC^{ON} signaling (Colbert and Bargmann, 1995; L'Etoile et al., 2002; Tsunozaki et al., 2008). This ability of AWC^{ON} to switch signaling modes was highlighted when a screen for altered butanone chemotaxis mutants isolated a mutation in a receptor-type guanylate cyclase gene *gcy-28* that caused animals to avoid butanone instead of approaching it (Tsunozaki et al., 2008). Examination of *gcy-28* function in AWC^{ON} revealed that the relevant GCY-28

isoform is localized to the axon and rescues attraction when expressed solely in AWC^{ON}, suggesting a presynaptic role. *gcy-28* genetically interacts with diacylglycerol (DAG) and protein kinase C signaling pathways. Butanone attraction is rescued by a loss-of-function mutation in *dgk-1*, which hydrolyzes DAG to phosphatidic acid and limits neurotransmission in cholinergic *C. elegans* motor neurons (Lackner, 1999). Acute treatment with the pharmacological DAG agonist PMA rescues chemotaxis in *gcy-28(lf)* mutants, indicating that the switch in preference can occur dynamically in adult animals (Tsunozaki et al., 2008). Conversely, loss of function mutations in the major DAG target *pkc-1*, the *C. elegans* homolog of the mammalian protein kinase C epsilon isoform, result in avoidance of AWC-sensed odors (Okochi et al., 2005; Tsunozaki et al., 2008). Furthermore, AWC^{ON} functional calcium imaging in both *gcy-28(lf)* and *pkc-1(lf)* mutants has shown that calcium signaling in these mutants is intact, suggesting that primary sensory transduction is likely unaffected in these mutants. Together, the work outlined by Tsunozaki *et al* suggests that changes in axonal cGMP and DAG/PKC-1 signaling result in synaptic changes in AWC^{ON} that signal either 'attraction' or 'avoidance' to downstream interneurons.

Interestingly, the DAG/*pkc-1* synaptic signaling pathway described above is also involved in controlling preference in two other sensory modalities in *C.elegans*, thermotaxis in AFD neurons and salt preference learning in ASER neurons. In thermotaxis, animals navigate toward the specific temperature at which they have been cultivated, a preference that is reset by exposure to a new temperature for an hour or more (Kimata et al., 2012). *pkc-1(lf)* creates

thermophilic animals that prefer warmer temperatures than the cultivation temperature, a defect that can be restored by AFD-specific expression of *pkc-1* (Luo et al., 2014; Okochi et al., 2005). In salt avoidance learning, animals that are normally attracted to salt learn to avoid it when paired with food deprivation, a behavior meditated in part by ASER sensory neurons (Tomioka et al., 2006). Salt avoidance learning requires an insulin-PI-3 kinase pathway, and persistent activation of PIP3 signaling by a mutation in the PTEN lipid phosphatase *daf-18* induces salt avoidance in naive animals. ASER calcium responses in *daf-18(lf)* mutants are normal, indicating that the change in ASER function is likely downstream of ASER primary sensory transduction (Tomioka et al., 2006). *pkc-1(lf)* naive animals lose their attraction to salt, but can still learn avoidance (Adachi et al., 2010). Expression of constitutively active *pkc-1* in ASER, or treatment with the DAG signaling agonist PMA, prevents avoidance learning (Adachi et al., 2010). Furthermore, expression of a constitutively active form of *pkc-1* in ASER restores salt attraction to *daf-18(lf)* mutants (Adachi et al., 2010). Together, these results suggest that the DAG/*pkc-1* pathway can be utilized by different sensory neurons to alter synaptic output for the common goal of altering sensory preference, highlighting the role of presynaptic modulation in circuit computation.

Because *pkc-1* modulates preference in several sensory modalities, we chose to focus on characterizing *pkc-1* function in butanone preference in AWC^{ON}. The protein kinase C family is a group of serine/threonine kinases that play many roles in signal transduction in the nervous system (Sun and Alkon,

2014). In mammals there are at least 12 PKC isozymes, and these are classified into three subgroups based on their structures and second messenger requirements: conventional PKCs (α, βI, βII, γ), which require both calcium and DAG for activation; novel PKCs (δ, ε, η, θ, μ) that only require DAG; and atypical PKCs (ζ, ι, λ,) that require neither calcium nor DAG. The substrate selectivity of PKCs is thought to be determined primarily by interaction partners and intracellular distribution (Mochly-Rosen and Gordon, 1998; Sun and Alkon, 2014). Many PKC isoforms can modulate synaptic release through a variety of mechanisms. *pkc-1* belongs to the novel PKC epsilon subgroup, and in addition to modulating the behaviors mentioned above, it also functions in *C. elegans* to regulate osmosensation, mechanosensation, and the release of neuropeptides from motor neurons (Hyde et al., 2011; Okochi et al., 2005; Sieburth et al., 2007).

In this chapter we investigate *pkc-1* function in AWC^{ON} through a combination of genetics, behavior, calcium imaging, and Vglut-pH imaging. We find that *pkc-1* functions in AWC^{ON} downstream of presynaptic calcium influx to modulate glutamate release, and that these changes affect communication with interneurons and behavioral output. We show that DAG signaling and *pkc-1* act in parallel pathways in AWC^{ON} to promote behavioral butanone attraction. Furthermore, we show that Gqα signaling modulates AWC^{ON} glutamate release and suggest a model for a dual function Gqα/DAG/*pkc-1* signaling pathway that regulates synaptic vesicle release and butanone preference in AWC^{ON}.

Results

pkc-1 functions in AWC^{ON} to regulate butanone olfactory preference

We began by examining the role of *pkc-1(lf)* in butanone chemotaxis in detail. Animals bearing a variety of *pkc-1(lf)* alleles predicted to cause different defects in protein activity produced animals that were repulsed by butanone (Fig 6.2A-B). The *pkc-1(nj1)* allele has a missense mutation in a conserved amino acid in the catalytic loop of the kinase domain, but should leave the rest of the protein intact (Okochi et al., 2005). *pkc-1(nj3)* results in an early translational stop and severally truncates the protein upstream of the kinase domain (Okochi et al., 2005). *pkc-1(ok563)* is a large deletion that produces a frameshift in the two confirmed isoforms of *pkc-1,* but would spare a third, unconfirmed, but predicted isoform (Hyde et al., 2011). In each case, *pkc-1* disruption resulted in butanone avoidance, suggesting that PKC-1 kinase activity, disrupted specifically in *pkc-1(nj1)* mutants, is likely important for mediating PKC-1's regulatory effects on butanone preference. For additional studies, we focused on using *pkc-1(nj1)* mutants because it was more extensively backcrossed than the other strains and more reagents with this allele were available. *pkc-1(nj1)* mutants avoided butanone over a wide range of concentrations (Fig 6.2C).

To ask if *pkc-1* functions in AWC to regulate butanone olfactory preference, we expressed *pkc-1* dsRNAi in AWC^{ON} using the AWC^{ON}-specific promoter *str-2*. The resulting animals avoided butanone in chemotaxis assays like *pkc-1(lf)* mutants (Fig 6.2D).

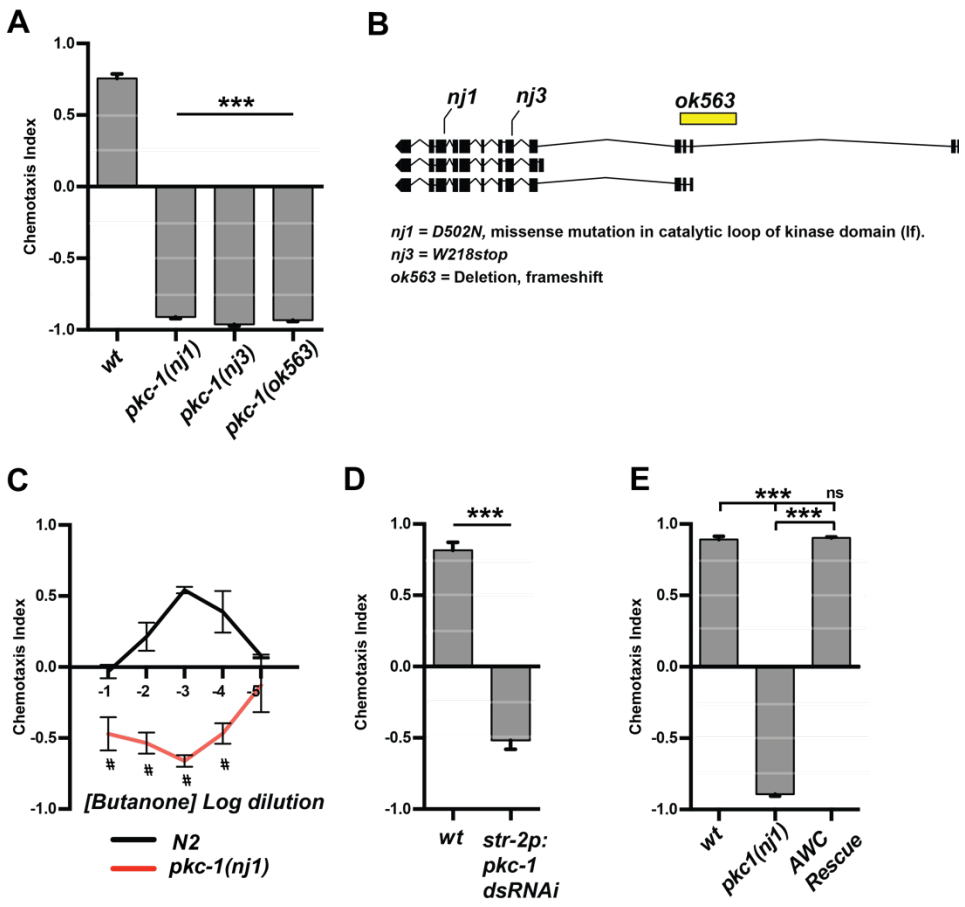

Figure 6.2. *pkc-1* functions in AWC^{ON} to regulate butanone preference.

(A) *pkc-1(lf)* results in butanone avoidance. Population assay (methods). *wt* n = 29, *pkc-1(nj1)* n = 26, *pkc-1(nj3)* n = 6, *pkc-1(ok653)* n = 2. Error = S.E.M. One-way ANOVA *** p <0.0001 **(B)** Gene structure of three predicted *pkc-1* isoforms and the location and description of *pkc-1(lf)* alleles used in this thesis. **(C)** *pkc-1(nj1)* mutants are repulsed by a wide range of butanone concentrations. n = 3 population chemotaxis assays for all data points. # = statistically different from *wt*, p <0.0001, t-tests corrected for multiple comparisons (Holm-Sidak). Butanone 10^-3 dilution is the standard butanone concentration at the gradient source for plate-based chemotaxis assays (used in A,D,E). **(D)** Expression of *pkc-1* dsRNAi in AWC^{ON} under the *str-2p* promoter generates butanone repulsion. *wt* n = 9, *str-2p:pkc-1* dsRNAi n = 9, population chemotaxis assays. Error = S.E.M. t-test *** p <0.0001. **(E)** Expression of a *pkc-1* cDNA in AWC^{ON} using the *str-2p* promoter restores butanone attraction to *pkc-1(nj1)* mutants (AWC Rescue). *wt*, *pkc-1(nj1)*, and rescue n = 3, population chemotaxis assays. One-way ANOVA *** p < 0.0001. ns = not significant.

Expression of a *pkc-1* cDNA in AWC^{ON} under the *str-2* promoter fully rescued butanone chemotaxis defects in *pkc-1(nj1)* mutants (Fig 6.2E). Together, these results indicate that *pkc-1* functions in AWC largely cell-autonomously to regulate butanone olfactory preference.

pkc-1 functions downstream of calcium influx

pkc-1 is hypothesized to function at the synapse, downstream of primary sensory transduction (Tsunozaki et al., 2008). In agreement with this possibility, calcium responses to odor in the AWC cell body measured with GCaMP1 were similar to wild type in *pkc-1(nj1)* mutants. We repeated these experiments with newer versions of GCaMP that are more sensitive, faster, and less cytotoxic than GCaMP1 (Akerboom et al., 2012; Tian et al., 2009). To ensure that the concentration of butanone used in imaging experiments was behaviorally relevant, we conducted microfluidic behavioral assays that allowed us to precisely control the odor concentration (Albrecht and Bargmann, 2011). Animals were loaded in microfluidic arenas that permit crawling-like locomotion and were presented with a butanone gradient. The peak of this gradient was set to the standard butanone imaging concentration of 11.2 uM (10^{-6} dilution of pure butanone) (Fig 6.3A). *pkc-1(lf)* mutants exhibited excessive pausing during locomotion in microfluidic behavioral arenas that precluded assaying them directly, but animals expressing *pkc-1* dsRNAi in AWC^{ON} had locomotion patterns similar to wild-type animals.

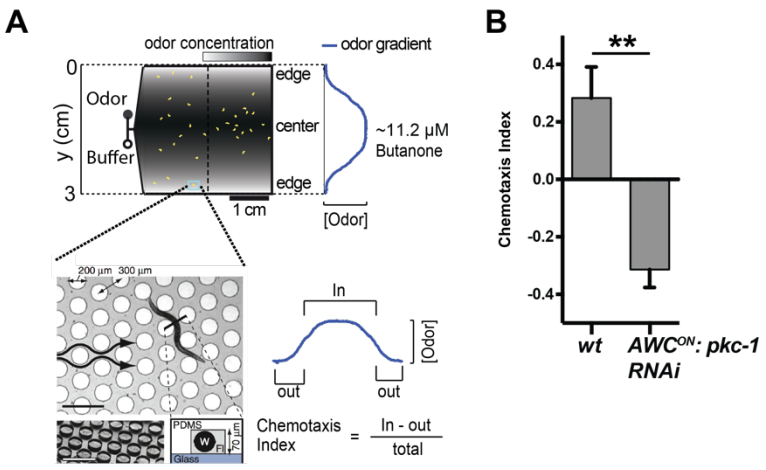

Figure 6.3. 11.2 uM butanone is behaviorally relevant for both attraction and avoidance behavior. **(A)** Diagram of microfluidic device used for recoding behavioral responses to odor stimulation. Top: Top-down view of microfluidic chamber. Odor and buffer enter the device through two channels and then are mix together at the front of the device to produce a symmetric gradient across the device, with the highest odor concentration (11.2 uM butanone) in the center (shading and blue gradient profile). Yellow lines represent animals in the device. Bottom left: high-resolution view of the device showing liquid flow direction, and displaying the posts that the animals use for crawling-like locomotion. Bottom right: locations in the gradient that are used to quantify animal location and calculate the chemotaxis index. Adapted and modified from: (Albrecht and Bargmann, 2011; Larsch et al., 2015). **(B)** Average chemotaxis index of wild-type controls and animals expressing *pkc-1* dsRNAi under the AWC^{ON} *str-2* promoter. n=4 experiments per genotype, 28-38 animals per experiment. Error = S.E.M. t-test ** p<0.005. Gradient conditions as in (A).

During the presentation of a butanone gradient, wild-type animals moved to the peak of the odor gradient and remained there for the duration of the 30 minute long assay, occasionally leaving the gradient peak and then returning. Animals expressing *pkc-1* dsRNAi in AWC^{ON} moved in the opposite direction, avoiding the peak of the gradient, and moving towards the location of the lowest butanone concentration. We calculated a chemotaxis index by binning the microfluidic arena into distinct regions and quantifying the total time spent in each region for the duration of the assay (30 minutes) (Fig 6.3A, bottom). Wild-type animals produced a positive chemotaxis index, whereas animals expressing *pkc-1* dsRNAi in AWC^{ON} produced a negative index (Fig 6.3B). These experiments indicate that 11.2uM butanone is a concentration sufficient to generate attractive and repulsive chemotaxis and is an appropriate concentration to correlate results from imaging experiments to behavioral results.

To image AWC^{ON} calcium responses, animals expressing GCaMP5A in AWC^{ON} were restrained within a microfluidic device and stimulated with 30 second pulses of butanone. Consistent with previous work, we did not detect any significant changes to AWC^{ON} odor-evoked calcium transient responses measured at the cell body (Tsunozaki et al., 2008) (Fig 6.4A). Similar results were found with pulses of various durations, short 1 second flicker-type stimuli, and for responses measured with GCaMP3 (data not shown). Calcium signals in *C. elegans* are generally consistent between cellular compartments, but vary in some cell types (Chalasani et al., 2007; Chalasani et al., 2010; Gordus et al., 2015; Hendricks et al., 2012).

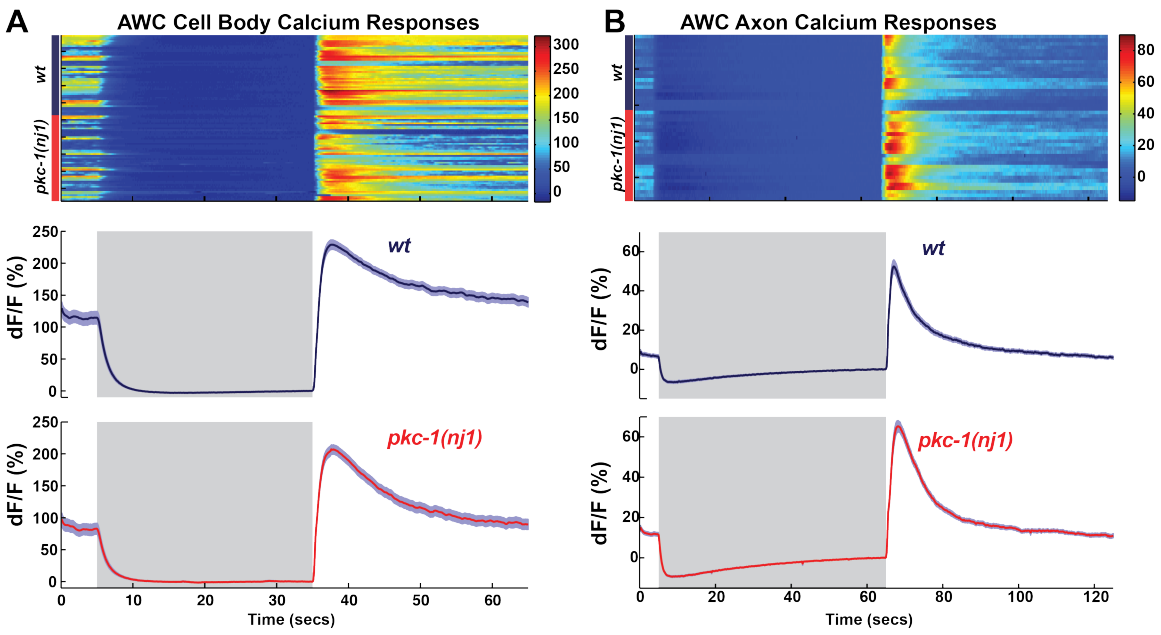

Figure 6.4. *pkc-1* functions downstream of primary signal transduction in AWC^{ON}. **(A)** Butanone evoked GCaMP5 responses in the AWC^{ON} cell body. *wt* n = 47 trials from 16 animals, 2-3 trials each. *pkc-1(nj1)* n = 50 trials from 17 animals, 2-3 trials each. **(B)** Butanone evoked AWC^{ON} axonal calcium responses measured with syGCaMP (Chapter 1). *wt* n = 21 trials from 7 animals, 3 trials each. *pkc-1(nj1)* n = 25 trials from 9 animals, 1-3 trials each. Gray bar = 11.2 uM butanone. Shading = S.E.M.

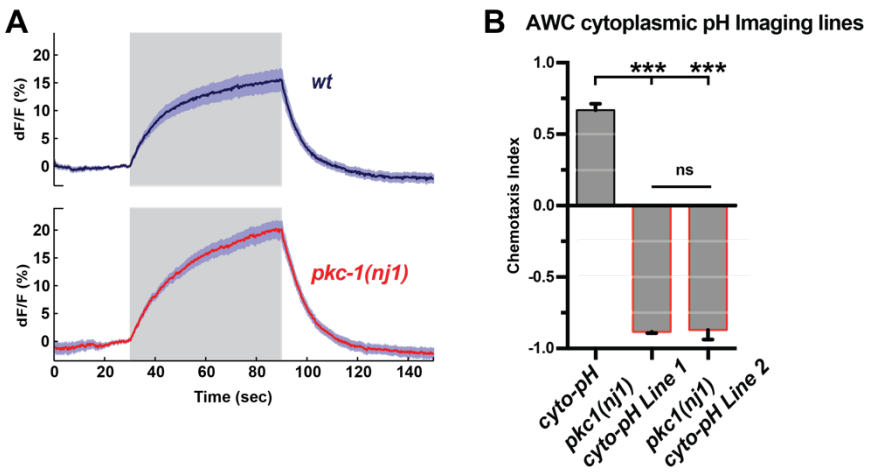

Figure 6.5. Odor-evoked cytoplasmic pH changes in AWC^{ON} are intact in *pkc-1(nj1)* mutants. **(A)** AWC cyto-pH responses. *wt* n = 18 trials from 6 animals, 3 trials each. *pkc-1(nj1)* n = 18 trials from 6 animals, 3 trials each. Gray bar = stimulus, 11.2 uM butanone. Shading = S.E.M. **(B)** Butanone chemotaxis of cyto-pH imaging lines. Butanone repulsion is intact in *pkc-1(nj1)* cyto-pH imaging lines. Error = S.E.M. n = 3, One-way ANOVA, *** p <0.0001. ns = not significant.

To test if *pkc-1* regulates calcium influx specifically in the axon at synapses, we targeted GCaMP3 to synapses by fusion to the synaptic vesicle protein synaptogyrin (as described in chapter 1). Odor-evoked axonal calcium responses in AWC^{ON} were also intact in *pkc-1(nj1)* mutants (Fig 6.4B). Similar results were found for 10-second and 3-minute odor pulses, and when a range of odor concentrations were used (data not shown). In addition, odor-evoked axonal changes in cytoplasmic pH in AWC^{ON} were also intact in *pkc-1(nj1)* mutants, correlating with the calcium imaging results (Fig 6.5). These results are consistent with the possibility that PKC-1 functions to modify some aspect of synaptic output downstream of calcium influx.

pkc-1 regulates AWC^{ON} synaptic release

We measured AWC^{ON} glutamate release using Vglut-pH imaging and found that the dynamics of Vglut-pH responses in *pkc-1(lf)* mutants were significantly altered (Fig 6.6A-C). In *pkc-1(nj1)* and *pkc-1(nj3)* alleles, the response to odor addition was completely absent, and in *pkc-1(ok563)* it was strongly diminished. The response to odor removal in all mutants was blunted and had slower kinetics. Unlike in wild-type, 10-second odor pulses were insufficient to generate significant Vglut-pH responses in *pkc-1(nj1)* mutants, and a 3-minute pulse did not increase the response compared to 60-second pulses (Fig 6.6D). Expression of *pkc-1* cDNA in AWC^{ON} fully rescued AWC^{ON} Vglut-pH defects of *pkc-1(nj1)* mutants (Fig 6.6E-F).

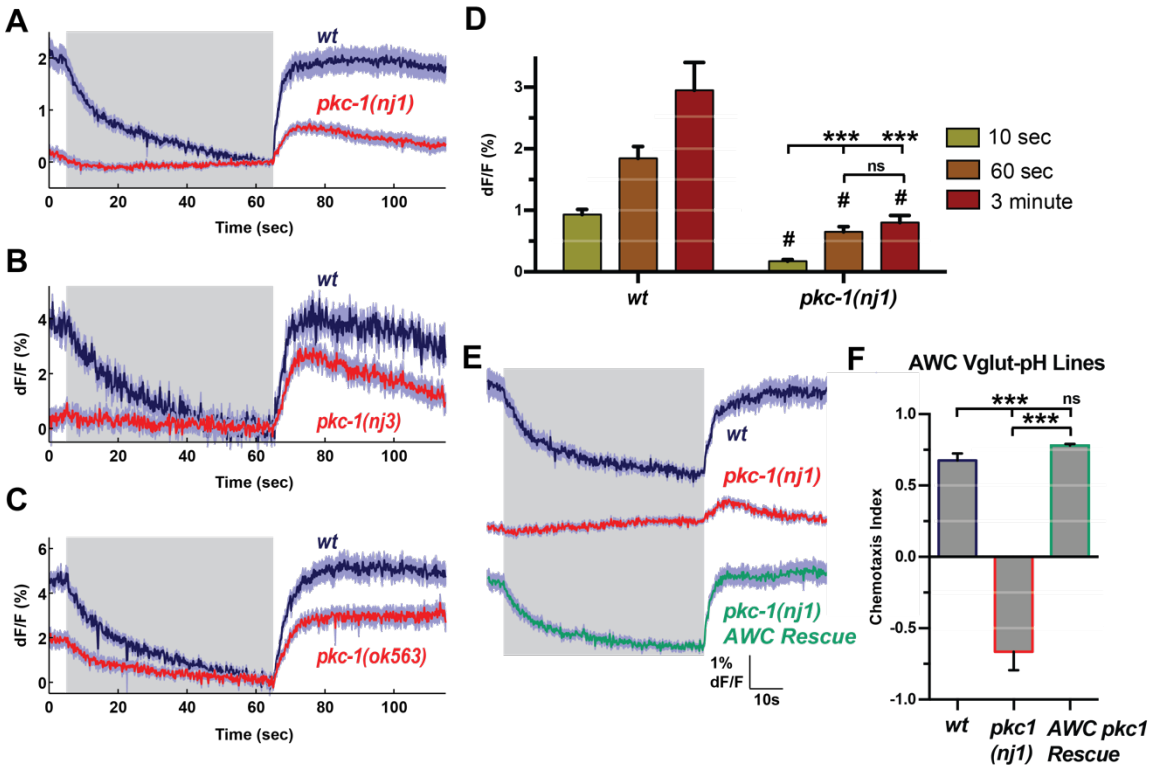

Figure 6.6. *pkc-1* regulates glutamate release in AWC^{ON}.

(A) - (C) AWC Vglut-pH responses in *pkc-1(lf)* mutants. (A) *wt* n = 29 trials from 10 animals, 2-3 trials each. *pkc-1(nj1)* n = 48 trials from 17 animals, 2-3 trials each. (B) *wt* n = 6 trials from 2 animals 3 trials each. *pkc-1(nj3)* n = 18 trials from 6 animals, 3 trials each. (C) *wt* n = 27 trials from 9 animals, 3 trials each. *pkc-1(ok563)* n = 48 trials from 17 animals, 2-3 trials each. **(D)** Average AWC Vglut-pH peak response magnitude after odor removal for indicated stimulation durations. # = different from wild-type p <0.0001. *** = different from 10 sec pulse p <0.0001. All wild-type pulses, p <0.0001. Two-way ANOVA. Tukey correction. Error = S.E.M. 10-second pulses : *wt* n = 60 trials, from 10 animals, 6 trials each. *pkc-1(nj1)* n = 102 trials from 17 animals, 4-6 trials each. 60-second pulses: as in (A). 3-minute pulses: *wt* n = 8 trials from 8 animals, 1 trial each. *pkc-1(nj1)* n = 15 trials, from 15 animals, 1 trials each. **(E)** Expression of *pkc-1* cDNA in AWC under the *str-2p* promoter rescues glutamate release. *wt* n = 18 trials from 6 animals, 3 trials each. *pkc-1(nj1)* n = 30 trials from 10 animals, 3 trials each. *str-2p:pkc-1cDNA* rescue n = 30 trials from 10 animals, 3 trials each. **(F)** Butanone chemotaxis of AWC Vglut-pH transgenics; The Vglut-pH reporter does not affect butanone attraction or avoidance. n = 3 population assays per genotype. One-way ANOVA, *** p <0.0001. ns = not significant. Gray bar = 11.2 uM butanone. Shading = S.E.M.

Together, these results indicate that *pkc-1* functions in AWC^{ON} to regulate glutamate release downstream of calcium influx and that this defect correlates with butanone repulsion.

AWC^{ON} Vglut-pH imaging in *gcy-28* mutants.

As *gcy-28(lf)* mutants lacking an axonal transmembrane guanylate cyclase are also repulsed by butanone, we asked if AWC^{ON} glutamate release was altered in these mutants as well. We first confirmed that AWC^{ON} calcium responses were normal in *gcy-28(tm2411)* mutants. Cell body measurements of odor-evoked GCaMP5 signals in *gcy-28(tm2411)* mutants were similar to wild-type controls for 30s and 60s odor pulses and for 1-second flicker-type stimuli (Fig 6.7A and data not shown). However, AWC^{ON} Vglut-pH responses in *gcy-28(tm2411)* mutants were decreased compared to wild-type controls (Fig 6.7B). On average, the Vglut-pH response in *gcy-28(tm2411)* mutants was only slightly weaker than wild-type, but responses were heterogeneous with some responses appearing similar to wild-type. The AWC^{ON} Vglut-pH signal triggered by odor removal has three components: an initial fast rise, a transitional phase with a slower rate of increase, and a stable steady state of exocytosis balanced by endocytosis (Chapter 1). In many *gcy-28(tm2411)* responses, the 'fast' release component triggered by odor removal was blunted or absent, and traces were dominated by a slower component of release (Fig 6.7C).

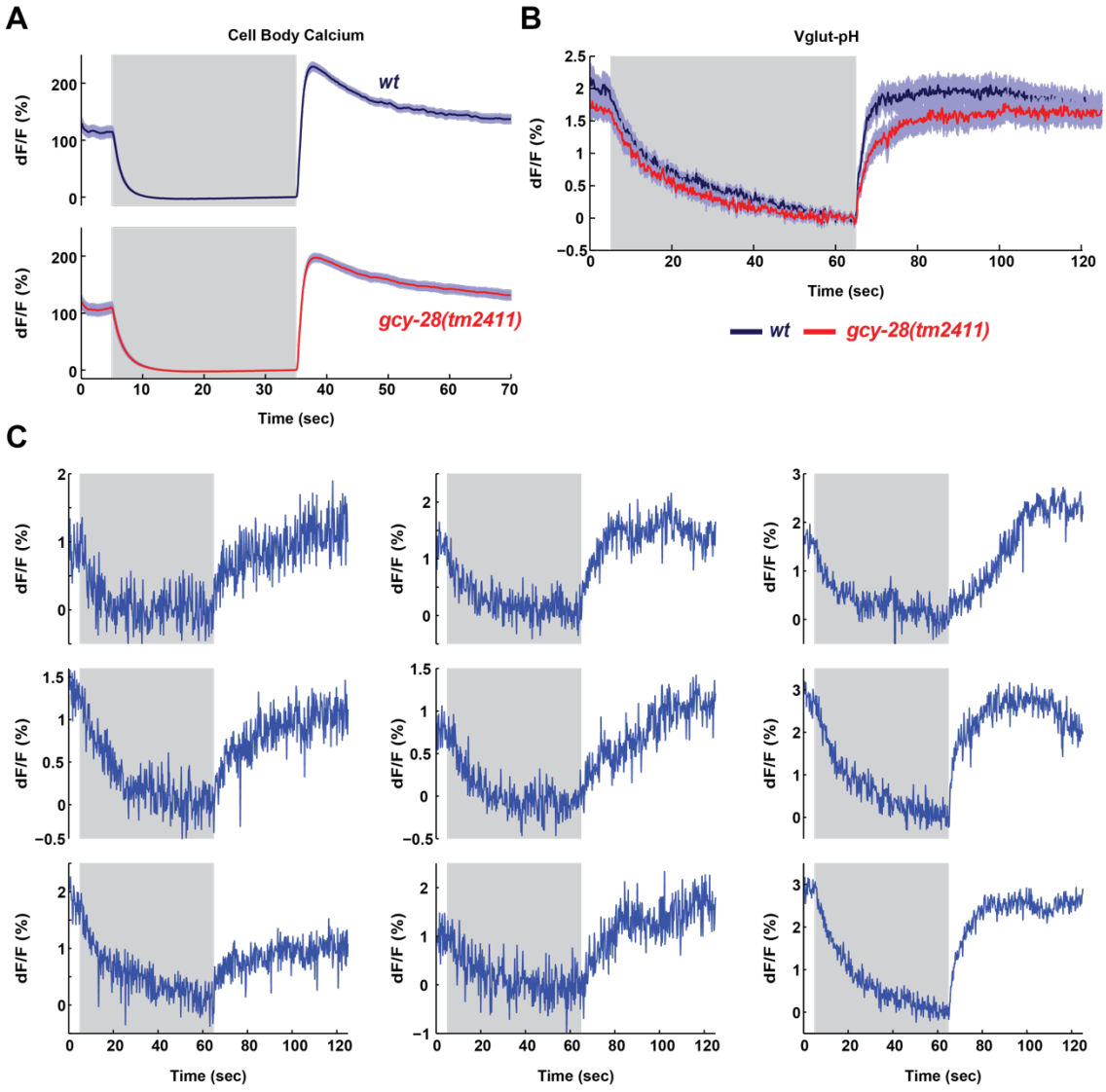

Figure 6.7. *gcy-28* functions downstream of primary sensory transduction and modulates AWC^{ON} glutamate release.

(A) AWC GCaMP5 response to butanone in *gcy-28(tm2411)* mutants. *wt* n = 47 trials from 16 animals, 2-3 trials each. *gcy-28(tm2411)* n = 57 trials from 19 animals, 2-3 trials each. **(B)** AWC Vglut-pH responses in *gcy-28(tm2411)* mutants. *wt* n = 29 trials, from 10 animals, 2-3 trials each. *pkc-1(nj1)* n = 48 trials, from 17 animals, 2-3 trials each. **(C)** Nine individual Vglut-pH traces from *gcy-28(tm2411)* mutants in (B). Gray bar = 11.2 uM butanone. Shading = S.E.M.

The changes to glutamate release in *gcy-28(tm2411)* mutants were different from the effects found in *pkc-1(nj1)* mutants, but the overall effect of decreased AWC^{ON} glutamate release is similar and aligns with the hypothesis that *gcy-28* functions in the regulation of AWC^{ON} synaptic release (Tsunozaki et al., 2008).

pkc-1 **has cell-specific effects on glutamate release.**

pkc-1 has been suggested to regulate distinct signaling events in different sensory neurons (Okochi et al., 2005). To ask if PKC-1 affects glutamate release in other neurons, we tested ASH Vglut-pH responses. *pkc-1(nj1)* mutants have defects in ASH-mediated behaviors (Hyde et al., 2011; Okochi et al., 2005). Stimulation of ASH with a 500 mM NaCl osmotic stimulus generated Vglut-pH responses that were normal in the first pulse, but decreased during the subsequent two pulses within the trial (Fig 6.8A,D). This effect was temporary and by the next trial (~1 min after the last stimulus) the first pulse was again normal (Fig 6.8B). We measured the rate of endocytosis after the first pulse and did not detect a significant difference from wild-type controls (Fig 6.8C). These results indicate that glutamate exocytosis responses in ASH are initially intact, but are not well-sustained across trials.

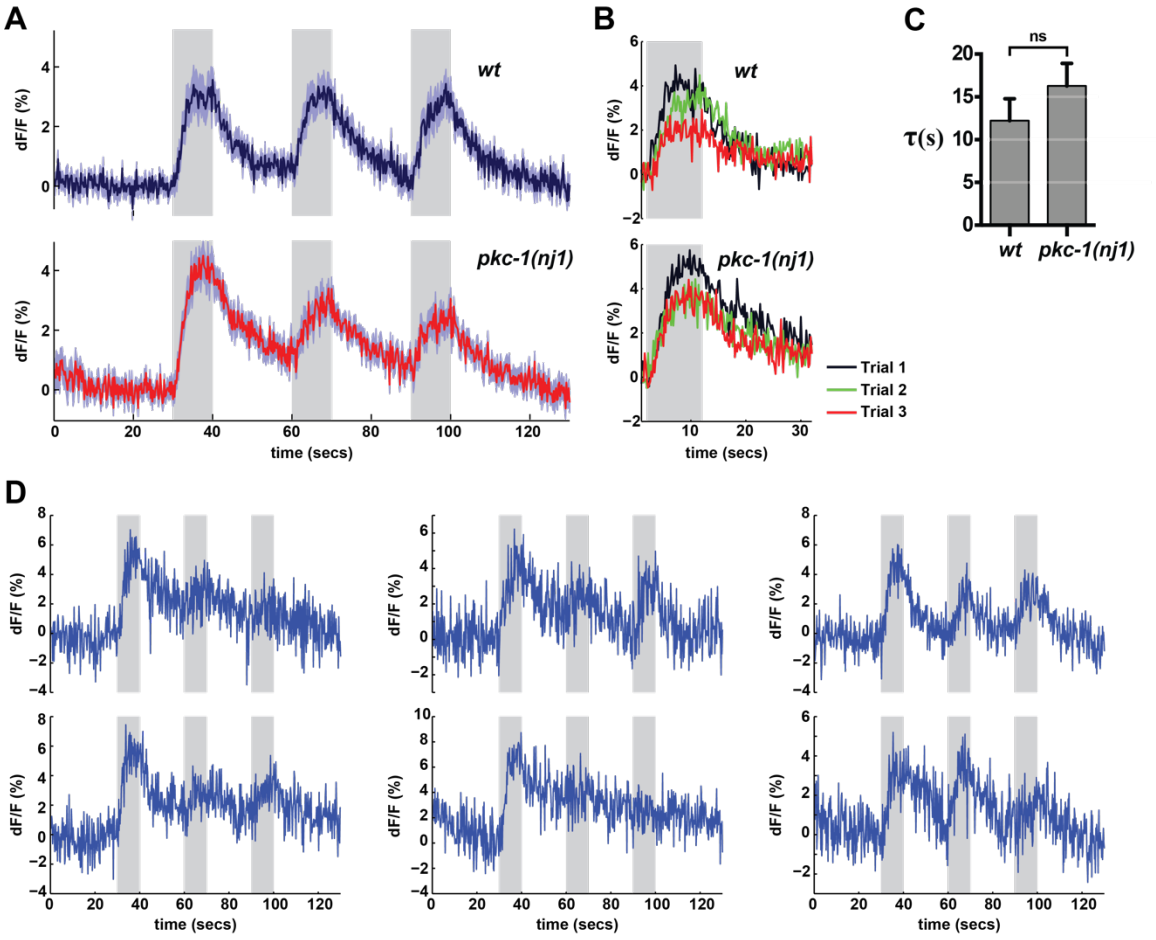

Figure 6.8. ASH Vglut-pH responses in *pkc-1(nj1)* mutants.

(A) ASH Vglut-pH responses in *pkc-1(nj1)* mutants. *wt* n = 15 trials from 5 animals, 3 trials each. *pkc-1(nj1)* n = 15 trials from 6 animals, 2-3 trials each. **(B)** ASH Vglut-pH responses in *pkc-1(nj1)* mutants recover by the next trial. Data from (A) but grouped by trial number. First stimulus of each trial. Average traces, without error shading. Trials separated from another by ~ 1 minute. **(C)** Endocytosis constants for the first stimulus pulse of each trial. Data from (A). Single exponential fit. Error = S.E.M. t-test. $p > 0.9$. ns= not significant. **(D)** Individual ASH Vglut-pH trials from six *pkc-1(nj1)* mutant animals. Gray Bar = 500 mM NaCl. Shading = S.E.M.

AWC^{ON} communication with downstream interneurons is altered in *pkc-1(lf)* mutants.

AWC^{ON} signals to interneurons that influence the initiation, frequency, and duration of locomotory behaviors such as reversals and turns. To ask how changes to AWC^{ON} synaptic release alter its communication with postsynaptic partners, we conducted calcium imaging in the interneurons AIB, AVA, and AIY.

AIB and AVA are closely associated with reversal behavior (Gordus et al., 2015; Gray et al., 2005; Piggott et al., 2011; Pokala et al., 2014), and increases in their activity are strongly correlated with reversals. The current model for AWC-mediated chemotaxis suggests that AWC regulates reversals by activating AIB, which then relays signals to the backward command interneuron AVA that stimulates motor neurons to control reversals (Gordus et al., 2015) (Fig 6.9A). AWC has been reported to form excitatory connection (s) with AIB mediated by the AMPA-type ionotropic glutamate receptor *glr-1* (Chalasani et al., 2007). There are also other direct and indirect synapses from AWC to AVA (White et al., 1986). Calcium responses in AIB and AVA can be imaged simultaneously within the same animal, and exhibit bistable coupled activity that is part of a larger network state of activity (Gordus et al., 2015; Prevedel et al., 2014) (Fig 6.9B-C). Stimulation of AWC with the odor isoamyl alcohol results in a probabilistic odor-response in AIB/AVA that is dependent on network state (Gordus et al., 2015). The response of AIB and AVA to butanone stimulation was also probabilistic, with most, but not all, animals shifting to a lower activity state with odor addition (Fig 6.9D-E).

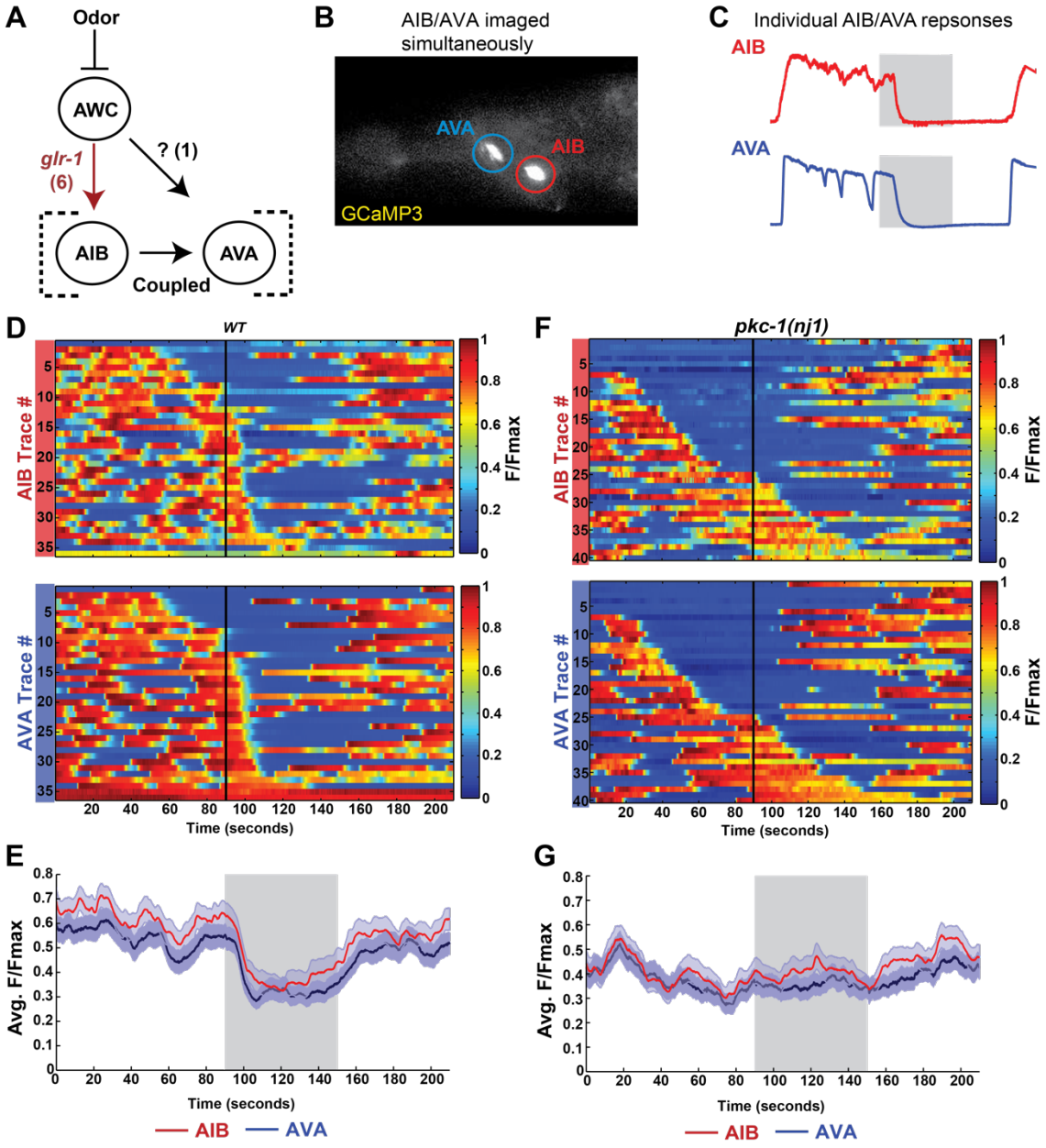

Figure 6.9. AWC^{ON} communication with AIB/AVA is altered in *pkc-1(lf).*

(A) Synaptic diagram of AWC communication with AIB and AVA interneurons. # = synapse number. **(B)** Animal expressing GCaMP3 in which AIB and AVA are imaged simultaneously. Circles indicate cell bodies. **(C)** Simultaneous recording of AIB/AVA GCaMP3 signals. **(D)** AIB/AVA responses to butanone stimulation. Heat maps show individual trials (black line indicates stimulus addition). Traces are organized according to the ON to OFF transition in AVA relative to odor addition. AIB and AVA traces with the same trace number correspond to the AIB/AVA pair recorded in the same animal. *wt* n = 36 trials from 9 animals, 4 trials each. **(E)** **A**verage response from data in (D). **(F)-(G)** As in (D)- (E) but for *pkc-1(nj1)* n = 40 trials from 10 animals, 3 trials each. Shading = S.E.M. Gray Bar = 11.2 uM Butanone.

In contrast, AIB and AVA did not appear to response to odor stimulation in *pkc-1(nj1)* mutants, and their overall activity was slightly decreased (Fig 6.9F-G). These results are consistent with the presynaptic defects in glutamate release observed in AWC^{ON} with Vglut-pH imaging, and suggest that in *pkc-1(lf)* mutants, AWC^{ON} may not be able to couple sensory information to the downstream circuity coordinating reversal behavior. To address this possibility directly, we quantified the behavioral response of animals subjected to pulses of butanone in microfluidic behavioral arenas. In wild-type animals, odor addition suppressed reorientations such as reversals and odor removal strongly triggered reversal-coupled pirouettes (Fig 6.10A). In animals expressing *pkc-1* dsRNAi in AWC^{ON}, butanone stimulation failed to modulate reversal behavior during either odor addition or removal (Fig 6.10B). These transgenic animals were still able to reverse when presented with a dye stimulus sensed by another neuron (Fig 6.10, blue stimulus bar) indicating that the ability to generate sensory-evoked reversal-behavior is still intact. These results are consistent with our findings from AIB/AVA imaging experiments, and support the hypothesis that butanone stimulation is unable to engage the reversal circuitry in *pkc-1(nj1)* mutants.

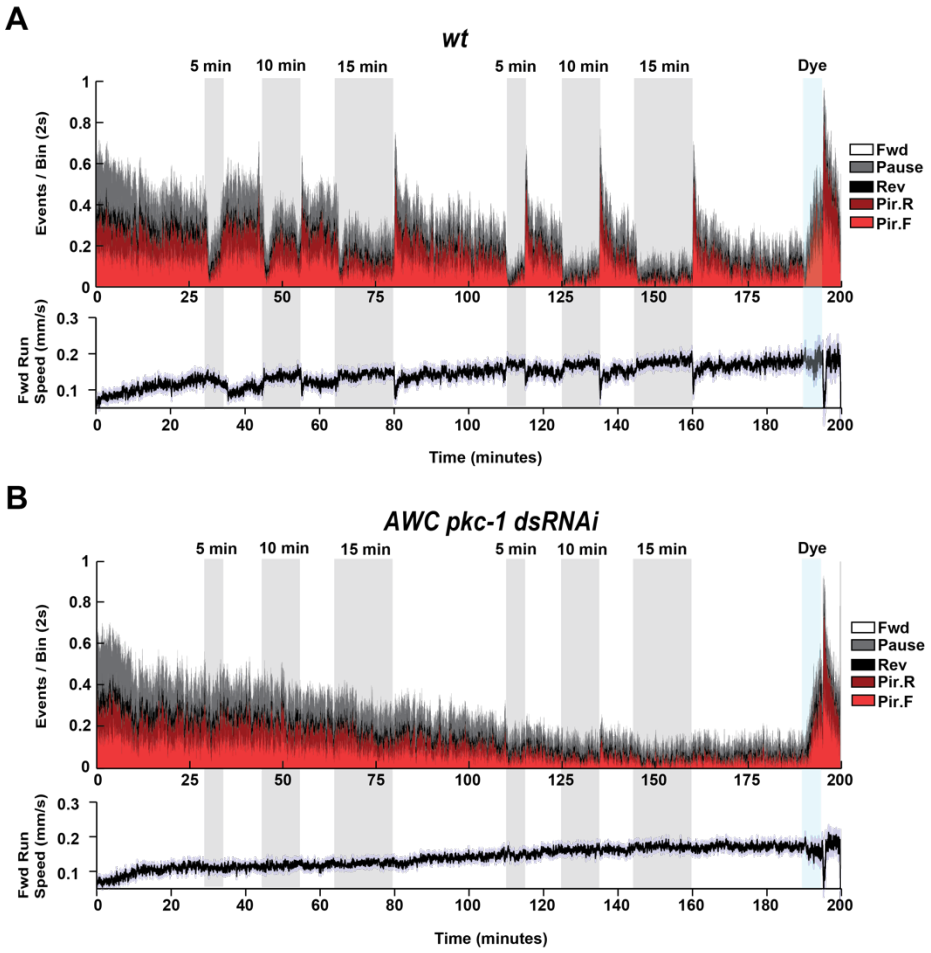

Figure 6.10. Animals expressing *pkc-1 dsRNAi* in AWC^{ON} do not regulate reversals in response to butanone pulses.

(A)-(B) Instantaneous behavioral state probabilities of animals subjected to butanone pulses in microfluidic arenas. *wt* and animals expressing *pkc-1* dsRNAi in AWC^{ON}: n= 3 separate experiments, with each genotype tested in two different arenas per experiment. ~25-32 animals per arena. Fwd = forward movement, Rev = reversal behavior, Pir.R and Pir.F = pirouette forward and reverse behaviors respectively. Bottom trace under each graph = locomotion speed. Gray bar = 11.2 uM butanone. Blue bar = aversive dye stimulus.

AIY is another major postsynaptic target of AWC (White et al., 1986). The connections between AWC and AIY have been reported to be inhibitory and to be mediated by the glutamate-gated chloride channel, *glc-3* (Chalasani et al., 2007) (Fig 6.11A). AIY inhibits turns and reversals (Gray et al., 2005), but how AIY activity levels contribute to locomotion during chemotaxis is not fully understood. We initially had some concerns that AIY activity might be influenced by the blue light used for GCaMP illumination. Strong blue-light illumination of can trigger avoidance behavior and is dependent on the phototransduction receptor *lite-1* (Liu et al., 2010). As *lite-1(ce314)* mutants fail to respond to blue-light illumination (Edwards et al., 2008) we used the *lite-1(ce314)* background to image AIY. We tested butanone chemotaxis in *lite-1(ce314)* and *lite-1(ce314);pkc-1(nj1)* double mutants and found that the *lite-1(ce314)* mutation did not alter butanone preference (Fig 6.11B).

AIY in *lite-1(ce314)* animals exhibited spontaneous calcium transients, as previously described in wild type animals (Chalasani et al., 2007). Butanone addition triggered an acute calcium increase in about half of the trials, followed by an overall increase in AIY activity during the one minute of stimulation (Fig 6.11C-E). Odor removal triggered a decrease in AIY activity that lasted ~10-15 seconds before returning to baseline. These responses are consistent with an inhibitory signal from AWC^{ON} to AIY (Chalasani et al., 2007). In contrast to AIB and AVA, AIY odor responses were increased in *lite-1(ce314); pkc-1(nj1)* double mutants compared to *lite-1* controls, with the overall magnitude of AIY fluctuations increased throughout all phases of the recording (Fig 6.11D).

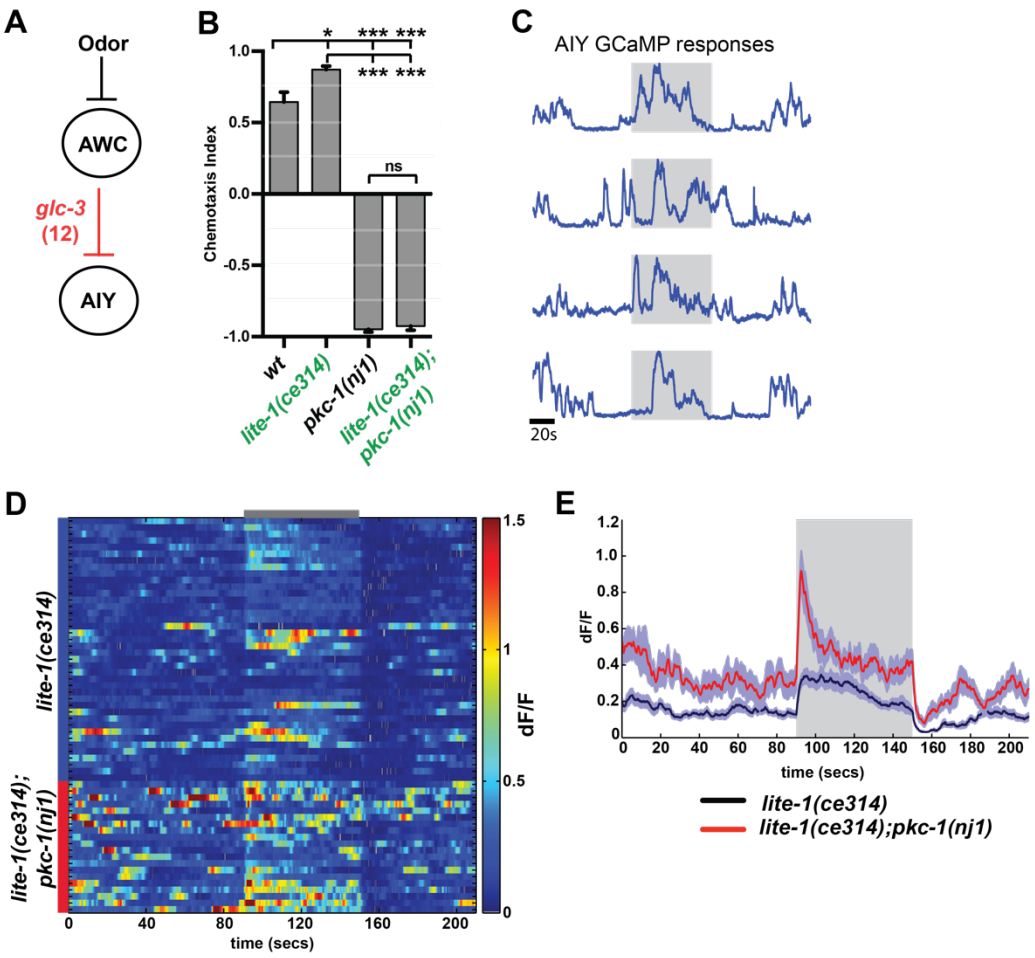

Figure 6.11. AIY activity is increased in *pkc-1(nj1)* mutants.

(A) AWC-to-AIY signaling diagram. **(B)** Butanone chemotaxis behavior is intact in lite-1 (ce314) mutants and AIY imaging lines (green genotypes). AIY imaging line = *mod-1p*:GCaMP5A. n = 3 population assays per genotype. error = S.E.M. Two-way ANOVA Tukey correction, * p <0.05, *** p <0.0001. **(C)** Individual AIY GCaMP traces from four *lite-1(ce314)* animals. Traces are normalized by their maximum value. **(D)** Heat map of AIY GCaMP responses. *lite-1(ce314)* n = 40 trials from 10 animals, 4 trials each. *lite-1(ce314);pkc-1(nj1)* n = 20 trials from 5 animals, 4 trials each. **(E)** Average AIY GCaMP response of data in (D). Gray bar = 11.2 uM butanone. Shading = S.E.M.

This effect was also evident in the average AIY activity (Fig 6.11E). The tonic increase in AIY activity in *pkc-1(nj1)* mutants may be the result of decreased tonic inhibitory glutamatergic input from AWC, but also indicates that another signal, from AWC or other synaptic inputs, is triggered by butanone stimulation. Together, our results from AIB, AVA, and AIY imaging indicate that the changes we observe in AWC^{ON} glutamate release in *pkc-1(lf)* mutants result in changes to AWC^{ON} communication with post-synaptic targets, consistent with a shift in AWC^{ON} glutamatergic signaling away from AIB/AVA and toward AIY subcircuits.

Epistatic interactions with synaptic vesicle regulators

We next asked whether increasing glutamate release from AWC^{ON} could restore attraction to butanone. Tomosyn-1 (*tom-1)* has been proposed to be a negative regulator of synaptic vesicle release (Gracheva et al., 2006a), and we previously found that *tom-1* loss-of-function increases synaptic vesicle release and calcium influx in AWC^{ON} (see Chapter 3). *tom-1(ok285)* mutants failed to restore basal release levels in *pkc-1(nj1)* mutants, but did partially restore the exocytic response to odor removal (Fig 6.12A-B). As *pkc-1(nj1)* mutants did not respond to odor addition and their response to odor removal was very weak, it was difficult to accurately measure their endocytosis kinetics. The increased AWC^{ON} odor-removal response in *pkc-1(nj1); tom-1(ok285)* double mutants allowed us to assess endocytosis by applying a second odor pulse during the peak of the response. The *tom-1(ok285)* mutation did not appear to impact endocytosis in this protocol (see Chapter 3, Fig 3.6).

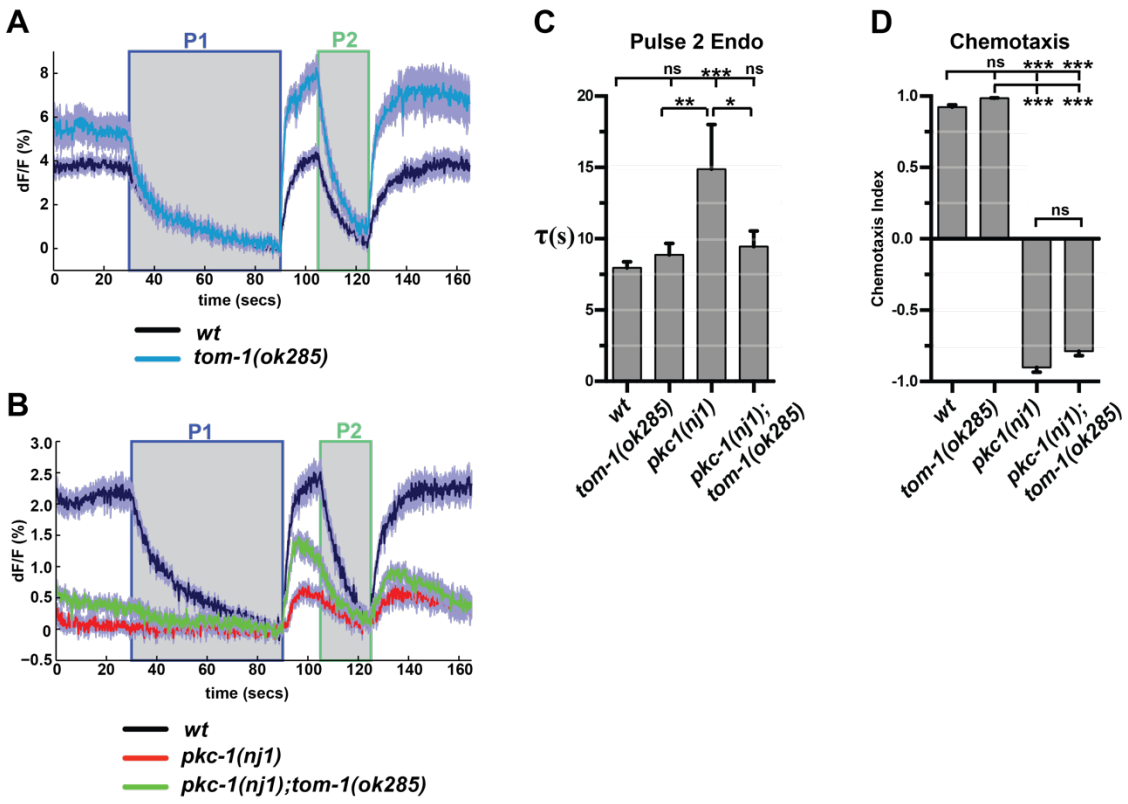

Figure 6.12. *pkc-1* epistasis interactions with *tomosyn-1.*

(A) AWC Vglut-pH responses in *tom-1(ok285)* mutants. *wt* n = 21 trials from 7 animals, 3 trials each. *tom-1(ok285)* = 17 trials from 7 animals, 2-3 trials each. **(B)** AWC Vglut-pH responses in *pkc-1(nj1); tom-1(ok285)* double mutants. *wt* n = 18 trials, from 6 animals, 3 trials each. *pkc-1(nj1)* n = 18 trials from 6 animals, 3 trials each. *pkc-1(nj1);tom-1(ok285)* n = 18 trials from 6 animals, 3 trials each. (A) and (B) Gray bar = stimulus, 11.2 uM butanone. Shading = S.E.M. **(C)** Average endocytosis rate constants for second pulse (P2) in panels (A) and (B). *wt* n = 39, *tom-1* n = 16, *pkc-1(nj1)* n = 8, *pkc-1(nj1);tom-1(ok285)* n = 16. Error = S.E.M. One-way ANOVA Tukey correction, * p <0.05, ** p<0.001, *** p <0.0001. **(D)** Butanone chemotaxis. *wt, tom-1, pkc-1(nj1)* n = 3 population assays per genotype. *tom-1(ok258); pkc-1(nj1)* n = 5. Error = S.E.M. One-way ANOVA Tukey correction, *** p <0.0001. ns = not significant.

Endocytosis during the second odor pulse was intact in both *tom-1(ok285)* and *pkc-1(nj1); tom-1(ok285)* double mutants (Fig 6.12C), indicating that the *pkc-1(lf)* mutant is able to support normal endocytosis.

The partial rescue of *pkc-1*-evoked SV release by a *tom-1* mutation might or might not be relevant to behavior. We found that *pkc-1(nj1); tom-1(ok285)* double mutants were repulsed by butanone in chemotaxis assays, like *pkc-1(nj1)* mutants (Fig 6.12D). Therefore, the increased response to odor removal in *pkc-1(nj1); tom-1(ok285)* mutants was insufficient to restore butanone attraction.

The apparent absence of AWC^{ON} basal release in *pkc-1(nj1); tom-1(ok285)* double mutants suggested that *pkc-1(nj1)* may specifically regulate tonic release levels. Complexin-1 (*cpx-1*) is proposed to serve as a negative regulator of tonic release in *C. elegans,* and *cpx-1(lf)* dramatically increases tonic release at the neuromuscular junction (NMJ) (Martin et al., 2011). However, *cpx-1(ok1552)* mutants had only minor effects on AWC^{ON} glutamate release (see Chapter 3) and failed to restore basal release in *pkc-1(nj1)*; *cpx-1(ok1552)* double mutants (Fig 6.13).

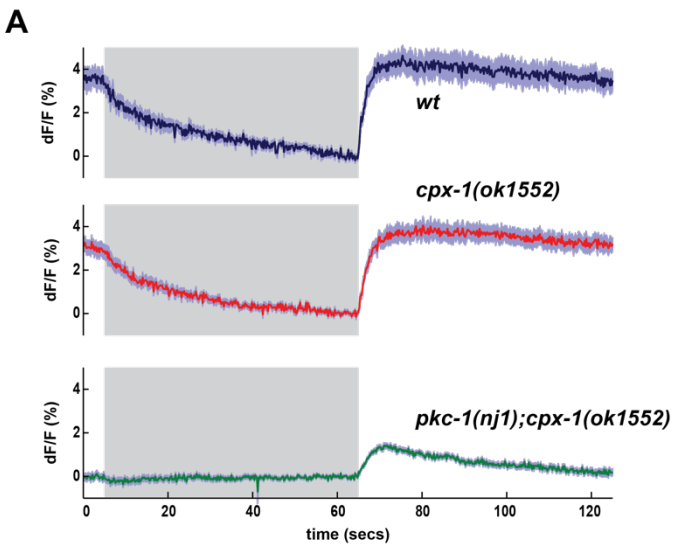

Figure 6.13. *pkc-1* epistasis interactions with *complexin-1.*

(A) AWC Vglut-pH responses to butanone stimulation. *wt* n = 12 trials from 4 animals, 3 trials each. *cpx-1(ok1552)* n = 15 trials from 5 animals, 3 trials each. *pkc-1(nj1); cpx-1(ok1552)* n = 43 trials from 15 animals, 1-3 trials each. Gray bar = 11.2 uM butanone. Shading = S.E.M.

The G_q heterotrimeric G-protein alpha subunit *egl-30* is a proposed regulator of tonic SV release at the *C. elegans* NMJ (Hu et al., 2015). Gqα signaling increases DAG production to increase SV release from motor neurons (Lackner, 1999; Mizuno and Itoh, 2009). Since increasing DAG signaling in *gcy-28(lf)* mutants restores butanone attraction (Tsunozaki et al., 2008), *egl-30* appeared as a candidate for linking changes in tonic release to changes in butanone preference.

The role of *egl-30* in synaptic transmission has been mainly inferred from behavioral assays: *egl-30(lf)* results in decreased locomotion, pharyngeal pumping, and egg-laying, as well as resistance to the cholinesterase inhibitor aldicarb (Lackner, 1999). Likewise, *egl-30(gf)* mutants increase these behaviors and are hyper-sensitive to aldicarb (Lackner, 1999). A direct effect of *egl-30* on synaptic release has not been reported. We conducted AWC^{ON} Vglut-pH imaging in *egl-30(n686sd)* partial loss-of-function mutants, and found that the response to odor removal was decreased (Fig 6.14A-C). Endocytosis appeared to be unaffected (Fig 6.14D). Responses in *egl-30(n686sd)* mutants were somewhat heterogeneous, reminiscent of the AWC^{ON} Vglut-pH defects in *gcy-28(tm2411)* mutants (Fig 6.14E). A complementary change was seen in the *egl-30(js126)* gain-of-function mutation, which strongly enhanced AWC^{ON} Vglut-pH responses, increasing the response magnitude (Fig 6.15A) and reducing the time to peak (Fig 6.15B).

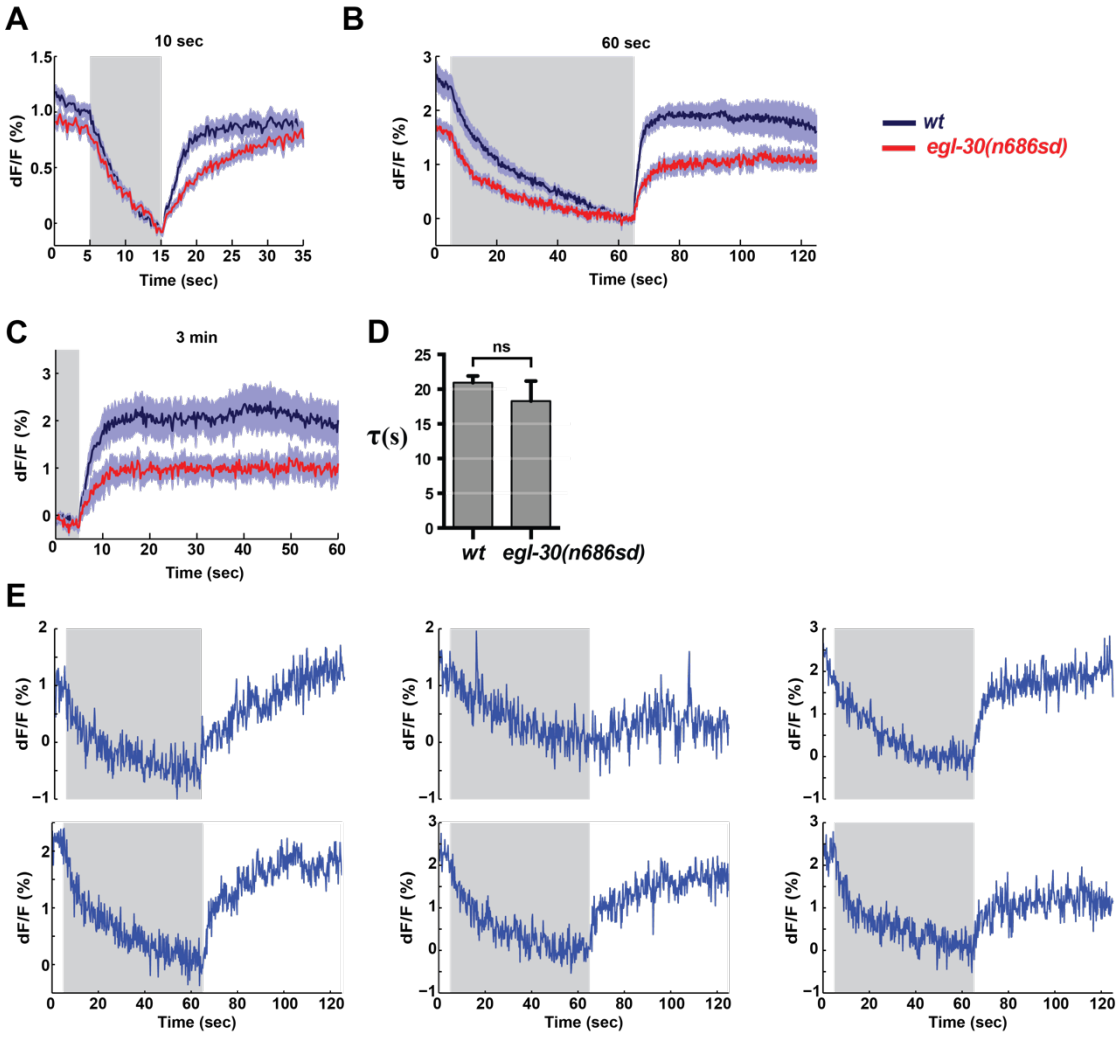

Figure 6.14. *egl-30(lf)* decreases AWC^{ON} glutamate release.

(A) AWC Vglut-pH responses in *egl-30(n686sd)* loss of function mutants. (A) 10-second stimulus. *wt* n = 83 trials from 17 animals, 4-6 trials each. *egl-30(n686sd)* n = 65 trials from 14 animals, 4-6 trials each. **(B)** 60-second stimulus. *wt* n = 51 trials from 17 animals, 3 trials each. *egl-30(n686sd)* n = 26 trials from 14 animals, 2-3 trials each. **(C)** 3-minute stimulus. *wt* n = 11 trials from 11 animals, 1 trial each. *egl-30(n686sd)* n = 8 trials from 8 animals, 1 trial each. **(D)** Endocytosis constants for 60-second stimulus from data from (B). Single exponential fit. Error = S.E.M. t-test. p > 0.2. ns= not significant. **(E)** Six individual Vglut-pH traces in *egl-30(n686sd)* mutants from data in (B). Gray bar = 11.2 uM butanone. Shading = S.E.M.

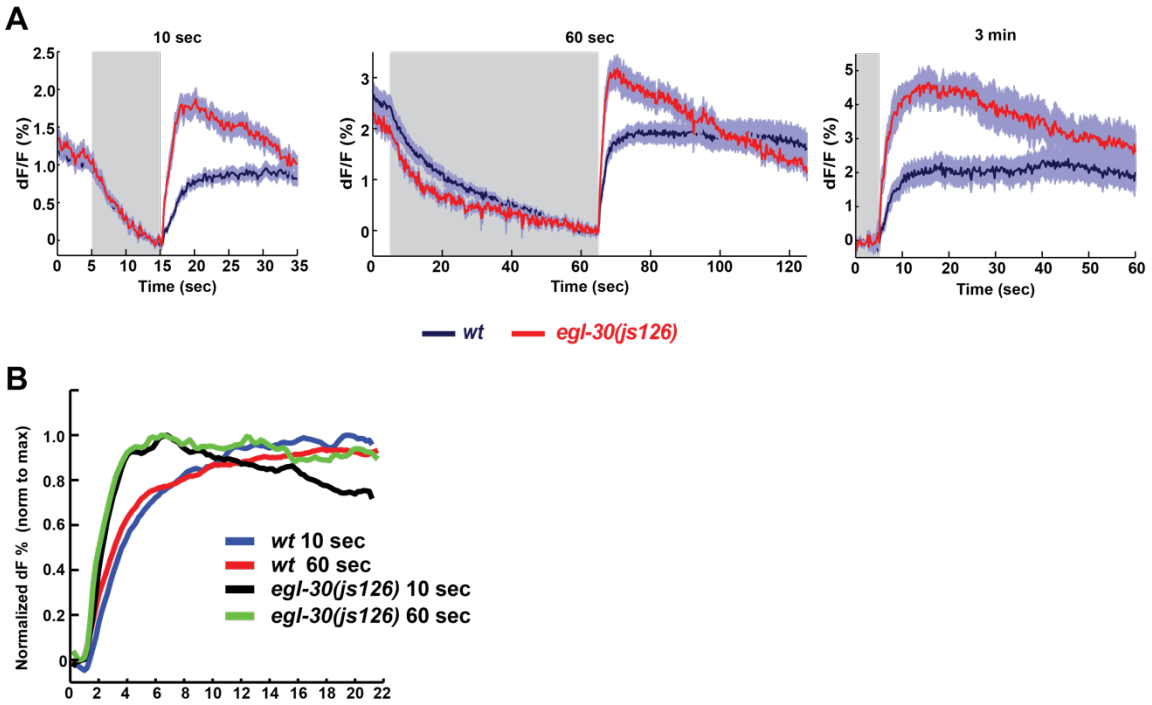

Figure 6.15. *egl-30(gf)* enhances AWC^{ON} glutamate release.

(A) AWC Vglut-pH responses in *egl-30(js126)* mutants. 10-second stimulus: *wt* n = 83 trials from 17 animals 4-6 trials each. *egl-30(n686sd)* n = 30 trials from 5 animals, 6 trials each.

60-second stimulus: *wt* n = 51 trials from 17 animals, 3 trials each. *egl-30(n686sd)* n = 15 trials from 5 animals, 3 trials each. 3-minute stimulus: *wt* n = 11 trials from 11 animals, 1 trials each. *egl-30(n686sd)* n = 5 trials from 5 animals, 1 trials each. Gray bar = 11.2 uM butanone. Shading = S.E.M. **(B)** Comparison of the mean AWC^{ON} Vglut-pH odor-removal responses for 10-second and 60-second stimuli in (A). Traces are normalized to their peak value (F/F_{MAX}).

To define the genetic relationship between *egl-30* and *pkc*-1, we asked if an *egl-30(gf)* mutation could restore AWC^{ON} Vglut-pH responses and/or butanone attraction in *pkc-1(nj1)* mutants. AWC^{ON} Vglut-pH responses in *egl-30(js126); pkc-1(nj1)* double mutants showed normal levels of basal SV release as well as near-normal responses to odor removal (Fig 6.16A). In addition, in chemotaxis assays, butanone attraction was restored in *egl-30(js126); pkc-1(nj1)* double mutants (Fig 6.16B). These results define an antagonistic relationship between *egl-30* and *pkc-1* at the AWC^{ON} synapse that matches an antagonistic behavioral function.

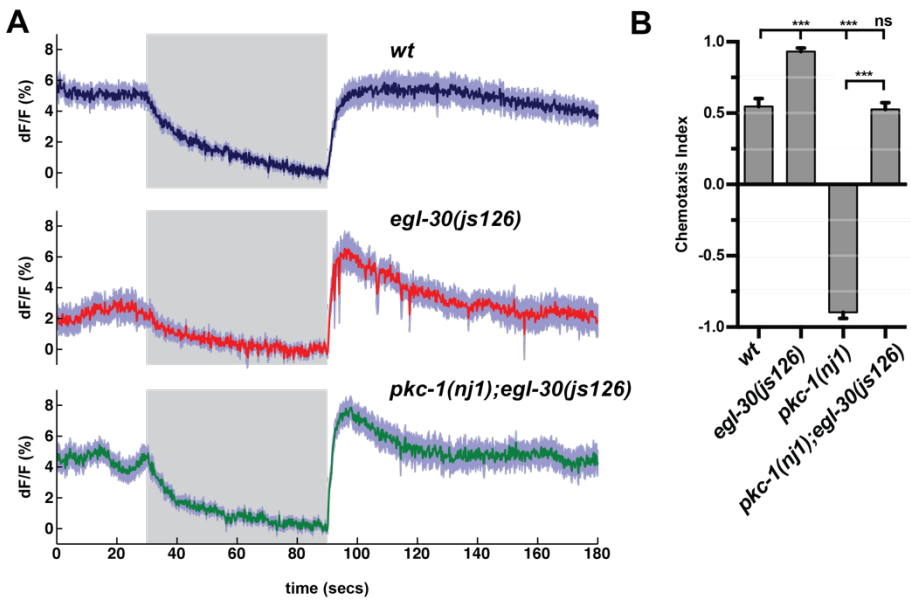

Figure 6.16. *egl-30(gf)* enhances AWC^{ON} glutamate release in *pkc-1(nj1)* mutants and restores butanone attraction. **(A)** AWC Vglut-pH responses to butanone stimulation. *wt* n = 14 trials from 5 animals, 1-3 trials each. *egl-30(js126)* n = 9 trials from 6 animals, 3 trials each. *pkc-1(nj1); egl-30(js126)* n = 25 trials from 9 animals, 1-3 trials each. Gray bar = 11.2 uM butanone. Shading = S.E.M. (B) Butanone chemotaxis. All genotypes are in the Vglut-pH imaging line background. *wt* n = 6, *egl-30(js126)* n = 6, *pkc-1(nj1)* n = 6, *pkc-1(nj1); egl-30(gf)* n = 7, population assays. Error = S.E.M. One-way ANOVA, Tukey correction. *** < 0.0001. ns= not significant.

Acute rescue of butanone repulsion in *pkc-1* by treatment with DAG agonist PMA

At the *C. elegans* NMJ, *egl-30* has been proposed to potentiate synaptic vesicle release in part by increasing DAG production. Diacylglyercol (DAG) is a lipid signaling molecule that activates PKCs and the active zone protein UNC-13, and DAG stimulates synaptic vesicle release in many systems (Hu et al., 2015; Lackner et al., 1999; Wierda et al., 2007). Repulsion to the AWC-detected odors isoamyl alcohol and benzaldehyde in *pkc-1(nj1)* mutants can be acutely rescued by treatment with PMA (phorbol 12-myristate 13-acetate), a small-molecule DAG analog (Okochi et al., 2005). We asked if PMA could rescue butanone attraction in *pkc-1(nj1)* mutants as reported for other AWC odors, an effect that is dependent on protein kinase C delta encoded by the gene *tpa-1* (Okochi et al., 2005). One-hour treatment of *pkc-1(nj1)* mutants with PMA was sufficient to restore butanone attraction, and this rescue required *tpa-1* (Fig 6.17A). To determine if PMA acts through *tpa-1* cell-autonomously in AWC^{ON}, we expressed *tpa-1* cDNA in AWC^{ON} in *pkc-1(nj1); tpa-1(k501)* double mutants and performed butanone chemotaxis assays with and without PMA treatment. Without PMA treatment, expression of *tpa-1* cDNA in AWC^{ON} had no effect on *pkc-1(nj1); tpa-1(k501)* butanone chemotaxis, but upon PMA treatment butanone attraction was restored (Fig 6.17B). This indicates that PMA can act cell-autonomously through *tpa-1* in AWC^{ON} to restore butanone attraction in *pkc-1(nj1)* mutants. We next asked if PMA treatment could restore AWC^{ON} Vglut-pH responses in *pkc-1(nj1)*.

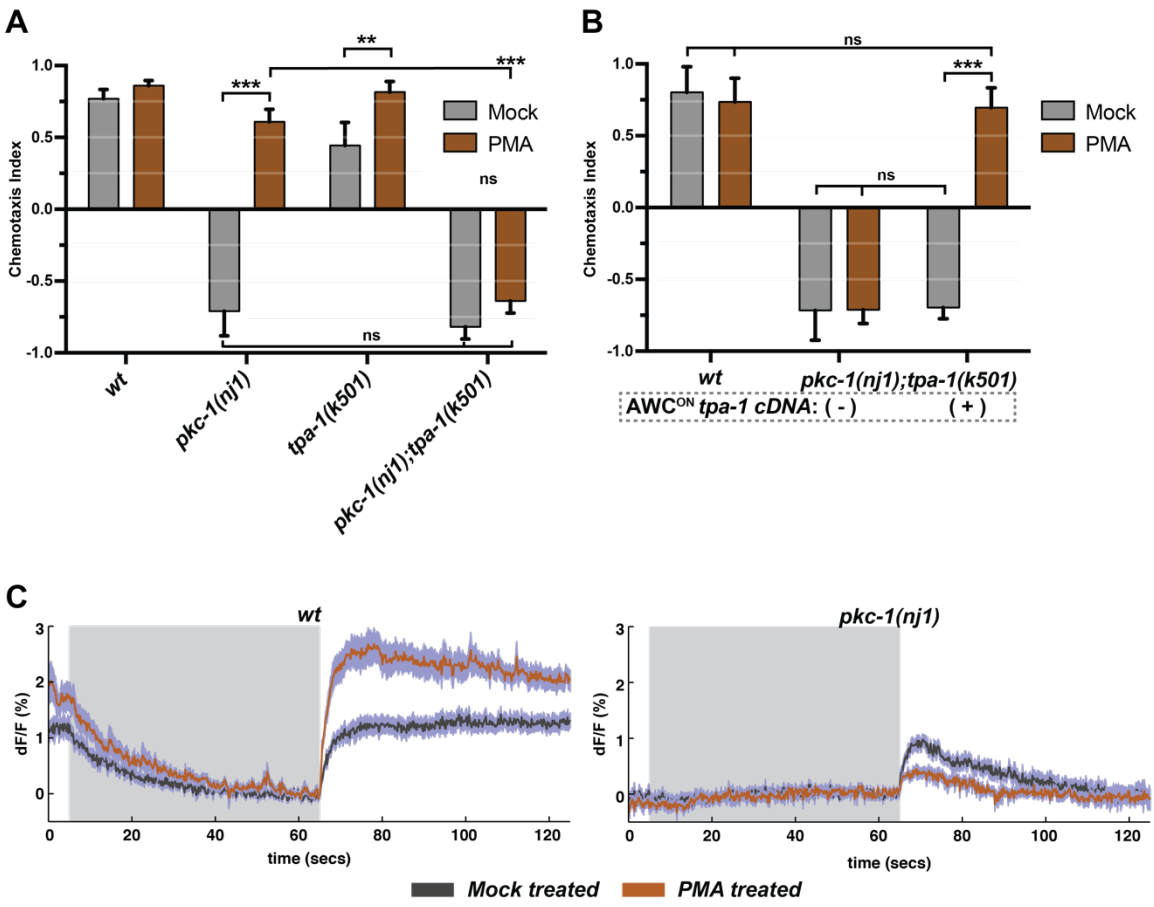

Figure 6.17. PMA treatment acutely rescues butanone attraction in *pkc-1(nj1)* mutants but does not rescue AWC^{ON} Vglut-pH defects.

(A) Butanone chemotaxis after 1 hour treatment with PMA. *wt* n = 6, *pkc-1(nj1)* n = 6, *tpa-1(k501)* n = 3, *pkc-1(nj1); tpa-1(k501)* n = 6, population assays. *** p <0.0001. ** = p <0.001, Two-way ANOVA with Tukey correction. Error= S.E.M. **(B)** Expression of *tpa-1.a* cDNA in AWC^{ON} using *str-2 promoter* restores action of PMA treatment. n = 6 population assays for all genotypes. AWC^{ON} *tpa-1 cDNA* = *str-2p:tpa-1.a cDNA* rescue. Two-way ANOVA, Tukey correction. *** p <0.0001. Error= S.E.M. **(C)** AWC Vglut-pH responses after 1-hour treatment with PMA or mock treated with DMSO. Mock treated: *wt* n = 21 trials, from 7 animals, 3 trials each. *pkc-1(nj1)* n = 18 trials from 6 animals, 3 trials each. PMA treated: *wt* n = 15 trials from 5 animals, 3 trials each. *pkc-1(nj1)* n = 27 trials from 9 animals, 3 trials each. Gray bar = 11.2 uM butanone. Shading = S.E.M. ns= not significant.

Wild-type animals treated with PMA for one hour had increased AWC^{ON} Vglut-pH responses to odor removal compared to mock-treated controls, but PMA treatment of *pkc-1(nj1)* mutants failed to restore Vglut-pH responses (Fig 6.17C). Therefore, the altered glutamate signaling in *pkc-1(lf)* mutants may not be identical to altered odor preference.

To address the relationship between glutamate release and behavior by another approach, we tested butanone preference in *pkc-1(nj1)* mutants lacking the major vesicular glutamate transporter, *eat-4* (Vglut-1 homolog). Animals that lack *eat-4* are weakly attracted to butanone in chemotaxis assays (Chalasani et al., 2007) (Fig 6.18). *pkc-1(nj1); eat-4(ky5)* double mutants still avoided butanone, although more weakly than *pkc-1* single mutants. Butanone attraction could be rescued in *pkc-1(nj1); eat-4(ky5)* double mutants by expressing a *pkc-1* cDNA in AWC^{ON}. Together, these results indicate that the defects in AWC^{ON} glutamate release via *eat-4* cannot fully explain changes in butanone olfactory preference. *pkc-1* likely regulates two processes in AWC^{ON}: *eat-4* dependent glutamate release and another form of synaptic output.

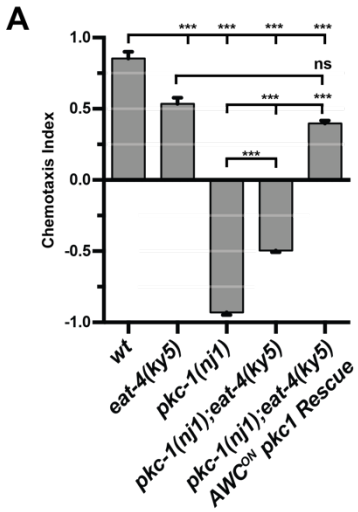

Figure 6.18. *eat-4*-dependent glutamate release is not required for *pkc-1(nj1)* induced changes in butanone preference.

(A) Butanone chemotaxis of indicated genotypes. n = 3 population assays per genotype. One-way ANOVA, Tukey correction. Error= S.E.M. *** = p <0.0001, ns= not significant

Butanone repulsion in *unc-31* mutants

pkc-1 regulates the release of dense-core vesicles at the *C. elegans* NMJ (Sieburth et al., 2007). It is possible that neuropeptides might be the other form of AWC^{ON} output regulated by *pkc-1*, and therefore important for specifying butanone preference. To test this hypothesis, we evaluated three mutants with broad defects in neuropeptide signaling: *egl-3, egl-21*, and *unc-31*. *egl-3* and *egl-21* encode enzymes that process several classes of neuropeptides (Li and Kim, 2008), and *unc-31* encodes the ortholog to the mammalian protein CAPS (calcium-dependent activator protein for secretion) required for dense-core vesicle exocytosis (Sieburth et al., 2007; Speese et al., 2007). Butanone chemotaxis was normal in *egl-3(ok979)* and *egl-21(n476)* mutants, but multiple *unc-31(lf)* alleles were strongly repulsed by butanone (Fig 6.19A-B). AWC^{ON} Vglut-pH responses were normal in *unc-31(e928)* mutants (Fig 6.19C), indicating that synaptic vesicle release was not affected and that butanone olfactory preference can be separated from AWC^{ON} glutamate release.

Treatment of *unc-31(e928)* mutants with PMA for one hour was able to restore butanone attraction, indicating that *unc-31* is not a required target of the PMA/*tpa-1* pathway that restores butanone attraction (Fig 6.19D). Expression of *unc-31.a* cDNA pan-neuronally rescued butanone attraction, as did expression under the *eat-4* promoter (labelling glutamatergic neurons), but we were unable to obtain rescue in AWC^{ON} under the *str-2* promoter (AWC^{ON}), the *cat-1* promoter (serotonergic, dopaminergic, and tyraminergic neurons), or the *glr-1* promoter (AIB and command interneurons) (Fig 6.19E).

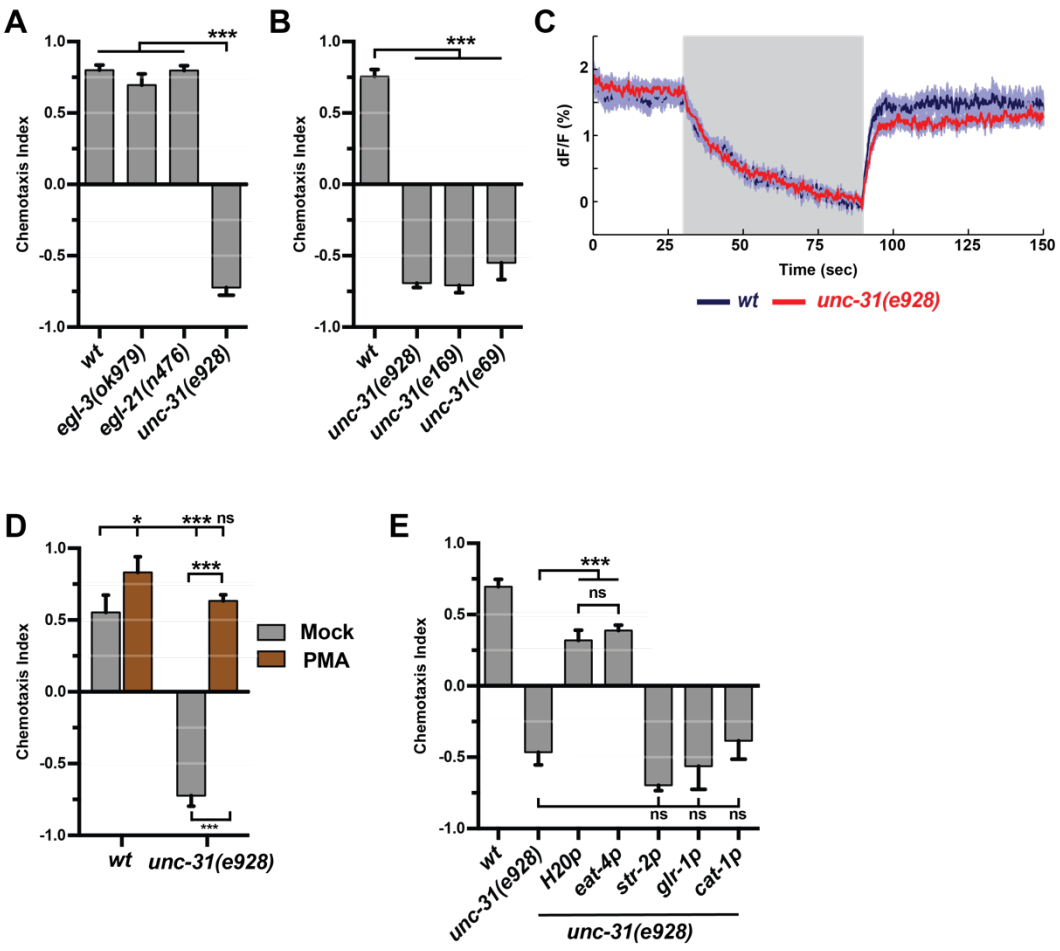

Figure 6.19. *unc-31* regulates butanone odor preference.

(A) Butanone chemotaxis of indicated genotypes. *wt* n = 9, *egl-3(ok979)* n = 6, *egl-21(n476)* n = 6, *unc-31(e928)* n = 3, population assays. *** p < 0.0001. One-way ANOVA, Sidak correction. Error= S.E.M. **(B)** Butanone chemotaxis of *unc-31(lf)* mutants. *wt* n = 6, *unc-31(e928)* n = 6, *unc-31(e169)* n = 3, *unc-31(e69)* n = 3, population assays. *** p <0.0001 One-way ANOVA, Sidak correction. Error= S.E.M. **(C)** AWC Vglut-pH responses in *unc-31(e928)* mutants. *wt* n = 25 trials, from 10 animals, 1-3 trials each. *unc-31(e928)* n = 42 trials from 14 animals, 3 trials each. Gray bar = 11.2 uM butanone. Shading = S.E.M. **(D)** Butanone chemotaxis of *unc-31(e928)* mutants treated with PMA for 1hr. All genotypes n = 3 population assays. *** p < 0.0001, * p <0.05 Two-way ANOVA, Tukey correction. Error= S.E.M. **(E)** Butanone chemotaxis of *unc-31* rescue strains. *wt* n = 9, *unc-31(e928)* n = 6, *H20p* rescue n = 6, *eat-4p* rescue n = 5, *str-2p* rescue n = 6, *glr-1p* rescue n = 2, *cat-1p* rescue n = 3, population assays. *** p <0.0001. * p = 0.012. Two-way ANOVA, Tukey correction. Error= S.E.M. ns= not significant.

Discussion

These results identify *pkc-1, gcy-28,* and *egl-30* as important regulators of AWC^{ON} synaptic release, and identify *unc-31* as an additional genetic determinate of butanone olfactory preference. *pkc-1* regulates *eat-4* dependent AWC^{ON} glutamate release and a second form of AWC^{ON} output that is important for specifying butanone olfactory preference. *pkc-1* has a different function in ASH neurons, where it maintains SV release across multiple stimuli. Below we discuss the role of *pkc-1* in the regulation of AWC^{ON} synaptic release, the regulation of butanone olfactory preference by *pkc-1, gcy-28,* and *unc-31,* and hypotheses to integrate our findings and provide a framework for future study.

The role of *pkc-1* in AWC^{ON} synaptic release.

pkc-1 is a critical regulator of AWC^{ON} glutamate release that functions downstream of odor-evoked calcium influx. The dynamics of AWC^{ON} Vglut-pH responses in *pkc-1(lf)* mutants and the epistatic interactions with *tom-1* and *egl-30* indicate that *pkc-1* is required for the release of SVs, rather than generating a general defect in SV maturation or endocytosis. In *pkc-1(lf)* mutants, AWC^{ON} SV release triggered by odor removal could only be detected after a long odor stimulus (60-second or 3-minute pulses), but not by short (10-second) pulses. Odor removal after longer odor pulses generates a large calcium influx in the axon that overshoots baseline calcium levels, suggesting that only during these brief periods of highly elevated calcium can SVs from AWC^{ON} be released in *pkc-1(lf)* mutants. It is possible that basal calcium levels in AWC^{ON} are not sufficient

to maintain tonic release in *pkc-1(lf)* mutants, and that higher levels of calcium are required for SV release. The enhanced odor-removal responses in *pkc-1(nj1); tom-1(ok285)* double mutants are consistent with this model, as *tom-1(lf)* strongly enhances the AWC^{ON} calcium response to odor removal (see chapter 3). We hypothesize that *pkc-1* regulates the calcium sensitivity of synaptic release in AWC^{ON}, a proposed PKC function in other systems as well (Yang et al., 2005; Yang et al., 2002; Yawo, 1999; Zhu et al., 2002).

egl-30(gf) can rescue AWC^{ON} Vglut-pH responses in *pkc-1(lf)* mutants, as well as butanone attraction. At the *C. elegans* NMJ, the genetic pathway underlying *egl-30* function in motor neurons uses canonical Gqα signaling through phospholipase PLCβ to produce DAG that regulates ACh release (Lackner, 1999; Mizuno and Itoh, 2009). As PMA was unable to restore AWC^{ON} Vglut-pH response in *pkc-1(nj1)* mutants, the mechanism by which *egl-30(gf)* restores AWC^{ON} Vglut-pH responses is unlikely to act solely through DAG production. PLCβ cleavage of PIP2 produces inositol trisphosphate (IP3) as well as DAG. IP3 regulates intracellular calcium stores and IP3 signaling increases cytoplasmic calcium by mobilizing intracellular calcium stores (Llano et al., 2000; Rizzuto and Pozzan, 2006). If *pkc-1* decreases the calcium sensitivity of SV release in AWC^{ON}, *egl-30(gf)* may restore AWC^{ON} SV release by elevating baseline cytosolic calcium levels through increased IP3 levels. This possibility could be examined by asking if an *itr-1(gf)* mutation (producing constitutive activation of the IP3 receptor) also rescues *pkc-1* (Baylis and Vazquez-Manrique, 2012). Interestingly, knockout of the synaptic vesicle calcium sensor

synaptotagmin-1 (*snt-1*) resulted in Vglut-pH signals that resemble those of *pkc-1(lf)* mutants in part (see Chapter 5). Perhaps *pkc-1* acts via *snt-1* to regulate the calcium sensitivity of synaptic release in AWC^{ON} (de Jong et al., 2016).

Vglut-pH responses in *gcy-28(lf)* mutants and *egl-30(lf)* mutants were similar, suggesting that decreases in both axonal cGMP and Gq signaling have the common effect of decreasing glutamate release. The Vglut-pH defects in these mutants preferentially affected the dynamics of the evoked response after odor removal: the fast phase appeared to be blunted and the transitional phase slowed. Both endocytosis and calcium responses were intact in *gcy-28(lf)* mutants.

AWC^{ON} glutamate signaling through EAT-4 vesicles is not the only mediator of butanone olfactory preference. First, both butanone avoidance and AWC^{ON}-specific rescue of butanone attraction in *pkc-1(lf)* mutants are intact in mutants lacking the vesicular glutamate transporter *eat-4.* Second, while *pkc-1(lf)* strongly alters the dynamics of glutamate release from AWC^{ON}, and this can be rescued by expressing a *pkc-1* cDNA in AWC^{ON}, defects in glutamate release remained after butanone attraction was restored by PMA treatment. Third, *unc-31* mutants did not have defects in AWC^{ON} glutamate release but are repulsed to butanone. Fourth, PMA treatment could rescue attraction in all mutants, strongly suggesting that the mutants share a common pathway in the regulation of butanone preference (discussed below).

In *pkc-1(lf)* mutants, AIB/AVA interneurons were unresponsive to butanone stimulation, which could reflect either a defect in AWC^{ON} signaling or a

change in network dynamics more generally. At a behavioral level, *pkc-1* has clear effects in AWC^{ON}. Animals expressing *pkc-1* dsRNAi in AWC^{ON} navigate away from butanone in gradients and fail to response to butanone on/off pulses with reversals. Odor preference remains a mystery, but could involve another class of glutamate vesicles, peptidergic vesicles, or the rare gap junctions formed by AWC.

The role of *pkc-1* in ASH nociceptive neurons

pkc-1 affected the sustained component of Vglut-pH responses in ASH neurons. The ASH Vglut-pH response to the first pulse of noxious NaCl stimuli was normal in each trial, but responses to subsequent stimuli within the trial were very weak, and in some cases undetectable. Adaptation to repetitive stimuli is a characteristic component of the ASH calcium response and ASH-directed behaviors as well (Hilliard et al., 2005; Kato et al., 2014). Our results from ASH Vglut-pH imaging suggest that *pkc-1* is required to maintain vesicle release across repeated stimuli, rather than directly disrupting ASH glutamate release. Notably, PKC epsilon (PKCε) is expressed in peripheral nociceptive neurons of mice and is involved in nociceptive sensitization through modulation of TRPV1 channels, likely through direct phosphorylation (Khasar et al., 1999; Numazaki et al., 2002; Premkumar and Ahern, 2000; Tominaga et al., 2001). ASH responses to osmotic stimuli utilize TRPV channels for signal transduction as well. To understand this process further, it will be helpful to examine ASH calcium

responses to repeated stimuli in wild-type and *pkc-1(lf)* mutant animals. The effect of *pkc-1(lf)* appears to be different between ASH and AWC^{ON}. Although, the inability of ASH to sustain release to repetitive stimulation has some parallels to the loss of basal (or sustained) release in AWC^{ON}, in ASH these effects were only temporary and release was restored after ~ 1-minute of inactivity. In contrast, suppressing AWC^{ON} activity for as long as 3 minutes did not restore of odor removal responses. This suggests that *pkc-1* may have distinct roles in AWC^{ON} and ASH, and may represent a case in which *pkc-1* has neuron-specific roles.

***pkc-1* and DAG act in parallel pathways to specify butanone attraction.**

egl-30(gf) restores butanone attraction in *pkc-1(nj1)* mutants and also restored Vglut-pH responses in AWC^{ON}. PMA treatment also restored butanone attraction in *pkc-1(nj1)* mutants, but was unable to restore AWC^{ON} glutamate release. These results suggest that two pathways are regulated by *pkc-1* in AWC^{ON}: one that affects the release of EAT-4 SVs and another, which is sensitive to DAG signaling, that regulates butanone chemotaxis preference (Fig 6.20). PMA rescue of butanone attraction through AWC^{ON} required protein kinase C delta (*tpa-1*), a direct target of DAG. Thus *tpa-1* likely acts downstream of DAG in this second pathway. As *tpa-1(lf)* mutants are still attracted to AWC-detected odors, *tpa-1* and *pkc-1* probably have overlapping roles in mediating attraction butanone (Okochi et al., 2005).

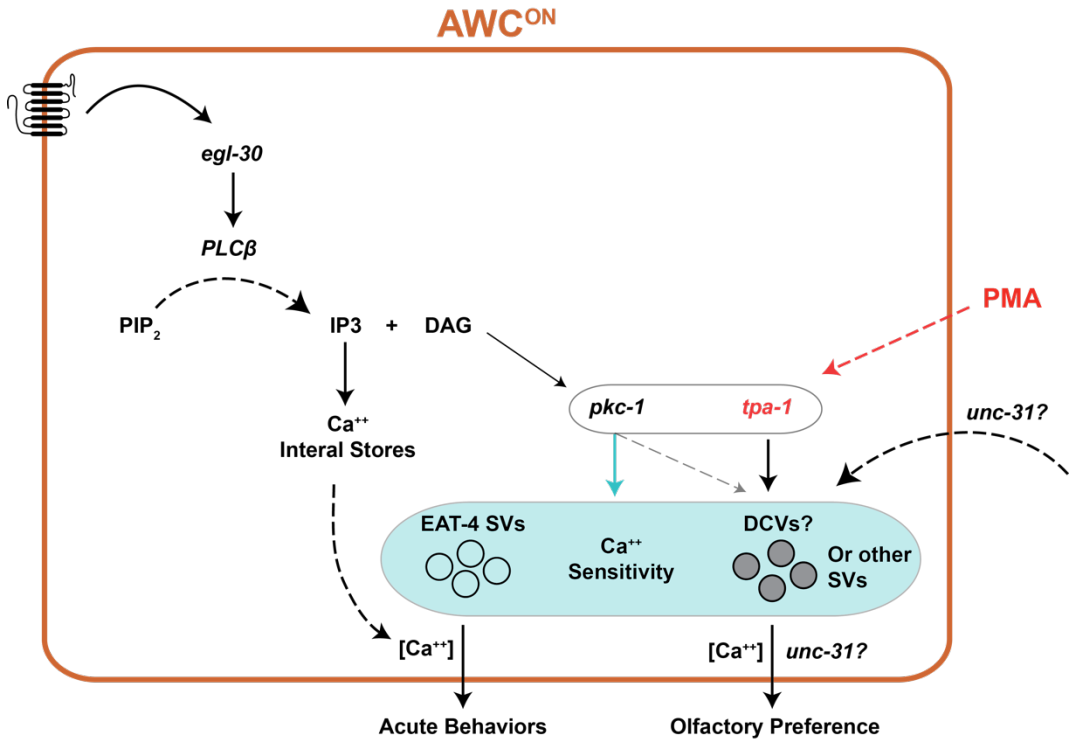

Figure 6.20. Cartoon of the hypothesized roles of *pkc-1* function in AWC^{ON}.

We hypothesize that *pkc-1* functions in AWC^{ON} to regulate the calcium sensitivity of both synaptic vesicles (SVs) and dense-core vesicles (DCVs) containing neuropeptides. AWC^{ON} glutamatergic output is envisioned to mediate responses to acute changes in odor concentrations, whereas neuropeptide secretion is used for setting odor preference. In the absence of *pkc-1,* increased DAG signaling (mediated by *tpa-1)* can specifically restore the DCV pathway. This restores butanone attraction, but leaves SV release defective, as observed when *pkc-1(lf)* mutants are treated with PMA. Activation of *egl-30* signaling produces both DAG and IP3. In *pkc-1(lf)* mutants, *egl-30* activation restores butanone preference through DAG and restores SV release through IP3 signaling that increase in cytosolic calcium levels, thus compensating for the decreased SV calcium sensitivity of *pkc-1(lf)* mutants.

pkc-1 is known to affect neuropeptide release, so DCV release may be the form of AWC^{ON} output that is used to generate butanone avoidance. This idea is further strengthened by the fact that neuropeptide signaling is a component of AWC^{ON} adaptation (Chalasani et al., 2010), which can also result in butanone avoidance (Tsunozaki et al., 2008). *unc-31/CAPS* regulates the secretion of neuropeptides (Berwin et al., 1998; Renden et al., 2001; Sieburth et al., 2007), and our finding that *unc-31* regulates butanone preference would support a role for neuropeptide secretion in butanone avoidance, but we were unable to localize *unc-31* function solely to AWC^{ON}. These results are difficult to interpret. In *gcy-28(lf)* mutants, butanone repulsion could be rescued with a cDNA encoding the *gcy-28.c* isoform when expressed pan-neuronally, but only a cDNA encoding the *gcy-28.d* isoform could rescue when expressed solely in AWC^{ON} (Tsunozaki et al., 2008). *unc-31* has many alternative isoforms, so a similar situation may be occurring and a more specific isoform may be required for its rescue in AWC^{ON}. Alternatively, *unc-31* could function in a non-cell-autonomous fashion to regulate AWC^{ON} odor preference. The mechanism by which *pkc-1* modulates neuropeptide release from motor neurons is not known, but it has been hypothesized that *pkc-1* may modify the calcium sensitivity of DCV release (Sieburth et al., 2007). For example, PKC phosphorylation of the t-SNARE SNAP-25 increases DCV calcium sensitivity in adrenal chromaffin cells (Nagy et al., 2002; Yang et al., 2002). This suggests that our hypothesis for *pkc-1* function in AWC^{ON} SV release could also extend to DCVs, providing a common

mechanism to link the regulatory role of *pkc-1* in glutamate release and olfactory preference in AWC^{ON}.

Thesis Closing Discussion

In this thesis, we used Vglut-pH to explore the presynaptic properties regulating glutamate release in the two sensory neurons AWC^{ON} and ASH. In part one, we show that Vglut-pH is a robust reagent and perform a series of experiments to validate the use of Vglut-pH imaging as a tool for measuring synaptic vesicle release and recycling in *C. elegans.* We characterize the dynamics of synaptic vesicle exo- and endocytosis, outline their dependence on the conserved synaptic vesicle machinery, and probe the calcium-dependence of synaptic vesicle release through the analysis of synaptotagmins. In part two, we utilize Vglut-pH imaging to investigate AWC^{ON} synaptic signaling pathways that modulate butanone olfactory preference. Our work supports a role for presynaptic diversity among distinct neuronal cell types in *C. elegans* and emphasizes that the presynaptic regulation of neurotransmitter release is an important component to specifying circuit function, especially in sensory cells.

Conserved or convergent synaptic signaling mechanisms

The initial characterization of AWC signaling revealed similarity to photoreceptor neurons of the vertebrate visual system: basal activity that is suppressed with stimulation, similar transduction machinery, circuitry that bifurcates into two streams of ON/OFF neurons, and common developmental control by otx-family Hox genes (*ceh-36* family) (Chalasani et al., 2007). We

found that these conserved or convergent attributes extend to the properties of neurotransmitter release as well. Here, we make the comparison with the measurements available from OFF bipolar cells, but these synapses are likely very similar to photoreceptors (Morgans, 2000). Both calcium influx at the synaptic terminals of AWC^{ON} measured with syGCaMP, and SV release measured using Vglut-pH, matched the dynamics of similar measurements made in OFF bipolar neurons (Chapter 1, Fig 10). The detailed components of exocytosis were also the same. Like OFF bipolar neurons, AWC^{ON} glutamate release had three exocytic components of release, each with qualitatively similar kinetics (Neves and Lagnado, 1999). Interestingly, genetic perturbations suggest that these three components likely represent distinct modes of release: *egl-30(lf)* and *gcy-28(lf)* disrupted the 'fast' phase of release, whereas *egl-30(gf)* and *tom-1(lf)* enhanced the fast phase. This suggests that specific components of exocytosis, in both AWC^{ON} and OFF bipolar cells, may be used to convey distinct types of information. Synaptic vesicle endocytosis in AWC^{ON} also mirrored OFF bipolar neurons, with each cell type having 'fast' and 'slow' modes of synaptic vesicle retrieval that are modulated in response to neuronal activity (Neves et al., 2001). Given the similarities between these two sensory synapses across multiple aspects of synaptic function, it is likely that many of the molecular components at these different synapses may be conserved. SV priming at photoreceptor and bipolar neurons of the mammalian visual system has been suggested to be largely independent of *Munc-13* (Cooper et al., 2012). In a similar vein, we found that some synaptic vesicle release can still be elicited from

AWC^{ON} in *unc-13(lf)* mutants, further supporting a likeness in molecular composition. Together, our examination of AWC^{ON} synapses paints a picture of either conserved or convergent function from neuronal differentiation and sensory transduction, all the way to synaptic signaling and circuitry. This highlights the possibility that the signaling mechanisms employed by these similar cell types likely represents an important form of sensory information processing that will be prevalent in many animals.

Synaptic diversity among *C. elegans* neurons

By examining mutants in the components that control synaptic vesicle fusion, we find that AWC, ASH, and the synapses of motor neurons at the neuromuscular junction (NMJ) are functionally distinct. At the level of core release machinery and its regulators, we find a variable synaptic dependency on *unc-13* and complexin-1 (*cpx-1)* mutants. As mentioned above, in *unc-13(lf)* mutants significant residual responses were found in AWC^{ON} but were not present in either ASH or the NMJ (Richmond et al., 1999), suggesting that AWC^{ON} has a distinct ability to prime some vesicles in the absence of *unc-13*. In *cpx-1(lf)* mutants, electrophysiologically-evoked synaptic release at the NMJ is strongly defective, but tonic release is greatly increased. In contrast, AWC^{ON} and ASH sensory stimulus-evoked release was increased. Although there are several potential interpretations to these results (see Chapter 3 discussion), these results suggest that the dependencies of synaptic release between these synapses are distinct.

AWC^{ON} and ASH synapses also appear to rely on specific synaptotagmins to different extents. AWC^{ON} basal release was highly dependent on *snt-1* whereas ASH exocytic responses were largely intact. These results highlight our findings from Chapter 1 in which AWC^{ON} and ASH appeared to have distinct transformations between calcium influx and synaptic release; AWC^{ON} had multiple components with distinct rates in its exocytic response to calcium influx whereas ASH appeared to have only a single component, dominated by a single rate. Similar to AWC^{ON}, synaptic release at the NMJ appears to be partially dependent on *snt-1* (Liewald et al., 2008; Nonet et al., 1993). These differences suggest that each of these synapses employ a unique combination of synaptotagmins to fine-tune their release, as proposed for neurons in other systems (Sudhof, 2002).

Our initial interest in comparing presynaptic release in AWC^{ON} and ASH originated from literature documenting the diversity of synaptic function in different cell types (Atwood and Karunanithi, 2002). AWC^{ON} and ASH are both glutamatergic chemosensory neurons with some overlapping postsynaptic partners, but they regulate very different types of behaviors. ASH initiates fast escape behaviors, whereas AWC mediates slower behaviors required for gradient navigation (Bargmann, 2006). Our results, although not directly linked to behavior, support that glutamate release has distinct features in these neurons that are likely important for mediating their respective behaviors. For example, AWC^{ON} basal release, promoted by *snt-1* function, may be important for mediating synaptic release necessary for chemotaxis. In ASH, the strong calcium

responses elicited by nociceptive stimuli may make *snt-1*-mediated synaptic release dispensable for triggering escape behavior. Future work using cell-specific manipulations could address these types of hypotheses. Our comparative analysis of presynaptic function in AWC^{ON} and ASH suggests that diversity at the level of presynaptic release could be a general feature of the nervous system. In combination with the *C. elegans* synaptic wiring diagram, characterizing the presynaptic properties of additional neurons will add important functional information to the anatomical map of synaptic connections. *C. elegans* has a unique potential to provide a deeper understanding of how presynaptic diversity, both in terms of molecular components and activity dynamics, contribute to nervous system function.

Presynaptic modulation for altering circuit function

In part two of this thesis, we investigated how *pkc-1(lf)* switches AWC^{ON} butanone olfactory preference. We show that *pkc-1* acts in AWC^{ON} downstream of calcium influx to modulate glutamate release and another form of AWC^{ON} output that is important for setting butanone preference. Based on epistatic interactions with other synaptic regulators, we put forth the hypothesis that *pkc-1* functions to modulate the calcium-sensitivity of synaptic release and provide a model for its interaction with several other signaling pathways that modulate AWC^{ON} output. Furthermore, we show that *pkc-1* has neuron-specific signaling roles, as changes in ASH glutamate release were significantly different from AWC^{ON}. This again highlights the role of diversification in synaptic function; ASH

glutamate release is not dependent on the same *pkc-1* signaling pathway necessary to maintain glutamate release in AWC^{ON}.

Several forms of sensory neuron preference plasticity in *C. elegans* rely upon a DAG/*pkc-1* signaling pathway that has been hypothesized to modulate synapses (Adachi et al., 2010; Luo et al., 2014; Okochi et al., 2005; Tsunozaki et al., 2008). A major finding from our work is that these pathways do indeed modulate the dynamics of synaptic release downstream of primary sensory transduction. In the case of our work in AWC^{ON} butanone preference, changes in preference do not seem to be correlated with changes in SV release but another form of AWC output (possibly neuropeptides). As *pkc-1* has neuron-specific signaling roles, it will be interesting to see if the DAG/*pkc-1* pathway is similarly utilized in other sensory neurons to modulate preference. We suggest that the use of intracellular signaling pathways to tune neuron output downstream of primary sensory transduction may be an important mechanism for modulating sensory encoding.

Outlook

The work presented in this thesis outlines a new role for *C. elegans* as a model system to study the *in vivo* dynamics of synaptic vesicle (SV) release and recycling, from within intact neural circuits, at single cell resolution. This should provide many research opportunities, for not only synaptic biologists, but also those interested in exploring the roles of synaptic modulation on circuit function.

Our work points to roles for presynaptic diversity and regulation as an important mechanism for nervous system function. This could be explored further through several avenues. Exploring glutamate release in other neuronal cell types, such as interneurons like AIB, AVA, and RIM will provide an interesting comparison to the distinct types of release we observe in AWC^{ON} and ASH. Furthermore, neurons like AVA and RIM make presynaptic contacts to a diverse set of cell types, such as other interneurons, sensory neurons, and even muscle cells in the case of RIM (White et al., 1986). With the ability to acquire signals along the axon, it will be interesting to ask here if there are target-dependent differences in the dynamics or requirements for neurotransmitter release, as has been observed in *in vitro* systems (Branco and Staras, 2009). A related avenue is to explore is the release dynamics of different SV pools (Alabi and Tsien, 2012) or SVs containing different neurotransmitters from within the same neuron. The advent of red-shifted pHluorins should permit multimodal imaging at the synapse, where SV release and calcium responses, or the release of two different classes of vesicles, could be imaged simultaneously (Kavalali and Jorgensen, 2014).

At the molecular level, there is a clear diversity in the composition of synapses indicated by the differential expression of distinct proteins or distinct protein isoforms (Atwood and Karunanithi, 2002). The power of *C. elegans* genetics in combination with pHluorin imaging techniques may provide a useful platform of the identification of new regulators of SV release and recycling. Although pHluorin imaging needs to be conducted at high resolution, at the level of a single animal, the ability to obtain single trial recordings with the resolution to

discern meaningful dynamics means that candidate-based genetic screens for synaptic phenotypes can be conducted. A single neuron RNAseq protocol has been developed in our lab (Steve Flavell, Christine Cho, unpublished) providing a powerful method for designing such pHluorin imaging, candidate-based, genetic screens for synaptic phenotypes. Furthermore, to assess the roles of specific isoforms, more precise genetic lesions need to be made. These are now obtainable through the CRISPR/Cas9 mutagenesis protocol (Arribere et al., 2014) that we used to create the putative *snt-3* null mutation. This more refined approach should provide many new insights into synaptic function and the roles of presynaptic diversity.

Methods

C. elegans culture

All *C. elegans* strains were maintained under standard conditions and fed OP50 bacteria (Brenner, 1974). OP50 cultures were grown from a single colony by inoculation into 100 mL of LB and grown for 24-36 hours at room temperature (20-22°C). Wild type animals correspond to the Bristol strain N2. Transgenic lines were generated using standard injection methods: Young adult hermaphrodites were injected with the desired transgene and a co-injection plasmid that expresses a fluorescent marker. In some cases, empty vector was included to increase the overall DNA concentration to a maximum of 100 ng/ul.

Imaging activity-dependent fluorescence reporters.

For all imaging experiments presented in this thesis, imaging was conducted in custom-built microfluidic chambers designed for calcium imaging (Chronis et al., 2007). Animals were age-synchronized by picking L4s onto fresh NGM OP50 seeded plates 12-18 hours before experiments. Imaging experiments were conducted in S basal buffer (Brenner, 1974). To further prevent animal movement during imaging experiments, animals were paralyzed with 1 mM (-)-Tetramisole hydrochloride (Sigma-Aldrich) during acquisition. Tetramisole was not used in interneuron imaging experiments. After loading in the microfluidic chambers, all animals were allowed to acclimate for 5 minutes before imaging. For all recordings of AWC^{ON} activity, animals were starved for 20-30 minutes in

an S basal bath prior to loading into the microfluidic chamber. For all recordings of ASH activity, a 90-second recording was performed before any stimulation to allow animals to adapt to the blue light used for imaging. TIFF time-stacks were acquired at 5 frames per second (fps) using a 200 msec acquisition time. Images were acquired using a 100x objective on an Andor iXon+ camera with Metamorph 7.7.6 -7.7.8 acquisition software (See also Supplemental Methods). For interneuron imaging and AWC^{ON} GCaMP5 cell body recordings, TIFF time-stacks were acquired using a 40x objective at 10 fps, 100 msec acquisition-time. Data analysis is described in Supplemental Methods.

Stimulus triggering was performed through Metamorph via digital input from a National Instruments NI-DAQmx box to an Auotmate Valvebank 8 II actuator that triggered Lee Corporation solenoid valves. Custom journals specified pre-programmed recording parameters and performed automated file naming and storage. Most stimulation protocols involved multiple trials per animal, as detailed in figure legends. The interval length for all trials was 30 seconds in addition to the time recorded before or after the stimulation. For AWC^{ON} recordings in which the pulse length was varied, stimulation was ordered sequentially as follows: 6 trials of 10-second pulses, 3 trials of 60-second pulses, and a single 3-minute pulse.

Butanone (Sigma) or NaCl (Fisher) stimuli were prepared fresh on the day of the experiment from pure stock solutions. Stimuli and control solutions were prepared in S basal buffer, in amber glass vials. For butanone odor dilutions, 11.2 uM butanone was prepared by serial dilution (30 ul in 30 mL S basal buffer) in amber glass vials. Control buffer and stimuli were delivered via reservoirs made from 30 mL syringes (Fisher).

Statistical Analysis and curve fitting.

All statistical tests are indicated in figure legends and were performed using Prism 6 GraphPad software.

All fitting of decay curves was performed in Matlab using the 'fit' function with a custom 'fitType' equation. For single exponential fits fitType = a1*exp (-x/tau1) + C. For double exponential fits fitType = a1*exp (-x/tau1) + a2*exp (-x/tau2) + C. For triple exponential fits fitType = a1*exp (-x/tau1) + a2*exp (-x/tau2) + a3*exp (-x/tau3) + C. In each case, all 'a' and 'tau' variables are fitted parameters and are constrained to be > 0. C = the baseline to which traces decayed. Unless stated otherwise, fitting was applied to the entire decay period of the trace. For AWC^{ON} this corresponds to the odor-addition phase. For ASH, this corresponds to the 20 seconds immediately following stimulus removal. For comparison of AWC^{ON} decays with different stimulus durations (i.e. 60-second vs 20-second), we fit both traces using the initial 20-seconds to keep comparisons consistent. Decay

constant averages reported for a given condition were performed as follows: Each individual trace for a given data set was fitted individually. Each fit was then plotted on its trace and then inspected. Traces that could not be fit due to high noise or did not exhibit a decay were removed from the analysis. The decay constants for each condition were then collected and exported to Prism 6 for statistical analysis.

Comparing exponential fits using AIC_C.

To compare the different exponential models we fit to our data, we used the Akaike's Information Criterion (AIC) as described in (Motulsky and Christopoulos, 2004): AIC = $N * \ln\left(\frac{SS}{N}\right) + 2K$, where N = number of data points, K = number of parameters, and SS= is the sum of the square of the vertical distances of the points from the curve. We used the corrected version for small N: $AIC_C = AIC + \frac{2K(K+1)}{(N-K-1)}$. AIC_C was performed for the fit on each individual trace. To determine of the relative likelihood of two models, we computed the probability that one model is more likely than the other (AIC_P): $AIC_P = \frac{e^{-0.5\Delta}}{1+e^{-0.5\Delta}}$, where Δ = the difference in AIC_C scores. All AIC based analysis was conducted in Matlab using custom scripts.

Microfluidic behavioral assays

Microfluidic gradient and pulse behavioral assays were conducted as described in (Larsch et al., 2015) and analyzed in Matlab using software designed by (Albrecht and Bargmann, 2011). Groups of 20-30 animals were loaded into each chamber of the device and allowed to acclimate for 30 minutes before stimulation. Dye was used to confirm proper flow and rate at the end of each assay, which was stable throughout our experiments. Butanone odor was prepared as described for imaging experiments.

Butanone chemotaxis assays

Butanone chemotaxis assays were conducted on square plates containing 20 ml chemotaxis agar (1.6% Agar, 5mM potassium phosphate buffer pH 6.0, 1 mM $CaCl_2$, 1 mM $MgSO_4$) poured 18-24 hours before the assay. Adult animals were removed from NGM growth plates with chemotaxis buffer (5mM potassium phosphate buffer pH 6.0, 1 mM $CaCl_2$, 1 mM $MgSO_4$) and transfer to 1.5 ml microcentrifuge tubes (Eppendorf). After 4 minutes, the supernatant was aspirated off and the tube filled with chemotaxis buffer. This process was repeated two additional times (3 washes total). During the second wash phase 1 ul of 1 M sodium azide was spotted to the locations where odor and control spots will be placed to immobilize animals that reach odor sources. After washes a drop of chemotaxis wash buffer containing ~100-350 animals was spotted onto the center of chemotaxis plate. Two 1 ul spots of butanone diluted in ethanol

were place on one side of plate (each 1 ul drop spaced apart vertically). On the other side of the plate, two 1 ul spots of ethanol control were added. The liquid drop contain the animals was then wicked away using a KIM wipe and the plate turned upside down, starting the assay. Assays were allowed to run for 1 - 2 hours and then moved to 4°C to stop the assay. Unless otherwise noted, the butanone dilution was 1:1000. Chemotaxis was quantified by counting the animals that had left the origin on each side of the plate and in the middle and calculating the chemotaxis index = (# Odor side – # Control side) / Total # counted animals.

PMA treatments

PMA (Phorbol 12-myristate 13-acetate) (Sigma) was prepared by diluting the stock drug in DMSO. Treatments for chemotaxis assays were conducted as follows: Adult animals were washed from growth plates in S basal buffer containing 1 ug/ml PMA. Animals were washed once more with S basal buffer containing 1 ug/ml PMA (as described for chemotaxis assays) and then transfer to 2 ml glass vials (VWR 66009-556). Vials were then laid on their side and gently rocked, once every 15-20 minutes. After 1 hour of treatment in PMA, animals were washed in chemotaxis buffer three times and chemotaxis was performed as described for normal chemotaxis assays. Mock controls (DMSO solvent lacking PMA) were conducted together with PMA treatments in the exact same manner.

For PMA treatments in Vglut-pH imaging experiments, 10-20 animals were picked from growth plates to an unseeded NGM plate and allowed to crawl away from food (1 – 2 minutes) and then were transferred to 2 ml glass vials containing 1 ml of S basal buffer with 1 ug/ml PMA or DMSO (mock control). Vials were then laid on their side and gentled rocked, once every 15-20 minutes. After 1 hour of treatment, animals were then transferred to an unseeded NGM plate containing a pool of S basal buffer. Based on chemotaxis assays, PMA's effect on behavior (after 1-hour of PMA treatment) lasts at least 2 hours. Two animals from each group of PMA treated and mock controls were then tested. Imaging was completed within 1-hour post treatment. This process was repeated for replicate animals.

Vglut-pH construct

To create the Vglut-pH expression construct we subcloned super-ecliptic pHluorin into the first luminal loop domain of the *C. elegans* vesicular glutamate transporter *eat-4.* This was done based on to homology the mammalian homolog of Vglut-1 and performed as described in *Volgmarier et al, 2006* (Voglmaier et al., 2006). Using site-directed mutagenesis (Stratagene quickchange protocol) we inserted a *kpn-1* restriction site into the *eat-4.a* cDNA (wormbase CDS ZK512.6a) in-between two conserved glycine residues (AA positions 106-107) corresponding to the pHluorin insertion site used in *Volgmarier et al, 2006.*

Super-ecliptic pHluorin was PCRed using the primers below, which adds a 14 amino acid linker used in *Volgmarier et al, 2006.* This PCR product was subcloned into the *Knp1* restriction site of the modified *eat-4 cDNA* contained in a pSM expression vector.

Forward:

'5-GAATCGTAGGTACCTCTACCTCTGGAGGATCTGGAGGAACCGGAGG

ATCTATGGGAAGTAAAGGAGAAGAACTTT-3'

Reverse:

'5-GAATCGTAGGTACCTCCGGTTCCTCCAGATCCTCCGGTTCCTCCGG

TTCCTCCACCGGTTTTGTATAGTTCATCCA-3'

For AWC^{ON} expression the *str-2* promoter was cloned into the pSM Vglut-pH construct using the standard Asc-1/Fse-1 restriction sites. For ASH expression we used the *sra-6* promoter.

Synaptically localized GCaMP3 (syGCaMP) construct

syGCaMP was created by fusing GCaMP3 to the C-terminus of synaptogryin-1 (*sng-1)*. *sng-1 cDNA* (wormbase CDS T08A9.3) was isolated from a N2 whole worm cDNA library and subcloned into a pSM expression vector containing GCaMP3 using AflII and SacII restriction enzymes. *sng-1* was fused to GCaMP3 through a 6x Glycine-Serine linker. GCaMP3 cDNA was kindly provided by Loren Looger. *sng-1* cDNA isolation primers:

Forward: *5'- CAAATGATGACAGCGAAGTGGCTTAAGCATGGTATTGATAT*

CTGAGC-3'

Reverse:*5'- GAATCGTACCGCGGGAACCACTACCACTACCATAACCATATCCT*

TCCGACTGA-3'

For AWC^{ON} expression the *str-2* promoter was cloned into the pSM Vglut-pH construct using the standard Asc-1/Fse-1 restriction sites.

Extracellularly localized pHluorin (CD4-pH) construct

Super-ecliptic pHlourin was localized to the extracellular surface by fusion to the C-terminus of a modified form of CD4 described by (Feinberg et al., 2008). CD4-pH was produced by exchanging the spGFP 1-10 in the pSM vector CD4-2::spGFP1-10 (Feinberg et al., 2008) for super-ecliptic pHlourin using the restriction sites Nhe1 and Sal1. The inserted super-ecliptic pHlourin contained the N-terminal linker domain: Gly-Gly--Gly--Gly--Gly-Ser-Gly--Gly--Gly--Gly-Ser. Super-ecliptic pHlourin was amplified with the following primers:

Forward: ‘5-GAATCGTAGCTAGCATGGGAAGTAAAGGAGAAGAACTTT-3'

Reverse: ‘5-GAATCGTAGTCGACCGAGCCTCCACCTCCACTTCCGCCGCC

ACCACCGGTTTTGTATAGTTCATCC-3’

AWC^{ON} pkc-1 dsRNAi Knockdown

Cell-specific dsRNAi knockdown followed the method outlined by (Esposito et al., 2007). The *pkc-1* dsRNAi target sequence (wormbase reagent ID: sjj_F57F5.5) was chosen based on (Sieburth et al., 2005). This sequence corresponds to the genomic sequence of *pkc-1* encompassed between the flanking primers:

Forward: *'5-GATCATCTTCATTGTCAGCTTCA-3'*

Reverse: *'5-GAGACAAAGGCGCGGTG-3'*

This *pkc-1* genomic PCR product was then fused to the *str-2* promoter in both sense and anti-sense orientation using PCR fusion as described in (Hobert, 2002). Primers for creating the *str-2* promoter PCR products for fusion are:

str-2 forward: *'5-CTTCGCTGCCCCAATTAAAG-'3*

str-2 reverse (sense): *'5-*

GACAACCACCATTTGAAGCTGACAACAGTCGGCATTTTTATG

GATC-3'

str-2 reverse (anti-sense): *'5-*

TAAGCACCTAATTTGAATCACCGCGCAGTCGGCATTTTTATG

GATC-3'

Isolation of cDNA used in rescue experiments

All cDNA was isolated from N2 whole worm cDNA libraries and subcloned into the pSM expression vectors.

pkc-1.a cDNA. Wormbase CDS F57F5.5a. Subcloned with Nhe1 and Kpn1 restriction sites. Isolation primers:

Forward:

'5-GAATCGTAGCTAGCATGCTGTTCACAGGCACCGTGC-3'

Reverse:

'5-GAATCGTAGGTACCTTAGTAGGTAAAATGCGGATTGA-3'

tpa-1.a cDNA. Wormbase CDS B0545.1a. Subcloned with AflII and Kpn1 restriction sites. Isolation primers:

Forward:

'5-GAATCGTACTTAAGATGGCACAGGCTGAGAATG-3'

Reverse:

'5-TTCCAATCGGTACCCTATTTTGAGAAGTGAGGATTCG-3'

unc-31.a cDNA. Wormbase CDS ZK897.1a. Subcloned with Nhe1 and Kpn1 restriction sites. Isolation primers:

Forward:

'5- GAATCGTAGCTAGCATGTTAGGAGCAAGTAGTAGTGAAGAA-3'

Reverse:

'5-GAATCGTAGGTACCTTAATGTTTTCGTATACCTTCTTGAA-3'

Generation of *snt-3(ky1034)*

The *snt-3(k1034)* null allele was generated through CRISPR/Cas9 mutagenesis using the coCRISPR protocol developed by (Arribere et al., 2014). Young adult animals were injected with a mixture of plasmids containing Cas9, *rol-6* guideRNA, ssDNA template for inducing a dominate *rol-6(su1006)* mutation, and the guideRNA targeting the first exon of *snt-3*. F1 animals with the roller phenotype were isolated, allowed to produce progeny, and then were screened for a mutation in the *snt-3* target region by Sanger sequencing. The *snt-3(ky1034)* mutant strain was allowed to segregate from the dominate *rol-6(su1006)* mutation and then was crossed into our ASH Vglut-pH imaging line (CX16921).

Supplemental Methods

Microscope optimization for Vglut-pH Imaging

All imaging was conducted on a Zeiss Axiovert 100TV wide-field microscope. Images were acquired through a 100x 1.4NA Zeiss APOCHROMAT objective onto an Andor ixon+ DU-987 EMCCD camera. Camera settings: 14-bit EM-GAIN enable digitizer (3MHz). Baseline clamped. Overlapped recording mode. 0.3 uS vertical clock speed. Binning = 1. Images were cropped to fit around the head of animal. Most experiments used a pre-amplifier gain of 5x. Illumination: Lumencore SOLA-LE solid-state LED lamp. Illumination input was passed through a 1.3 ND filter. Narrow bandwidth blue light illumination (484-492 nm) was produced using the CHROMA 49904-ET Laser Bandpass filter set (%T 90>).

Quantification of fluorescence changes

dF/F was calculated as:

$$\text{Eq 1. } \frac{dF}{F_o}(t) = \left(\frac{\mathrm{F(t)} - F_o}{F_o}\right)$$

Where F (t) = is the fluorescence of a ROI minus the background at time (t) and F_o = fluorescence of the ROI minus the background at some reference time point or value.

For AWC^{ON}, F_o was chosen to be the mean background corrected signal 2-seconds before odor removal. We chose to do this because AWC^{ON} pre-stimulus activity levels are variable, whereas activity levels during the odor stimulus were stable and consistent (Suppl. Fig 1). For stimulation protocols that included multiple stimuli during the trial, F_o was determined by the first stimulus.

For ASH recordings, F_o was set to the mean background corrected signal 2-seconds before the first stimulus for each trial.

For AIB, AVA, and AIY recordings, F_o was set to the mean of the lowest 10% of background corrected intensity measurements.

Acquisition of Fluorescence Measurements

To extract fluorescence measurements from Vglut-pHluorin images, we developed custom semi-automated tracking software in ImageJ. Images were first corrected for x-y drift using image registration, which places the axon at a specific set of image coordinates for the entire recording by shifting each frame in x and/or y. The microfluidic device prevents most z-plane drift, but images in which significant z-plane drift was detected were discarded. To aid in axon selection, images underwent rolling-ball background subtraction and then were averaged over space (2 pixels in x and y) and time (average of time-stack). The

entire segment of the axon that was in view was then specified by the user and outlined by hand with the aid of pixel intensity thresholding. From this axon outline, intensity and pixel information was extracted from the raw drift-corrected recording along with local background measurements along the axon (Suppl. Fig 2). This process was also used to acquire measurements of AWC^{ON} syGCaMP images. For ASH, the *sra-6p* promoter is also expressed in the neurons ASI and PVQ, the axons of which are posterior to the ASH axon. Vglut-pH fluorescence could also be detected in these other axons (mainly PQV) but did not significantly respond to stimulation. In any given experiment, we recorded Vglut-pH signals from a single ASH axon, either the on right or left side of the animal. Because of ASI and PVQ Vglut-pH fluorescence, only the anterior background ROIs were used in analysis of ASH Vglut-pH recordings.

For cell body measurements of GCaMP responses in AWC^{ON}, ASH, AIB, and AVA we used a custom written Image-J script designed by (Gordus et al., 2015) to track cell body position, and extract intensity measurement. For AIY GCaMP recordings we also used this Image-J script, but tracked the axonal process of the AIY neuron closet to the objective.

Vglut-pH fluorescence changes along the axon

To validate using the whole axon segment as a single integrated measurement in Vglut-pH experiments we measured Vglut-pH responses from small equally spaced ROIs along the axon. These were produced by taking the outlined axon segment as in (Suppl. Fig 2D) and cutting the axon into smaller ROI segments, each 8 pixels long in the y-axis. Although, we could detect some differences in magnitudes between ROI regions, all regions appeared to reflect the integrated mean activity of the axon quite well. This appeared true for all genotypes and conditions we tested in this thesis. To assess this more quantitatively, we performed a correlation analysis on a large dataset of AWC^{ON} Vglut-pH recordings from wild-type animals that were stimulated with a 60-second pulse of 11.2 uM butanone (data mostly from Chapter 1, Fig 3D). For 120 stimulated axons, we measured the correlation between ROIs along the axon, with the signal from the mean integrated axon (Suppl. Fig 3). We found that all regions were positively correlated, indicating that with our resolution, variation along the axon is not a significant factor affecting Vglut-pH measurements.

Exclusion of non-responders in Vglut-pH experiments

Non-responding trials in certain cases were removed from the average to more accurately reflect the dynamics of Vglut-pH signals that did occur. For all cases in which a trial was excluded it is indicated in the corresponding figure legend. Non-responders were selected by the user following a strict guideline: only traces that

did not show any stimulus correlated changes (above baseline noise) were excluded. Examples of such cases are presented in (Suppl. Fig 4).

Background Correction of VGlut-pHluorin Signals

Vglut-pH has a low baseline signal that is relatively close in intensity to the background auto-fluorescence generated by the surrounding tissue of the head. This became problematic when attempting to apply background subtraction and perform comparisons of fluorescence change. Most commonly, this is done with the deltaF function (dF/F) described above (Eq.1). The deltaF function normalizes the fluorescence change to its baseline intensity, allowing a comparison of signal changes between conditions with different absolute values. However, the deltaF function is highly sensitive to fluctuations in F_o when F_o is small. For a given change in fluorescence signal, the deltaF function changes by the square of F_o.

$$\text{Eq. 2} \quad \frac{df}{dF_o} = \frac{\Delta F}{F_o^2}$$

Where f is the deltaF function (Eq.1), ΔF = fluorescent signal change, and F_o = baseline axon intensity.

Given the average signal change produced by Vglut-pH, as F_o approaches less than 200 a.u. the change in deltaF per axon intensity unit unacceptably becomes large (Suppl. Fig 5A). For Vglut-pH, a further confound is created by reporter

localization to parts of secretory pathway(s) that do not participate in synaptic release. These can be seen as small puncta that do not contribute to Vglut-pH responses and, in rare events, these puncta can be observed undergoing translocation within the axon towards the cell body. These contribute to F_o but not to fluorescence changes. To prevent background correction from shifting F_o into a realm where small variations in F_o generate large fluctuations in deltaF, we subtract only the fluctuations in the background signal.

$$\text{Eq 3. } BG_{Delta} = BG - BGmin$$

Where BG = the background and $BGmin$ = the minimum background value during the recording.

This approach allows for the correction of fluctuations in illumination during the recording, but preserves the majority of the pixel intensity value of the axon. Using this method removes background fluctuations in VGlut-pH signals and prevents the shift in F_o that generates large deltaF variance (Suppl. Fig 5B and Suppl. Fig 6). This procedure cannot account for changes to overall background levels, which could also contribute to differences in deltaF magnitudes. However, when we separately tested for correlations between the deltaF magnitude and axon baseline intensity, we did not find any cases where the baseline intensity could account for changes in deltaF magnitudes. Furthermore, using the BG_{Delta} method we did not detect correlations between the measured background and DeltaF response magnitude (Suppl. Fig 5C).

Bleaching Correction of Vglut-pHluorin Recordings

Vglut-pH has very slow bleaching kinetics (Ariel and Ryan, 2010; Balaji and Ryan, 2007), essentially showing little to no bleaching over the time-course of our recordings. This is likely the result of the reporter existing mainly within synaptic vesicles in the quenched state, and the rapid cycling of the fluorescent form back into this state. Unlike the Vglut-pH reporter, background auto-fluorescence does show significant bleaching, and there were cases where the background appears to bleach independently from the axon. When this occurs, using this background signal for correction can result in an artificial increase in the Vglut-pHuorin signal over time. To avoid this artifact effect, we corrected the background bleaching before performing our background correction in these instances (Suppl. Fig 7). Bleaching was assumed to be approximately linear and was modeled by line fitting using the Matlab function ‘polyfit.’ A threshold for specifying significant bleaching was set to a 0.5% drop in mean fluorescence intensity over 2 minutes of recording time. Bleaching was corrected by subtracting the linear fit from the background signal.

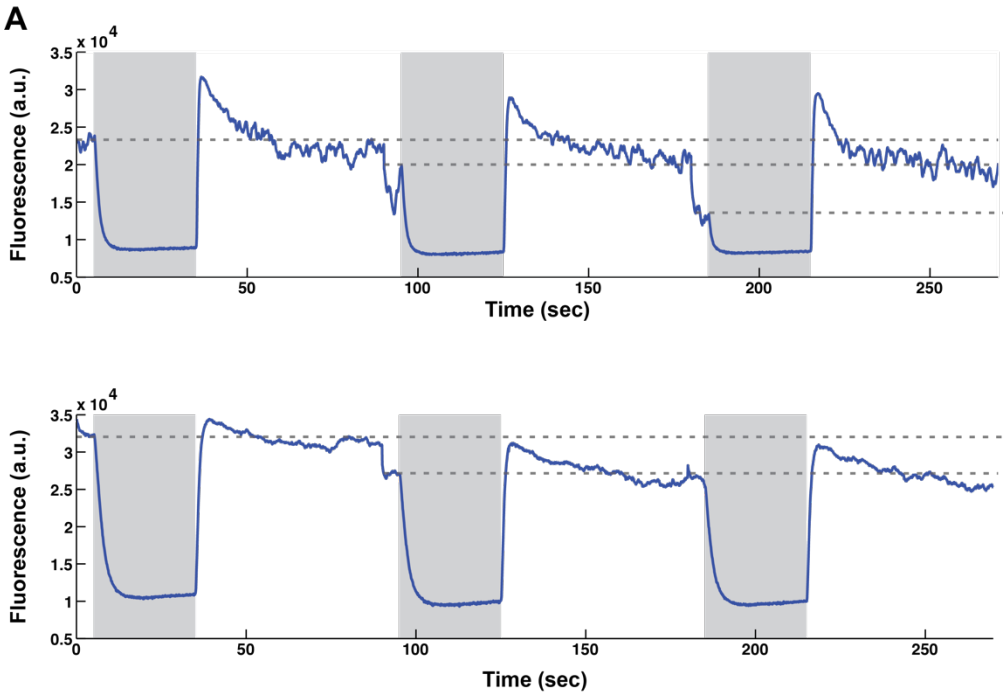

Supplemental Fig 1. AWC^{ON} baseline activity varies over time.

(A) Two examples of raw AWC^{ON} GCaMP5 recordings. AWC^{ON} baseline activity (dotted lines) can vary over time and therefore be different for each odor trial (gray box). In contrast, the activity levels during the odor stimulus is stable and comparable between each odor trial. Stimulus = 11.2 uM butanone.

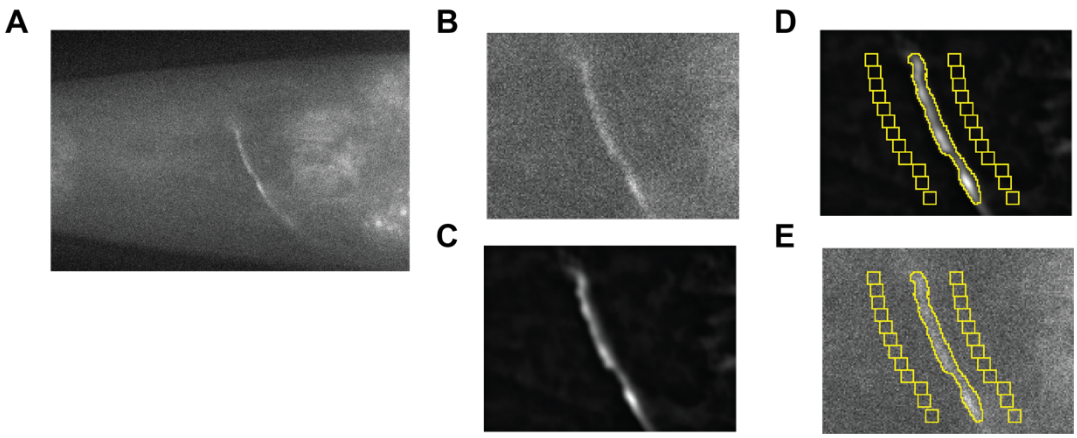

Supplemental Fig 2. Example of AWC^{ON} Vglut-pH data acquisition.

(A) Single plane of AWC^{ON} Vglut-pH recording after drift-registration correction. **(B)** Zoomed view around the axon in (A). **(C)** Mean intensity projection after the recording was processed by rolling background subtraction and 3D-averaging. **(D)** Selection of axon and background ROIs. **(E)** Intensity measurements are then taken from the raw drift-corrected recording.

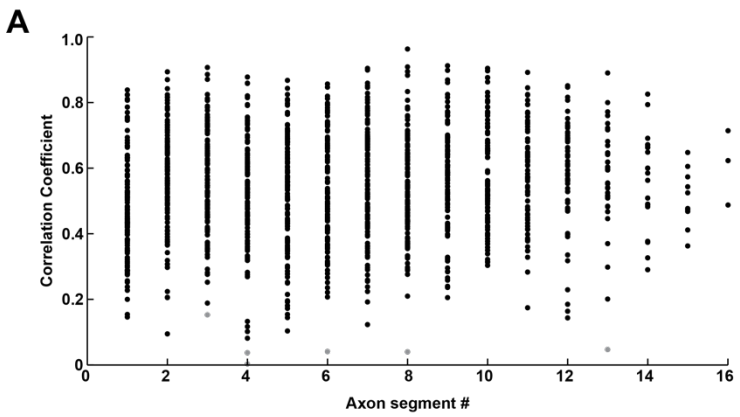

Supplemental Fig 3. Vglut-pH fluorescence changes along the axon are highly correlated.

(A) ROI segments along the axon are correlated with overall mean activity of the axon. Each point represents the correlation coefficient of an axon segment with the mean signal of the axon during a standard recording (see text). Data from 120 AWC^{ON} Vglut-pH axons, stimulated with 11.2 uM butanone. Each axon had 8 – 16 ROI segments. $p < 0.000001$ for all correlation coefficients except the points labeled in light gray, which were not significant $p > 0.05$.

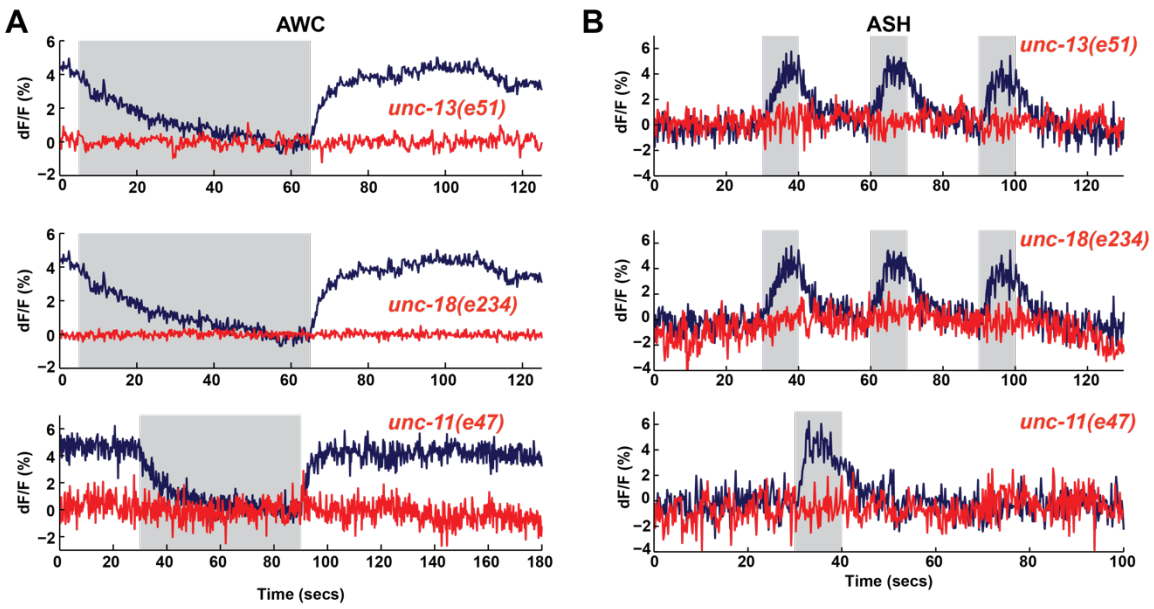

Supplemental Fig 4. Examples of Vglut-pH non-responders.

(A) Examples of AWC^{ON} Vglut-pH non-responders in the indicated mutant genotypes (red). Wild-type controls are in purple. Single trials. Gray bar = stimulus, 11.2 uM butanone. **(B)** Examples of ASH Vglut-pH non-responders in the indicated mutant genotypes (red). Wild-type controls are in purple. Single trials. Gray bar = stimulus, 500 mM NaCl.

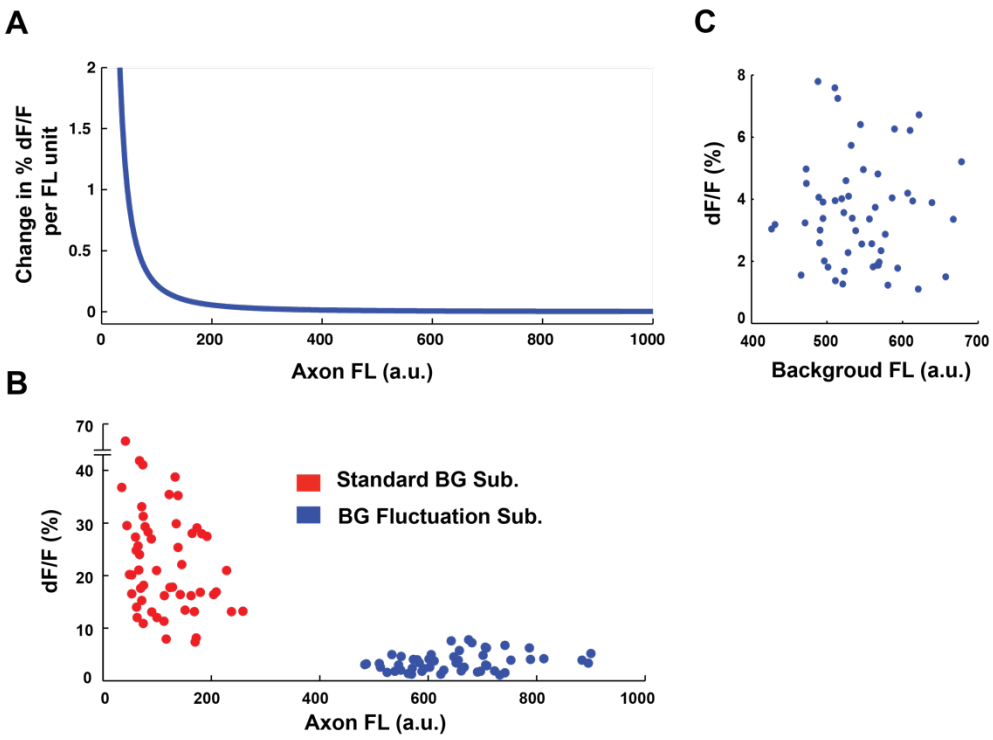

Supplemental Fig 5. Subtraction of only background fluctuations prevents large fluctuations in VGlut-pH DeltaF measurements.

(A) Change in dF/F (%) as a function of F_o for the average Vglut-pH change (Eq. 2). As F_o becomes approaches < 200 a.u. the deltaF function varies largely for each FL unit. Average axon based on data in (B). **(B)** Comparison of AWC VGlut-pH odor removal responses using standard (red) or BG_{Delta} (blue) background subtraction. For the same data, standard background subtraction generates a large range of DeltaF magnitudes, because low baseline fluorescence amplifies small variations. X-axis = baseline axon intensity (F_o). **(C)** AWC butanone removal responses show no significant correlation with their background fluorescence. Correlation coefficient = 0.004, p = 0.98. Same data for all panels = 54 AWC^{ON} axons, collected from multiple datasets. Butanone = 11.2 uM. FL = fluorescence, a.u. = arbitrary units.

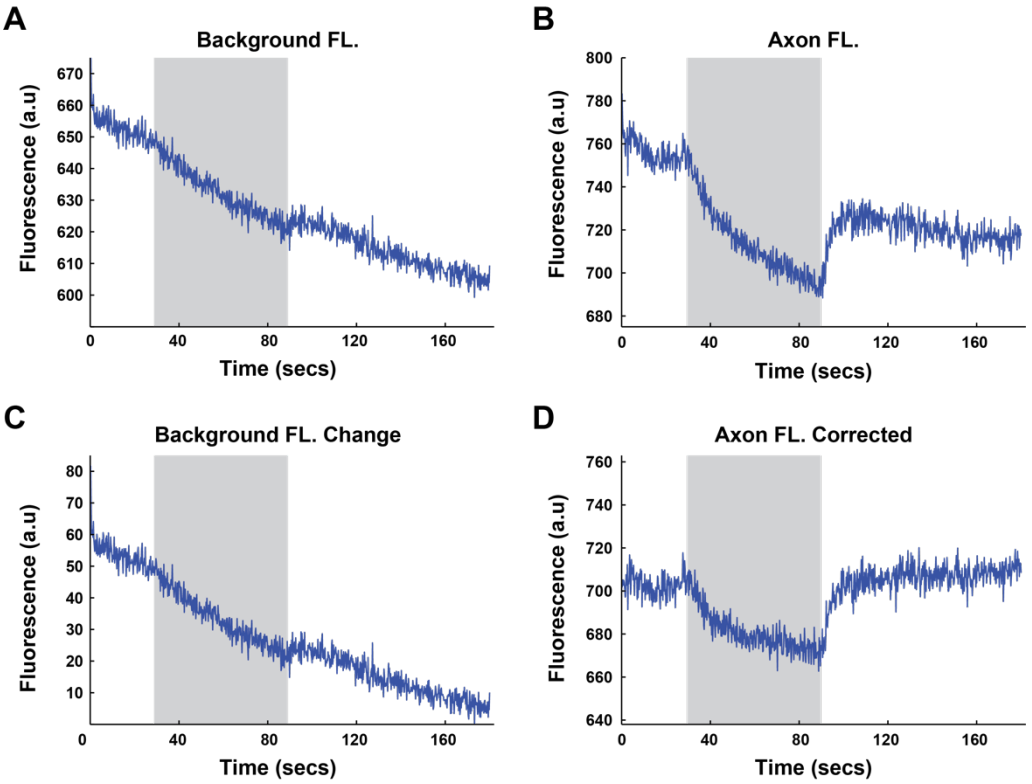

Supplemental Fig 6. VGlut-pH background correction method.

(A-D) Process of correcting a single AWC Vglut-pH trace. **(A)** Raw mean background intensity surrounding axon. **(B)** Raw mean intensity of the axon. **(C)** The change in background (BG_{Delta}) over time, generated using Eq. 3. **(D)** Subtraction of the background trace in (C) from the axon signal in (A). Gray bar = butanone stimulus (11.2 uM). FL = fluorescence, a.u. = arbitrary units.

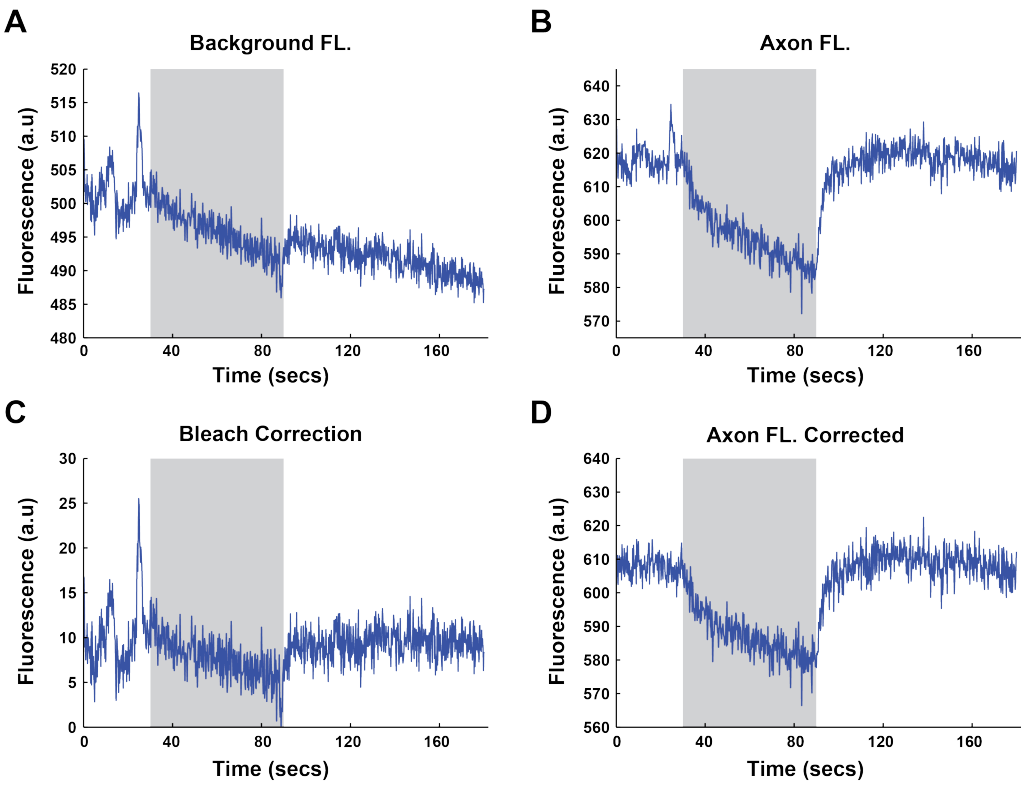

Supplemental Fig 7. Correction of background bleaching in VGlut-pH experiments.

(A-D) Process of correcting a single AWC Vglut-pH trace for background bleach correction. **(A)** Raw mean background intensity surrounding axon. Background displays bleaching. **(B)** The raw mean intensity of the axon. The Vglut-pH signal shows no apparent bleaching. **(C)** Correction of the background bleaching and conversion to BG_delta with Eq. 3 above. **(D)** Subtraction of the background trace in (C) from the axon signal in (A). Gray bar = butanone stimulus (11.2 uM). FL = fluorescence, a.u. = arbitrary units.

Appendix I. *C. elegans* Strains

Chapter 1

CX14174 *kyEx4435 AWC^{ON} Vglut-pH Line*

CX16644 *kyIs623 AWC^{ON} Vglut-pH Line*

CX16921 *kyIs673 ASH Vglut-pH Line*

CX15571 *kyEx5236 AWC^{ON} syGCaMP3*

CX10979 *kyEx2865 ASH GCaMP3*

Chapter 2

CX14174 *kyEx4435 AWC^{ON} Vglut-pH Line*

CX16644 *kyIs623 AWC^{ON} Vglut-pH Line*

CX16921 *kyIs673 ASH Vglut-pH Line*

CX17096 *unc-11(e47); kyIs623*

CX17109 *unc-11(e47); kyIs673*

Chapter 3

CX14174 *kyEx4435 AWC^{ON} Vglut-pH Line*

CX16644 *kyIs623 AWC^{ON} Vglut-pH Line*

CX16921	*kyIs673 ASH Vglut-pH Line*
CX17105	*kyIs623; kyEx5969 AWC^{ON} Tetanus toxin*
CX17068	*kyIs673; KyEx1661 ASH Tetanus toxin*
CX16954	*unc-64(e246); kyIs623*
CX17076	*unc-64(e246); kyIs673*
CX17071	*ric-4(md1088); kyIs623*
CX17104	*ric-4(md1088); kyIs673*
CX14175	*unc-13(e51); kyEx4435*
CX15568	*unc-13(s69); kyEx4435*
CX17073	*unc-13(e51); kyIs673*
CX17072	*unc-13(s69); kyIs673*
CX15416	*unc-18(e234); kyEx4435*
CX17075	*unc-18(e234); kyIs673*
CX17080	*unc-10(md1117); kyIs623*
CX17074	*unc-10(md1117); kyIs673*
CX15850	*cpx-1(ok1552); kyIs623*
CX17069	*cpx-1(ok1552); kyIs673*
CX15567	*tom-1(ok285); kyEx4435*
CX17102	*tom-1(ok285); kyEx5236*
CX17078	*tom-1(ok285); kyIs673*

CX10979 *kyEx2865 ASH GCaMP3*

CX17119 *tom-1(ok285); kyEx2865*

Chapter 4

CX16451 *kyEx5608 AWC^{ON} cyto-pH*

CX16963 *kyEx5901 ASH cyto-pH*

CX16644 *kyIs623 AWC^{ON} Vglut-pH Line*

CX16921 *kyIs673 ASH Vglut-pH Line*

CX16491 *unc-18(e234); kyEx5608*

CX16494 *unc-13(s69); kyEx5608*

CX16967 *kyEx5904 ASH CD4-pH*

CX17096 *unc-11(e47); kyIs623*

CX17110 *unc-11(e47) kyEx5608*

CX15571 *kyEx5236 AWC^{ON} syGCaMP3*

Chapter 5

CX15744 *kyIs622 AWC^{ON} Vglut-pH Line on chromosome X*

CX16644 *kyIs623 AWC^{ON} Vglut-pH Line*

CX16921 *kyIs673 ASH Vglut-pH Line*

CX17165 *snt-1(md290); kyIs622*

CX17166	*snt-1(md172); kyIs622*
CX15571	*kyEx5236 AWC^{ON} syGCaMP3*
CX16315	*snt-1(md290); kyEx5236*
CX17254	*snt-1(md290); kyIs673*
CX17162	*snt-1(md172); kyIs673*
CX17140	*snt-2(tm1711); kyIs623*
CX17126	*snt-2(tm7111) kyIs673*
CX17149	*snt-3(ky1034); kyIs673*
CX17098	*snt-4(ok503) kyIs673*
CX17036	*snt-5(tm3786) kyIs673*
CX17100	*snt-6(tm3686) kyIs673*
CX17161	*snt-1(md290); snt-6(tm3686) kyIs673*

Chapter 6

IK105	*pkc-1(nj1)*
IK130	*pkc-1(nj3)*
RB781	*pkc-1(ok563)*
CX13658	*kyEx4152 str-2:pkc-1 dsRNAi*
CX15246	*pkc-1(nj1); kyEx5125 str-2:pkc-1.a cDNA:sl2:mCherry*
CX13914	*kyEx4275 str-2:GCaMP5A*

CX16165	*pkc-1(nj1); kyEx4275 str-2:GCaMP5A*
CX15571	*kyEx5236 AWC^{ON} syGCaMP3*
CX16318	*pkc-1(nj1); KyEx5236*
CX16451	*kyEx5608 AWC^{ON} cyto-pH*
CX16660	*pkc-1(nj1); kyEx5608*
CX14174	*kyEx4435 AWC^{ON} Vglut-pH Line*
CX15609	*pkc-1(nj1); kyEx4435*
CX16644	*kyIs623 AWC^{ON} Vglut-pH Line*
CX16630	*pkc-1(nj3); kyIs623*
CX15848	*pkc-1(nj1); kyIs623*
CX15849	*pkc-1(nj1); kyIs623; kyEx5354 str-2:pkc-1.a cDNA:sl2:mCherry*
CX15610	*gcy-28(tm2411); kyEx4435*
CX16921	*kyIs673 ASH Vglut-pH Line*
CX16950	*pkc-1(nj1); kyIs673*
CX15611	*pkc-1(nj1); kyEx4283 AIB/AVA GCaMP3*
CX13922	*kyEx4283= AIB/AVA GCaMP3*
CX14780	*lite-1(ce314); kyEx4857 AIY GCaMP5A*
CX15572	*pkc-1(nj1); lite-1(ce314); kyEx4857*
VC223	*tom-1(ok285)*
CX16204	*pkc-1(nj1); tom-1(ok285)*

CX17079	*tom-1(ok285); kyIs623*
CX16207	*pkc-1(nj1); tom-1(ok285) kyIs623*
CX15850	*cpx-1(ok1552); kyIs623*
CX16351	*pkc-1(nj1); cpx-1(ok1552);kyIs623*
CX15414	*egl-30(n686sd); kyEx4435*
CX15415	*egl-30(js126); kyEx4435*
CX15840	*egl-30(js126);kyIs623*
CX16769	*pkc-1(nj1); egl-30(js126); kyIs613*
MJ500	*tpa-1(k501) IV*
CX10285	*tpa-1(k501) IV; pkc-1(nj1) V*
CX15932	*pkc-1(nj1) ;tpa-1(k501); kyEx5396 str-2:tpa-1.a cDNA:sl2:mCherry*
CX13503	*eat-4(ky5)*
CX16446	*pkc-1(nj1); eat-4(ky5)*
CX16449	*pkc-1(nj1); eat-4(ky5) kyEx5354 str-2:pkc-1.a cDNA:sl2:mCherry*
CB928	*unc-31(e928)*
CB169	*unc-31(e169)*
CB69	*unc-31(e69)*
CX15936	*unc-3 (e928); kyEx5400 tag168:unc-31L(cDNA):sl2:mcherry*
CX16013	*unc-31(e928); kyIs623*
CX16018	*unc-31(e928); kyEx5444 eat-4p(5.5kb version):unc-31 long cDNA:sl2:mchry*

CX16016 *unc-31(e928); kyEx5442 cat-1p:unc-31 long cDNA:sl2:mchry*

CX16014 *unc-31(e928); kyEx5440 glr-1p:unc-31 long cDNA:sl2:mchry*

CX15934 *unc-31(e928); kyEx5398 Str-2p:unc-31L(cDNA):sl2:mcherry (15ng/ul)*

References:

Abbott, L.F., and Regehr, W.G. (2004). Synaptic computation. Nature *431*, 796-803.

Abraham, C., Bai, L., and Leube, R.E. (2011). Synaptogyrin-dependent modulation of synaptic neurotransmission in Caenorhabditis elegans. Neuroscience *190*, 75-88.

Ackermann, F., Waites, C.L., and Garner, C.C. (2015). Presynaptic active zones in invertebrates and vertebrates. EMBO Rep *16*, 923-938.

Adachi, T., Kunitomo, H., Tomioka, M., Ohno, H., Okochi, Y., Mori, I., and Iino, Y. (2010). Reversal of salt preference is directed by the insulin/PI3K and Gq/PKC signaling in Caenorhabditis elegans. Genetics *186*, 1309-1319.

Akerboom, J., Chen, T.-W.W., Wardill, T.J., Tian, L., Marvin, J.S., Mutlu, S., Calderón, N.C., Esposti, F., Borghuis, B.G., Sun, X.R.*, et al.* (2012). Optimization of a GCaMP calcium indicator for neural activity imaging. The Journal of neuroscience : the official journal of the Society for Neuroscience *32*, 13819-13840.

Alabi, A.A., and Tsien, R.W. (2012). Synaptic vesicle pools and dynamics. Cold Spring Harb Perspect Biol *4*, a013680.

Alabi, A.A., and Tsien, R.W. (2013). Perspectives on Kiss-and-Run: Role in Exocytosis, Endocytosis, and Neurotransmission. Annual review of physiology *75*, 393-422.

Albrecht, D.R., and Bargmann, C.I. (2011). High-content behavioral analysis of Caenorhabditis elegans in precise spatiotemporal chemical environments. Nature methods *8*, 599-605.

Ariel, P., and Ryan, T.A. (2010). Optical mapping of release properties in synapses. Frontiers in neural circuits *4*.

Armbruster, M., Messa, M., Ferguson, S.M., Camilli, P., and Ryan, T.A. (2013). Dynamin phosphorylation controls optimization of endocytosis for brief action potential bursts. eLife *2*.

Arribere, J.A., Bell, R.T., Fu, B.X., Artiles, K.L., Hartman, P.S., and Fire, A.Z. (2014). Efficient marker-free recovery of custom genetic modifications with CRISPR/Cas9 in Caenorhabditis elegans. Genetics *198*, 837-846.

Ashery, U., Bielopolski, N., Barak, B., and Yizhar, O. (2009). Friends and foes in synaptic transmission: the role of tomosyn in vesicle priming. Trends Neurosci *32*, 275-282.

Atluri, P.P., and Ryan, T.A. (2006). The Kinetics of Synaptic Vesicle Reacidification at Hippocampal Nerve Terminals. The Journal of Neuroscience *26*, 2313-2320.

Atwood, H.L., and Karunanithi, S. (2002). Diversification of synaptic strength: presynaptic elements. Nature reviews Neuroscience *3*, 497-516.

Augustin, I., Rosenmund, C., Südhof, T.C., and Brose, N. (1999). Munc13-1 is essential for fusion competence of glutamatergic synaptic vesicles. Nature *400*, 457-461.

Bacaj, T., Wu, D., Yang, X., Morishita, W., Zhou, P., Xu, W., Malenka, R.C., and Südhof, T.C. (2013). Synaptotagmin-1 and synaptotagmin-7 trigger synchronous and asynchronous phases of neurotransmitter release. Neuron *80*, 947-959.

Bai, J., Tucker, W.C., and Chapman, E.R. (2004). PIP2 increases the speed of response of synaptotagmin and steers its membrane-penetration activity toward the plasma membrane. Nat Struct Mol Biol *11*, 36-44.

Bailey, C.H., Kandel, E.R., and Harris, K.M. (2015). Structural Components of Synaptic Plasticity and Memory Consolidation. Cold Spring Harb Perspect Biol *7*, a021758.

Balaji, J., and Ryan, T.A. (2007). Single-vesicle imaging reveals that synaptic vesicle exocytosis and endocytosis are coupled by a single stochastic mode. Proceedings of the National Academy of Sciences of the United States of America *104*, 20576-20581.

Banerjee, A., Barry, V.A., DasGupta, B.R., and Martin, T.F. (1996). N-Ethylmaleimide-sensitive factor acts at a prefusion ATP-dependent step in Ca2+-activated exocytosis. J Biol Chem *271*, 20223-20226.

Bargmann, C.I. (1998). Neurobiology of the Caenorhabditis elegans genome. Science *282*, 2028-2033.

Bargmann, C.I. (2006). Chemosensation in C. elegans. *Wormbook, ed.* The *C. elegans* Resreach Community, Wormbook, doi/10.1985/wormbook.1.123.1, http://www.wormbook.org

Baylis, H.A., and Vazquez-Manrique, R.P. (2012). Genetic analysis of IP3 and calcium signalling pathways in C. elegans. Biochim Biophys Acta *1820*, 1253-1268.

Beg, A.A., Ernstrom, G.G., Nix, P., Davis, M.W., and Jorgensen, E.M. (2008). Protons act as a transmitter for muscle contraction in C. elegans. Cell *132*, 149-160.

Berg, H.C., and Brown, D.A. (1972). Chemotaxis in Escherichia coli analysed by three-dimensional tracking. Nature *239*, 500-504.

Berwin, B., Floor, E., and Martin, T.F. (1998). CAPS (mammalian UNC-31) protein localizes to membranes involved in dense-core vesicle exocytosis. Neuron *21*, 137-145.

Betz, A., Thakur, P., Junge, H.J., Ashery, U., Rhee, J.S., Scheuss, V., Rosenmund, C., Rettig, J., and Brose, N. (2001). Functional interaction of the active zone proteins Munc13-1 and RIM1 in synaptic vesicle priming. Neuron *30*, 183-196.

Bhalla, A., Tucker, W.C., and Chapman, E.R. (2005). Synaptotagmin isoforms couple distinct ranges of Ca2+, Ba2+, and Sr2+ concentration to SNARE-mediated membrane fusion. Mol Biol Cell *16*, 4755-4764.

Borst, J.G. (2010). The low synaptic release probability in vivo. Trends Neurosci *33*, 259-266.

Boschert, U., O'Shaughnessy, C., Dickinson, R., Tessari, M., Bendotti, C., Catsicas, S., and Pich, E.M. (1996). Developmental and plasticity-related differential expression of two SNAP-25 isoforms in the rat brain. J Comp Neurol *367*, 177-193.

Bozza, T., McGann, J.P., Mombaerts, P., and Wachowiak, M. (2004). In vivo imaging of neuronal activity by targeted expression of a genetically encoded probe in the mouse. Neuron *42*, 9-21.

Branco, T., and Staras, K. (2009). The probability of neurotransmitter release: variability and feedback control at single synapses. Nature Reviews Neuroscience.

Brechenmacher, C., and Rodeau, J.L. (2000). Intracellular pH regulation in ventral horn neurones cultured from embryonic rat spinal cord. Mol Membr Biol *17*, 101-108.

Brenner, S. (1974). The genetics of Caenorhabditis elegans. Genetics *77*, 71-94.

Cao, P., Maximov, A., and Sudhof, T.C. (2011). Activity-dependent IGF-1 exocytosis is controlled by the Ca (2+)-sensor synaptotagmin-10. Cell *145*, 300-311.

Chalasani, S.H., Chronis, N., Tsunozaki, M., Gray, J.M., Ramot, D., Goodman, M.B., and Bargmann, C.I. (2007). Dissecting a circuit for olfactory behaviour in Caenorhabditis elegans. Nature *450*, 63-70.

Chalasani, S.H., Kato, S., Albrecht, D.R., Nakagawa, T., Abbott, L.F., and Bargmann, C.I. (2010). Neuropeptide feedback modifies odor-evoked dynamics in Caenorhabditis elegans olfactory neurons. Nature neuroscience *13*, 615-621.

Charvin, N., L'Eveque, C., Walker, D., Berton, F., Raymond, C., Kataoka, M., Shoji-Kasai, Y., Takahashi, M., De Waard, M., and Seagar, M.J. (1997). Direct interaction of the calcium sensor protein synaptotagmin I with a cytoplasmic domain of the alpha1A subunit of the P/Q-type calcium channel. EMBO J *16*, 4591-4596.

Chatzigeorgiou, M., Bang, S., Hwang, S.W., and Schafer, W.R. (2013). tmc-1 encodes a sodium-sensitive channel required for salt chemosensation in C. elegans. Nature *494*, 95-99.

Chesler, M. (1990). The regulation and modulation of pH in the nervous system. Progress in neurobiology.

Chesler, M., and Kaila, K. (1992). Modulation of pH by neuronal activity. Trends Neurosci *15*, 396-402.

Chronis, N., Zimmer, M., and Bargmann, C.I. (2007). Microfluidics for in vivo imaging of neuronal and behavioral activity in Caenorhabditis elegans. Nature methods *4*, 727-731.

Clayton, E.L., and Cousin, M.A. (2009). The molecular physiology of activity-dependent bulk endocytosis of synaptic vesicles. Journal of neurochemistry.

Colbert, H.A., and Bargmann, C.I. (1995). Odorant-specific adaptation pathways generate olfactory plasticity in C. elegans. Neuron *14*, 803-812.

Cooper, B., Hemmerlein, M., Ammermüller, J., Imig, C., Reim, K., Lipstein, N., Kalla, S., Kawabe, H., Brose, N., Brandstätter, J.*, et al.* (2012). Munc13-Independent Vesicle Priming at Mouse Photoreceptor Ribbon Synapses. The Journal of Neuroscience *32*, 8040-8052.

Crawford, D.C., and Kavalali, E.T. (2015). Molecular underpinnings of synaptic vesicle pool heterogeneity. Traffic *16*, 338-364.

Craxton, M. (2010). A manual collection of Syt, Esyt, Rph3a, Rph3al, Doc2, and Dblc2 genes from 46 metazoan genomes--an open access resource for neuroscience and evolutionary biology. BMC Genomics *11*, 37.

de Bono, M., and Maricq, A.V. (2005). Neuronal substrates of complex behaviors in C. elegans. Annu Rev Neurosci *28*, 451-501.

de Jong, A.P., Meijer, M., Saarloos, I., Cornelisse, L.N., Toonen, R.F., Sorensen, J.B., and Verhage, M. (2016). Phosphorylation of synaptotagmin-1 controls a post-priming step in PKC-dependent presynaptic plasticity. Proc Natl Acad Sci U S A *113*, 5095-5100.

de Steveninck, R.R., and Laughlin, S.B. (1996). The rate of information transfer at graded-potential synapses. Nature *379*, 642-645.

Dean, C., Dunning, F.M., Liu, H., Bomba-Warczak, E., Martens, H., Bharat, V., Ahmed, S., and Chapman, E.R. (2012). Axonal and dendritic synaptotagmin isoforms revealed by a pHluorin-syt functional screen. Mol Biol Cell *23*, 1715-1727.

Del Castillo, J., and Katz, B. (1954). Quantal components of the end-plate potential. J Physiol *124*, 560-573.

Dittman, J. (2009). Worm watching: imaging nervous system structure and function in Caenorhabditis elegans. Adv Genet *65*, 39-78.

Dittman, J., and Ryan, T.A. (2009a). Molecular circuitry of endocytosis at nerve terminals. Annu Rev Cell Dev Biol *25*, 133-160.

Dittman, J., and Ryan, T.A. (2009b). Molecular circuitry of endocytosis at nerve terminals. Molecular circuitry of endocytosis at nerve terminals.

Dittman, J.S., and Kaplan, J.M. (2006). Factors regulating the abundance and localization of synaptobrevin in the plasma membrane. Proceedings of the National Academy of Sciences of the United States of America *103*, 11399-11404.

Dittman, J.S., Kreitzer, A.C., and Regehr, W.G. (2000). Interplay between facilitation, depression, and residual calcium at three presynaptic terminals. J Neurosci *20*, 1374-1385.

Dreosti, E., and Lagnado, L. (2011). Optical reporters of synaptic activity in neural circuits. Exp Physiol *96*, 4-12.

Dreosti, E., Odermatt, B., Dorostkar, M.M., and Lagnado, L. (2009). A genetically encoded reporter of synaptic activity in vivo. Nat Methods *6*, 883-889.

Edwards, M.R., Johnson, J.R., Rankin, K., Jenkins, R.E., Maguire, C., Morgan, A., Burgoyne, R.D., and Barclay, J.W. (2012). PKC-2 phosphorylation of UNC-18 Ser322 in AFD neurons regulates temperature dependency of locomotion. J Neurosci *32*, 7042-7051.

Edwards, S.L., Charlie, N.K., Milfort, M.C., Brown, B.S., Gravlin, C.N., Knecht, J.E., and Miller, K.G. (2008). A novel molecular solution for ultraviolet light detection in Caenorhabditis elegans. PLoS Biol *6*, e198.

Esposito, G., Schiavi, E., Bergamasco, C., and Bazzicalupo, P. (2007). Efficient and cell specific knock-down of gene function in targeted C. elegans neurons. Gene *395*, 170-176.

Fatt, P., and Katz, B. (1952). Spontaneous subthreshold activity at motor nerve endings. J Physiol *117*, 109-128.

Feinberg, E.H., Vanhoven, M.K., Bendesky, A., Wang, G., Fetter, R.D., Shen, K., and Bargmann, C.I. (2008). GFP Reconstitution Across Synaptic Partners (GRASP) defines cell contacts and synapses in living nervous systems. Neuron *57*, 353-363.

Fernández-Alfonso, T., Kwan, R., and Ryan, T.A. (2006). Synaptic Vesicles Interchange Their Membrane Proteins with a Large Surface Reservoir during Recycling. Neuron *51*, 179-186.

Fujita, Y., Shirataki, H., Sakisaka, T., Asakura, T., Ohya, T., Kotani, H., Yokoyama, S., Nishioka, H., Matsuura, Y., Mizoguchi, A*., et al.* (1998). Tomosyn: a syntaxin-1-binding protein that forms a novel complex in the neurotransmitter release process. Neuron *20*, 905-915.

Gaillard, S., and Dupont, J.L. (1990). Ionic control of intracellular pH in rat cerebellar Purkinje cells maintained in culture. J Physiol *425*, 71-83.

Geppert, M., Goda, Y., Hammer, R.E., Li, C., Rosahl, T.W., Stevens, C.F., and Sudhof, T.C. (1994). Synaptotagmin I: a major Ca2+ sensor for transmitter release at a central synapse. Cell *79*, 717-727.

Giordano, F., Saheki, Y., Idevall-Hagren, O., Colombo, S.F., Pirruccello, M., Milosevic, I., Gracheva, E.O., Bagriantsev, S.N., Borgese, N., and De Camilli, P. (2013). PI (4,5)P (2)-dependent and Ca (2+)-regulated ER-PM interactions mediated by the extended synaptotagmins. Cell *153*, 1494-1509.

Goodman, M.B. (2006). Mechanosensation. *Wormbook, ed.* The *C. elegans* Resreach Community, Wormbook, doi/10.1985/wormbook.1.62.1, http://www.wormbook.org

Goodman, M.B., Hall, D.H., Avery, L., and Lockery, S.R. (1998). Active currents regulate sensitivity and dynamic range in C. elegans neurons. Neuron *20*, 763-772.

Gordus, A., Pokala, N., Levy, S., Flavell, S.W., and Bargmann, C.I. (2015). Feedback from network states generates variability in a probabilistic olfactory circuit. Cell *161*, 215-227.

Gracheva, E.O., Burdina, A.O., Holgado, A.M., Berthelot-Grosjean, M., Ackley, B.D., Hadwiger, G., Nonet, M.L., Weimer, R.M., and Richmond, J.E. (2006a). Tomosyn inhibits synaptic vesicle priming in Caenorhabditis elegans. PLoS biology *4*.

Gracheva, E.O., Burdina, A.O., Holgado, A.M., Berthelot-Grosjean, M., Ackley, B.D., Hadwiger, G., Nonet, M.L., Weimer, R.M., and Richmond, J.E. (2006b). Tomosyn inhibits synaptic vesicle priming in Caenorhabditis elegans. PLoS Biol *4*, e261.

Gracheva, E.O., Hadwiger, G., Nonet, M.L., and Richmond, J.E. (2008a). Direct interactions between C. elegans RAB-3 and Rim provide a mechanism to target vesicles to the presynaptic density. Neurosci Lett *444*, 137-142.

Gracheva, E.O., Hadwiger, G., Nonet, M.L., and Richmond, J.E. (2008b). Direct interactions between C. elegans RAB-3 and Rim provide a mechanism to target vesicles to the presynaptic density. Neuroscience letters *444*, 137-142.

Gracheva, E.O., Maryon, E.B., Berthelot-Grosjean, M., and Richmond, J.E. (2010). Differential Regulation of Synaptic Vesicle Tethering and Docking by UNC-18 and TOM-1. Frontiers in Synaptic Neuroscience *2*, 141.

Granseth, B., Odermatt, B., Royle, S.J., and Lagnado, L. (2006). Clathrin-mediated endocytosis is the dominant mechanism of vesicle retrieval at hippocampal synapses. Neuron *51*, 773-786.

Gray, J.M., Hill, J.J., and Bargmann, C.I. (2005). A circuit for navigation in Caenorhabditis elegans. Proceedings of the National Academy of Sciences of the United States of America *102*, 3184-3191.

Gu, M., Schuske, K., Watanabe, S., Liu, Q., Baum, P., Garriga, G., and Jorgensen, E.M. (2008). Mu2 adaptin facilitates but is not essential for synaptic vesicle recycling in Caenorhabditis elegans. J Cell Biol *183*, 881-892.

Hao, W., Luo, Z., Zheng, L., Prasad, K., and Lafer, E.M. (1999). AP180 and AP-2 interact directly in a complex that cooperatively assembles clathrin. Journal of Biological ….

Hatsuzawa, K., Lang, T., Fasshauer, D., Bruns, D., and Jahn, R. (2003). The R-SNARE motif of tomosyn forms SNARE core complexes with syntaxin 1 and SNAP-25 and down-regulates exocytosis. J Biol Chem *278*, 31159-31166.

Haucke, V., Neher, E., and Sigrist, S.J. (2011). Protein scaffolds in the coupling of synaptic exocytosis and endocytosis. Nat Rev Neurosci *12*, 127-138.

Heidelberger, R. (2007). Mechanisms of tonic, graded release: lessons from the vertebrate photoreceptor. The Journal of physiology *585*, 663-667.

Hendricks, M., Ha, H., Maffey, N., and Zhang, Y. (2012). Compartmentalized calcium dynamics in a C. elegans interneuron encode head movement. Nature *487*, 99-103.

Heuser, J.E., and Reese, T.S. (1973). Evidence for recycling of synaptic vesicle membrane during transmitter release at the frog neuromuscular junction. J Cell Biol *57*, 315-344.

Heuser, J.E., Reese, T.S., Dennis, M.J., Jan, Y., Jan, L., and Evans, L. (1979). Synaptic vesicle exocytosis captured by quick freezing and correlated with quantal transmitter release. The Journal of cell biology *81*, 275-300.

Hilliard, M.A., Apicella, A.J., Kerr, R., Suzuki, H., Bazzicalupo, P., and Schafer, W.R. (2005). In vivo imaging of C. elegans ASH neurons: cellular response and adaptation to chemical repellents. EMBO J *24*, 63-72.

Hobert, O. (2002). PCR fusion-based approach to create reporter gene constructs for expression analysis in transgenic C. elegans. Biotechniques *32*, 728-730.

Holt, M., Cooke, A., Wu, M.M., and Lagnado, L. (2003). Bulk membrane retrieval in the synaptic terminal of retinal bipolar cells. J Neurosci *23*, 1329-1339.

Hu, Z., Vashlishan-Murray, A.B., and Kaplan, J.M. (2015). NLP-12 Engages Different UNC-13 Proteins to Potentiate Tonic and Evoked Release. Journal of Neuroscience.

Hua, Z., Leal-Ortiz, S., Foss, S.M., Waites, C.L., Garner, C.C., Voglmaier, S.M., and Edwards, R.H. (2011). v-SNARE composition distinguishes synaptic vesicle pools. Neuron *71*, 474-487.

Hyde, R., Corkins, M.E., Somers, G.A., and Hart, A.C. (2011). PKC-1 acts with the ERK MAPK signaling pathway to regulate Caenorhabditis elegans mechanosensory response. Genes, brain, and behavior *10*, 286-298.

Jorgensen, E.M., Hartwieg, E., Schuske, K., and Nonet, M.L. (1995). Defective recycling of synaptic vesicles in synaptotagmin mutants of Caenorhabditis elegans. Nature.

Kaeser, P.S., and Regehr, W.G. (2014). Molecular mechanisms for synchronous, asynchronous, and spontaneous neurotransmitter release. Annu Rev Physiol *76*, 333-363.

Kaplan, J.M., and Horvitz, H.R. (1993). A dual mechanosensory and chemosensory neuron in Caenorhabditis elegans. Proc Natl Acad Sci U S A *90*, 2227-2231.

Kasai, H., Takahashi, N., and Tokumaru, H. (2012). Distinct initial SNARE configurations underlying the diversity of exocytosis. Physiol Rev *92*, 1915-1964.

Kato, S., Xu, Y., Cho, C.E., Abbott, L.F., and Bargmann, C.I. (2014). Temporal responses of C. elegans chemosensory neurons are preserved in behavioral dynamics. Neuron *81*, 616-628.

Katz, B. (1969). The release of neural transmitter substances (Springfield, Ill.,: Thomas).

Katz, B., and Miledi, R. (1967a). A study of synaptic transmission in the absence of nerve impulses. J Physiol *192*, 407-436.

Katz, B., and Miledi, R. (1967b). Tetrodotoxin and neuromuscular transmission. Proc R Soc Lond B Biol Sci *167*, 8-22.

Kavalali, E.T. (2015). The mechanisms and functions of spontaneous neurotransmitter release. Nat Rev Neurosci *16*, 5-16.

Kavalali, E.T., and Jorgensen, E.M. (2014). Visualizing presynaptic function. Nature neuroscience *17*, 10-16.

KENNEDY, D., and TAKEDA, K. (1965). Reflex Control of Abdominal Flexor Muscles in the Crayfish. II The Tonic System *43*, 229-246.

Khasar, S.G., Lin, Y.H., Martin, A., Dadgar, J., and McMahon, T. (1999). A novel nociceptor signaling pathway revealed in protein kinase C ε mutant mice. A novel nociceptor signaling pathway revealed in protein kinase C ε mutant mice.

Kim, S.H., and Ryan, T.A. (2009). Synaptic vesicle recycling at CNS snapses without AP-2. J Neurosci *29*, 3865-3874.

Kim, S.H., and Ryan, T.A. (2010). CDK5 serves as a major control point in neurotransmitter release. Neuron *67*, 797-809.

Kim, S.H., and Ryan, T.A. (2013). Balance of calcineurin Aα and CDK5 activities sets release probability at nerve terminals. The Journal of neuroscience : the official journal of the Society for Neuroscience *33*, 8937-8950.

Kimata, T., Sasakura, H., Ohnishi, N., Nishio, N., and Mori, I. (2012). Thermotaxis of C. elegans as a model for temperature perception, neural information processing and neural plasticity. Worm *1*, 31-41.

Kneen, M., Farinas, J., Li, Y., and Verkman, A.S. (1998). Green fluorescent protein as a noninvasive intracellular pH indicator. Biophys J *74*, 1591-1599.

Kohn, R.E., Duerr, J.S., McManus, J.R., Duke, A., Rakow, T.L., Maruyama, H., Moulder, G., Maruyama, I.N., Barstead, R.J., and Rand, J.B. (2000). Expression of multiple UNC-13 proteins in the Caenorhabditis elegans nervous system. Mol Biol Cell *11*, 3441-3452.

Kononenko, N.L., and Haucke, V. (2015). Molecular Mechanisms of Presynaptic Membrane Retrieval and Synaptic Vesicle Reformation. Neuron *85*, 484-496.

Kononenko, N.L., Puchkov, D., Classen, G.A., Walter, A.M., Pechstein, A., Sawade, L., Kaempf, N., Trimbuch, T., Lorenz, D., Rosenmund, C.*, et al.* (2014).

Clathrin/AP-2 mediate synaptic vesicle reformation from endosome-like vacuoles but are not essential for membrane retrieval at central synapses. Neuron *82*, 981-988.

Koo, S.J., Kochlamazashvili, G., Rost, B., and Puchkov, D. (2015). Vesicular synaptobrevin/VAMP2 levels guarded by AP180 control efficient neurotransmission. Neuron, 88(2), 330-344

Korber, C., and Kuner, T. (2016). Molecular Machines Regulating the Release Probability of Synaptic Vesicles at the Active Zone. Front Synaptic Neurosci *8*, 5.

Koushika, S.P., Richmond, J.E., Hadwiger, G., Weimer, R.M., Jorgensen, E.M., and Nonet, M.L. (2001). A post-docking role for active zone protein Rim. Nature neuroscience *4*, 997-1005.

Krizaj, D., Mercer, A.J., Thoreson, W.B., and Barabas, P. (2011). Intracellular pH modulates inner segment calcium homeostasis in vertebrate photoreceptors. Am J Physiol Cell Physiol *300*, C187-197.

L'Etoile, N.D., Coburn, C.M., Eastham, J., Kistler, A., Gallegos, G., and Bargmann, C.I. (2002). The cyclic GMP-dependent protein kinase EGL-4 regulates olfactory adaptation in C. elegans. Neuron *36*, 1079-1089.

Lackner, M. (1999). Facilitation of Synaptic Transmission by EGL-30 Gq? and EGL-8 PLC?DAG Binding to UNC-13 Is Required to Stimulate Acetylcholine Release. Neuron *24*, 335-346.

Lackner, M.R., Nurrish, S.J., and Kaplan, J.M. (1999). Facilitation of synaptic transmission by EGL-30 Gqalpha and EGL-8 PLCbeta: DAG binding to UNC-13 is required to stimulate acetylcholine release. Neuron *24*, 335-346.

Larsch, J., Flavell, S.W., Liu, Q., Gordus, A., Albrecht, D.R., and Bargmann, C.I. (2015). A Circuit for Gradient Climbing in C. elegans Chemotaxis. Cell Rep *12*, 1748-1760.

Leitz, J., and Kavalali, E.T. (2015). Ca2+ Dependence of Synaptic Vesicle Endocytosis. Neuroscientist.

Li, C., and Kim, K. (2008). Neuropeptides. *Wormbook, ed.* The *C. elegans* Resreach Community, Wormbook, doi/10.1985/wormbook.1.142.1, http://www.wormbook.org

Liewald, J.F., Brauner, M., Stephens, G.J., Bouhours, M., Schultheis, C., Zhen, M., and Gottschalk, A. (2008). Optogenetic analysis of synaptic function. Nat Methods *5*, 895-902.

Lindgren, C.A., Emery, D.G., and Haydon, P.G. (1997). Intracellular acidification reversibly reduces endocytosis at the neuromuscular junction. J Neurosci *17*, 3074-3084.

Lindner, R., and Ungewickell, E. (1992). Clathrin-associated proteins of bovine brain coated vesicles. An analysis of their number and assembly-promoting activity. J Biol Chem *267*, 16567-16573.

Littleton, J.T., Serano, T.L., Rubin, G.M., Ganetzky, B., and Chapman, E.R. (1999). Synaptic function modulated by changes in the ratio of synaptotagmin I and IV. Nature *400*, 757-760.

Littleton, J.T., Stern, M., Schulze, K., Perin, M., and Bellen, H.J. (1993). Mutational analysis of Drosophila synaptotagmin demonstrates its essential role in Ca (2+)-activated neurotransmitter release. Cell *74*, 1125-1134.

Liu, J., Ward, A., Gao, J., Dong, Y., Nishio, N., Inada, H., Kang, L., Yu, Y., Ma, D., Xu, T.*, et al.* (2010). C. elegans phototransduction requires a G protein-dependent cGMP pathway and a taste receptor homolog. Nat Neurosci *13*, 715-722.

Liu, Q., Chen, B., Yankova, M., Morest, D.K., Maryon, E., Hand, A.R., Nonet, M.L., and Wang, Z.W. (2005). Presynaptic ryanodine receptors are required for normal quantal size at the Caenorhabditis elegans neuromuscular junction. J Neurosci *25*, 6745-6754.

Liu, Q., Hollopeter, G., and Jorgensen, E.M. (2009). Graded synaptic transmission at the Caenorhabditis elegans neuromuscular junction. Proceedings of the National Academy of Sciences of the United States of America *106*, 10823-10828.

Llano, I., Gonzalez, J., Caputo, C., Lai, F.A., Blayney, L.M., Tan, Y.P., and Marty, A. (2000). Presynaptic calcium stores underlie large-amplitude miniature IPSCs and spontaneous calcium transients. Nat Neurosci *3*, 1256-1265.

Llinas, R., Steinberg, I.Z., and Walton, K. (1981). Relationship between presynaptic calcium current and postsynaptic potential in squid giant synapse. Biophys J *33*, 323-351.

Luo, L., Cook, N., Venkatachalam, V., Martinez-Velazquez, L.A., Zhang, X., Calvo, A.C., Hawk, J., MacInnis, B.L., Frank, M., Ng, J.H.*, et al.* (2014). Bidirectional thermotaxis in Caenorhabditis elegans is mediated by distinct sensorimotor strategies driven by the AFD thermosensory neurons. Proc Natl Acad Sci U S A *111*, 2776-2781.

Malsam, J., Kreye, S., and Sollner, T.H. (2008). Membrane fusion: SNAREs and regulation. Cell Mol Life Sci *65*, 2814-2832.

Manford, A.G., Stefan, C.J., Yuan, H.L., Macgurn, J.A., and Emr, S.D. (2012). ER-to-plasma membrane tethering proteins regulate cell signaling and ER morphology. Dev Cell *23*, 1129-1140.

Mani, M., and Ryan, T.A. (2009). Live imaging of synaptic vesicle release and retrieval in dopaminergic neurons. Front Neural Circuits *3*, 3.

Martin, J.A., Hu, Z., Fenz, K.M., Fernandez, J., and Dittman, J.S. (2011). Complexin has opposite effects on two modes of synaptic vesicle fusion. Current biology : CB *21*, 97-105.

Maximov, A., and Sudhof, T.C. (2005). Autonomous function of synaptotagmin 1 in triggering synchronous release independent of asynchronous release. Neuron *48*, 547-554.

McMahon, H.T., Missler, M., Li, C., and Sudhof, T.C. (1995). Complexins: cytosolic proteins that regulate SNAP receptor function. Cell *83*, 111-119.

Miesenböck, G., Angelis, D.D.A., and Rothman, J.E. (1998). Visualizing secretion and synaptic transmission with pH-sensitive green fluorescent proteins. Nature *394*, 192-195.

Millar, A.G., and Atwood, H.L. (2004). Crustacean phasic and tonic motor neurons. Integr Comp Biol *44*, 4-13.

Min, S.W., Chang, W.P., and Sudhof, T.C. (2007). E-Syts, a family of membranous Ca2+-sensor proteins with multiple C2 domains. Proc Natl Acad Sci U S A *104*, 3823-3828.

Mizuno, N., and Itoh, H. (2009). Functions and regulatory mechanisms of Gq-signaling pathways. Neurosignals *17*, 42-54.

Mochly-Rosen, D., and Gordon, A.S. (1998). Anchoring proteins for protein kinase C: a means for isozyme selectivity. FASEB J *12*, 35-42.

Moghadam, P.K., and Jackson (2013a). The functional significance of synaptotagmin diversity in neuroendocrine secretion. The functional significance of synaptotagmin diversity in neuroendocrine secretion.

Moghadam, P.K., and Jackson, M.B. (2013b). The functional significance of synaptotagmin diversity in neuroendocrine secretion. Front Endocrinol (Lausanne) *4*, 124.

Morgans, C.W. (2000). Neurotransmitter release at ribbon synapses in the retina. Immunol Cell Biol *78*, 442-446.

Motulsky, H., and Christopoulos, A. (2004). Fitting models to biological data using linear and nonlinear regression : a practical guide to curve fitting (Oxford ; New York: Oxford University Press).

Muller, M., Genc, O., and Davis, G.W. (2015). RIM-binding protein links synaptic homeostasis to the stabilization and replenishment of high release probability vesicles. Neuron *85*, 1056-1069.

Muller, M., Liu, K.S., Sigrist, S.J., and Davis, G.W. (2012). RIM controls homeostatic plasticity through modulation of the readily-releasable vesicle pool. J Neurosci *32*, 16574-16585.

Nagy, G., Matti, U., Nehring, R.B., Binz, T., Rettig, J., Neher, E., and Sorensen, J.B. (2002). Protein kinase C-dependent phosphorylation of synaptosome-associated protein of 25 kDa at Ser187 potentiates vesicle recruitment. J Neurosci *22*, 9278-9286.

Nakai, J., Ohkura, M., and Imoto, K. (2001). A high signal-to-noise Ca (2+) probe composed of a single green fluorescent protein. Nat Biotechnol *19*, 137-141.

Neves, G., Gomis, A., and Lagnado, L. (2001). Calcium influx selects the fast mode of endocytosis in the synaptic terminal of retinal bipolar cells. Proceedings of the National Academy of Sciences *98*, 15282-15287.

Neves, G., and Lagnado, L. (1999). The kinetics of exocytosis and endocytosis in the synaptic terminal of goldfish retinal bipolar cells. J Physiol. 181-202.

Nicholson-Tomishima, K., and Ryan, T.A. (2004). Kinetic efficiency of endocytosis at mammalian CNS synapses requires synaptotagmin I. Proc Natl Acad Sci U S A *101*, 16648-16652.

Nonet, M.L., Grundahl, K., Meyer, B.J., and Rand, J.B. (1993). Synaptic function is impaired but not eliminated in C. elegans mutants lacking synaptotagmin. Cell *73*, 1291-1305.

Nonet, M.L., Holgado, A.M., Brewer, F., Serpe, C.J., Norbeck, B.A., Holleran, J., Wei, L., Hartwieg, E., Jorgensen, E.M., and Alfonso, A. (1999). UNC-11, a Caenorhabditis elegans AP180 Homologue, Regulates the Size and Protein Composition of Synaptic Vesicles. Molecular Biology of the Cell.

Numazaki, M., Tominaga, T., Toyooka, H., and Tominaga, M. (2002). Direct phosphorylation of capsaicin receptor VR1 by protein kinase Cepsilon and identification of two target serine residues. J Biol Chem *277*, 13375-13378.

O'Rourke, N.A., Weiler, N.C., Micheva, K.D., and Smith, S.J. (2012). Deep molecular diversity of mammalian synapses: why it matters and how to measure it. Nature reviews Neuroscience *13*, 365-379.

Odermatt, B., Nikolaev, A., and Lagnado, L. (2012). Encoding of luminance and contrast by linear and nonlinear synapses in the retina. Encoding of luminance and contrast by linear and nonlinear synapses in the retina.

Okochi, Y., Kimura, K.D., Ohta, A., and Mori, I. (2005). Diverse regulation of sensory signaling by C. elegans nPKC-epsilon/eta TTX-4. The EMBO journal *24*, 2127-2137.

Osborne, S.L., Herreros, J., Bastiaens, P.I., and Schiavo, G. (1999). Calcium-dependent oligomerization of synaptotagmins I and II. Synaptotagmins I and II are localized on the same synaptic vesicle and heterodimerize in the presence of calcium. J Biol Chem *274*, 59-66.

Ou-yang, Y., Mellergard, P., and Siesjo, B.K. (1993). Regulation of intracellular pH in single rat cortical neurons in vitro: a microspectrofluorometric study. J Cereb Blood Flow Metab *13*, 827-840.

Pan, P.-Y.Y., and Ryan, T.A. (2012). Calbindin controls release probability in ventral tegmental area dopamine neurons. Nature neuroscience *15*, 813-815.

Parsons, T.D., Lenzi, D., Almers, W., and Roberts, W.M. (1994). Calcium-triggered exocytosis and endocytosis in an isolated presynaptic cell: capacitance measurements in saccular hair cells. Neuron *13*, 875-883.

Petrov, A.M., Giniatullin, A.R., and Sitdikova, G.F. (2008). The role of cGMP-dependent signaling pathway in synaptic vesicle cycle at the frog motor nerve terminals. J Neurosci. 3;28(49):13216-22

Pierce-Shimomura, J.T., Morse, T.M., and Lockery, S.R. (1999). The fundamental role of pirouettes in Caenorhabditis elegans chemotaxis. The J Neurosci. *19*, 9557-9569.

Piggott, B.J., Liu, J., Feng, Z., Wescott, S.A., and Xu, X.Z. (2011). The neural circuits and synaptic mechanisms underlying motor initiation in C. elegans. Cell *147*, 922-933.

Poirier, M.A., Xiao, W., Macosko, J.C., Chan, C., Shin, Y.K., and Bennett, M.K. (1998). The synaptic SNARE complex is a parallel four-stranded helical bundle. Nat Struct Biol *5*, 765-769.

Pokala, N., Liu, Q., Gordus, A., and Bargmann, C.I. (2014). Inducible and titratable silencing of Caenorhabditis elegans neurons in vivo with histamine-gated chloride channels. Proceedings of the National Academy of Sciences of the United States of America *111*, 2770-2775.

Poskanzer, K.E., Marek, K.W., Sweeney, S.T., and Davis, G.W. (2003). Synaptotagmin I is necessary for compensatory synaptic vesicle endocytosis in vivo. Nature *426*, 559-563.

Premkumar, L.S., and Ahern, G.P. (2000). Induction of vanilloid receptor channel activity by protein kinase C. Nature *408*, 985-990.

Prevedel, R., Yoon, Y.G., Hoffmann, M., Pak, N., Wetzstein, G., Kato, S., Schrodel, T., Raskar, R., Zimmer, M., Boyden, E.S.*, et al.* (2014). Simultaneous whole-animal 3D imaging of neuronal activity using light-field microscopy. Nat Methods *11*, 727-730.

Raley-Susman, K.M., Cragoe, E.J., Jr., Sapolsky, R.M., and Kopito, R.R. (1991). Regulation of intracellular pH in cultured hippocampal neurons by an amiloride-insensitive Na+/H+ exchanger. J Biol Chem *266*, 2739-2745.

Raley-Susman, K.M., Sapolsky, R.M., and Kopito, R.R. (1993). Cl-/HCO3- exchange function differs in adult and fetal rat hippocampal neurons. Brain Res *614*, 308-314.

Ramirez, D.M.O., and Kavalali, E.T. (2012). The role of non-canonical SNAREs in synaptic vesicle recycling. Cellular logistics.

Rangaraju, V., Calloway, N., and Ryan, T.A. (2014). Activity-driven local ATP synthesis is required for synaptic function. Cell *156*, 825-835.

Regehr, W.G. (2012). Short-term presynaptic plasticity. Cold Spring Harb Perspect Biol *4*, a005702.

Renden, R., Berwin, B., Davis, W., Ann, K., Chin, C.T., Kreber, R., Ganetzky, B., Martin, T.F., and Broadie, K. (2001). Drosophila CAPS is an essential gene that regulates dense-core vesicle release and synaptic vesicle fusion. Neuron *31*, 421-437.

Richmond, J. (2007). Synaptic function. *Wormbook, ed.* The *C. elegans* Resreach Community, Wormbook, doi/10.1985/wormbook.1.69.1, http://www.wormbook.org

Richmond, J.E., Davis, W.S., and Jorgensen, E.M. (1999). UNC-13 is required for synaptic vesicle fusion in C. elegans. Nature neuroscience *2*, 959-964.

Richmond, J.E., Weimer, R.M., and Jorgensen, E.M. (2001). An open form of syntaxin bypasses the requirement for UNC-13 in vesicle priming. Nature *412*, 338-341.

Rieke, F., and Schwartz, E.A. (1996). Asynchronous transmitter release: control of exocytosis and endocytosis at the salamander rod synapse. J Physiol *493 (Pt 1)*, 1-8.

Ritucci, N.A., Chambers-Kersh, L., Dean, J.B., and Putnam, R.W. (1998). Intracellular pH regulation in neurons from chemosensitive and nonchemosensitive areas of the medulla. Am J Physiol *275*, R1152-1163.

Rizo, J., and Sudhof, T.C. (2012). The membrane fusion enigma: SNAREs, Sec1/Munc18 proteins, and their accomplices--guilty as charged? Annu Rev Cell Dev Biol *28*, 279-308.

Rizo, J., and Xu, J. (2015). The Synaptic Vesicle Release Machinery. Annu Rev Biophys *44*, 339-367.

Rizzuto, R., and Pozzan, T. (2006). Microdomains of intracellular Ca2+: molecular determinants and functional consequences. Physiol Rev *86*, 369-408.

Robinson, M.S. (2015). Forty Years of Clathrin coated Vesicles. Traffic *16*, 1210-1238.

Rossano, A.J., Chouhan, A.K., and Macleod, G.T. (2013). Genetically encoded pH-indicators reveal activity-dependent cytosolic acidification of Drosophila motor nerve termini in vivo. The Journal of physiology *591*, 1691-1706.

Royle, S.J., and Lagnado, L. (2003). Endocytosis at the synaptic terminal. J Physiol *553*, 345-355.

Ruffin, V.A., Salameh, A.I., Boron, W.F., and Parker, M.D. (2014). Intracellular pH regulation by acid-base transporters in mammalian neurons. Front Physiol *5*, 43.

Ruiz-Montasell, B., Aguado, F., Majo, G., Chapman, E.R., Canals, J.M., Marsal, J., and Blasi, J. (1996). Differential distribution of syntaxin isoforms 1A and 1B in the rat central nervous system. Eur J Neurosci *8*, 2544-2552.

Saheki, Y., and Bargmann, C.I. (2009). Presynaptic CaV2 calcium channel traffic requires CALF-1 and the alpha (2)delta subunit UNC-36. Nature neuroscience *12*, 1257-1265.

Sankaranarayanan, S., Angelis, D.D., Rothman, J.E., and Ryan, T.A. (2000). The use of pHluorins for optical measurements of presynaptic activity. Biophysical journal *79*, 2199-2208.

Sankaranarayanan, S., and Ryan, T.A. (2000). Real-time measurements of vesicle-SNARE recycling in synapses of the central nervous system. Nature cell biology *2*, 197-204.

Sankaranarayanan, S., and Ryan, T.A. (2001). Calcium accelerates endocytosis of vSNAREs at hippocampal synapses. Nature neuroscience *4*, 129-136.

Sato, K., Ernstrom, G.G., Watanabe, S., Weimer, R.M., Chen, C.H., Sato, M., Siddiqui, A., Jorgensen, E.M., and Grant, B.D. (2009). Differential requirements for clathrin in receptor-mediated endocytosis and maintenance of synaptic vesicle pools. Proc Natl Acad Sci U S A *106*, 1139-1144.

Schafer, W.R. (2006). Neurophysiological methods in C. elegans: an introduction. *Wormbook, ed.* The *C. elegans* Resreach Community, Wormbook, doi/10.1985/wormbook.1.111.1, http://www.wormbook.org

Schiavo, G., Benfenati, F., Poulain, B., Rossetto, O., Polverino de Laureto, P., DasGupta, B.R., and Montecucco, C. (1992). Tetanus and botulinum-B neurotoxins block neurotransmitter release by proteolytic cleavage of synaptobrevin. Nature *359*, 832-835.

Schiavo, G., Gu, Q.M., Prestwich, G.D., Sollner, T.H., and Rothman, J.E. (1996). Calcium-dependent switching of the specificity of phosphoinositide binding to synaptotagmin. Proc Natl Acad Sci U S A *93*, 13327-13332.

Schneggenburger, R., and Neher, E. (2005). Presynaptic calcium and control of vesicle fusion. Curr Opin Neurobiol *15*, 266-274.

Schwiening, C.J., and Willoughby, D. (2002). Depolarization-induced pH microdomains and their relationship to calcium transients in isolated snail neurones. J Physiol *538*, 371-382.

Shang, Y., Claridge-Chang, A., Sjulson, L., Pypaert, M., and Miesenbock, G. (2007). Excitatory local circuits and their implications for olfactory processing in the fly antennal lobe. Cell *128*, 601-612.

Sieburth, D., Ch'ng, Q., Dybbs, M., Tavazoie, M., Kennedy, S., Wang, D., Dupuy, D., Rual, J.-F.F., Hill, D.E., Vidal, M.*, et al.* (2005). Systematic analysis of genes required for synapse structure and function. Nature *436*, 510-517.

Sieburth, D., Madison, J.M., and Kaplan, J.M. (2007). PKC-1 regulates secretion of neuropeptides. Nature neuroscience *10*, 49-57.

Slepnev, V.I., and Camilli, D.P. (2000). Accessory factors in clathrin-dependent synaptic vesicle endocytosis. Nature Reviews Neuroscience.

Smith, Renden, R., and von Gersdorff, H. (2008). Synaptic vesicle endocytosis: fast and slow modes of membrane retrieval. Trends Neurosci. 559-568

Smith, S.M., Renden, R., and von Gersdorff, H. (2008b). Synaptic vesicle endocytosis: fast and slow modes of membrane retrieval. Trends Neurosci *31*, 559-568.

Sollner, T., Bennett, M.K., Whiteheart, S.W., Scheller, R.H., and Rothman, J.E. (1993). A protein assembly-disassembly pathway in vitro that may correspond to sequential steps of synaptic vesicle docking, activation, and fusion. Cell *75*, 409-418.

Speese, S., Petrie, M., Schuske, K., Ailion, M., Ann, K., Iwasaki, K., Jorgensen, E.M., and Martin, T.F. (2007). UNC-31 (CAPS) is required for dense-core vesicle but not synaptic vesicle exocytosis in Caenorhabditis elegans. J. Neurosci *27*, 6150-6162.

Sudhof, T.C. (2002). Synaptotagmins: why so many? J Biol Chem *277*, 7629-7632.

Sudhof, T.C. (2004). The synaptic vesicle cycle. Annual review of neuroscience *27*, 509-547.

Sudhof, T.C. (2012). Calcium control of neurotransmitter release. Cold Spring Harb Perspect Biol *4*, a011353.

Südhof, T.C. (2013a). A molecular machine for neurotransmitter release: synaptotagmin and beyond. Nature medicine *19*, 1227-1231.

Südhof, T.C. (2013b). Neurotransmitter release: the last millisecond in the life of a synaptic vesicle. Neuron.

Sugita, S., Shin, O.H., Han, W., Lao, Y., and Sudhof, T.C. (2002). Synaptotagmins form a hierarchy of exocytotic Ca (2+) sensors with distinct Ca (2+) affinities. EMBO J *21*, 270-280.

Sun, M.K., and Alkon, D.L. (2014). The "memory kinases": roles of PKC isoforms in signal processing and memory formation. Prog Mol Biol Transl Sci *122*, 31-59.

Thoreson, W.B., Rabl, K., Townes-Anderson, E., and Heidelberger, R. (2004). A highly Ca2+-sensitive pool of vesicles contributes to linearity at the rod photoreceptor ribbon synapse. Neuron *42*, 595-605.

Tian, L., Hires, S.A., Mao, T., Huber, D., Chiappe, M.E., Chalasani, S.H., Petreanu, L., Akerboom, J., McKinney, S.A., Schreiter, E.R.*, et al.* (2009). Imaging neural activity in worms, flies and mice with improved GCaMP calcium indicators. Nature methods *6*, 875-881.

Tolkovsky, A.M., and Richards, C.D. (1987). Na+/H+ exchange is the major mechanism of pH regulation in cultured sympathetic neurons: measurements in single cell bodies and neurites using a fluorescent pH indicator. Neuroscience *22*, 1093-1102.

Tominaga, M., Wada, M., and Masu, M. (2001). Potentiation of capsaicin receptor activity by metabotropic ATP receptors as a possible mechanism for ATP-evoked pain and hyperalgesia. Proc Natl Acad Sci U S A *98*, 6951-6956.

Tomioka, M., Adachi, T., Suzuki, H., Kunitomo, H., Schafer, W.R., and Iino, Y. (2006). The insulin/PI 3-kinase pathway regulates salt chemotaxis learning in Caenorhabditis elegans. Neuron *51*, 613-625.

Torayama, I., Ishihara, T., and Katsura, I. (2007). Caenorhabditis elegans integrates the signals of butanone and food to enhance chemotaxis to butanone. The Journal of neuroscience : the official journal of the Society for Neuroscience *27*, 741-750.

Toulmay, A., and Prinz, W.A. (2012). A conserved membrane-binding domain targets proteins to organelle contact sites. J Cell Sci *125*, 49-58.

Trapp, S., Lückermann, M., Kaila, K., and Ballanyi, K. (1996). Acidosis of hippocampal neurones mediated by a plasmalemmal Ca2+/H+ pump. Neuroreport *7*, 2000-2004.

Traub, L.M. (2009). Tickets to ride: selecting cargo for clathrin-regulated internalization. Nat Rev Mol Cell Biol *10*, 583-596.

Trimble, W.S., Gray, T.S., Elferink, L.A., Wilson, M.C., and Scheller, R.H. (1990). Distinct patterns of expression of two VAMP genes within the rat brain. J Neurosci *10*, 1380-1387.

Troemel, E.R., Sagasti, A., and Bargmann, C.I. (1999). Lateral signaling mediated by axon contact and calcium entry regulates asymmetric odorant receptor expression in C. elegans. Cell *99*, 387-398.

Tsalik, E.L., and Hobert, O. (2003). Functional mapping of neurons that control locomotory behavior in Caenorhabditis elegans. J Neurobiol *56*, 178-197.

Tsunozaki, M., Chalasani, S.H., and Bargmann, C.I. (2008). A behavioral switch: cGMP and PKC signaling in olfactory neurons reverses odor preference in C. elegans. Neuron *59*, 959-971.

Ullrich, B., Li, C., Zhang, J.Z., McMahon, H., Anderson, R.G., Geppert, M., and Sudhof, T.C. (1994). Functional properties of multiple synaptotagmins in brain. Neuron *13*, 1281-1291.

Vanlandingham, P.A., Barmchi, M.P., Royer, S., and Green, R. (2014). AP180 Couples Protein Retrieval to Clathrin-Mediated Endocytosis of Synaptic Vesicles. Traffic.

Varoqueaux, F., Sigler, A., Rhee, J.-S.S., Brose, N., Enk, C., Reim, K., and Rosenmund, C. (2002). Total arrest of spontaneous and evoked synaptic transmission but normal synaptogenesis in the absence of Munc13-mediated vesicle priming. Proceedings of the National Academy of Sciences of the United States of America *99*, 9037-9042.

Varshney, L.R., Chen, B.L., Paniagua, E., Hall, D.H., and Chklovskii, D.B. (2011). Structural properties of the Caenorhabditis elegans neuronal network. PLoS Comput Biol *7*, e1001066.

Verhage, M., Maia, A.S., Plomp, J.J., Brussaard, A.B., Heeroma, J.H., Vermeer, H., Toonen, R.F., Hammer, R.E., van den Berg, T.K., Missler, M.*, et al.* (2000). Synaptic assembly of the brain in the absence of neurotransmitter secretion. Science *287*, 864-869.

Voglmaier, S.M., Kam, K., Yang, H., Fortin, D.L., Hua, Z., Nicoll, R.A., and Edwards, R.H. (2006). Distinct endocytic pathways control the rate and extent of synaptic vesicle protein recycling. Neuron *51*, 71-84.

von Gersdorff, H., and Matthews, G. (1994). Dynamics of synaptic vesicle fusion and membrane retrieval in synaptic terminals. Nature *367*, 735-739.

Wakabayashi, T., Kitagawa, I., and Shingai, R. (2004). Neurons regulating the duration of forward locomotion in Caenorhabditis elegans. Neurosci Res *50*, 103-111.

Wang, G.J., Randall, R.D., and Thayer, S.A. (1994). Glutamate-induced intracellular acidification of cultured hippocampal neurons demonstrates altered energy metabolism resulting from Ca2+ loads. J Neurophysiol *72*, 2563-2569.

Wang, H., Girskis, K., Janssen, T., Chan, J.P., Dasgupta, K., Knowles, J.A., Schoofs, L., and Sieburth, D. (2013). Neuropeptide secreted from a pacemaker activates neurons to control a rhythmic behavior. Curr Biol *23*, 746-754.

Watanabe, S., Liu, Q., Davis, W.M., Hollopeter, G., Thomas, N., Jorgensen, N.B., and Jorgensen, E.M. (2013a). Ultrafast endocytosis at Caenorhabditis elegans neuromuscular junctions. eLife *2*.

Watanabe, S., Rost, B.R., Camacho-Pérez, M., Davis, M.W., Söhl-Kielczynski, B., Rosenmund, C., and Jorgensen, E.M. (2013b). Ultrafast endocytosis at mouse hippocampal synapses. Nature *504*, 242-247.

Watanabe, S., Trimbuch, T., Camacho-Pérez, M., Rost, B.R., Brokowski, B., Söhl-Kielczynski, B., Felies, A., Davis, W.M., Rosenmund, C., and Jorgensen, E.M. (2014). Clathrin regenerates synaptic vesicles from endosomes. Nature *515*, 228-233.

Weber, T., Zemelman, B.V., McNew, J.A., Westermann, B., Gmachl, M., Parlati, F., Sollner, T.H., and Rothman, J.E. (1998). SNAREpins: minimal machinery for membrane fusion. Cell *92*, 759-772.

Weimer, R.M., Gracheva, E.O., Meyrignac, O., Miller, K.G., Richmond, J.E., and Bessereau, J.L. (2006). UNC-13 and UNC-10/rim localize synaptic vesicles to specific membrane domains. J Neurosci *26*, 8040-8047.

Weimer, R.M., Richmond, J.E., Davis, W.S., Hadwiger, G., Nonet, M.L., and Jorgensen, E.M. (2003). Defects in synaptic vesicle docking in unc-18 mutants. Nature neuroscience *6*, 1023-1030.

Werth, J.L., and Thayer, S.A. (1994). Mitochondria buffer physiological calcium loads in cultured rat dorsal root ganglion neurons. J Neurosci *14*, 348-356.

Wes, P.D., and Bargmann, C.I. (2001). C. elegans odour discrimination requires asymmetric diversity in olfactory neurons. Nature *410*, 698-701.

White, J.G., Southgate, E., Thomson, J.N., and Brenner, S. (1986). The Structure of the Nervous-System of the Nematode Caenorhabditis-Elegans. Philos T Roy Soc B *314*, 1-340.

Wierda, K.D., Toonen, R.F., de Wit, H., Brussaard, A.B., and Verhage, M. (2007). Interdependence of PKC-dependent and PKC-independent pathways for presynaptic plasticity. Neuron *54*, 275-290.

Wragg, R.T., Snead, D., Dong, Y., Ramlall, T.F., Menon, I., Bai, J., Eliezer, D., and Dittman, J.S. (2013). Synaptic vesicles position complexin to block spontaneous fusion. Neuron *77*, 323-334.

Wu, L.G., Ryan, T.A., and Lagnado, L. (2007). Modes of vesicle retrieval at ribbon synapses, calyx-type synapses, and small central synapses. J. Neurosci. 11793-802

Xie, C., Su, H., Guo, T., Yan, Y., Peng, X., Cao, R., Wang, Y., Chen, P., Wang, X., and Liang, S. (2014). Synaptotagmin I delays the fast inactivation of Kv1.4 channel through interaction with its N-terminus. Mol Brain *7*, 4.

Xu, J., Mashimo, T., and Südhof, T.C. (2007). Synaptotagmin-1,-2, and-9: Ca 2+ sensors for fast release that specify distinct presynaptic properties in subsets of neurons. Neuron, 54(4):567-81.

Xue, M., Lin, Y.Q., Pan, H., Reim, K., Deng, H., and Bellen, H.J. (2009a). Tilting the balance between facilitatory and inhibitory functions of mammalian and Drosophila Complexins orchestrates synaptic vesicle exocytosis. Neuron.

Xue, M., Lin, Y.Q., Pan, H., Reim, K., Deng, H., Bellen, H.J., and Rosenmund, C. (2009b). Tilting the balance between facilitatory and inhibitory functions of mammalian and Drosophila Complexins orchestrates synaptic vesicle exocytosis. Neuron *64*, 367-380.

Yang, H., Liu, H., Hu, Z., Zhu, H., and Xu, T. (2005). PKC-induced sensitization of Ca2+-dependent exocytosis is mediated by reducing the Ca2+ cooperativity in pituitary gonadotropes. J Gen Physiol *125*, 327-334.

Yang, Y., Udayasankar, S., Dunning, J., Chen, P., and Gillis, K.D. (2002). A highly Ca2+-sensitive pool of vesicles is regulated by protein kinase C in adrenal chromaffin cells. Proc Natl Acad Sci U S A *99*, 17060-17065.

Yao, H., Ma, E., Gu, X.Q., and Haddad, G.G. (1999). Intracellular pH regulation of CA1 neurons in Na (+)/H (+) isoform 1 mutant mice. J Clin Invest *104*, 637-645.

Yawo, H. (1999). Protein kinase C potentiates transmitter release from the chick ciliary presynaptic terminal by increasing the exocytotic fusion probability. The Journal of physiology *515 (Pt 1)*, 169-180.

Yizhar, O., Matti, U., Melamed, R., Hagalili, Y., Bruns, D., Rettig, J., and Ashery, U. (2004). Tomosyn inhibits priming of large dense-core vesicles in a calcium-dependent manner. Proc Natl Acad Sci U S A *101*, 2578-2583.

Zaslaver, A., Liani, I., Shtangel, O., Ginzburg, S., Yee, L., and Sternberg, P.W. (2015). Hierarchical sparse coding in the sensory system of Caenorhabditis elegans. Proc Natl Acad Sci U S A *112*, 1185-1189.

Zhan, R.Z., Fujiwara, N., Yamakura, T., Taga, K., Fukuda, S., Endoh, H., and Shimoji, K. (1997). NMDA induces a biphasic change in intracellular pH in rat hippocampal slices. Brain Res *760*, 179-186.

Zhang, B., Koh, Y.H., Beckstead, R.B., Budnik, V., Ganetzky, B., and Bellen, H.J. (1998). Synaptic vesicle size and number are regulated by a clathrin adaptor protein required for endocytosis. Neuron *21*, 1465-1475.

Zhang, X., and Cote, R.H. (2005). cGMP signaling in vertebrate retinal photoreceptor cells. Frontiers in bioscience *10*, 1191-1204.

Zhang, Z., Nguyen, K.T., Barrett, E.F., and David, G. (2010). Vesicular ATPase inserted into the plasma membrane of motor terminals by exocytosis alkalinizes cytosolic pH and facilitates endocytosis. Neuron *68*, 1097-1108.

Zhao, H., and Nonet, M.L. (2001). A conserved mechanism of synaptogyrin localization. Mol Biol Cell *12*, 2275-2289.

Zhu, H., Hille, B., and Xu, T. (2002). Sensitization of regulated exocytosis by protein kinase C. Proc Natl Acad Sci U S A *99*, 17055-17059.